DOE/ER-0045/2

Alloy Development for Irradiation Performance

Quarterly Progress Report
For Period Ending March 31, 1980

U.S. Department of Energy
Assistant Secretary for Energy Technology
Office of Fusion Energy

Printed in the United States of America. Available from
National Technical Information Service
U.S. Department of Commerce
5285 Port Royal Road, Springfield, Virginia 22161
NTIS price codes—Printed Copy: A12 Microfiche A01

This report was prepared as an account of work sponsored by an agency of the United States Government. Neither the United States Government nor any agency Ihereof, nor any of their employees, makes any warranty, express or implied, or assumes any legal liability or responsibility for the accuracy, completeness, or usefulness of any information, apparatus, product, or process disclosed, or represents that its use would not infringe privately owned rights. Reference herein to any specific commercial product, process, or service by tradename, trademark, manufacturer, or otherwise, does not necessarily constitute or imply its endorsement, recommendation, or favoring by the United States Government or any agency thereof. The views and opinions of authors expressed herein do not necessarily state or reflect those of the United States Government or any agency thereof.

DOE/ER-0045/2
Distribution
Category
uc-20. 20c

ALLOY DEVELOPMENT FOR IRRADIATION PERFORMANCE QUARTERLY PROGRESS REPORT FOR PERIOD ENDING MARCH 31,1980

Compiled and Edited by B. G. Ashdown. ORNL,
from Contributions of Participating Laboratories

ARGONNE NATIONAL LABORATORY

GENERAL ATOMIC COMPANY

HANFORD ENGINEERING DEVELOPMENT LABORATORY

McDONNELL DOUGLAS ASTRONAUTICS COMPANY

NAVAL RESEARCH LABORATORY

OAK RIDGE NATIONAL LABORATORY

SANDIA NATIONAL LABORATORIES

WESTINGHOUSE FUSION POWER SYSTEMS

Date Published: June 1980

Prepared by
OAK RIDGE NATIONAL LABORATORY
Oak Ridge, Tennessee 37830
operated by
UNION CARBIDE CORPORATION
for the
DEPARTMENT OF ENERGY
Under Contract No. W-7405-eng-26

FOREWORD

This report is the ninth in a series of Quarterly Technical Progress Reports on *"Alloy Development for Irradiation Performance"* (ADIP), which is one element of the Fusion Reactor Materials Program, conducted in support of the Magnetic Fusion Energy Program of the U.S. Department of Energy. Other elements of the Materials Program are:

- *Damage Analysis and Fundamental Studies (DAFS)*
- *Plasma-Materials Interaction (PMI)*
- *Special-Purpose Materials (SPM)*

The first seven reports in this series are numbered DOE/ET-0058/1 through 7. This report is the second in a new numbering sequence that begins with DOE/ER-0045/1.

The ADIP program element is a national effort composed of contributions from a number of National Laboratories and other government laboratories, universities, and industrial laboratories. It was organized by the Materials and Radiation Effects Branch, Office of Fusion Energy, DOE, and a Task Group on *Alloy Development for Irradiation Performance,* which operates under the auspices of that Branch. The purpose of this series of reports is to provide a working technical record of that effort for the use of the program participants, for the fusion energy program in general, and for the Department of Energy.

This report is organized along topical lines in parallel to a Program Plan of the same title so that activities and accomplishments may be followed readily relative to that Program Plan. Thus, the work of a given laboratory may appear throughout the report. Chapters 1, 2, 8, and 9 review activities on analysis and evaluation, test methods development, status of irradiation experiments, and corrosion testing and hydrogen permeation studies, respectively. These activities relate to each of the alloy development paths. Chapters 3, 4, 5, 6, and 7 present the ongoing work on each alloy development path. The Table of Contents is annotated for the convenience of the reader.

This report has been compiled and edited under the guidance of the Chairman of the Task Group on *Alloy Development for Irradiation Performance,* E. E. Bloom, Oak Ridge National Laboratory, and his efforts, those of the supporting staff of ORNL and the many persons who made technical contributions are gratefully acknowledged. T. C. Reuther, Materials and Radiation Effects Branch, is the Department of Energy Counterpart to the Task Group Chairman and has responsibility for the ADIP Program within DOE.

Klaus M. Zwilsky, Chief,
Materials and Radiation Effects Branch
Office of Fusion Energy

CONTENTS

FOREWORD.. iii

1. ANALYSIS AND EVALUATION STUDIES 2

1.1 Materials Handbook for Fusion Energy Systems (McDonnell Douglas Astronautics Company and Hanford Engineering Development Laboratory) . . . . . .

The handbook activity is well underway with requests for data sheets being issued and initial information sheets relating to format, contents, and objectioe completed and ready for publication. The schedule for publication of the data sheets on Austenitic stainless steel is targeted for September 1, with the sheets ready for review on July 15. Discussions with M. L. Grossbeck, who has lead responsibility for the preparation of the austenitic stainless steel data sheets, indicates that work is currently progressing on schedule. Requests for data sheets and/or assistance in developing correlations have been directed to the DAFS and PMI tusk groups. The DAFS group has been asked to develop correlations relating dpa, He, and MW•Yr/m^2. The PMI group has been requested to develop a uniform set of sputtering yields and a model or approach to predict the particle fluxes to the first wall, limiter, and divertor collector plates.

2. TEST MATRICES AND TEST METHODS DEVELOPMENT 5

2.1 Prototype Testing of MFE-5 In-Reactor Fatigue Crack Growth Experiment (Hanford Engineering Development Laboratory) . . 6

Fabrication of the prototypic fatigue mzchine is completed, and testing at HEDL has commenced. Successful performance of the prototype was demonstrated through a series of tests on mock-up and actual specimens. Results of specimen chain tests were consistent with previously published results obtained from conventional specimens and test apparatus.

2.2 Progress on the ORR-MFE-4 Spectral Tailoring Experiment (Oak Ridge National Laboratory) 14

The hardware for ME-4A (300 and 400°C) is now fabricated and assembled to the point of specimen loading. Only pressurization of the Prime Candidate Alloy tubes remains to be completed. All other specimens are ready for loading. Experiment MFE-4A is scheduled to be installed in the ORR in the latter half of April 1980. Experiment MFE-4B (500 and 600°C) is scheduled for insertion in June 1980.

2.3 Neutronic Calculations for the Conceptual Design of an "In-Pile" Solid Breeder Experiment IPSB-01 (Oak Ridge National Laboratory) 16

A model has been developed that represents the solid breeder experiment and the adjacent fuel regions of the ORR core. This model and appropriate data sets will be used in transport calculations to provide tritium production and nuclear heating rates for operation of the experiment in the ORR.

3. PATH A ALLOY DEVELOPMENT — AUSTENITIC STAINLESS STEELS 19

3.1 Design and Fabrication of Preirradiation Microstructures in Path A Prime Candidate Alloy (Oak Ridge National Laboratory) 20

Previous work designed microstructures that might provide optimum irradiation response of the Path A PCA. The fabrication problems encountered with producing homogeneous Path A PCA material were solved, and the response to short-tern thermal aging was investigated. The specification of desired microstructures was revised to be consistent with the aging results; practical fabrication sequences and TMTs were suggested. The current work examines the success of the revised fabrication and TMT in producing the desired microstructures and characterizes the microstructures achieved.

3.2 High-Cycle Fatigue Testing of HFIR-Irradiated 20%-Cold-Worked Type 316 Stainless Steel (Oak Ridge National Laboratory) 33

Work is now in progress to extend previously reported low-cycle fatigue data to the high-cycle regime. A series of unirradiated specimens was tested under high-cycle conditions, but only one irradiated specimen has been tested. Results are encouraging in that an endurance limit appears to have been reached at a strain range of 0.3%.

3.3 The Effect of Preinjected Helium on the Microstructure and Tensile Properties of EBR-11-Irradiated 20%-Cold-Worked Type 316 Stainless Steel (Oak Ridge National Laboratory) 35

Samples of 20%-cold-worked type 316 stainless steel have been irradiated to 8.4 dpa in EBR-II. Irradiation temperatures were 500 and 625°C, and the content of helium (injected near room temperature) was 0, 110, or 200 at. ppm. Samples for all conditions were examined by transmission electron microscopy (TEM), and those irradiated at 625°C were postirradiation tensile tested at the

same temperature. The microstructure of uninjected material shows sparse precipitation of tau and eta phase, a recovered dislocation structure, and no cavities or voids at either 500 or 625°C. Helium preinjection has no significant effect on the dislocation structure at either temperature. Furthermore, preinjection of 110 at. ppm He and irradiation at 500°C produces no resolvable (greater than about 3 nm) distribution of cavities but does reduce slightly eta and tau formation and does enhance Laves formation compared with uninjected material. Preinjection of either 110 or 200 at. ppm He and irradiation at 625°C produces a distribution of about 1 × 10^{22} cavities/m^3, 4 to 5 nm in diameter, on the dislocation structure. Copious precipitation of Laves, eta, and/or tau was observed. These results are compared with the same material after thermal aging or HFIR irradiation at similar temperatures and times. Some microstructural components differ significantly. Tensile testing at 625°C of the uninjected material shows a decrease in strength and increase in elongation compared with unirradiated material. Helium preinjected material generatty shows greater strength but reduced ductility compared with uninjected material.

4. PATH B ALLOY DEVELOPMENT — Fe-Ni-Cr ALLOYS 59

5. PATH C ALLOY DEVELOPMENT — REACTIVE *AND* REFRACTORY ALLOYS . . . 61

5.1 TZM and Nb-1Zr Irradiated to High Fluence (Hanford Engineering Development Laboratory) . . . . . .

TZM and Nb-1Zr are found to be low swelling materials during irradiation to 1.4 × 10^{23} n/cm^2 (E >0.1 MeV) over the temperature range 400 to 650°C. Peak swelling in TZM after irradiation at 590 and 650°C is 3%, and peak swelling in Nb-1Zr after irmdiation at 650°C is 0.6%. Neither void shrinkage nor swelling saturation was observed in TZM.

5.2 Effect of Hydrogen on Flaw Growth of Titanium Alloy Ti-6242s (McDonnell Douglas Astronautics Company) . . 71

Hydrogen charging of Ti-6242s material is complete. Machining of modified-WOL specimens is in progress. No spontaneous hydride precipitation was observed in the material hydrogen charged to 24,100 appm (530 wppm). Room temperature tensile properties were slightly higher for the hydrogen charged specimens than for the as-received specimens.

5.3 Mechanical Property Testing of Unirradiated Path C Alloys (Oak Ridge National Laboratory) 79

Miniature hourglass-shaped fatigue specimens of V—15% Cr—5% Ti have been machined and heat-treated to the desired microstructure of cyclic fatigue testing. Strain-controlled fatigue tests on Nb—1% Zr indicate that the alloy has about the same fatigue resistance at room temperature and at 650°C. Limited data suggest that this alloy has marginally better fatigue properties than does 20%-cold-worked type 316 stainless steel for low strain ranges at 430°C.

6. PATH D ALLOY DEVELOPMENT — INNOVATIVE MATERIAL CONCEPTS 85

7. PATH E ALLOY DEVELOPMENT — FERRITIC STEELS 87

7.1 Mechanical Property Measurements of HT-9 Hydrogen: 25 to 400°C (Sandia National Laboratories) 88

The presence of interstitial hydrogen, in concentrations as low as 1-2 weight ppm, is known to severely affect the fracture behavior of martensitic steels. The embrittling effect increases with lattice concentration of hydrogen and with increases in the yield strength of the alloy in question. The effect of temperature is more complex, however, with a maximum in embrittlement evident near room temperature. This report summarizes the first experiments to evaluate the hydrogen compatibility of HT-9 and to separate the effects of temperature and hydrogen pressure. Tensile tests were performed in air and 15 psi hydrogen at test temperatures of 25, 200, 300 and 400°C and at 25°C in hydrogen pressures of 15, 1000, 2000, 3000 and 5000 psi. The results show that elevated temperatures eliminate any hydrogen effects, consistent with the behavior of other steels having similar strengths. Increasing pressures, however, cause a strong shift in ductility, with an -60% loss in ductility occurring in 5000 psi hydrogen.

7.2 Weldability of HT9: The Autogeneous GTA Process (Sandia National Laboratories) 98

The autogenous GTA process was selected in order to produce a variety of microstructures which will normally be observed in HT9 weldments. Evaluation of the as-welded microstructures indicated that the rapid cooling mtes associated with the weld thermal cycle imparted full martensitic hardness to the fusion zone and portions of the HAZ. At least four distinct regions have been identified within the HAZ; each region could be related to the equilibrium phase diagram of the Fe-12Cr-0.2C alloy system.

7.3 Procurement of National 12 Cr Heat and Evaluation of Welding Procedures for Irradiation Specimens (General Atomic Company) 109

A 14,700 kg (32,500 lb) heat of 12 Cr-1 Mo-0.3 V steel was procured for use by all participants in the National Fusion Ferritic Steel Program. Preliminary analysis indicated that the ingot composition met specifications.

A preliminary evaluation of candidate welding procedures for 12 Cr-1 Mo-0.3 V EBR-11 irradiation weld specimens was completed. The procedure selected for producing the specimens was completed. The procedure selected for producing the specimens was gas-tungsten arc (GTA) with a pre-heat temperature of 93°C.

7.4 **Microstructural and Fatigue Crack Growth Characterization of HT-9 (Hanford Engineering Development Laboratory) . . .** 132

A microstructural characterization of nonirradiated HT-9 has been completed. Selected thermomechanical heat treatments were chosen for study. Heat treatment times for 0.30 to 2.54 mm section thickness were identified by characterizing the austenization behavior of the ferritic alloy. A tempering curve was constructed and complementary transmission election microscopy micrographs taken. Fatigue crack growth and fracture toughness studies were completed on four over-tempered conditions of the alloy. Eased on the microstructural and mechanical properties studied, an optimum thermomechanicat heat treatment for HT-9 was selected.

7.5 Fracture Toughness Tests on HT-9 at Elevated Temperatures (Hanford Engineering Development Laboratory) 156

Single specimen J-integral fracture toughness measurements were rmde at 149°C and 232°C on HT-9 specimens. The electropotentiat technique developed in past work was applied for elevated temperature tests to obtain a calibration curve correlating voltage change to crack extension. Based on this calibration curve, the J versus a curves were generated from single specimens. The test results show that the electropotential technique for single specimen measurements is successful at elevated temperatures, where temperature gradients are of concern. The upper shelf fracture toughness of HT-9 is evaluated as a function of temperature.

7.6 The Fracture Resistance of HT-9 After Irradiation at Elevated Temperature (Naval Research Laboratory) 163

HT-9, a 12 percent Cr martensitic stainless steel of interest for use in ducts for fast reactors and as a first wall material in magnetic fusion reactors, was irradiated in EBR-11 to obtain the first evaluation of fracture toughness changes produced by high temperature-high fluence irradiation in this class of alloy.

Charpy-V notch, precracked Charpy and tensile specimens were used to evaluate the tensile and fracture behavior of this steel in the as-received condition, after 5000 h of aging at 427 and at 538°C and after irradiation to a fluence of 1.1 × 10^{22} n/cm^2 E > 0.1 MeV at 419°C in flowing sodium. The results show some tendency toward temper embrittlement at 538°C and a 108°C shift in the ductile-to-brittle transition after irmdiation at 419°C. Charpy-V energies on the upper shelf are also depressed by the irradiation but maintain adequate levels for the applications intended. Possible mechanisms for the observed response are discussed.

7.7 Environmental Effects on Properties of Ferritic Steels (Argonne National Laboratory) 181

This program is part of a more comprehensive program to investigate the potential of ferritic steels for fusion reactor first-wall blanket structures. Test environments to be investigated include lithium, water, and helium with appropriate impurities as well as candidate solid breeding materials and neutron multipliers. Emphasis will be placed on the combined effect of stress and chemical environment on corrosion and mechanical properties of ferritic steels. Initial tests will focus on the Sandvik Alloy HT-9 and a developmental Fe-9Cr-1Mo alloy.

This program was initiated in the first quarter of FY 1980 with initial phases of the program focused on (1) combined effects of stress and coolant environment on the corrosion behavior and fatigue properties of ferritic steels and (2) the compatibility of ferritic steels with candidate solid tritium-breeding mterials and neutron multipliers, viz., Li_2O, $LiAlO_2$, and Li_2SiO_3.

8. STATUS OF IRRADIATION EXPERIMENTS AND MATERIALS INVENTORY . . . 185

8.1 Irradiation Experiment Status and Schedule 186

Bar charts show the irradiation experiments schedule, including experiments completed, in progress, and planned. Experiments are presently under way in the ORR and the HFIR, which are mixed-spectrum reactors, and in the EBR-11, which is a fast reactor.

8.2 ETM Research Materials Inventory (Oak Ridge National Laboratory and McDonnell Douglas Astronautics Company) . . 193

The Office of Fusion Energy has assigned program responsibility to ORNL for the establishment and operation of a central inventory of research materials to be used in the Fusion Reactor Materials research and development programs. The objective is to provide a common supply of materials for the Fusion Reactor Materials Program. This wilt minimize unintended materials variables and provide for economy in procurement and for centralized record-keeping. Initially this inventory is to focus on materials related to first-wall and structural applications and related research, but various special purpose materials may be added in the future.

9. CORROSION TESTING AND HYDROGEN PERMEATION STUDIES 199

9.1 Hydrogen Dissolution and Permeation Studies of ADIP Program Alloys (Argonne National Laboratory) 200

Efforts to characterize the hydrogen dissolution and permeation characteristics of alloys currently under development in the ADIP Program have continued. Two sets of Ti-6Al-2Sn-4Zr-2Mo-0.08Si plates were loaded with controlled quantities of hydrogen using an existing tensimetric apparatus at ANL. Chemical analyses made at MDAC a one of the two sets confirmed the adequacy of the loading method (540-560 wppm H analyzed versus 500 ± 10 wppm H determined from tensimetric additions). During the course of the loadings, it was found that dehydriding of alloy plates from 500-700 wppm H to lower values) could not be readily achieved without heating the material to well over 600°C. These plates will be used by MDAC to conduct metallurgical and mechanical analyses of hydrogen effects on titanium alloys. In another study, an experiment was conducted to measure the hydrogen permeation characteristics of Fecralloy (Fe-16Cr-5Al-0.3Y) between 190 and 680°C using hydrogen driving pressures in the range from 2 to 1.5 × 10^4 Pa. Comparison of the data from this study with similar results for Fe-Cr alloys having 0 and 2 wt.% Al showed that the aluminum content required to achieve the maximum hydrogen permeation resistance for these alloys in oxidizing environments may be less than 2 wt.% in some cases and could be related to the chromium content in the alloy.

9.2 Vanadium Alloy/Lithium Pumped-Loop Studies (Argonne National Laboratory) 206

The stainless steel-clad vanadium alloy loop with circulating lithium has continued to operate through the second quarter of FY 1960. Test samples of zirconium, vanadium, V-15Cr-5Ti, titanium, and yttrium have been exposed at 600°C to investigate the distribution of nonmetallic elements in lithium/refractory metal systems. The zirconium, titanium, and yttrium exposures are being used to adjust and evaluate the nonmetallic (O, N, H, and C) concentration in lithium. Results of hydrogen analyses of the test samples have been compared with calculated distribution coefficients for hydrogen. Preliminary measurements of the distribution coefficients for nitrogen between vanadium and lithium at 600°C are in good agreement with calculated values.

9.3 Compatibility of 2 1/4 Cr-1 Mo Steel with Static Lithium (Oak Ridge National Laboratory) 213

Tensile specimens of 2 1/4 Cr-1 Mo steel were exposed to static molten lithium at 500°C. After 500 and 1000 h, weight changes were negligible; however, the yield and ultimate tensile strengths of the steel were consistently lower by 4 to 10% than those of specimens thermally aged in argon for the same lengths of time. Analysis of the post-test lithium indicated a transfer of carbon from the steel to the lithium during exposure. Specimens that were normalized and tempered lost less carbon than those that were simply annealed. The carbon concentration of the post-test lithium was greater than predicted by thermodynamic calculations. Therefore, it is believed that the predicted concentrations are in error because the assumption of equilibrium among carbon, molybdenum, and chromium in the steel is not met by the heat treatment conditions used.

9.4 Mass Transfer of Type 316 Stainless Steel and Path B Alloys in Lithium Thermal-Convection Loops (Oak Ridge National Laboratory) 219

Metallographic and surface composition data are reported for the corrosion of ADIP alloys B1 and B3 [58 Fe-24.5 Ni-10 Cr-1 Mo-1 Mn-1.5 Al-3 Ti (wt %) and 55 Fe-30 Ni-12 Cr-2 Nb-1 Mn-2 Ti (wt %), respectively] in lithium flowing between 500 and 300°C. At 500°C both alloys were severely depleted of nickel and exhibited porous near-surface regions. Alloy B3 had a larger volume fraction of porosity. Results on deposition rates vs

exposure time in lithiumtype 316 stainless steel thermal-convection loops are also presented. Deposition mtes in lithium flowing between 600 and 450°C are initially much higher than those measured at later operating times. The decrease in the deposition mte can be correlated with observed changes in the deposition process.

1. ANALYSIS AND EVALUATION STUDIES

1.1 MATERIALS HANDBOOK FOR FUSION ENERGY SYSTEMS - J. W. Davis (McDonnell Douglas Astronautics Company–St. Louis) and J. C. Spanner (Hanford Engineering Development Laboratory)

1.1.1 ADIP Task

Task Number 1.A.1 - Define material property requirements and make structural life predictions.

1.1.2 Objective

To provide an authoritative and consistent source of material property data for use by the fusion energy community in concept evaluation design, safety analysis, and performance/verification.

1.1.3 Summary

The handbook activity is well underway with requests for data sheets being issued and initial information sheets relating to format, contents, and objective completed and ready for publication. The schedule for publication of the data sheets on Austenitic stainless steel is targeted for September 1, with the sheets ready for review on July 15. Discussions with M. L. Grossbeck, who has lead responsibility for the preparation of the austenitic stainless steel data sheets, indicates that work is currently progressing on schedule. Requests for data sheets and/or assistance in developing correlations have been directed to the DAFS and PMI task groups. The DAFS group has been asked to develop correlations relating dpa, He, and $MW \cdot Yr/m^2$. The PMI group has been requested to develop a uniform set of sputtering yields and a model or approach to predict the particle fluxes to the first wall, limiter, and divertor collector plates.

1.1.4 Progress and Status

The Analysis and Evaluation sub-task group of ADIP has identified a series of data needs necessary to support the ETF design study. These data needs along with their associated priorities were developed from information supplied by R. E. Nygren (ETF materials) along with various design groups working on ETF. These data needs and priorities were

subsequently transmitted by the A&E sub-task group to the Materials Hand book activity for implementation. Acting upon these directives the Handbook activity has initiated a series of requests for data to the appropriate working group within **ADIP** following tne procedure described in the previous quarterly.

The most pressing data needs at this time are the properties pertaining to the type 316 austenitic stainless steel since it is the baseline or reference alloy for the ETF. As a result a request for data has been transmitted to M. L. Grossbeck (ORNL), Chairman of the sub-working group on austenitic stainless steels to assign an individual who would be responsible for coordinating the preparation of these data sheets. He has subsequently accepted this assignment and will be responsible for the preparation of data sheets relating to tensile properties and swelling. He has also requested the assistance of F. A. Smidt (NRL) in the preparation of data sheets relating to fatigue and B. A. Chin (HEDL) for data sheets on crack growth and creep; both are members of his working group on austenitic stainless steels. The anticipated schedule for completion of these data sheets by this group is July 15, at which time the prepared data sheets will be submitted for review and comments and released for inclusion in the handbook around September 1.

A back-up structural material for the ETF are the ferritic steels (martinsetic stainless steel). Original plans called for the project to explore the possible benefits of a ferritic first wall or shield in relation to the 316 stainless steel in the Spring. However, this effort has been differed to later in the year and as a result the schedule for preparation of these data sheets will be extended to late August. A letter requesting this work and associated schedule has been sent to S. N. Rossenwasser (GA), Chairman of the working group on Ferritic steels, requesting his assistance in this work.

Since in some cases the data requirements for ETF and other systems (EBT-P and Starfire) are broader than the expertise currently available in ADIP, requests have been made for support to other task groups, for example, the Damage and Fundamental Studies (DAFS) task group. The DAFS task group has been requested to develop a standardized approach for the treatment or correlation data relating to dpa, He, and $MW \cdot Yr/m^2$. Because

this type of information is key to the analysis of the irradiated data on stainless steel, a schedule of July 15 for this information was also requested. Another task group that has been asked to provide assistance is the one involving Plasma Materials Interaction (PMI). The surface erosion in ETF is currently an area of uncertainty because, depending upon the calculational model used, can be predicted to be a few centimeters at the end of the machine life. The traditional method to accommodate the surface erosion has been to increase the initial starting thickness of the material. However, with the longer lived machines this may not be possible since in some cases a 20% increase in thickness can result in a 50% decrease in component life. It is for this reason a request has been directed to the PMI to develop sputtering yield curves for stainless steel, suitable for design and to develop a calculational model to predict the flux of particles to the wall, limiter, and divertor collector plates.

In the interim, while the various task groups have been acting on the various requests, initial information sheets covering format, objectives, and contents have been prepared, reviewed and released for publication. These pages are currently being printed and will be distributed to the various handbook holders in the near future.

2. TEST MATRICES AND TEST METHODS DEVELOPMENT

2.1 PROTOTYPE TESTING OF MFE-5 IN-REACTOR FATIGUE CRACK GROWTH EXPERIMENT

A. M. Ermi (Hanford Engineering Development Laboratory)

2.1.1 ADIP Task

Task I.B.l, Fatigue Crack Growth in Austenitic Alloys (Path A)

2.1.2 Objective

An apparatus to perform in-reactor fatigue crack propagation tests on the Path A Reference Alloy is being developed. Effects of dynamic irradiation on crack growth behavior will be evaluated by comparing the results with those of unirradiated and postirradiated tests.

2.1.3 Summary

Fabrication of the prototypic fatigue machine is completed, and testing at HEDL has commenced. Successful performance of the prototype was demonstrated through a series of tests on mock-up and actual specimens. Results of specimen chain tests were consistent with previously published results obtained from conventional specimens and test apparatus.

2.1.4 Progress and Status

2.1.4.1 Introduction

Fatigue crack propagation (FCP) in the first wall of magnetic fusion reactors may be a limiting criterion governing reactor lifetimes. Previous studies of irradiation effects on FCP have all been conducted out of reactor on materials preirradiated in the unstressed condition. The ORR-MFE-5 experiment will investigate FCP during irradiation, where dynamic irradiation may effect crack growth characteristics.

2.1.4.2 Prototypic Fatigue Machine

Fabrication of a prototypic fatigue machine which will be used to perform elevated temperature FCP tests at HEDL was completed. Details of operation of the fatigue machine[1] and pneumatics actuating system[2] were reported earlier. Briefly, it is designed to perform tension-tension cycling on a chain of up to eight miniature center-cracked-tension

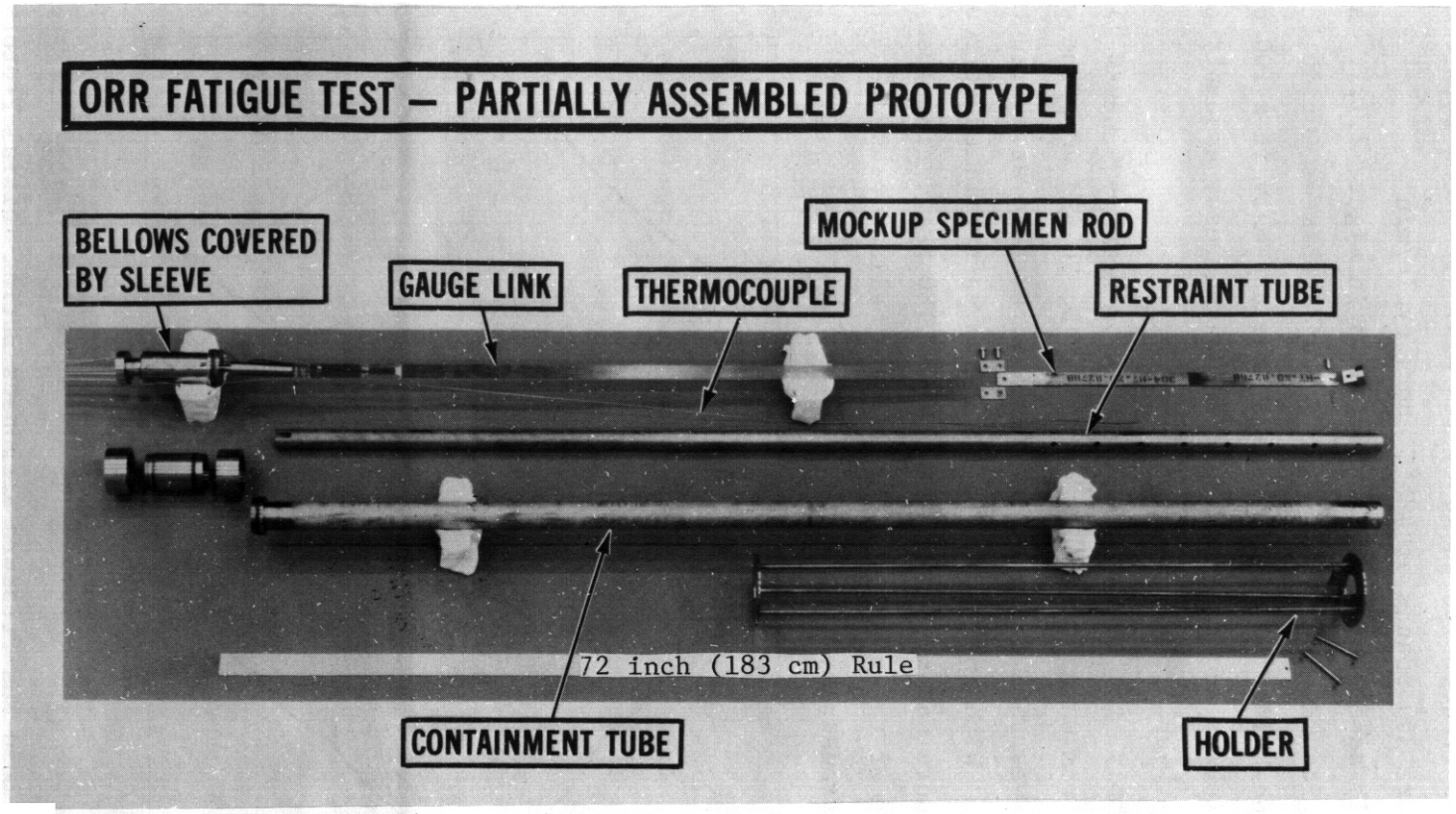

FIGURE 2.1.1 Partially Assembled Prototypic Fatigue Machine for the ORR-MFE-5 Fatigue Crack Growth Experiment.

(CCT) specimens. The system can operate at loads to 700 pounds, temperatures to 550°C and frequencies to 10 cycles/min. The actual in-reactor test conditions are 350 pounds at 425°C and 1 cycle/min.

The partially assembled prototype is shown in Figure 2.1.1. A 61 cm mock-up specimen rod was used instead of actual specimens during the initial test. The holder is used to center the assembly in a 100 cm electric kiln. Several components are threaded for easy assembly and disassembly in between prototypic testing.

Before assembly, the two strain gauges located on the gauge link were calibrated from 0 to 400 pounds using 5, 10, 20 and 40 pound weights. The initial test was then conducted at room temperature at a frequency of 1.5 cycle/min. With the prototype chamber pressure fixed at 200 psig, the bellows pressure was cycled between 30 and 180 psig. The load response from one of the strain gauges and the bellows pressure curve from a pressure transducer are illustrated in Figure 2.1.2.

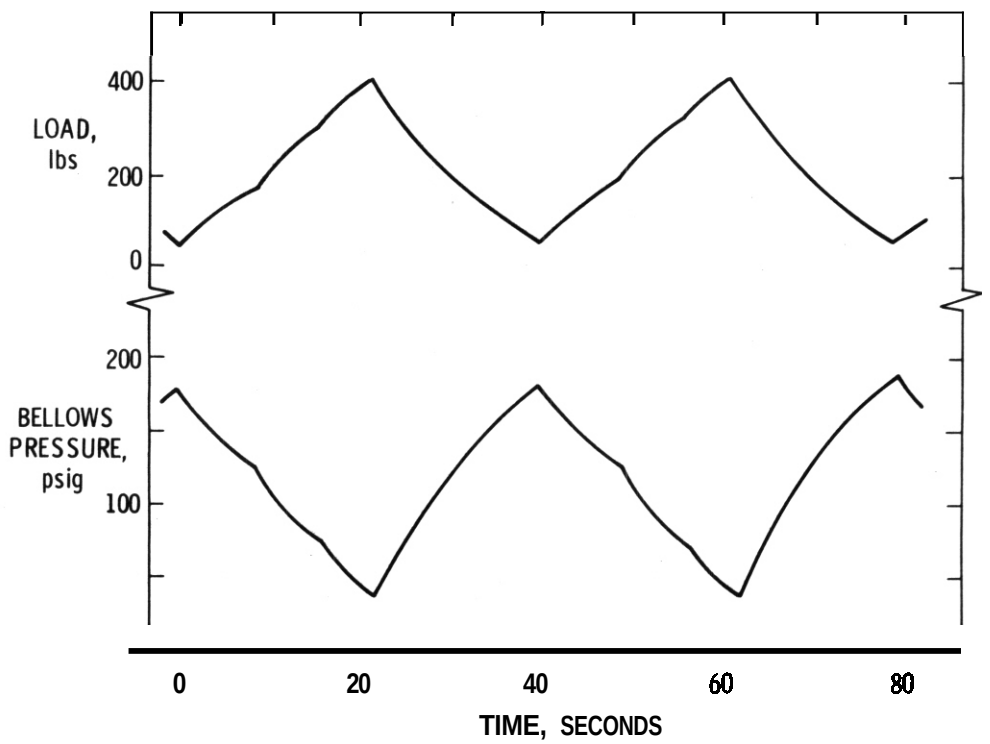

FIGURE 2.1.2 Load and Pressure Responses During Initial Prototype Testing.

The load-time response matched earlier expectations regarding the waveform (Ref. 1, pp. 52), yielding the triangular function desired for the in-reactor test.

After 4600 cycles (∿53 hrs.), the system was turned off and disassembled in preparation of a test using miniature CCT specimens.

2.1.4.3 Two-Specimen Chain Test

The first test on the prototype using specimens involved the cycling of two miniature CCT specimens. The material was the Path A Reference Alloy, 20% cold-worked 316 stainless steel. The specimens were precracked to different initial crack lengths, 4.6 and 9.9 mm. Based on previous crack growth data for 20% CW 316 SS, load conditions were selected which would result in the desired crack growth after ∿250,000 cycles.

In order to better evaluate the performance of the prototype and the results of the test, the electrical potential method[3] was used to continuously monitor the crack lengths of both specimens. Readings were recorded hourly, which for a frequency of 8.5 cycles/min translated to every 510 cycles. The frequency was increased from 1.5 cycles/min in order to complete the test in three weeks rather than four months. At room temperature, this does not effect the crack growth behavior.

Testing was carried out using a maximum load of 350 pounds and a load ratio R = 0.10. During the tenth continuous day of cycling, the system automatically stopped cycling as the bellows pressure was unable to reach the minimum set pressure which defines the peak load. This occurred after 118,900 cycles, or roughly half-way through the test. The cause of the shutdown was traced to a crack at an inner convolution weld of the bellows. The bellows used during these initial tests was used with full knowledge that they would probably fail. Since the bellows which was designed specifically for the test had not arrived when the prototype was being assembled, it was decided to insert a bellows which was on hand from a different experiment. The manufacturer of this bellows predicted a lifetime of only a few thousand cycles, not the 123,700 which resulted.

The two specimens were removed and visual measurements of the crack length were made. In addition, independent crack growth curves were constructed from the e.p. readings. These are shown in Figure 2.1.3

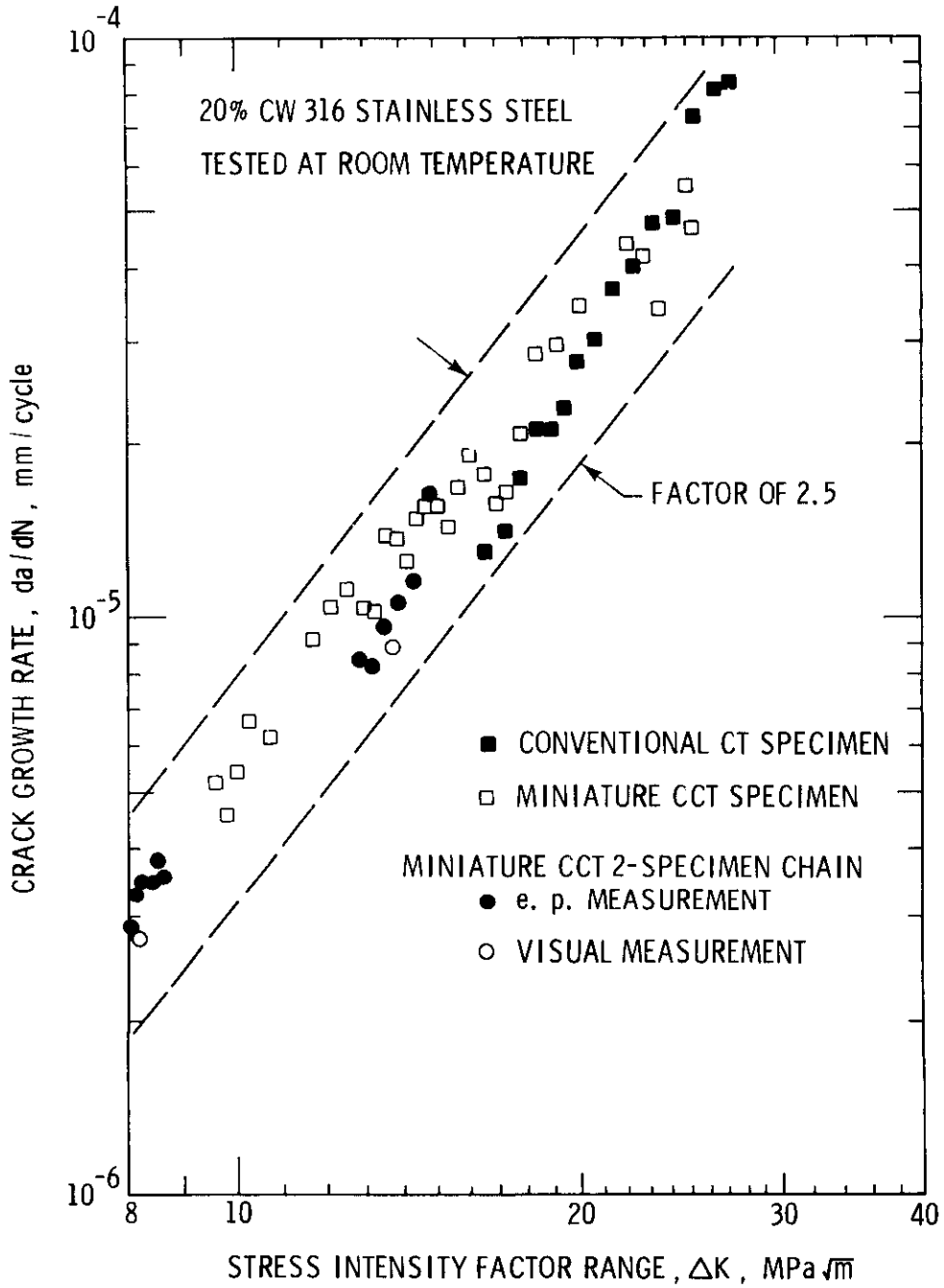

FIGURE 2.1.3 Comparison of the Prototype Two-Specimen Chain Test with Conventional Testing of a CT Specimen (James[4]) and a Miniature CCT Specimen (Mervyn, et al[5]).

along with results from a larger compact tension (CT) specimen by James,[4] and from a miniature CCT specimen tested conventionally by Mervyn, et al.[5] Not only do the results from the prototype agree well with the other investigators, but the visual measurements are in agreement with the continuously monitored e.p. data. This is important since during the actual in-reactor test, only visual measurements will be made as electrical monitoring is not possible in the sodium environment.

2.1.4.4 Eight-Specimen Chain Test

Shortly after the two-specimen chain test, the new bellows had been delivered and one was installed in the prototype. The next test consisted of a full chain of eight *20%* CW *316 SS* specimens. Initial crack lengths ranged from *4.6* to 9.0 mm. Again, the e.p. method was employed to monitor two of the specimens during the test. The frequency was increased slightly from the previous test, to 10 cycle/min. It should be noted that for these faster cyclic tests, stepwise venting was not implemented to obtain the triangular waveform shown in Figure *2.1.2.* Instead, only one valve was opened during the venting portion of the cycle. A sample of the resulting load output is given in Figure *2.1.4.*

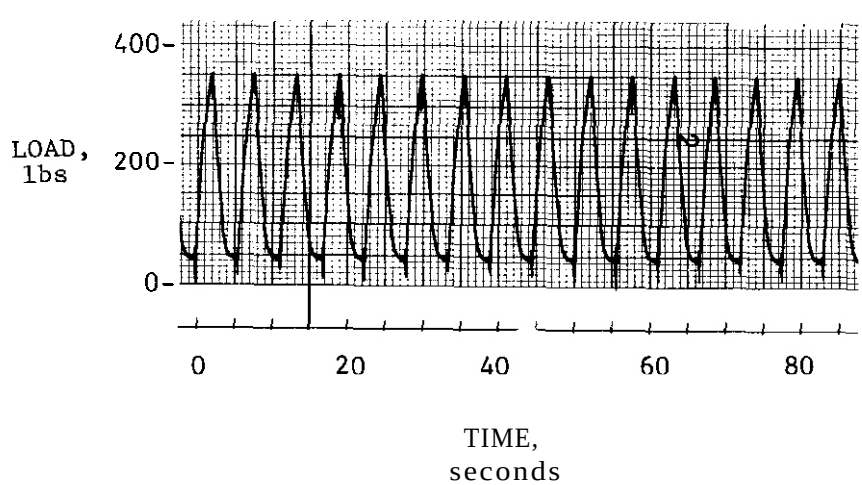

FIGURE *2.1.4* Load Response During the Eight-Specimen Chain Test

Testing was again conducted using a maximum load of *350* pounds and R = 0.10. After *256,325* cycles, the test was stopped and the specimens removed for visual crack length measurements. These results and those obtained from the e.p. method are depicted in Figure *2.1.5.*

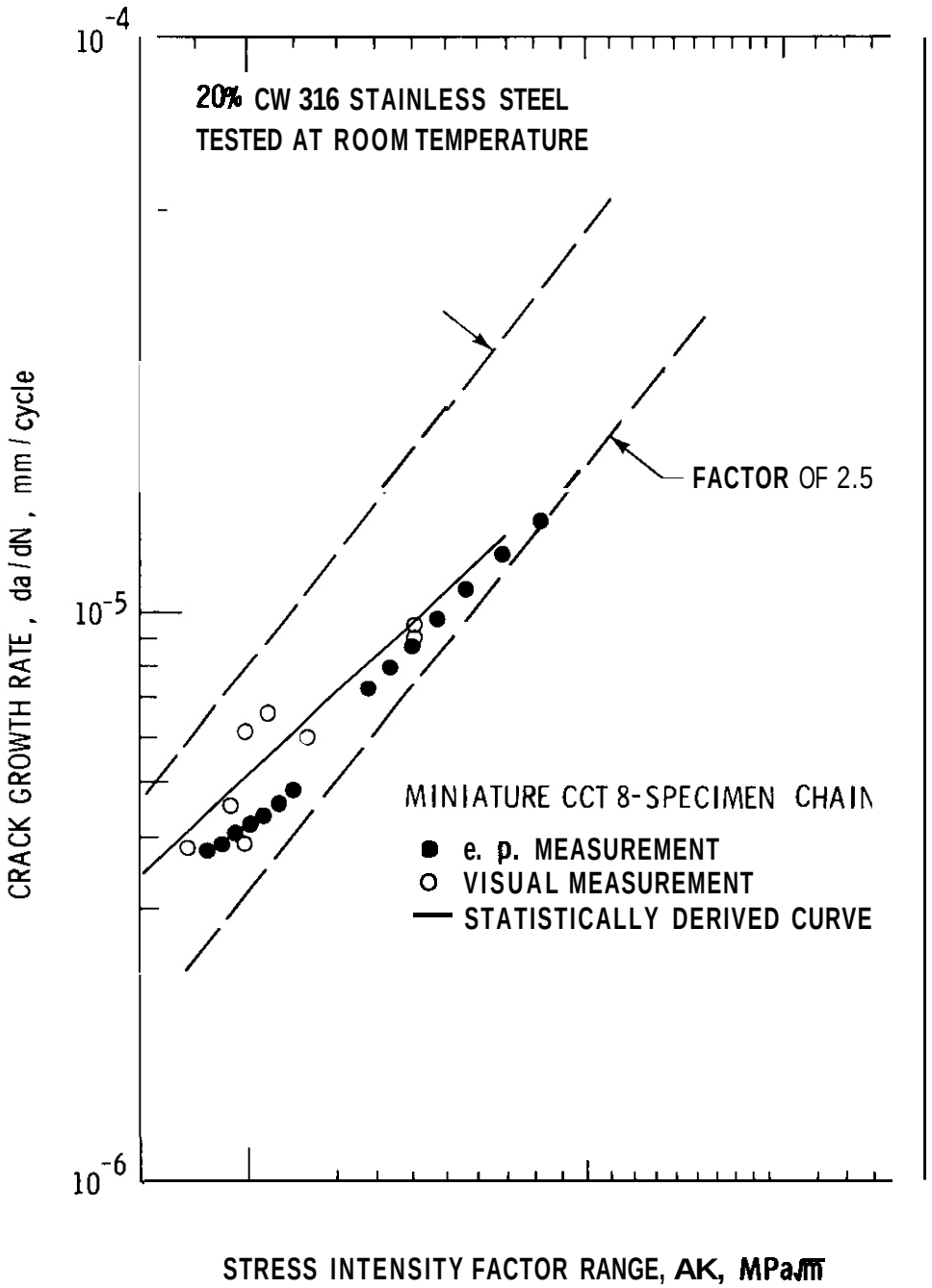

FIGURE **2.1.5** Comparison of the Prototype Eight-Specimen Chain Test with Results from Figure **2.1.3.**

The "factor of **2.5"** band from Figure 2.1.3 is included for comparison. The solid line was from a statistical analysis of only the initial and final crack length values.[2] The results from this and the previous test (1) verify the use of the prototype as a viable fatigue tester;

and (2) reinforce earlier claims regarding the use of specimen chain visual measurements to construct crack growth curves.

2.1.5 Conclusions

(a) A prototypic fatigue machine which will provide the desired load and waveform response has been successfully demonstrated.

(b) Results of chain tests on the prototype are consistent with results obtained by conventional methods.

(c) Crack growth curves constructed from only initial and final crack length measurements are consistent with those obtained from continuously monitoring the crack length.

2.1.6 Future Work

Fabrication of the in-reactor fatigue machine to be tested at ORNL is 50% complete. Insertion into the ORR is scheduled for the summer of 1980. Additional tests are planned for the prototype, the next being an eight-specimen chain test on 20% CW 316 SS at 425°C. One specimen in the chain will be wired to monitor the crack length using the e.p. method.

2.1.7 References

1. A. M. Ermi, "Status of an In-Reactor Fatigue Crack Growth Experiment," *ADIP Quarterly Progress Report, June 30, 1979,* DOE/ET-005/6, pp. 28-34.
2. A. M. Ermi, "Results of Prototypic Testing for the MFE-5 In-Reactor Fatigue Crack Propagation Experiment," *ADIP Quarterly Progress Report, September 30, 1979,* DOE/ET-0058/7, pp. 50-65.
3. J. L. Straalsund and D. A. Mervyn, "Adaptation of an Electrical Potential Technique to Measure Fatigue Crack Growth," *ADIP Quarterly Progress Report, December 31, 1978,* DOE/ET-0058/4, pp. 4-9.
4. L. A. James, "Fatigue Crack Growth in 20% Cold-Worked Type 316 Stainless Steel at Elevated Temperatures," *Nuclear Technology,* 16, October 1972.
5. D. A. Mervyn, M. M. Paxton and A. M. Ermi, "Development of the Miniature Fatigue Crack Growth Machine," *ADIP Quarterly Progress Report, September 30, 1979,* DOE/ET-0058/7, pp. 29-42.

2.2 PROGRESS ON THE ORR-MFE-4 SPECTRAL TAILORING EXPERIMENT — K. Thoms, T. A. Gabriel, B. L. Bishop, R. A. Lillie, J. A. Horak, and M. L. Grossbeck (ORNL)

2.2.1 ADIP Task

ADIP Task I.A.2, Define Test Matrices and Test Procedures.

2.2.2 Objective

The objective of this work is to produce the neutronic, thermal, and mechanical design of experiments for material irradiation in the Oak Ridge Research Reactor (ORR) core. The ORR-MFE-4 experiments will operate with spectral tailoring to control the fast and thermal fluxes and thus the displacement and helium production rates. The capsules are also designed for both discharging specimens and reloading with irradiated specimens several times during the experiment lifetime.

2.2.3 Summary

The hardware for MFE-4A (300 and 400°C) is now fabricated and assembled to the point of specimen loading. Only pressurization of the Prime Candidate Alloy tubes remains to be completed. All other specimens are ready for loading. Experiment MFE-4A is scheduled to be installed in the ORR in the latter half of April 1980. Experiment MFE-4B (500 and 600°C) is scheduled for insertion in June 1980.

2.2.4 Progress and Status

The details of the ORR spectral tailoring experiment have been described previously.[1,2] The MFE-4A irradiation capsule assembly is now complete to the point of loading the test specimens in the assembly. The experiment review questionnaire was completed, and a request for approval to install MFE-4A in the ORR has been made. Upon approval by the Reactor Experiment Review Committee, the experiment should be ready for installation in the ORR in the latter half of April 1980.

During this quarter we also completed the operation of a bench test to confirm the capability of the capsule design to independently control

the temperatures of the two temperature regions in each capsule. The bench test is now being used to develop a system utilizing the ORR Data Acquisition and Control System (ORRDACS) to automatically control the temperature of each region. While this system is being developed, the temperatures of the MFE-4A capsule will be controlled manually.

Since the first irradiations of the spectral tailoring experiment will begin shortly, plans have been made to maintain close contact between neutronic, reactor, design, and experimental personnel to ensure successful completion of the experiment. The baseline neutronic calculations will begin shortly after the core characteristics have been determined for the ORR cycle in which the spectral tailoring experiment will be placed.

2.2.5 Conclusions

The first capsule of the ORR spectral tailoring experiment, MFE-4, is scheduled for reactor insertion in April 1980. The final specimens are in preparation at the present time.

2.2.6 References

1. T. A. Gabriel, K. R. Thorns, and M. L. Grossbeck, "Design of Materials Irradiation Experiments in the ORR Utilizing Spectral Tailoring and Reencapsulation," *ADIP Quart. Prog. Rep. Mar. 31, 1979*, DOE/ET-0058/5, pp. 20—22.
2. T. A. Gabriel, K. R. Thorns, and J. W. Woods, "Design of Materials Irradiation Experiments Utilizing Spectral Tailoring," *ADIP Quart. Prog. Rep. Dec. 31, 2978*, DOE/ET-0058/4, pp. 10—17.

2.3 NEUTRONIC CALCULATIONS FOR THE CONCEPTUAL DESIGN OF AN "IN-PILE" SOLID BREEDER EXPERIMENT IPSB-01 — T. A. Gabriel, R. A. Lillie, and B. L. Bishop (ORNL)

2.3.1 ADIP Task

ADIP Task I.A.2, Define Test Matrices and Test Procedures.

2.3.2 Objective

The purpose of the "in-pile" solid breeder experiment is to simultaneously irradiate two candidate solid breeder materials in an encapsulated configuration that permits the breeder material to be both operated over a controlled temperature range between 450 and 800°C and swept by an inert gas purge stream that can be processed to remove the released tritium. The objective of the neutronics calculations is to provide tritium production and heating rate data that can be used to design the experimental apparatus for irradiation in the Oak Ridge Research Reactor (ORR).

2.3.3 Summary

A model has been developed that represents the solid breeder experiment and the adjacent fuel regions of the ORR core. This model and appropriate data sets will be used in transport calculations to provide tritium production and nuclear heating rates for operation of the experiment in the ORR.

2.3.4 Progress and Status

In support of the "in-pile" solid breeder experiment, a one-dimensional cylindrical model (Fig. 2.3.1) of the experimental ORR breeder core element, which will be surrounded by a fuel rod,* has been devised so that ANISN[1] calculations can be carried out to determine both the tritium production rates within the breeder region and the neutron and gamma ray heating rates within the core element. The neutron source distribution, which will be around the fuel rod, will be obtained from a VENTURE[2] calculation on a typical ORR core loading.

---

* This fuel rod represents eight ORR fuel elements.

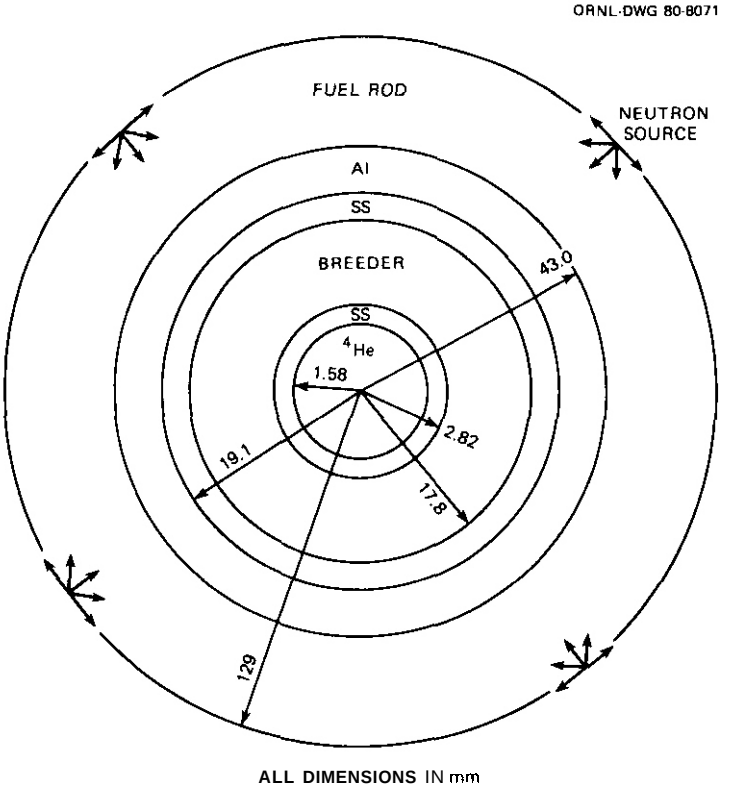

Fig. 2.3.1. Cylindrical One-Dimensional Representation of the Oak Ridge Research Reactor (ORR) Breeder Core Element and "Fuel Rod." The fuel rod represents eight ORR fuel elements surrounding the solid breeder experiment.

The coupled neutron and gamma ray transport cross-section data sets, the cross-section data sets for tritium production from lithium, and the kerma factor data sets for energy deposition are of prime importance to these calculations. The elements for which data sets are needed are given in Table 2.3.1. The processing of these data sets is under way and should be completed within the next two months. The gamma rays that are produced from fission product will also be included in the transport cross-section data sets.

Initially, four **ANISN** calculations are contemplated. The first two will be for the breeder materials Li_2O and Li_2SiO_3. The lithium will be taken to be natural lithium, that is 92.5% ^7Li—7.5% ^6Li. The final two calculations will be for the same breeder materials except that the lithium will be taken to be only ^7Li.

Table 2.3.1. Data Sets[a] Needed for the Conceptual Design Studies

Transport Cross Sections[b]		Production Cross Sections
Element	Temperature[c] (°C)	
^{4}He	300	$n + {}^{6}Li \rightarrow {}^{3}H + {}^{4}He$
Fe	400	$n + {}^{7}Li \rightarrow n + {}^{3}H + {}^{4}He$
Ni	400	
Cr	400	
^{6}Li	600	
^{7}Li	600	
O	600, 95	
Si	600	
^{235}U	95	
^{238}U	95	
Al	300, 95	
H	95	

[a]The kerma factors are the same as for transport cross sections.

[b]P_3 — third-order Legendre expansion of the cross section; 100 neutron groups, 21 gamma groups.

[c]Two temperatures indicate that these elements appear in two different regions of the model at these two temperatures.

2.3.5 References

1. W. W. Engle, Jr., ***A User's Manual for ANISN, A One-Dimensional Discrete Ordinates Code with Anisotropic Scattering,*** K-1693, Oak Ridge Gaseous Diffusion Plant (1967).
2. D. R. Vondy, T. B. Fowler, and G. W. Cunningham, VENTURE, ***A Code Block for Solving Multigroup Neutron Problems Applying Fixe-Diffusion-Theory Approximations to Neutron Transport,*** OWL-5062 (October 1975).

3. PATH A ALLOY DEVELOPMENT – AUSTENITIC STAINLESS STEELS

3.1 DESIGN AND FABRICATION OF PREIRRADIATION MICROSTRUCTURES IN PATH A PRIME CANDIDATE ALLOY — P. J. Maziasz, T. K. Roche, B. L. Cox, and E. E. Bloom (ORNL)

3.1.1 ADIP Tasks

ADIP Tasks I.A.5, Perform Fabrication Analysis, I.C.l, Microstructural Stability, and I.D.l, Materials Stockpile for MFE Program.

3.1.2 Objective

The objective is to combine microstructural design, fabrication, and thermal-mechanical treatment (TMT) to obtain Path A Prime Candidate Alloy (PCA) specimen material with desired microstructures.

3.1.3 Summary

Previous work designed microstructures that might provide optimum irradiation response of the Path A PCA. The fabrication problems encountered with producing homogeneous Path A PCA material were solved, and the response to short-term thermal aging was investigated. The specification of desired microstructures was revised to be consistent with the aging results; practical fabrication sequences and TMTs were suggested. The current work examines the success of the revised fabrication and TMT in producing the desired microstructures and characterizes the microstructures achieved.

3.1.4 Progress and Status

The initial inhomogeneity of the as-received Path A PCA and the problems of fabricating homogeneous material were addressed and solved previously.[1,2] Homogeneous PCA in either the solution-annealed (15 min at 1175°C) or 10 or 25%-cold-worked conditions was examined after short-term thermal aging for times ranging from 5 min to 166 h at temperatures from 650 to 900°C.[3] These results were combined with those from previous microstructural design,[4] which were based mainly on the examination of High Flux Isotope Reactor irradiated types 316 and titanium-modified 316 austenitic stainless steel, to obtain TMTs that produced several desirable preirradiation microstructures. These PCA microstructures contained

several different distributions of titanium-rich MC precipitate particles.[3] The TMTs were incorporated into the fabrication sequence to produce material with the desired microstructures. This work demonstrates that both simple and complex microstructures can be produced successfully. However, the original fabrication sequence and TMTs had to be adjusted to ensure success in large metal-treating facilities.

A general description of the desired microstructures is given in Table 3.1.1. Table 3.1.2 lists the recommended fabrication sequence expected to produce these microstructures. These fabrication sequences were used to produce sample material, and the microstructural features obtained were characterized and reported previously.[3] Microstructures Al, A2, A3, Bl, and C were produced successfully in 0.25 —m-thick sheet. These microstructures have been examined metallographically and by transmission electron microscopy (TEM), and the results are shown in Figs. 3.1.1 through 3.1.5. The solution-annealed microstructure Al (Fig. 3.1.1) indicates that the material is homogeneous. The annealing and heat treating during fabrication were performed in a static or pumped

Table 3.1.1. Proposed Preirradiation Microstructures That Can Be Achieved by Thermal-Mechanical Treatment of the Prime Candidate Alloy (PCA)

A. Simple microstructures resulting from:

1. solution annealing,
2. 5 to 10% cold working, or
3. 20 to 25% cold working.

B. Microstructures with both coarse grain boundary MC precipitation and intragranular MC precipitation consisting of:

1. coarse particles or particle clusters or
2. fine matrix precipitation.

C. Microstructures with both fine grain boundary MC precipitation and fine intragranular MC matrix precipitation.

D. Microstructures with both fine grain boundary MC precipitation and fine intragranular MC matrix precipitation plus increased dislocation density.

Table 3.1.2. Recommended Thermal-Mechanical Treatments to Produce Proposed Preirradiation Microstructures

Microstructure[a]	Initial Suggested Thermal-Mechanical Treatment	Revised Thermal-Mechanical Treatment
A1	25% cold worked plus 15 min at 1175°C	No change
A2	15 min at 1175°C plus 10% cold worked	No change
A3	15 min at 1175°C plus 25% cold worked	No change
B1	Solution annealed plus 8 h at 800°C plus 8 h at 900°C	No change
B2	Solution annealed plus 8 h at 800°C plus 25% cold worked plus 15 min at 750°C	Solution annealed plus 8 h at 800°C 25% cold worked plus 2 h at 750°C
C	25% cold worked plus 15 min at 750°C	25% cold worked plus 2 h at 750°C
D	10% cold worked plus 30 min at 750°C plus 10% cold worked	10% cold worked plus 2 h at 750°C plus 10% cold worked

[a]Letter and number codes refer to microstructures defined in Table 3.1.1.

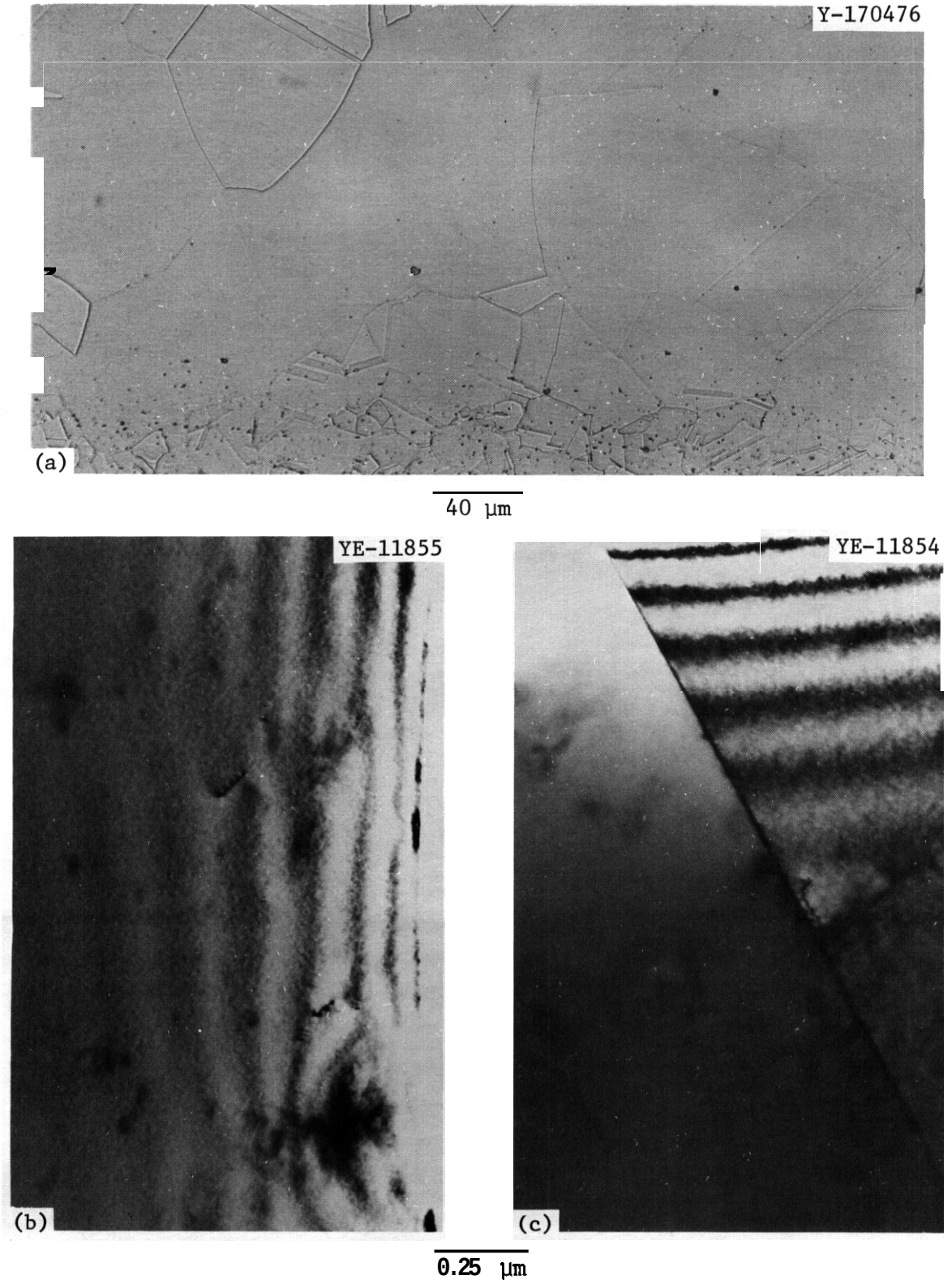

Fig. 3.1.1. Microstructure of Prime Candidate Alloy A1 Treated 15 min at 1175°C. (a) Metallographic results. (b) Transmission electron microscopy results in the matrix and (c) at the grain boundary.

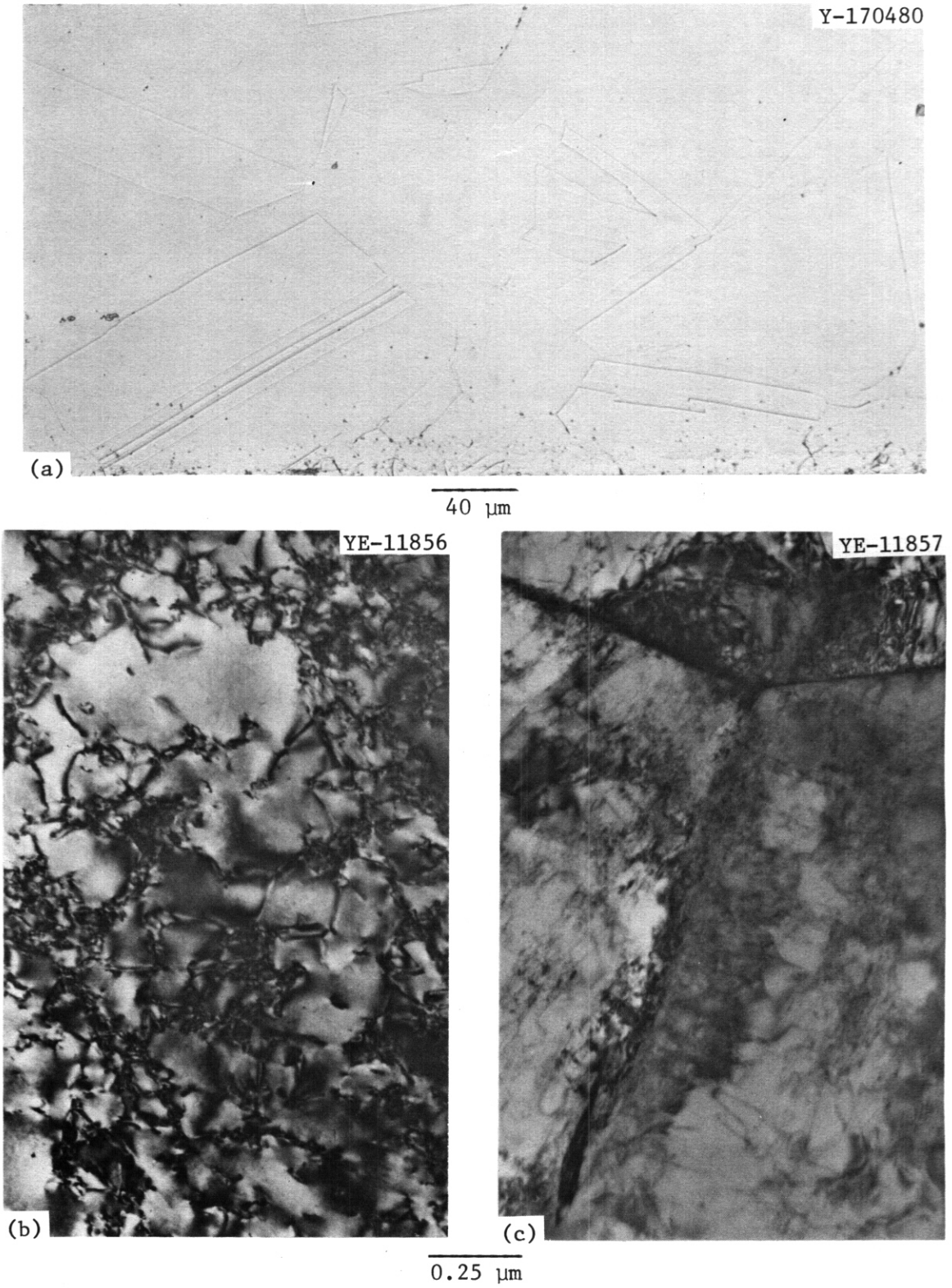

Fig. 3.1.2. Microstructure of Prime Candidate Alloy A2 Treated 15 min at 1175°C plus 10% Cold Worked. (a) Metallographic results. (b) Transmission electron microscopy results in the matrix and (c) at the grain boundary.

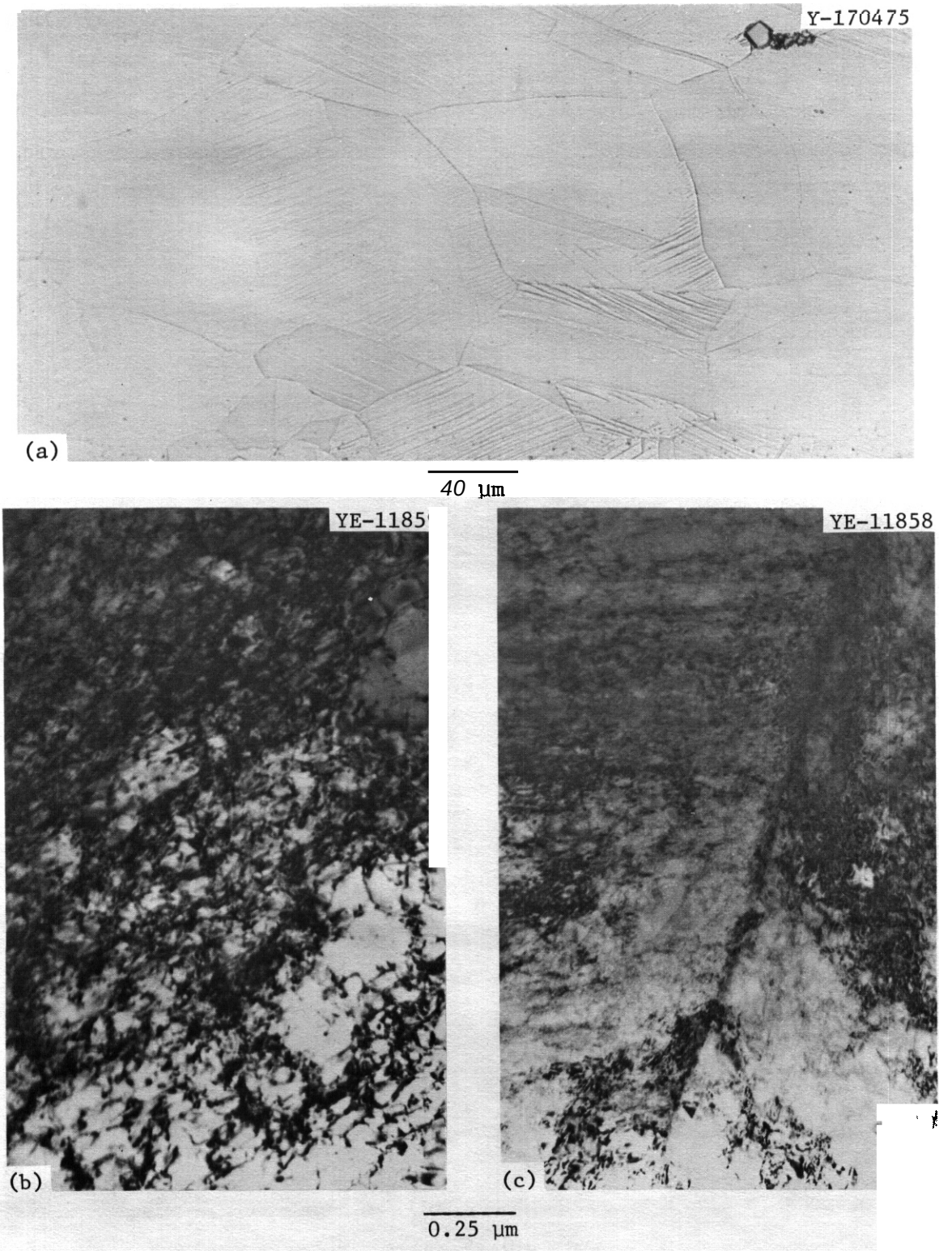

Fig. 3.1.3. Microstructure of Prime Candidate Alloy A3 Treated 15 min at 1175°C plus 25% Cold Worked. (a) Metallographic results. (b) Transmission electron microscopy results in the matrix and (c) at the grain boundary. The intergranular dislocation density is about a factor of 2 to 3 higher than for microstructure A2 in Fig. 3.1.2.

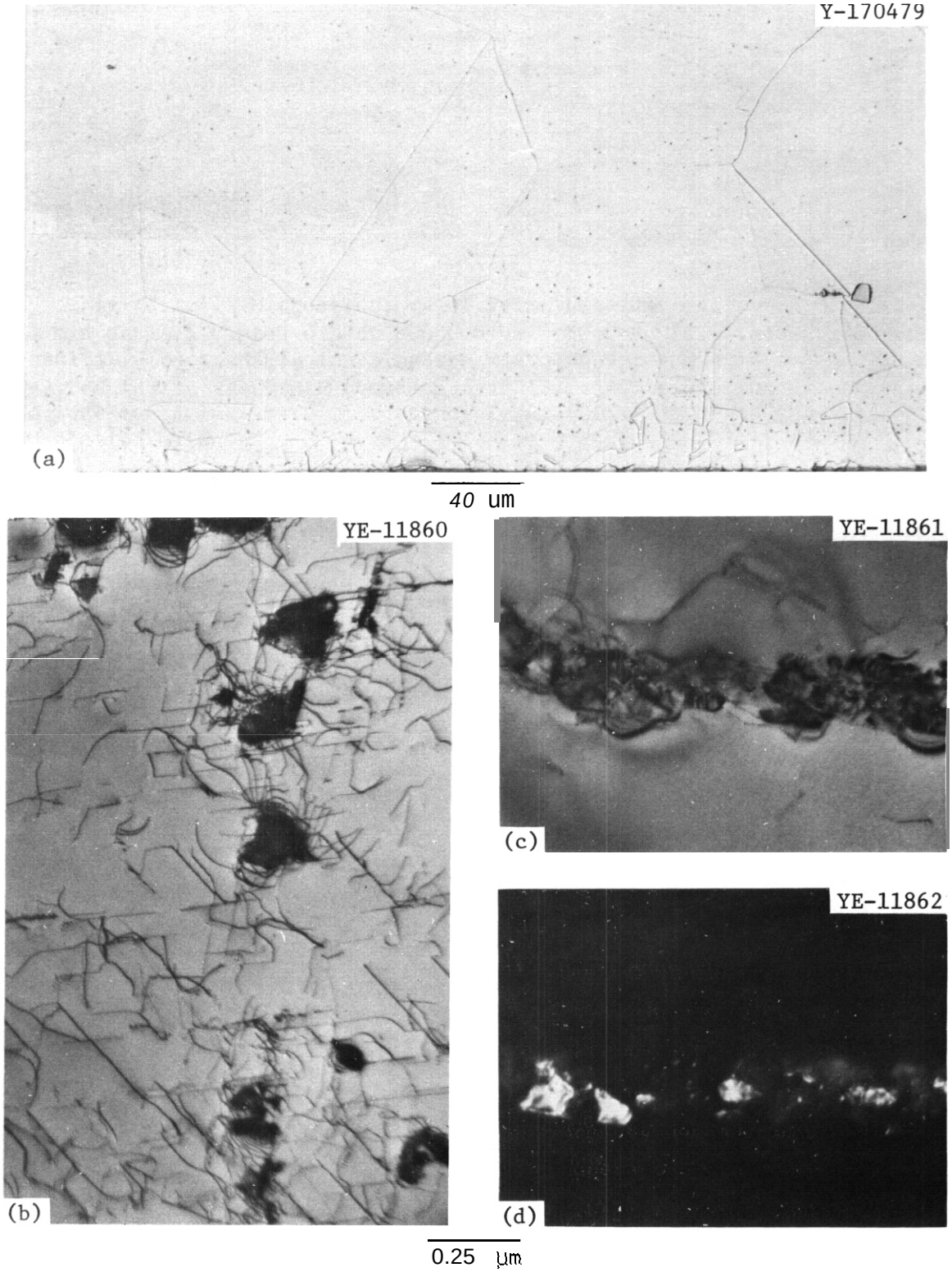

Fig. 3.1.4. Microstructure of Prime Candidate Alloy B1 Treated 15 min at 1175°C plus 8 h at 800°C plus 8 h at 900°C. (a) Metallographic results. (b) Transmission electron microscopy results in the matrix and (c) and (d) at the grain boundary. In (b) the dislocation density is shown to increase relative to microstructure A1 (Fig. 3.1.1) as a result of MC precipitation.

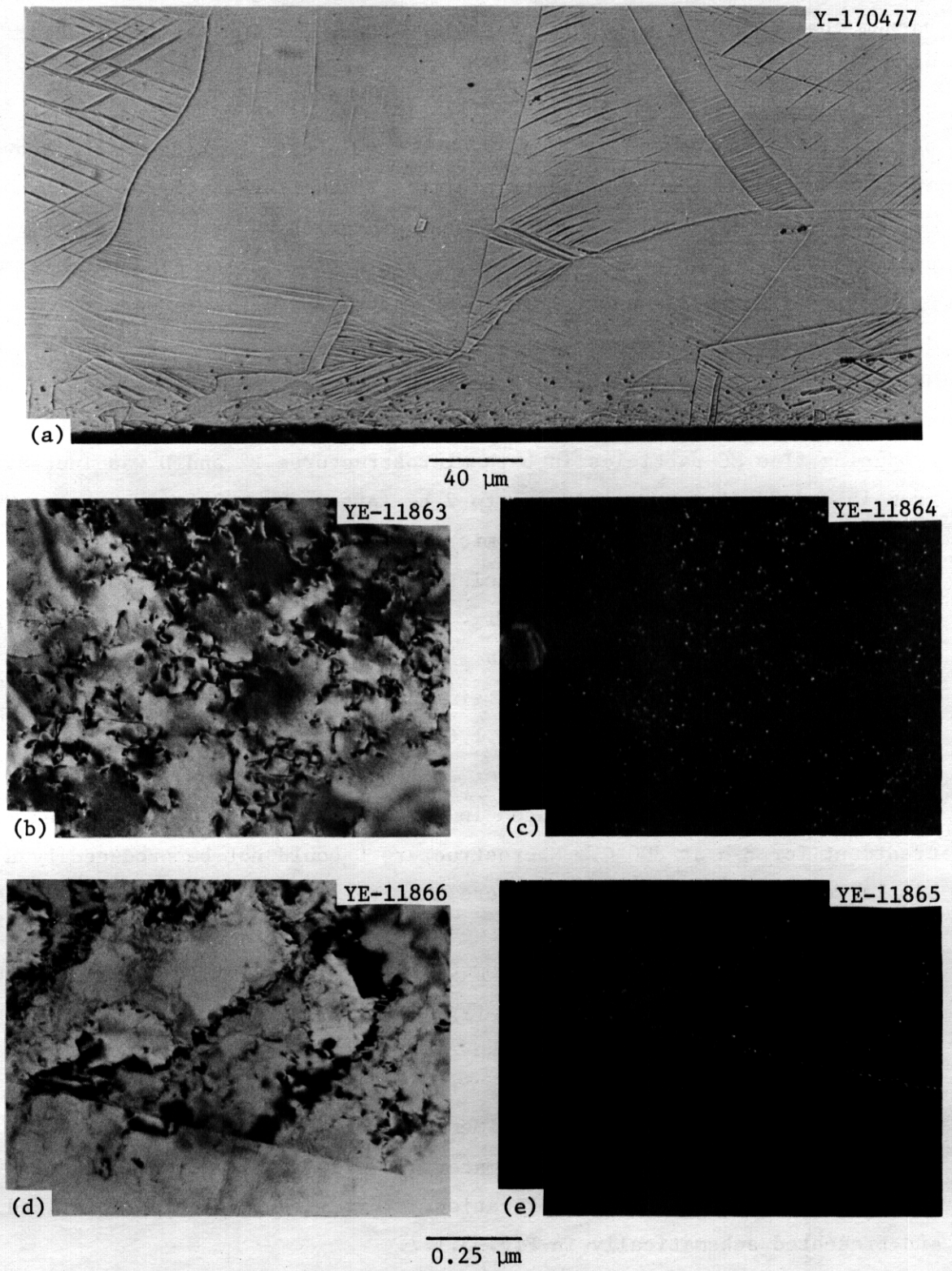

Fig. 3.1.5. Microstructure of Prime Candidate Alloy C Treated 15 min at 1175°C plus 25% Cold Worked plus 15 min at 750°C. (a) Metallographic results. (b) and (c) Transmission electron microscopy results in the matrix and (d) and (e) at the grain boundary. The intragranular MC particle size is no more than 3 to 5 nm, and the density is about 2×10^{22} particles/m^3.

vacuum that remained between 10^{-4} to 10^{-2} Pa or in high purity argon. However, earlier treatment at 1200°C in air introduced the small amount of surface nitride shown in Figs. 3.1.1 through 3.1.6 as discussed previously.[2] Subsequent material received all heat treating in the above mentioned furnace to eliminate or minimize this effect.

The fine matrix distribution of titanium-rich MC precipitate particles desired in microstructures B2 and D was not achieved on the first attempt at scale-up from test samples to production sheet. The difficulty was insufficient time at the aging temperature. Since the fine MC precipitate particles produced on aging cold-worked PCA showed no tendency to change or coarsen after 8 h at 750°C, the aging time for producing fine MC particles in both microstructures B2 and D was increased from 15 and 30 min, respectively, to 2 h. After the 0.25-mm sheet stock of B2 was re-treated accordingly, microstructure B2 was sucessfully produced with fine matrix MC particles. The B2 microstructure is shown metallographically and by TEM in Fig. 3.1.6. Note that the intragranular MC precipitation is the same as that of microstructure C (Fig. 3.1.5). The grain boundary MC, however, is similar to that of microstructure B1 [Fig. 3.1.4(c) and (d)]. Figure 3.1.6(d) and (e) together with Fig. 3.1.4(c) and (d) show the finer and coarser ends of average distribution of grain boundary MC produced in solution-annealed PCA by the thermal treatment for 8 h at 800°C. Microstructure D could not be produced by a simple reheat treatment and therefore must be refabricated from thicker sheet.

Final specimen fabrication from 0.25 —m-thick sheet involves blanking either 3-mm-diam TEM disks or SS-2 type[5] miniature sheet tensile specimens. Blanking "soft" microstructures like A1 or B1 by using a die and punch was difficult. Therefore, "fine tuning" the fabrication sequence includes specifying the point at which specimens can be blanked (or machined from thicker sheet or rod) from "hard" material. The specimens would then receive the last TMTs after fabrication. This information is summarized and presented schematically in Fig. 3.1.7.

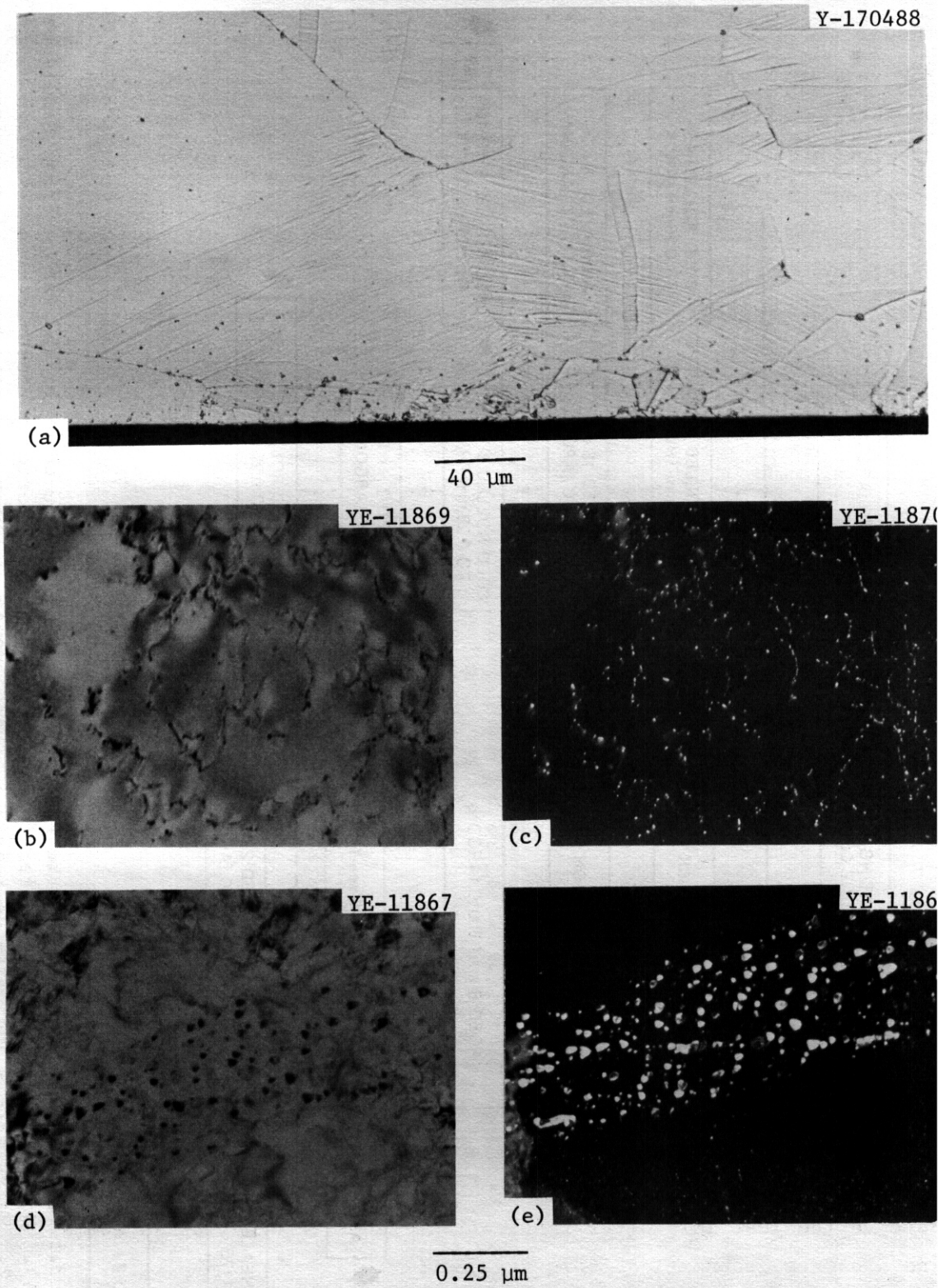

Fig. 3.1.6. Microstructure of Prime Candidate Alloy B2 Treated 15 min at 1175°C plus 8 h at 800°C plus 25% Cold Worked plus 2 h at 75 (a) Metallographic results. (b) and (c) Transmission electron microsc results in the matrix and (d) and (e) at the grain boundary.

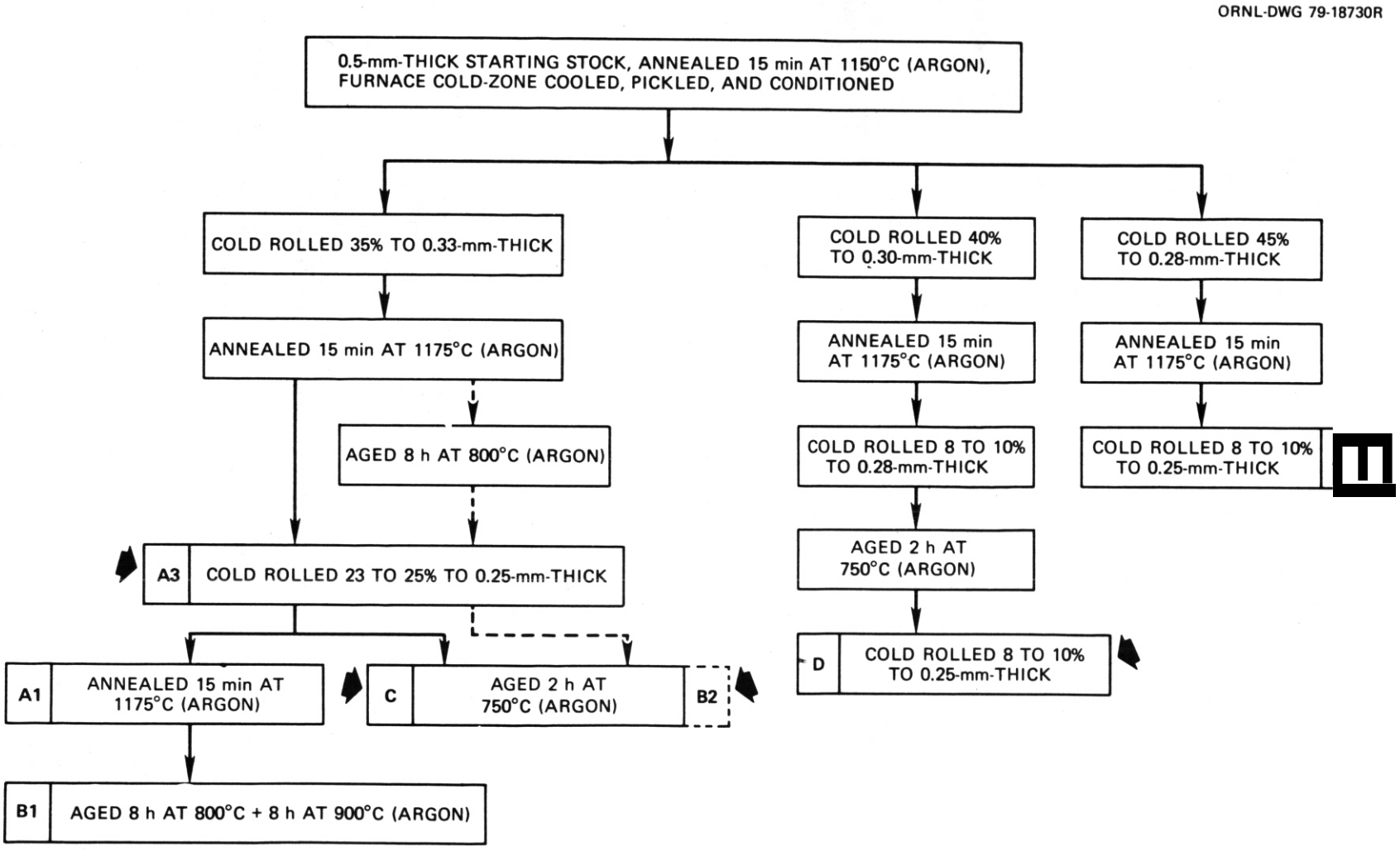

Fig. 3.1.7. Final Processing Steps to Produce Designed Microstructures of the Path A Prime Candidate Alloy (PCA). Number and letter codes refer to the proposed preirradiation microstructures listed in Table 3.1.2. Heavy arrows indicate the points in the sequence at which specimens can be blanked from "hard" material.

3.1.5 Conclusions and Future Work

1. The TMTs proposed and incorporated into the recommended fabrication sequence produce microstructures A1, A2, A3, B1, and C successfully in 0.25-mm-thick sheet.

2. The TMTs for microstructures B2 and D initially did not produce fine matrix MC precipitate particles. Increasing the time at 750°C to 1.5 h resulted in fine MC particles after retreatment of B2. Microstructure D must be refabricated on the revised schedule, including the longer time at 750°C.

3. The microstructure produced in the PCA demonstrated the considerable variety of grain boundary and matrix MC particle size distributions initially intended. They demonstrate both the necessity and success of proper fabrication of homogeneous PCA material.

Specimens of the Path A PCA have been produced with the designed microstructures and will be irradiated in future Oak Ridge Research Reactor and High Flux Isotope Reactor experiments. Comparison of the response to irradiation of these materials with type 316 stainless steel and other ADIP program alloys will quantify the improvement achieved with the PCA. Some evaluation should precede further microstructural "fine tuning" or significant compositional variation of the Path A PCA.

3.1.6 References

1. P. J. Maziasz and T. K. Roche, "Microstructural Characterization of As-Received Prime Candidate Alloy and Examination of Microstructural Sensitivity to Fabrication and Processing Variables," *ADIP Quart. Prog. Rep. Mar. 31, 1979*, DOE/ET-0058/5, pp. 36-62.
2. P. J. Maziasz and T. K. Roche, "Fabrication of Homogeneous Path A Prime Candidate Alloy," *ADIP Quart. Prog. Rep. Sept. 30, 1979*, DOE/ET-0058/7, pp. 83—102.
3. P. J. Maziasz, B. L. Cox, T. K. Roche, and E. E. Bloom, "Time-Temperature-Precipitation Curve Determination of the Path A Prime Candidate Alloy for Microstructural Design," *ADIP Quart. Prog. Rep. Sept. 30, 1979*, DOE/ET-0058/7, pp. 103-27.

4. P. J. Maziasz, "Microstructural Design for Fusion First-Wall Applications and Recommendations for Thermal-Mechanical Preirradiation Treatments," *ADIP Quart. Prog. Rep. Mar. 31, 1979,* DOE/ET-0058/5, pp. 48–56.

5. J. A. Horak, "Helium Implantation in Potential CTR Structural Materials," *Controlled Thermonuclear Materials Technology Program Annu. Prog. Rep. June 30, 1975,* OWL-5082, pp. 40–42.

3.2 HIGH-CYCLE FATIGUE TESTING OF HFIR-IRRADIATED 20%-COLD-WORKED TYPE 316 STAINLESS STEEL — M. L. Grossbeck and K. C. Liu (ORNL)

3.2.1 ADIP Task

ADIP Task I.B.5, Stress-Strain Controlled Fatigue of Austenitic Alloys.

3.2.2 Objective

This study evaluates the effects of simultaneous displacement damage and helium production during irradiation on the postirradiation fatigue of 20%-coldworked type 316 stainless steel.

3.2.3 Summary

Work is now in progress to extend previously reported low-cycle fatigue data to the high-cycle regime. A series of unirradiated specimens was tested under high-cycle conditions, but only one irradiated specimen has been tested. Results are encouraging in that an endurance limit appears to have been reached at a strain range of 0.3%.

3.2.4 Progress and Status

As previously reported[1] a series of unirradiated specimens was tested in the strain range 0.3 to 0.6%. The testing conditions, which were described in detail previously,[1] include a strain rate of 4×10^{-3}/s until a stable hysteresis loop is established followed by transfer to load control at a strain rate of 4×10^{-2}/s until specimen failure.

Only one irradiated specimen has been tested. It was irradiated at 430°C to a fluence of 1.1×10^{26} n/m^2 [>0.1 MeV (0.02 pJ)], producing 8.5 dpa and 360 at. ppm He. This test (at 430°C) was terminated at 1.1×10^7 cycles. It appears that an endurance limit has been reached, and this point will be investigated further.

3.2.5 Conclusions

Since only one fatigue test has been conducted to date, no conclusions will be made at this time. However, the exceptionally long fatigue life of a specimen containing 360 at. ppm He is very encouraging.

The 0.3% strain range is higher than expected in steady-state tokamak operation. Further tests will determine if fatigue will be a constraint in fusion reactor design.

3.2.6 Reference

1. M. L. Grossbeck and K. C. Liu, "Fatigue Behavior of 20%-Cold-Worked Type 316 Stainless Steel After Irradiation in the HFIR," *ADIP Quart. Prog. Rep. Sept. 30, 1979,* DOE/ET-0058/7, pp. 80–82.

3.3 THE EFFECT OF PREINJECTED HELIUM ON THE MICROSTRUCTURE AND TENSILE PROPERTIES OF EBR-11-IRRADIATED 20%-COLD-WORKED TYPE 316 STAINLESS STEEL — P. J. Maziasz, B. L. Cox, and J. A. Horak (ORNL)

3.3.1 ADIP Task

ADIP Tasks I.B.13, Tensile Properties of Austenitic Alloys, and I.C.2, Microstructure and Swelling in Austenitic Alloys.

3.3.2 Objective

The objective is to assess the effects of preinjected helium on the microstructure and tensile properties of 20%-cold-worked type 316 stainless steel after EBR-II irradiation and to compare these effects to thermal aging and High Flux Isotope Reactor (HFIR) irradiation effects.

3.3.3 Summary

Samples of 20%-cold-worked type 316 stainless steel have been irradiated to 8.4 dpa in EBR-II. Irradiation temperatures were 500 and 625°C, and the content of helium (injected near room temperature) was 0, 110, or 200 at. ppm. Samples for all conditions were examined by transmission electron microscopy (TEM), and those irradiated at 625°C were postirradiation tensile tested at the same temperature. The microstructure of uninjected material shows sparse precipitation of tau and eta phase, a recovered dislocation structure, and no cavities or voids at either 500 or 625°C. Helium preinjection has no significant effect on the dislocation structure at either temperature. Furthermore, preinjection of 110 at. ppm He and irradiation at 500°C produces no resolvable (greater than about 3 nm) distribution of cavities but does reduce slightly eta and tau formation and does enhance Laves formation compared with uninjected material. Preinjection of either 110 or 200 at. ppm He and irradiation at 625°C produces a distribution of about 1×10^{22} cavities/m^3, 4 to 5 nm in diameter, on the dislocation structure. Copious precipitation of Laves, eta, and/or tau was observed. These results are compared with the same material after thermal aging or HFIR irradiation at similar temperatures and times. Some microstructural components differ significantly. Tensile testing at 625°C of the

uninjected material shows a decrease in strength and increase in elongation compared with unirradiated material. Helium preinjected material generally shows greater strength but reduced ductility compared with uninjected material.

3.3.4 Progress and Status

Details of specimen preparation and helium preinjection were reported previously.[1-3] The final steps in producing 0.25-mm-thick sheet of type 316 stainless steel were annealing for 1 h at 1050°C and rolling to a 20% reduction in thickness. The SS-2 type tensile specimens[1] were punched from the sheet. These were 31.8 mm long with gage sections 12.7 mm long and 1.02 mm wide (shown in Fig. 3.3.1). These specimens were injected at about 20°C with 110 or 200 at. ppm He. A 60-MeV (9.6-pJ) alpha particle beam was used for injection with an energy degrader wheel to produce

Y-130368

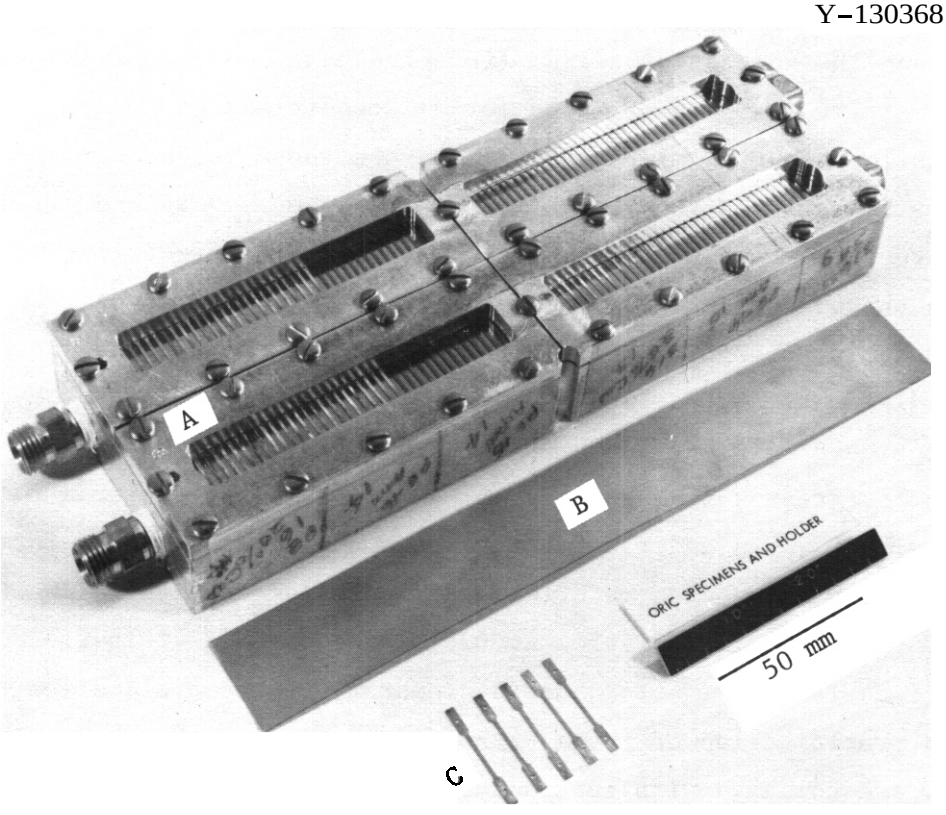

Fig. 3.3.1. A Water-cooled Sample Holder with a Full Set of Sheet and Tensile Specimens, A; the Initial Sheet, B; and Typical SS-2 Miniature Tensile Specimens, C.

uniform distribution. The accelerator was the Oak Ridge Isochronous Cyclotron (ORIC).[1] The specimen holder assembly for helium injection is also shown in Fig. 3.3.1. The chemical composition of the type 316 stainless steel used was:

Element	Content (wt %)	Element	Content (wt %)
Cr	18.0	si	0.80
Ni	13.0	P	0.013
Mo	2.6	S	0.016
Mn	1.9	N	0.05
C	0.05	B	0.0005
Ti	0.05		

Both injected and uninjected samples were irradiated in row 8 of EBR-II in subassembly X-264 to a neutron fluence of 1.6×10^{26} n/m^2 (>0.1 MeV) producing about 8.4 dpa and 5 at. ppm He. Specimen irradiation conditions are listed in Table 3.3.1. Specimens were irradiated at 625°C by locating them near the heat pipe at approximately the same temperature.

Table 3.3.1. EBR-II Irradiation Conditions for 20%-Cold-Worked Type 316 Stainless Steel

Irradiation Temperatures[a] (°C)	He, at. ppm			Neutron Fluence (>0.1 MeV) (n/m^2)	Displacement Damage Level (dpa)
	Nominal Injected	Actual Injected[b]	Continuously Produced[c]		
500, 625	none	none	~5	1.6×10^{26}	8.4
500, 625	80	110 ± 23	~5	1.6	8.4
625	200	200 ± 70	~5	1.6	8.4

[a]Some samples were irradiated at two temperatures with other conditions the same.

[b]Measured by vacuum fusion mass spectrometry by H. Farrar at Atomics International, Division of Rockwell International, 1976.

[c]Source of calculations: T. A. Gabriel, B. L. Bishop, and F. W. Wiffen, *Calculated Irradiation Response of Materials Using Fission Reactor (HFIR, ORR, and EBR-II) Neutron Spectra*, ORNL/TM-6367 (August 1979).

Specimens irradiated at 500°C were in a sodium-filled subcapsule, thermally separated from the reactor coolant with a helium gas gap to obtain the elevated temperature from gamma heating.

The tensile test matrix for the 20%-cold-worked type 316 stainless steel specimens has been published previously.[2] Transmission electron microscopy was performed on wafers .removed from the gage sections of untested tensile specimens and thinned by electropolishing to electron transparency. In some cases extraction replicas were produced from similar gage wafers to obtain well separated, matrix-free precipitate particles suspended on an electron transparent carbon film. These precipitate particles were analysed by quantitative x-ray energy dispersive spectroscopy (EDS).[4] Transmission electron microscopy and x-ray EDS were performed on a JEM 100-CX, 120-kV analytical electron microscope. Because of a limited number of samples, tensile testing was only performed on the duplicate samples irradiated at 625°C. Postirradiation tensile tests were performed at 625°C and a strain rate of 0.04/min.

3.3.4.1 Microstructure

Microstructural results for helium preinjected and uninjected 20%-cold-worked material after EBR-II irradiation are described below and summarized in Table 3.3.2.

No cavities are observed in uninjected material irradiated at 500°C (Fig. 3.3.2). The dislocation structure is a dense tangle but shows recovery to a dislocation density of about 3×10^{17} mm/m^3 compared with the 0.5×10^{19} to 1×10^{19} mm/m^3 typical of unirradiated 20%-cold-worked material. Transmission electron microscopy and selected area electron diffraction (SAD) reveal small particles of intragranular eta phase (diamond cubic, Fd3m, $E9_3$, a_0 = 1.07 nm) and discontinuous elongated particles of tau ($M_{23}C_6$) (face-centered cubic, Fm3m, D84, a_0 = 1.06 nm) at the grain boundaries. Gamma prime is not observed. An extraction replica confirms the presence of only these two phases. Figure 3.3.3 shows TEM, SAD from tau and eta in-foil, and characteristic x-ray EDS spectra and quantitative compositional information from extracted particles. Tau

Table 3 ∃.2. Microstructural Details for EBR-II-Irradiated 20%-Cold-Worked Type 316 Stainless Steel

Preinjected He (at. ppm)	Cavities			Dislocation Density (mm/m^3)	Precipitation
	Average Diameter (nm)	Average Concentration ($cavities/m^3$)	Volume Fraction, Swelling (%)		
			At 500°C		
none	*a*	*a*	*a*	3×10^{17}	Small eta particles in matrix. Isolated tau ($M_{23}C_6$) at grain boundaries.
110	*a*	*a*	*a*	4	Little or no eta or tau observed. Occasional moderately sized Laves particles observed in matrix and near grain boundaries.
			At 625°C		
none	*a*	*a*	*a*	2	Tau observed at grain boundaries. Very little matrix precipitation.
110	4	1×10^{22}	0.03	3	Considerable precipitation of tau and/or eta at grain boundary. Considerable eta and Laves phase particles along deformation bands in matrix.
200	5	1.2	0.08	3	Same as at 110 at. ppm He.

[a]None detected.

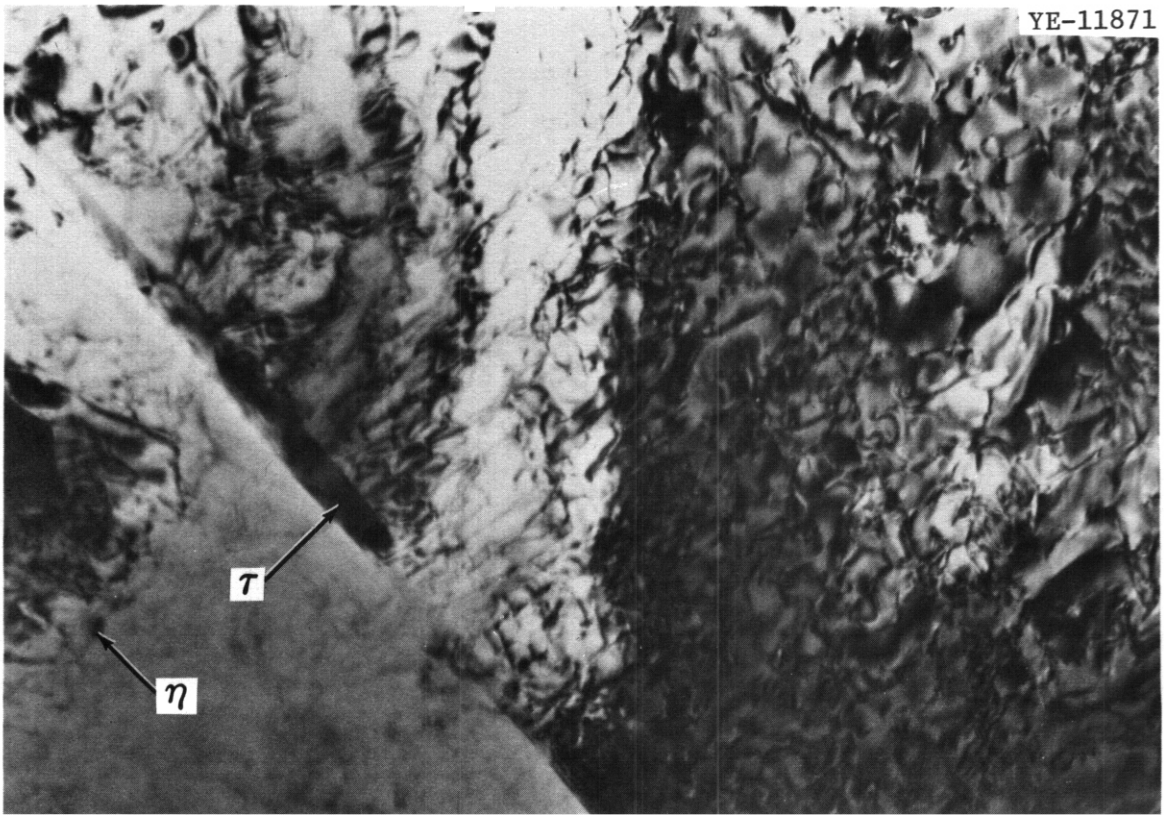

0.25 μm

Fig. 3.3.2. The microstructure of 20%-Cold-Worked Type 316 Stainless Steel Irradiated in EBR-II at 500°C to 8.4 dpa with No Preinjected Helium Shows Some Dislocation Recovery, No Cavities, and Sparse Precipitation of Eta and Tau.

is shown to be rich in Cr and Mo and poor in Fe and Ni. Silicon is contained at about the same level as the matrix. Eta phase on the other hand is clearly very rich in Si, Mo, Ni, and Cr and depleted in Fe. Both these compositions are nearly identical to those of the same phases produced in the same heat of material during thermal aging at 600 to 650°C.[5,6]

The microstructure of 20%-cold-worked material irradiated at 500°C with 110 at. ppm preinjected helium is not significantly different than uninjected material. No cavities are observable, and the dislocation structure is about the same, as shown in Fig. 3.3.4(a) and summarized in Table 3.3.2. Figure 3.3.4(b) shows the matrix in a weak diffracting, underfocused condition. No cavities are observable. However, even with

Y-165685

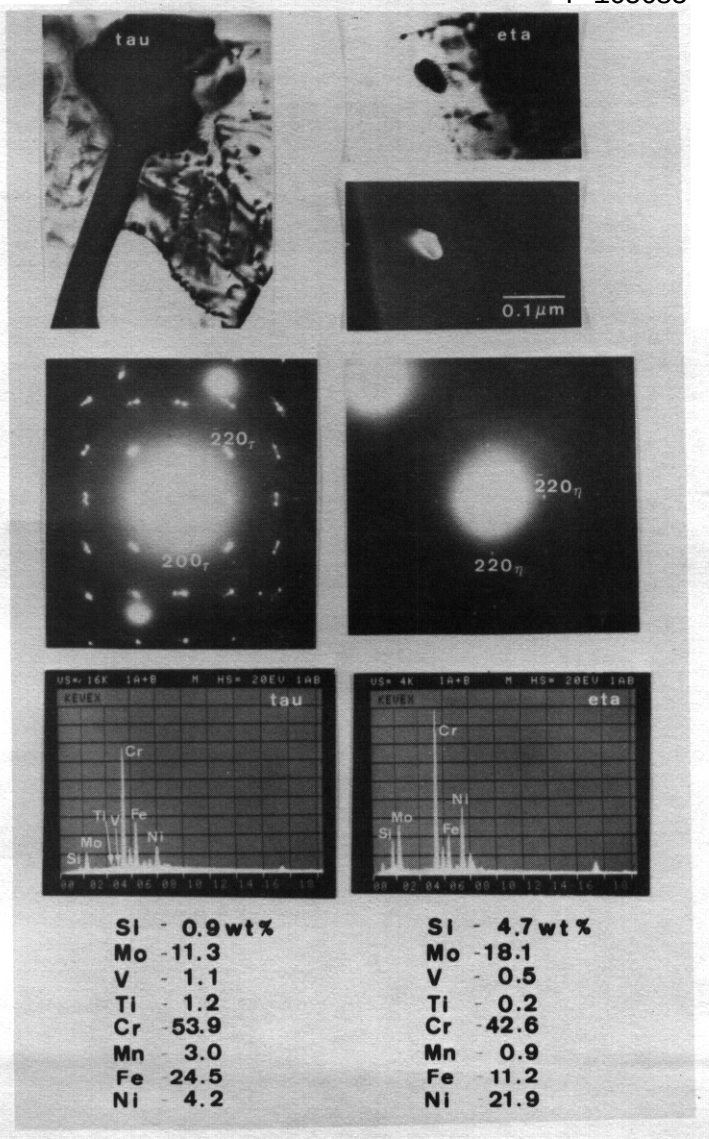

Fig. 3.3.3. This Composite Shows Transmission Electron Microscopy and Selected Area Diffraction of In-Foil Precipitate Particles or rau and Eta and the Characteristic X-Ray Energy Dispersive Spectroscopy Spectra with Hole Count Subtracted for the Same Phases Analyzed on a Carbon Extraction Replica. Also included is quantitative compositional information obtained from a standardless analysis of the measured integral peak intensities. (Source: N. J. Zaluzec, "Quantitative X-Ray Microanalysis: Instrumental Considerations and Applications to Materials Science," p. 83 in ***Introduction to Analytical Electron Microscopy.*** J. J. Hren, J. I. Goldstein, and D. C. Joy, Eds., Plenum Press, New York, 1970.)

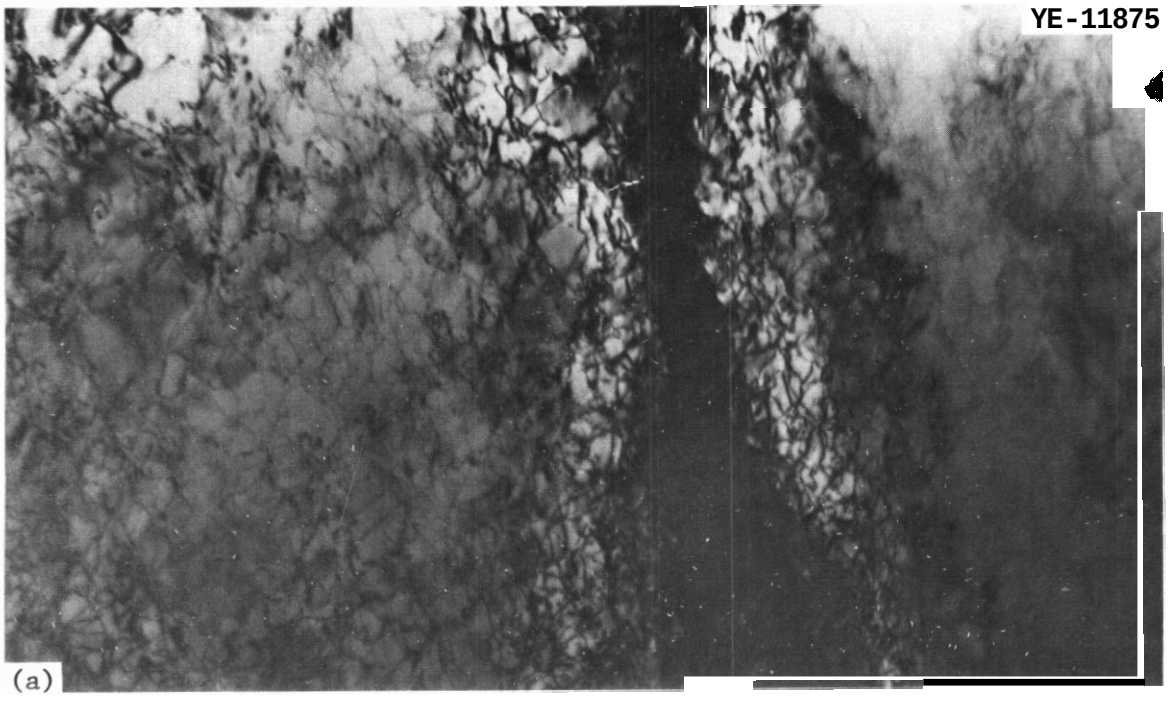

0.25 μm

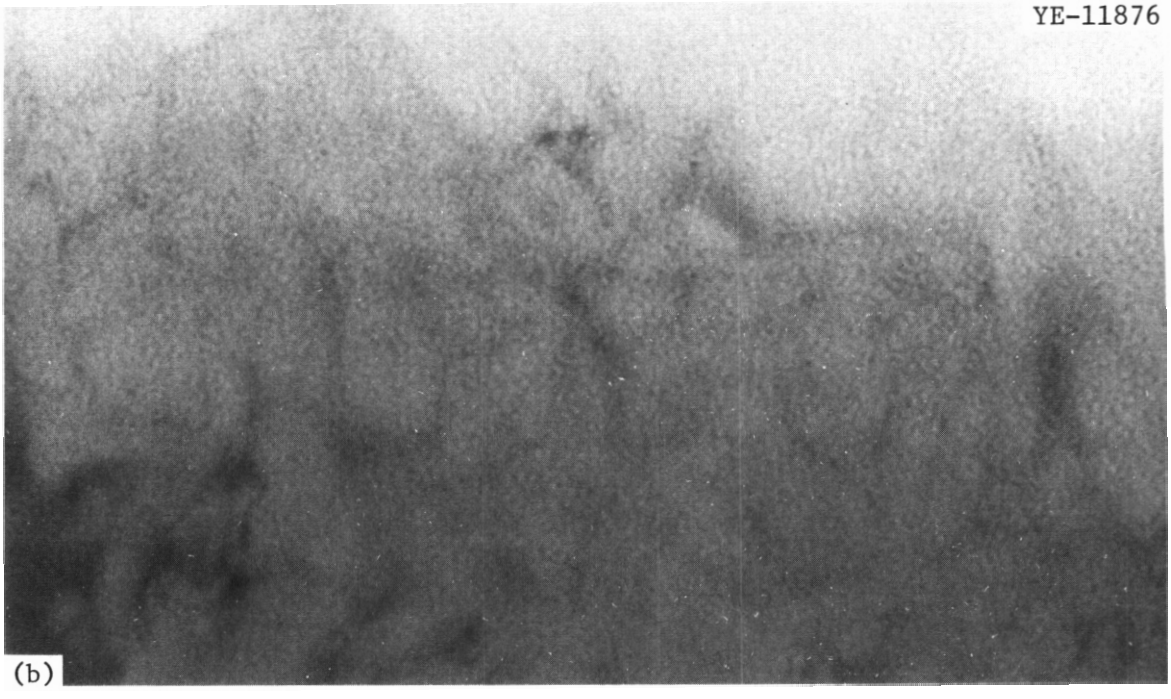

0.1 μm

Fig. 3.3.4. The Microstructure of 20%-Cold-Worked Type 316 Irradiated in EBR-II at 500°C to 8.4 dpa with 110 at. ppm Preinjected Helium. (a) The dislocation structure. (b) The matrix near the edge in a weak diffracting, underfocused condition. No cavities are discernable.

weak diffraction contrast, the residual contrast image of the dislocation is about 3 nm wide, which could obscure any smaller features. Small bubbles were shown previously to be attached typically to dislocation lines.[3,7] Relative to uninjected material, this material with 110 at. ppm He shows a reduction in the amounts of tau and eta and in addition shows some isolated Laves phase particles several hundred nanometers in size.

Figures 3.3.5, 3.3.6, and 3.3.7 show the microstructure of 20%-cold-worked type 316 stainless steel after EBR-II irradiation at 625°C with 0, 110, or 200 at. ppm preinjected helium. No cavities were observed in the uninjected material, as shown in Fig. 3.3.5 and summarized in Table 3.3.2. The dislocation structure was recovered from the original 20%-cold-worked state but differed little from the uninjected material irradiated at 500°C. Tau phase is observed at the grain boundaries, but little intragranular precipitation is present. By comparison helium preinjected material changes dramatically. Both Figs. 3.3.6 and 3.3.7 show that many tiny cavities are finely distributed along the dislocation structure. The cavity density is about 1 x 10^{22} cavities/m^3, and the average diameter is about 4 to 5 nm, as summarized in Table 3.3.2. The cavity density and size are both only slightly larger for material preinjected with 200 at. ppm He compared with 110 at. ppm He. The swelling is small in both cases but again slightly larger for the material with more helium. The dislocation structure is similar for both helium levels and only slightly increased compared with uninjected material. Figure 3.3.6 best illustrates the very obvious increase in precipitate particles for helium preinjected material compared with uninjected material. Profuse intragranular precipitation of Laves, eta, and/or tau can be seen along deformation bands In Fig. 3.3.6(a), and increased precipitation of tau and/or eta is visible on the grain boundaries in Fig. 3.3.6(b). Occasionally, grain boundaries contain coarse Laves phase particles. Laves phase is seldom observed at the grain boundaries for type 316 stainless steel in any environment.[6-10] Precipitation differs little between 110 and 200 at. ppm He preinjected material.

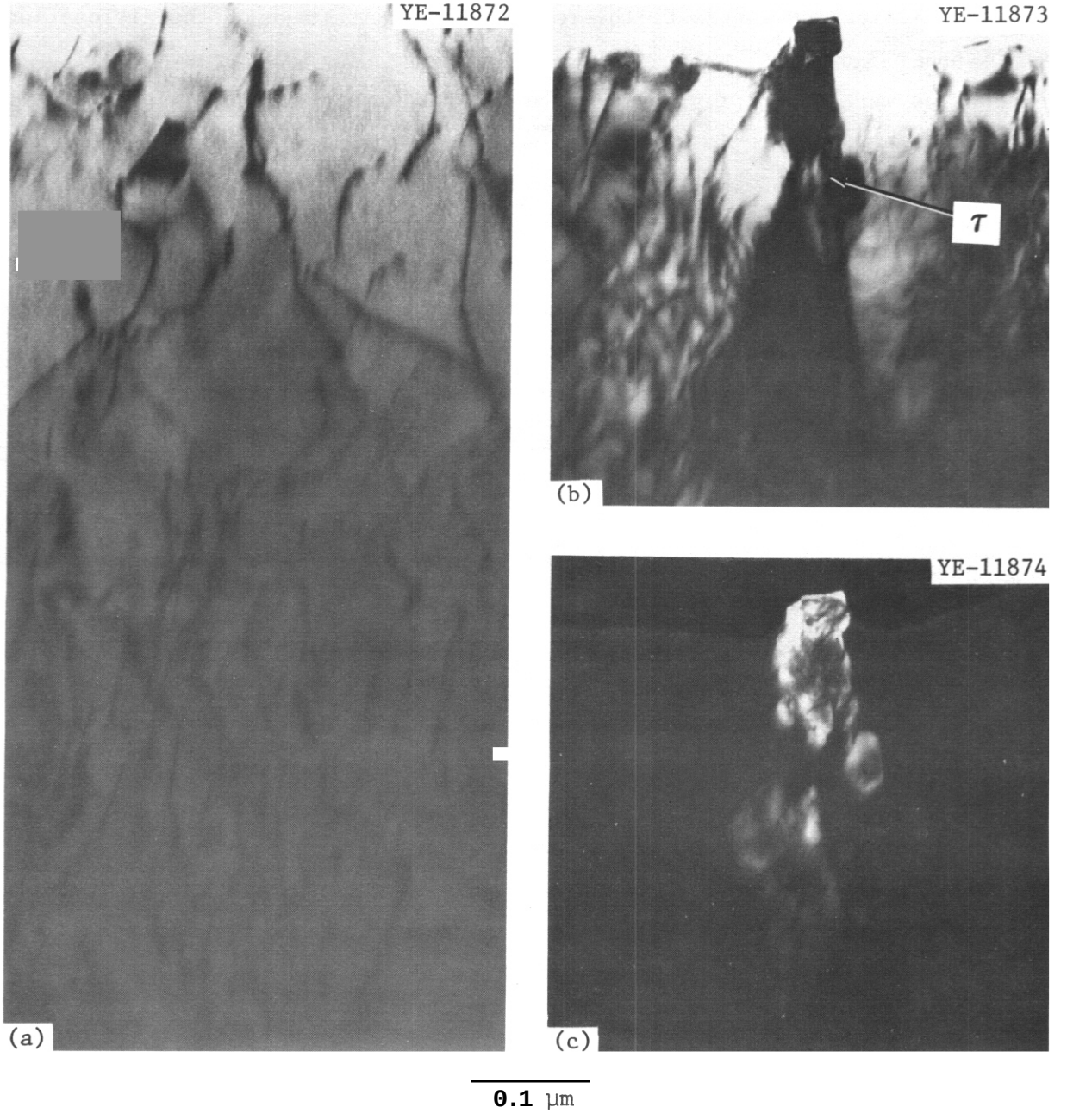

Fig. 3.3.5. The Microstructure of 20%-Cold-Worked Type 316 Stainless Steel Irradiated in EBR-II at 625°C to 8.4 dpa with No Preinjected Helium. (a) The dislocation structure. (b) and (c) Bright and dark field images, respectively, of tau and/or eta phase particles at the grain boundary.

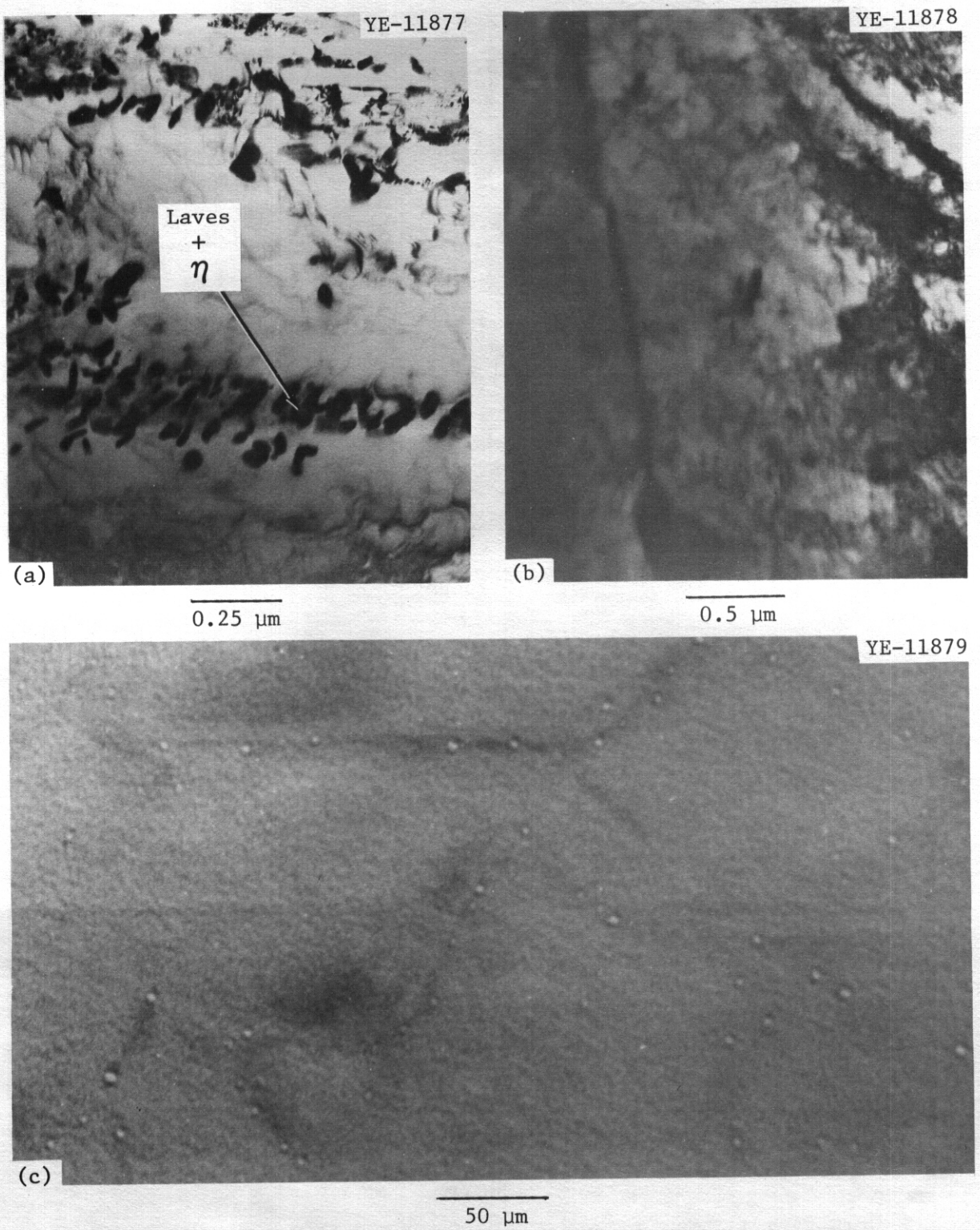

Fig. 3.3.6. The Microstructure of 20%-Cold-Worked Type 316 Stainless Steel Irradiated in EBR-II at 625°C with 110 at. ppm Preinjected Helium. (a) and (b) Laves, eta, and or tau have precipitated considerably in the matrix and the grain boundaries, respectively. (c) Small helium cavities are finely distributed along dislocations.

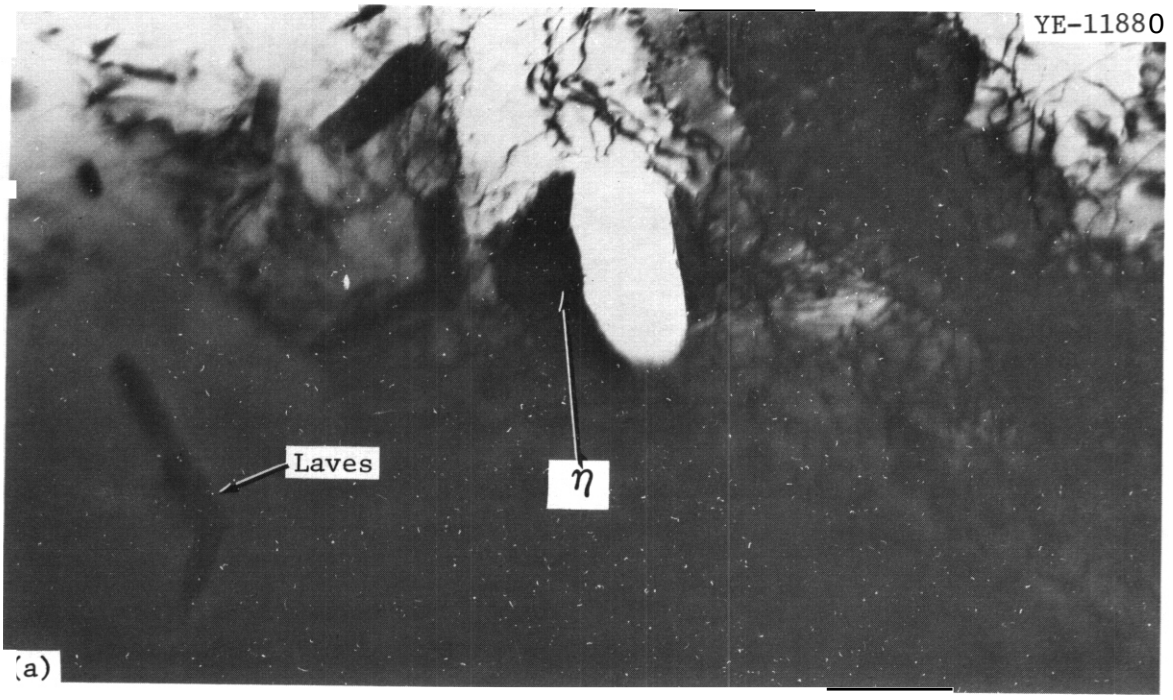

0.25 μm

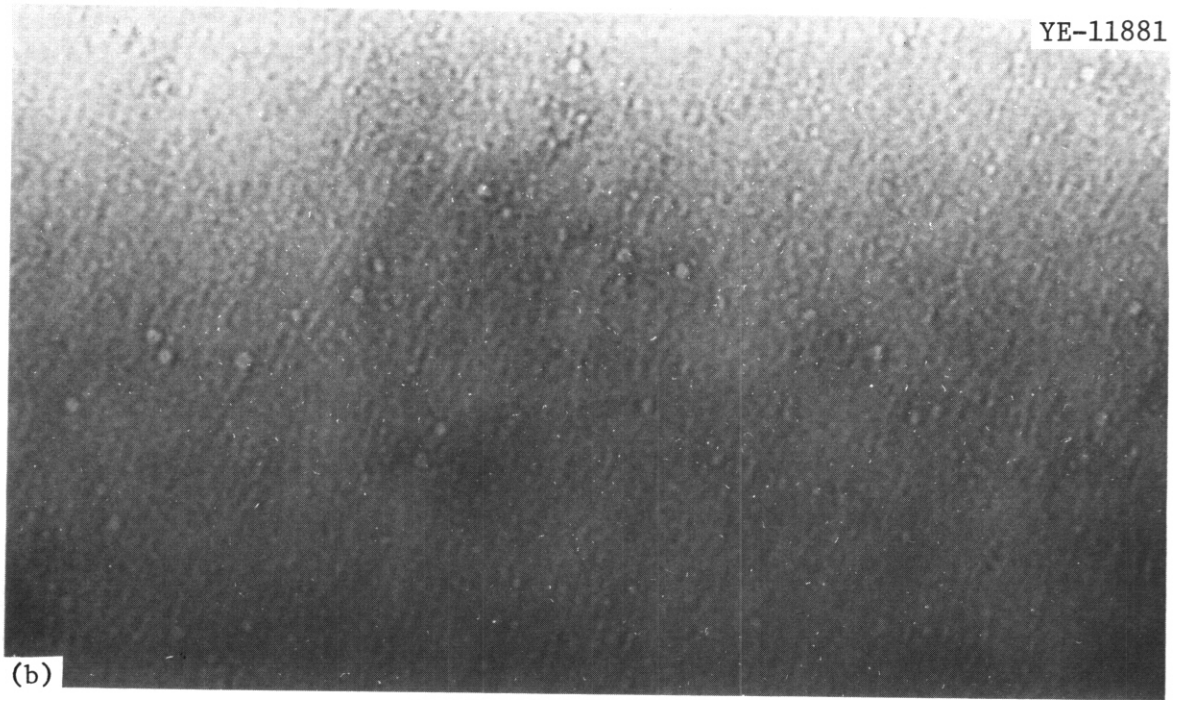

50 μm

Fig. 3.3.7. The Microstructure of 20%-Cold-Worked Type 316 Stainless Steel Irradiated in EBR-II at 625°C with 200 at. ppm Preinjected Helium. (a) The dislocation structure and matrix precipitation of Laves, eta, and/or tau. (b) Small helium cavities finely distributed along dislocations.

The amount of helium contained in cavities* at 625°C was calculated from the size distribution and a Van der Waals nonideal gas equation[7] of state and compared with the amount of gas measured in the sample. Assuming a surface energy of 1 J/m^2, the ratio at. ppm He measured-to-at. ppm He calculated ranges from 0.72 to 0.86 and 0.4 to 0.86 for material preinjected with 110 and 200 at. ppm He, respectively. The calculations are consistent with these cavities being either nearly equilibrium helium bubbles or containing a significant helium pressure. The result is similar to results for the HFIR irradiation of the same heat of steel[7] calculated with 1.5 J/m^2.

At the EBR-II row 8 damage rate of 7×10^{-7} dpa/s, the fluence produced in the EBR-11-irradiated 20%-cold-worked type 316 stainless steel corresponds to an exposure of about 3400 h. Figure 3.3.8 shows microstructures of samples of the same heat of 20%-cold-worked type 316 stainless steel after thermal aging for 2770 h at temperatures from 470 to 600°C. Figure 3.3.8(a) shows no recovery of the dislocation structure and no precipitation at 470°C. Figure 3.3.8(b) and (c) shows small intragranular particles of tau phase with dominantly tau and possibly some eta phase at the grain boundary at 560°C. At 600°C larger particles of tau and/or eta are present at the grain boundary with more and coarser intragranular precipitation of tau, eta, and Laves. Recovery of the dislocation structure coincides with the beginning of precipitation and increases with increased temperature. By comparison precipitation in the uninjected 20%-cold-worked type 316 stainless steel irradiated in EBR-II at 625°C appears retarded compared with thermally aged material. Helium preinjection increases precipitation to a level roughly comparable with thermally aged material. However, the relative amounts of Laves and eta appear to be increased. Laves is enhanced in the helium injected material irradiated at 500°C compared with thermally aged material at 560°C. Quite similar, trends were observed in a comparison of HFIR irradiation with thermally aged 20%-cold-worked type 316 stainless steel.

The microstructures of the same heat of 20%-cold-worked material irradiated in the HFIR at 470 and 560°C are shown for comparison in Figs. 3.3.9 and 3.3.10. These samples are irradiated to a neutron

---

*This assumes that $P = 2\lambda/r$, where P = pressure, λ = surface energy, and r = cavity radius.

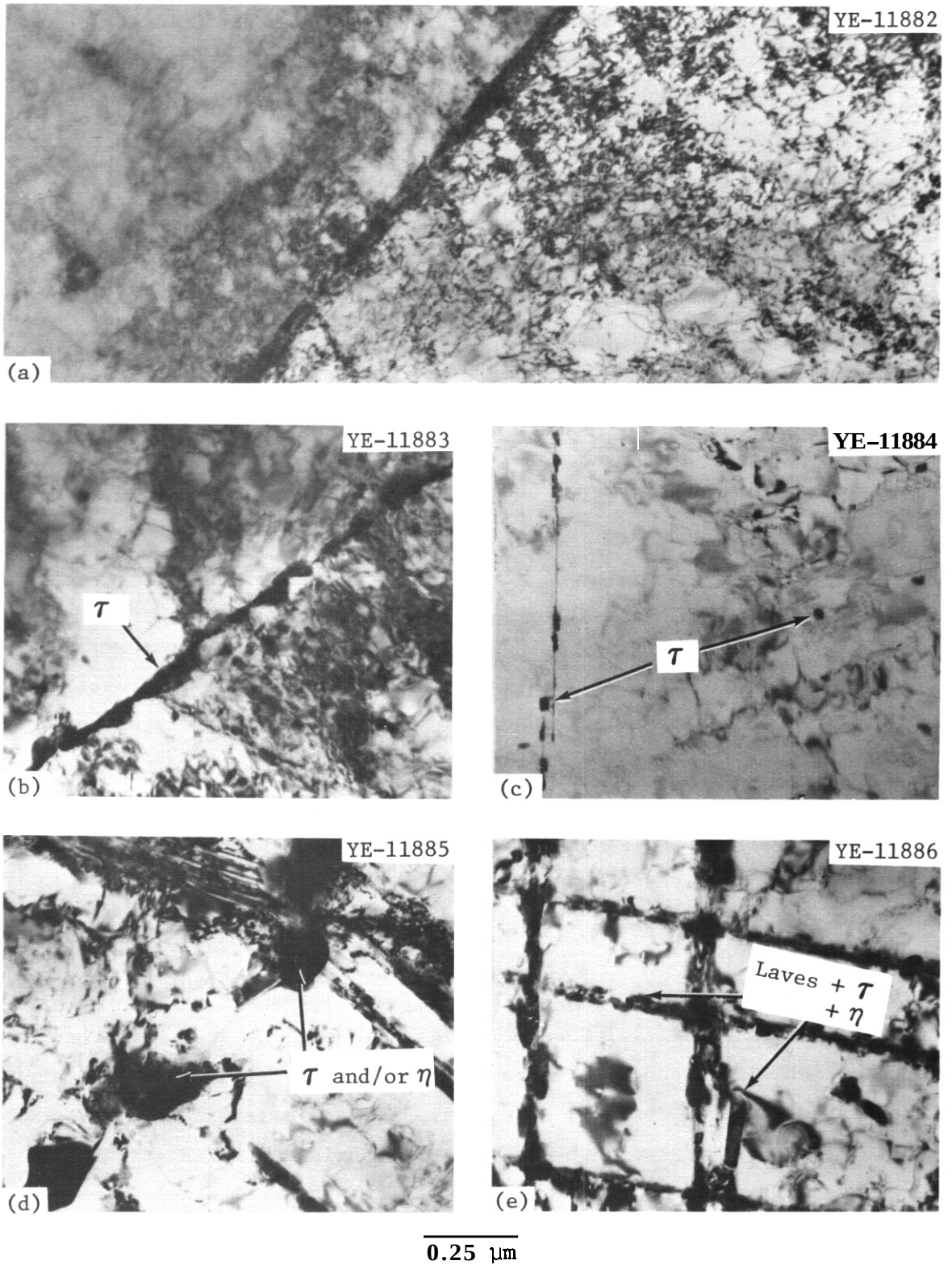

Fig. 3.3.8. The Microstructure of 20%-Cold-Worked Type 316 Stainless Steel After Thermal Aging for 2770 h at (a) 470°C, (b) and (c) 560°C, and (d) and (e) 600°C. (a) No change from unaged material. (b) through (e) Dislocation recovery coincides with precipitation of one or several phases.

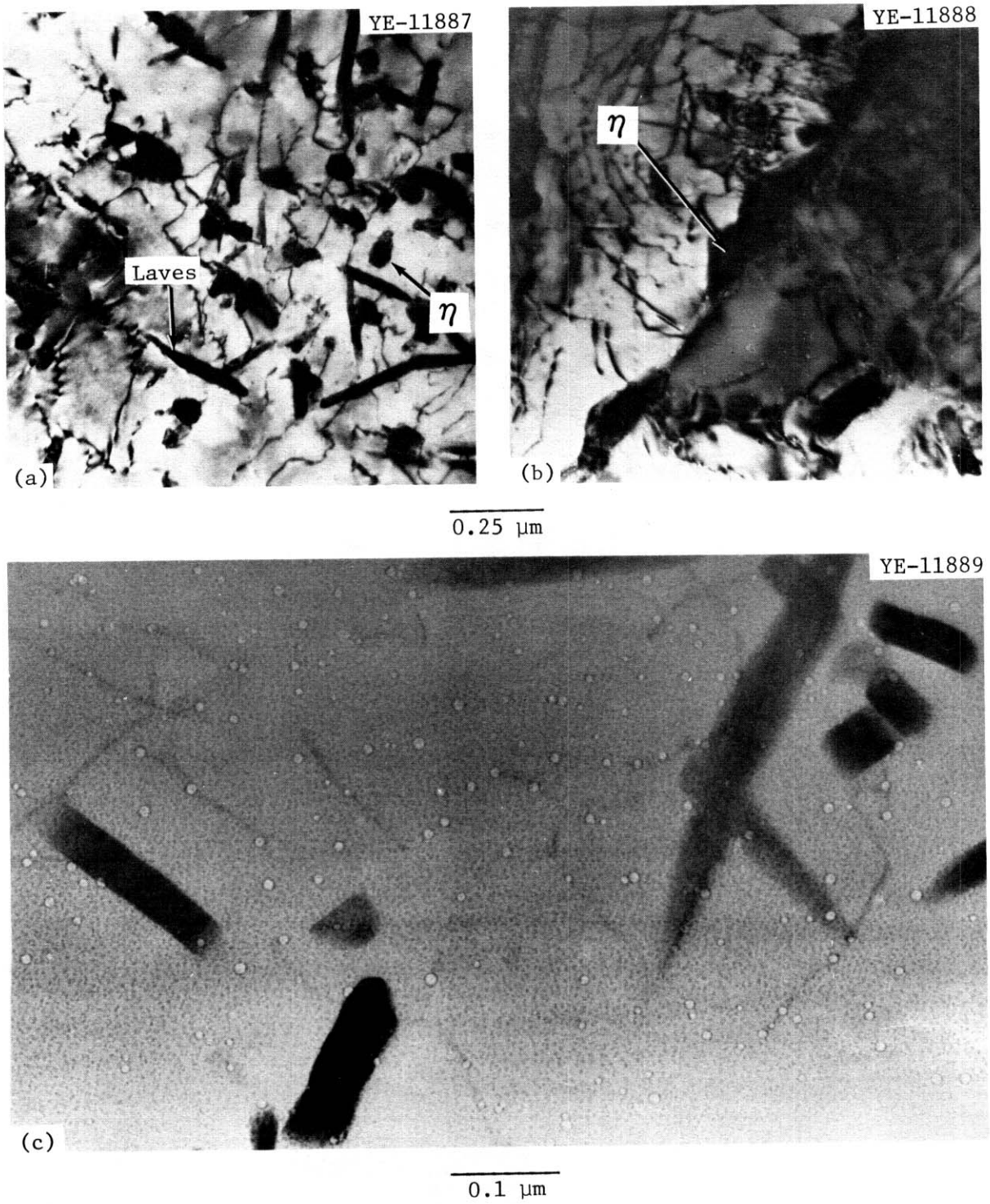

Fig. 3.3.9. The Microstructure of 20%-Cold-Worked Type 316 Stainless Steel Irradiated in the High Flux Isotope Reactor at 470°C to a Neutron Fluence of 1.4×10^{26} n/m^2 (>0.1 MeV), Producing 12 dpa and 540 at. ppm He. (a) The dislocation structure and intragranular precipitation of eta and Laves phases. (b) Eta phase and some cavitation at the grain boundary. (c) The cavity distribution.

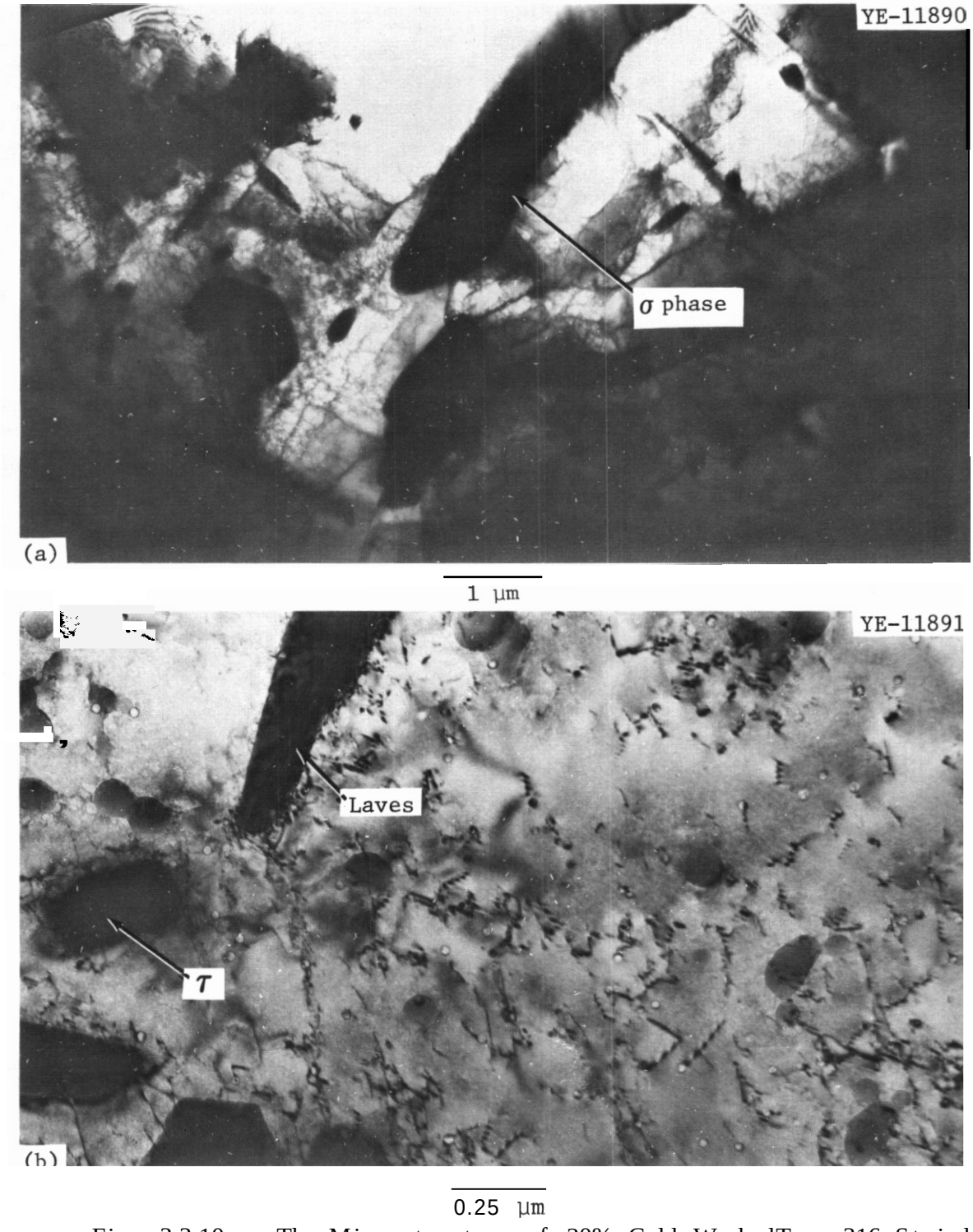

Fig. 3.3.10. The Microstructure of 20%–Cold–WorkedType 316 Stainless Steel Irradiated in the High Flux Isotope Reactor at 560°C to a Neutron Fluence of 1.3 × 10^{26} n/m^2 (>0.1 MeV), Producing 11 dpa and 490 at. ppm He. (a) Structural recovery and a large sigma phase particle at the grain boundary. (b) The dislocation structure, cavity distribution, and coarse Laves and tau precipitate particles in the matrix.

fluence of 1.3 $\times 10^{26}$ to 1.4 $\times 10^{26}$ n/m^2 (>0.1 MeV), which produces 10.8 to 11.8 dpa and 490 to 540 at. ppm He, respectively. The irradiation time was about 2770 h. Clearly the dislocation structure recovers tremendously and precipitation increases compared with thermally aged material (Fig. 3.3.8). The same trend for dislocation structure is observed relative to the uninjected 20%-cold-worked type 316 stainless steel irradiated in EBR-II at 500 and 625°C in Figs. 3.3.2 and 3.3.5, respectively. Precipitation is considerably increased in the HFIR-irradiated material at 470°C compared with EBR-11-irradiated material at 500°C with 110 at. ppm He (Figs. 3.3.4 and 3.3.9). Precipitation of similar phases is much coarser for HFIR-irradiated material at 560°C compared with EBR-11-irradiated material at 625°C with either 110 or 200 at. ppm He.

The microstructure of HFIR-irradiated 20%-cold-worked type 316 stainless steel at 470°C has a cavity density of about 2 x 10^{21} cavities/m^3 and an average cavity diameter of about 8 nm. The same material irradiated at 560°C has cavities about 20 to 25 nm in diameter with a density of about 4 $\times 10^{20}$ cavities/m^3. The cavity size and spacial distributions are much coarser for simultaneous helium and displacement damage produced during HFIR irradiation than for those produced in EBR-II irradiation of helium preinjected material at similar temperatures. Any upward correction of the calculated HFIR irradiation temperatures[5,6,8,11] of +0 to 50°C would make the comparison a little less stark. Both HFIR-irradiated and helium preinjected EBR-11-irradiated cavity distributions are much finer than void distributions that develop in uninjected EBR-II-irradiated 20%-cold-worked type 316 stainless steel at higher fluences.[3,7,12] Considering the total microstructure, microstructural development differs substantially among uninjected and helium preinjected EBR-11-irradiated and HFIR-irradiated 20%-cold-worked type 316 stainless steel. The method of introducing helium appears to play an important role in the microstructural differences that develop at reactor damage rates.

3.3.4.2 Mechanical Properties

The results of tensile tests conducted at 625°C are presented in Table 3.3.3. Tensile curves are plotted in Fig. 3.3.11 for comparison.

Table 3.3.3. Tensile Properties of Unirradiated and **EBR-II-**Irradiated 20%-Cold-Worked Type 316 Stainless Steel Tested at 625°C

Irradiation Temperature (°C)	Preinjected Helium (at. ppm)	Strength, MPa		Elongation, %	
		Yield	Ultimate Tensile	Uniform	Total
[a]		400	430	3.7	12.5
[a]		400	433	4.2	11.2
625	none	253	310	6.7	17.8
625	110	310	400	6.1	7.4
625	200	233	360	6.5	9.8

[a]Specimen was unirradiated.

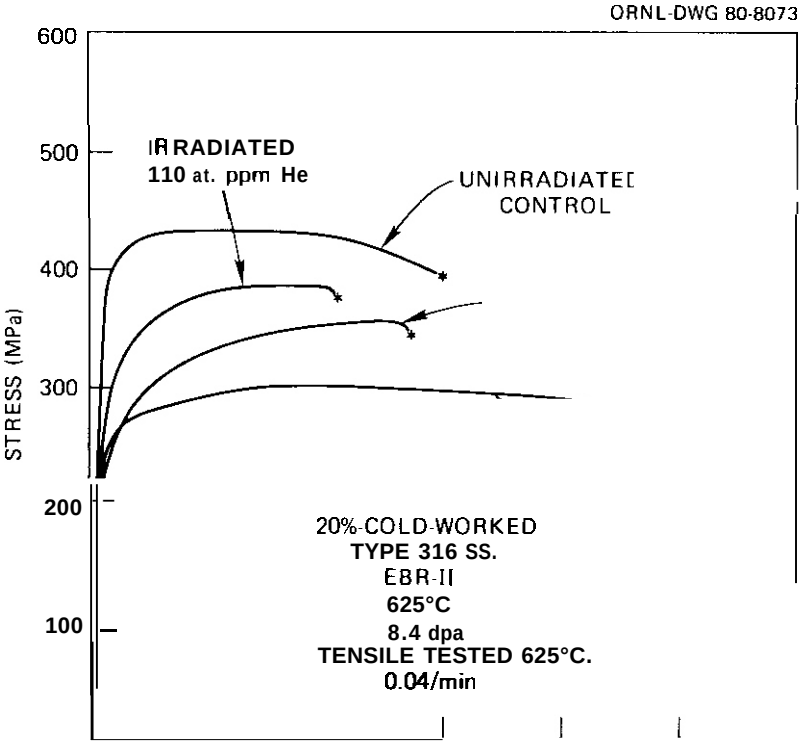

Fig. 3.3.11. Tensile Stress-Strain Curves for 20%-Cold-Worked Type 316 Stainless Steel Tested at 625°C. The irradiation and helium preinjection conditions are indicated, and an unirradiated control specimen is included for comparison.

Handbook data[13] for unirradiated 20%-cold-worked type 316 stainless steel indicate that at a test temperature of 625°C the ultimate tensile strength ranges from 470 to 530 MPa, the yield strength from 370 to 460 MPa, the uniform elongation from 1.5 to 5.0%, and the total elongation from 12.5 to 21.0%. The data for unirradiated specimens in Table 3.3.3 fall close or into these ranges. The uninjected material softens from EBR-II irradiation at this fluence as a result of recovery of the dislocation structure. The yield and ultimate strengths decrease, while the uniform and total elongation increase. This parallels results presented by Fish and Watrous[14] for EBR-11-irradiated 20%-cold-worked type 316 stainless steel irradiated at 593°C. It also correlates with the recovered dislocation structure shown in Fig. 3.3.5.

Both samples containing preinjected helium show decreased strength relative to unirradiated material. The same comparison shows that the uniform elongation increased and the total elongation decreased (Table 3.3.3 and Fig. 3.3.11). However, compared with irradiated, uninjected material, the helium preinjected steel shows increased ultimate strength and decreased total elongation. The differences between helium preinjected at 110 and 200 at. ppm are small with the material with less helium being slightly stronger and less ductile. Exact correlation of microstructure and properties is not straightforward because dislocation, cavity, and precipitate components of the microstructure change dramatically upon helium preinjection.

Small bubbles finely dispersed along dislocations should result in an increase in yield strength relative to the same dislocation configuration without bubbles; interstitial or substitutional helium can also cause strengthening.[15] Considerable solid-solution strengthening is also obtained from alloying elements that are interstitial, such as C and N, or substitutional, such as Si and Mo.[16] Precipitation of phases like eta, tau, and Laves removes silicon, molybdenum, and carbon and contributes little to precipitation strengthening. Thermal aging and testing of 20%-cold-worked type 316 stainless steel at 600 to 650°C leads to decreased strength and increased ductility that correlates well with both recovery and precipitation.[17] Any strengthening effect of the preinjected helium

in these samples is directly attributable to fine cavity distribution as a result of the dislocation structure not changing. This is because considerable precipitation of eta and/or tau and Laves occurs and because the cavities easily account for most of the helium. A reduction of total elongation is consistent with the trend normally observed for the same material irradiated in the HFIR to similar temperatures and fluences.[18] However, in this case, since considerable grain boundary precipitation occurs that includes Laves, it is not clear that the reduced ductility can be attributed solely to helium. The differences in strength and ductility for the two helium preinjection levels are small and may reflect subtle differences in precipitation as well as helium level.

3.3.5 Conclusions

For EBR-II irradiation of 20%-cold-worked type 316 stainless steel to a neutron fluence producing 8.4 dpa and about 5 at. ppm He:

1. Preinjection of either 110 or 200 at. ppm He produces a distribution of about 1×10^{22} cavities/m^3 of 4- to 5-mm-diam helium bubbles or cavities after irradiation at 625°C. Irradiation at 500°C with 110 at. ppm He results in a distribution of helium below the resolution limit (cavities at dislocations less than about 2 to 3 nm in diameter are very difficult to observe). No cavities are observed in uninjected material.

2. Recovery of the dislocation structure from 0.5×10^{19} to 1×10^{19} mm/m^3 before irradiation to about 2×10^{17} to 4×10^{17} mm/m^3 after irradiation occurs in uninjected material irradiated at either 500 or 625°C with virtually no observable change upon helium preinjection.

3. A small amount of intragranular eta phase and intergranular tau phase precipitates in uninjected material irradiated either at 500 or 625°C. Small changes occur for material with 110 at. ppm He irradiated at 500°C: Laves is introduced and eta and tau appear slightly decreased. Dramatic changes in precipitation occur for material with either 110 or 200 at. ppm He irradiated at 625°C: copious Laves, eta, and/or tau are produced both intra- and intergranularly.

4. Dislocation recovery is enhanced, but the amount of precipitation in uninjected irradiated material is about the same at 500°C and retarded at 625°C compared with the same material thermally aged for 2770 h at 470 to 600°C. Eta appears at lower temperatures in EBR-11-irradiated material. than in thermally aged material. Preinjection of helium enhances matrix Laves phase at both,temperatures and grain boundary Laves phase at 625°C relative to the thermally aged material.

5. Cavity formation and precipitation are tremendously enhanced and the dislocation structure is considerably more recovered for HFIR-irradiated material at similar fluences and temperatures compared with uninjected EBR-11-irradiated material. Preinjection of helium results in much finer distributions of helium and a finer size distribution of precipitate particles compared with similar uninjected material irradiated in the HFIR.

6. Yield and ultimate tensile strengths are decreased and total and uniform elongations are increased for uninjected compared with unirradiated material tested at 625°C. Preinjection of either 110 or 200 at. ppm He results in the same or increased strength and reduced total elongation relative to uninjected material tested at 625°C.

Further work will include examination and comparison of solution annealed type 316 stainless steel irradiated at the same conditions and of similar 20%-cold-worked type 316 stainless steel samples irradiated in EBR-II to a higher fluence in row 7. These results will also be compared with helium preinjection in other irradiation environments.

3.3.6 References

1. J. A. Horak, "Helium Implantation in Potential CTR Structural Materials," *Controlled Thermonuclear Materials Technology Program Annu. Prog. Rep. June 30, 1975,* ORNL-5082, pp. 40–42.
2. P. J. Maziasz and J. A. Horak, "Status of Helium-Preinjected Annealed and 20%-Cold-Worked Type 316 Stainless Steel Irradiated in EBR-II at 500 and 625°C," *ADIP Quart. Prog. Rep. June 30, 1978,* DOE/ET-0058/2, pp. 42–46.

3. P. J. Maziasz, "The Effect of 200 at. ppm Preinjected Helium on 20%-Cold-Worked Type 316 Stainless Steel Irradiated at 625°C in EBR-II," *ADIP Quart. Prog. Rep. Sept. 30, 1978*, DOE/ET-0058/3, pp. 26–31.

4. N. J. Zaluzec, "Quantitative X-Ray Microanalysis: Instrumental Considerations and Applications to Materials Science," p. 83 in *Introduction to Analytical Electron Microscopy*, J. J. Hen, J. I. Goldstein, and D. C. Joy, Eds., Plenum Press, New York, 1979.

5. P. J. Maziasz, "The Formation of Diamond-Cubic Eta ( ) Phase in Type 316 Stainless Steel Exposed to Thermal Aging or Irradiation Environments," *Scri. Metall.* 13(7): 621–26 (1979).

6. P. J. Maziasz, "The Precipitation Response of 20%-Cold-Worked Type 316 Stainless Steel to Simulated Fusion Irradiation," *J. Nucl. Mater.* 85 & 86(II,B): 71317 (December 1979).

7. P. J. Maziasz, F. W. Wiffen, and E. E. Rloom, "Swelling and Microstructure Changes in Type 316 Stainless Steel Irradiated Under Simulated CTR Conditions," *Radiation Effects and Tritium Technotogy for Fusion Reactors*, CONF-750989, Vol. 1, pp. 259–88 (March 1976).

8. P. J. Maziasz, "Precipitation Response of Austenitic Stainless Steel," pp. 160–80 in *The Metal Science of Stainless Steel*, E. W. Collins and H. W. King, Eds., The Metallurgy Society of AIME, New York, 1979.

9. B. Weiss and R. Stickler, "Phase Instabilities During High-Temperature Exposure of 316 Stainless Steel," *Metall. Trans.* 3: 851–66 (1972).

10. D. V. Edmonds and R.W.K. Honeycombe, "Precipitation in Iron-Base Alloys," pp. 121–60 in *Precipitation Processes in Solids*, K. C. Russell and H. I. Aaronson, Eds., The Metallurgy Society of AIME, New York, 1978.

11. M. L. Grossbeck, Oak Ridge National Laboratory, unpublished data, 1979.

12. H. R. Brager, "The Effect of Cold Working and Preirradiation Heat Treatment on Void Formation in Neutron-Irradiated Type 316 Stainless Steel," *J. Nucl. Mater.* 57: 103–18 (1975).

13. *Nuclear Systems Materials Handbook*, TID 26666, Vol. 1 (1978).

14. R. L. Fish and J. D. Watrous, "Effect of Test Reactor Irradiation on the Tensile Properties of 20%–Cold–Worked Type 316 Stainless Steel," pp. 91–100 in *Irradiation Effects on the Microstructure and Properties of Metals, Am. Soc. Tech. Mater. Spec. Tech. Publ.* 611, 1976.

15. P. Vela and B. Russell, "The Behavior of Helium Gas in Irradiated Copper–Boron Alloys," *J. Nucl. Mater.* 19: 312–26 (1966).

16. F. B. Pickering, "The Metallurgical Evolution of Stainless Steel," pp. 1–42 in *The Metallurgical Evolution of Stainless Steel,* F. B. Pickering, Ed., American Society for Metals, Metals Park, Ohio, and The Metals Society, London, 1979.

17. D. Fahr, "Analysis of Stress–Strain Behavior of Type 316 Stainless Steel," ORNL/TM-4292 (November 1973).

18. M. L. Grossbeck and P. J. Maziasz, "Tensile Properties of HFIR–Irradiated Types 316 and TiM 316 Stainless Steel at 200 to 1000 at. ppm He," *ADIP Quart. Prog. Rep. Sept. 30, 1978,* DOE/ET-0058/3, pp. 32–50.

4. PATH B ALLOY DEVELOPMENT — HIGHEK STRENGTH Fe–Ni–Cr ALLOYS

5. PATH C ALLOY DEVELOPMENT — REACTIVE AND REFRACTORY ALLOYS

5.1 TZM AND NB-1ZR IRRADIATED TO HIGH FLUENCE - D. S. Gelles and J. F. Bates (Hanford Engineering Development Laboratory)

5.1.1 ADIP Task

I.C.4 - Microstructures and Swelling in Special Reactive/Refractory Alloys (Path C).

5.1.2 Objective

The purpose of this effort is to provide high fluence swelling and microstructural information on molybdenum and niobium based commercial alloys.

5.1.3 Summary

TZM and Nb-1Zr are found to be low swelling materials during irradiation to *1.4* x 10^{23} n/cm^2 (E >0.1 MeV) over the temperature range *400* to 650°C. Peak swelling in TZM after irradiation at 590 and 650°C is 3%, and peak swelling in Nb-1Zr after irradiation at 650°C is 0.6%. Neither void shrinkage nor swelling saturation was observed in TZM.

5.1.4 Progress and Status

5.1.4.1 Introduction

As part of the National Cladding/Duct Materials Development Program (NCD) for LMFBR development, specimens of TZM and Nb-1Zr were included in the specimen matrix in the AA-Ia and AA-I swelling tests. As these materials are no longer of interest to the NCD program, they have been made available for fusion related studies.

5.1.4.2 Experimental Procedures

Annealed TZM bar stock was obtained from Climax Molybdenum Company of Michigan (heat number TZM 8967, heat treatment 1315°C/2.5 hours) and similar Nb-1Zr stock was obtained from Teledyne Wah Chang, Albany, Oregon (heat number 530126-Cb1Zr, heat treatment 1210°C/1 hour). Details of alloy chemistry are provided in Table 5.1.1.

TABLE 5.1.1

CHEMICAL COMPOSITIONS (IN WEIGHT PERCENT) FOR TZM AND Nb-1Zr AS PROVIDED BY THE MANUFACTURERS

Alloy	Code	Mo	Nb	Zr	Ti	C	O	H	N	Ta	Fe	Ni	Si	W
TZM	83	balance	NA	0.090	0.45	0.013	0.0007	<.0001	.0002	NA	0.003	<0.001	0.002	NA
Nb-1Zr	82	0.0025	balance	0.9	<.004	0.003	<.005	<.0005	.004	0.096	<.005	<.002	<.005	0.0077

NA = not available

The materials were machined into 0.3 cm diameter by 1.3 cm right solid cylinders and identification codes were stamped into the end faces. Specimens of TZM were included in pin B-109 of the AA-Ia swelling test and specimens of both TZM and Nb-1Zr were included in pins B-111, B-113 and B-115-117 of the AA-I swelling test. Irradiation vehicles were 3-7a capsules with eight subcapsules constructed to run at eight different temperatures. The temperatures are controlled by gas gap regulation of gamma heat loss. Within each subcapsule, specimens were immersed in static sodium to insure uniform temperatures.

Irradiations were performed in the Experimental Breeder Reactor II (EBR-II), Idaho Falls, ID. Pin B-109 was irradiated in Row 4 and pin B-117b was irradiated in Row 2. Maximum accumulated fluence was 14.7 x 10^{22} n/cm^2 (E >0.1 MeV) and fluences varied as a function of subcapsule position from core midplane.

Irradiation-induced swelling was determined by comparison of pre- and postirradiation immersion density measurements using at least two measurements. The acceptable maximum variation between individual measurements was 50.05%.

Specimens for transmission electron microscopy were prepared by slicing 0.03 cm thick wafers from rod specimens using a slow speed saw with diamond impregnated ganged blades and then by electro-jet polishing the wafers in a Metalthin electropolishing device. TZM was polished in a solution of 20% sulfuric acid in methanol, at 35V, 600ma and a moderate pump speed of 3. Nb-1Zr was polished in a solution of 15% hydrofluoric acid, 10% sulfuric acid in lactic acid at 30V, 100ma and a moderate pump speed of 3. Microscopy was performed on a JEM 200A outfitted with a side entry double tilting gonimeter stage.

5.1.4.3 Results

5.1.4.3.1 Density Change Measurements. Density change measurements revealed that both TZM and Nb-1Zr were low swelling materials. In almost all cases, swelling was considerably less than 1%. However, the exceptions, TZM irradiated at both 590 and 650°C to fluences in excess of 14 x 10^{22} n/cm^2 (E >0.1 MeV), showed density changes on the order of 3%.

The data is tabulated in Table 5.1.2 and plotted in Figure 5.1.1. Figure 5.1.1 also provides the fluence levels which correspond to each data point. From Figure 5.1.1 it can be seen that: 1) above 550°C, swelling in TZM increases dramatically as fluence increases from 5.4 x 10^{22} n/cm^2 to 14.6 x 10^{22} n/cm^2 (E >0.1 MeV); 2) at all irradiation temperatures, TZM develops increased swelling with increasing fluence; and 3) compared to TZM, Nb-1Zr develops much less swelling, about 0.64% at 650°C and 0.25% at lower temperatures. A maximum swelling rate of 0.32%/10^{22} n cm^{-2} can be estimated for TZM based on the data of Table 5.1.2.

5.1.4.3.2 Microstructural Examination. Transmission electron microscopywas performed on specimens of TZM irradiated at 425, 540 and 650°C and specimens of Nb-1Zr irradiated at 425 and 650°C. Microstructural examination revealed that the density change observed in TZM irradiated at 650°C to 14.6 x 10^{22} n/cm^2 was indeed due to void swelling. A void lattice had formed throughout the sample and relatively large void free regions in bands 30 nm wide were centered along grain boundaries. The void lattice was not perfect and consisted of voids arrayed on {110} planes with very large variations in void size. The largest voids were on the order of 10 nm in diameter. Examples of the void array in specimen 83H7 are provided in Figures 5.1.2 a, b, and c, showing an area in 111, 131, and 010 orientation. Void swelling measurements from this area demonstrated 3.01% swelling with a mean void diameter of 7.2 nm and a number density of 1.3 x 10^{17} cm^{-3}.

In comparison, the TZM specimen irradiated at 540°C to 13.6 n/cm^2 (E >0.1 MeV) had developed similar void arrays, but on a much less extensive scale. Void development was patchy, with some areas having developed void lattices with voids as large as 10 nm and other adjacent areas containing no resolvable voids. An example is provided for comparison in Figure 5.1.2d for a foil in 113 orientation. The TZM specimen irradiated at 425°C to 12.2 x 10^{22} n/cm^2 (E >0.1 MeV) was found to contain no resolvable voids.

5 1 2

DENSITY CHANGES IN IRRADIATED TZM AND Nb-1Zr

Temp/Fluence*	TZM[1] Code	TZM[1] $-\%\Delta\rho/\rho_o$	Temp/Fluence*	TZM[2] e	TZM[2] $-\%\Delta\rho/\rho_o$	Nb-1Zr[2] Code	Nb-1Zr[2] $-\%\Delta\rho/\rho_o$
400 / 3.3	ZM	0.00	400 / 10.0	6	0.16	82M6	0.28
425 / 4.3	ZL	-0.04	425 / 12.2	6	0.09	82L6	0.22
450 / 3.4	ZE	-0.02	450 / 9.7	6	0.14	82E6	0.31
480 / 4.4	ZF	-0.01	480 / 12.0	6	0.18	82F6	0.25
500 / 5.1	ZK	0.00	510 / 14.0	6	0.13	82K6	0.22
510 / 5.1	ZG	-0.02	540 / 13.6	6	0.33		
560 / 5.4	ZJ	-0.01	590 / 14.7	6	3.01	82J6	0.30
600 / 5.4	ZH	0.06	650 / 14.6	7	2.96	82H7	0.64

*Temperature (°C)/Fluence (10^{22} n/cm^2, E >0 1 MeV)

[1]From AA-Ia - B-109

[2]From AA-I - B-117b

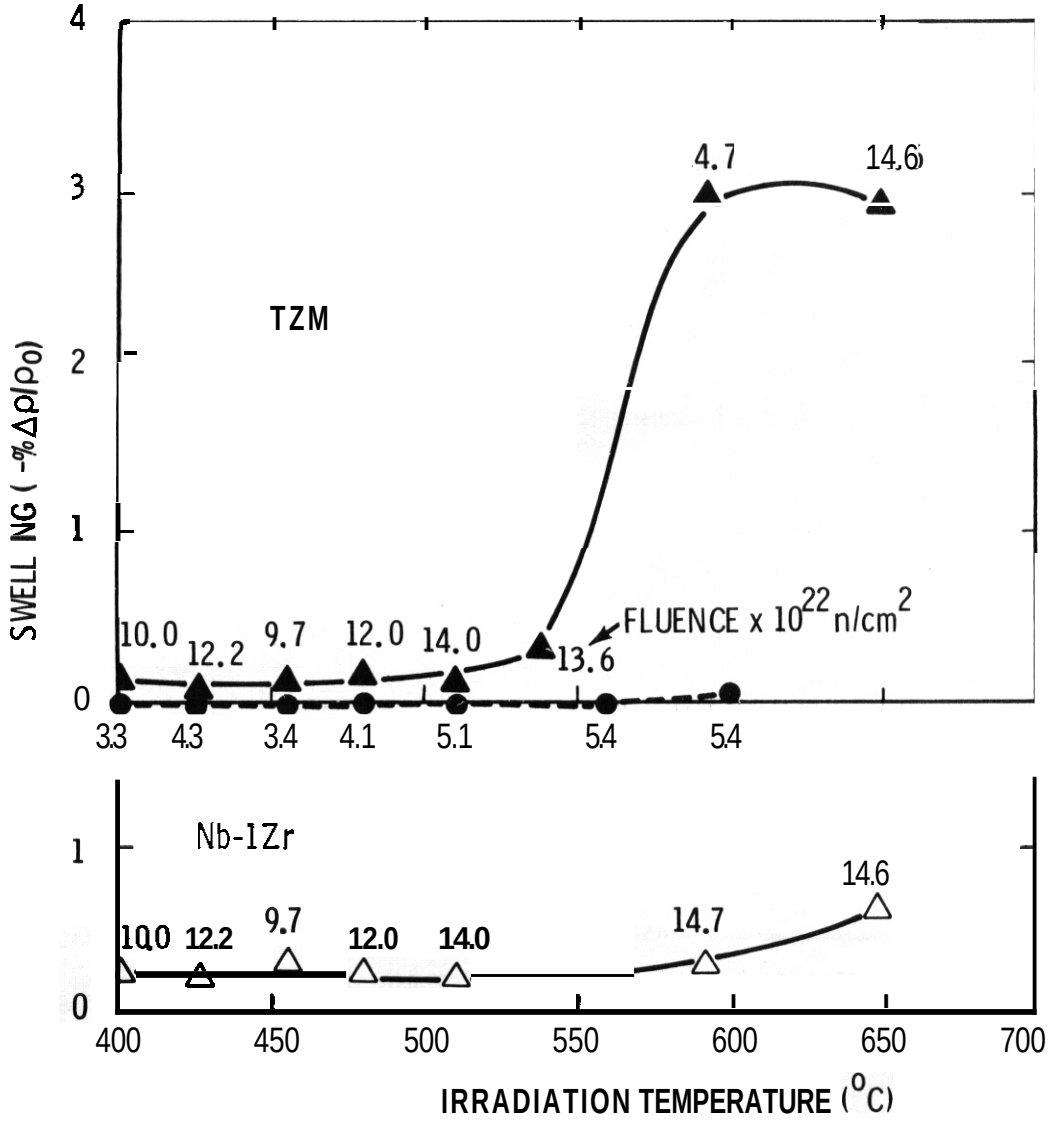

Figure 5.1.1 Density Change Measurements as a Function of Irradiation Temperature for Irradiated Specimens of TZM and Nb-1Zr.

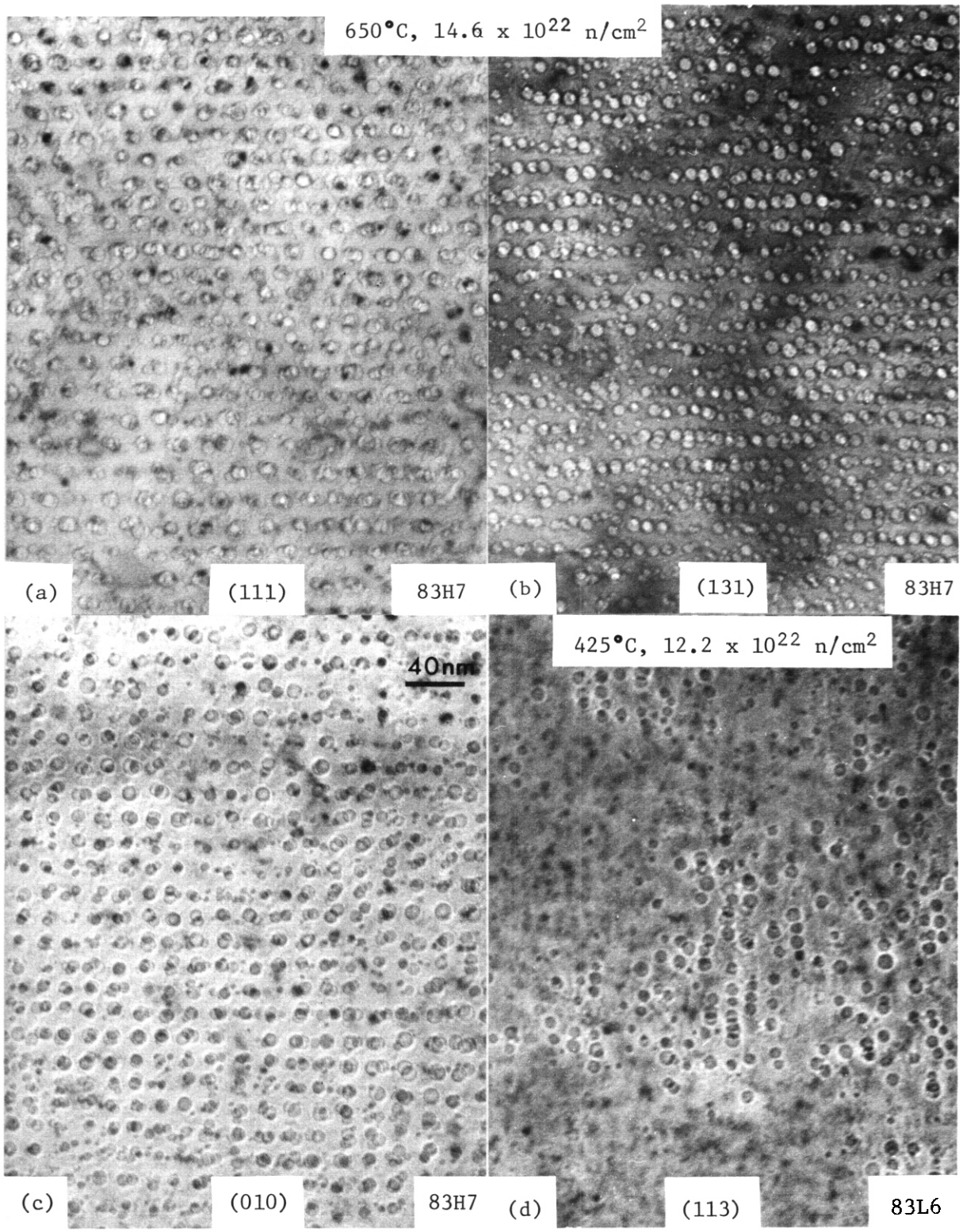

Figure 5.1.2 Void Arrays in Irradiated TZM Specimens. The irradiation conditions and specimen orientations are as indicated.

The dislocation structure in irradiated TZM specimens consisted primarily of features identified in the literature as dislocation loops. The loops were on the order of 10 nm in diameter or less in all specimen conditions examined. After irradiation at 650°C, the loop density was relatively low, and a significant number of irregularly shaped dislocation lines were found. After irradiation at lower temperatures, the loop density was much higher and approached the value of the void density particularly in regions where voids had not formed.

The Nb-1Zr specimen irradiated at 650°C to 14.6 x 10^{22} n/cm^2 (E >0.1 MeV) contained a very non-uniform density of small voids and a high density of small precipitates. The largest voids were 8 nm in diameter and were associated with dislocations. The mean void diameter was 5.1 nm, a minimum size was 2 nm, and the void density was 9 x 10^{15} cm^{-3}. This corresponding void swelling was *0.07%.* No evidence for a void array could be found. The precipitate phase consisted of a fine uniform distribution of 7 nm particles and a coarser distribution of 20 nm particles. Attempts to identify the precipitate from its electron diffraction lattice parameters have been unsuccessful and it is therefore concluded that this precipitate is a radiation induced phase. However, it is anticipated that the low void swelling observed and the discrepancy between void swelling and density change measurements is due to the precipitation which occurs in the alloy. In comparison, no resolvable void swelling and no evidence for an irradiation induced phase could be found in the Nb-1Zr specimen irradiated at *425°C* to **12.2** x 10^{22} n/cm^2 (E >0.1 MeV). The primary effect of irradiation was to produce a high density of small dislocation loops.

5.1.4.4 Discussion

The present results represent the highest known neutron fluence data reported for TZM and Nb-1Zr and therefore should provide the most realistic description of the microstructural development to be expected in these materials at high fluence. It is of interest in this discussion to comment on the applicability of previous predictions in light of the present results.

In a recent paper by Evans[1] it was reported that void swelling in molybdenum and TZM saturated at 0.75% at a fluence of 8 x 10^{22} n/cm^2 and more importantly, for irradiation temperatures below 600°C, void shrinkage had occurred. The effect was explained in terms of a solute segregation/ void suppression mechanism involving the transmutation product technetium. A thin coating of technetium on void surfaces was invoked as a plausible explanation and it was presumed that technetium rich regions would inhibit void growth and eventually cause shrinkage by inhibiting vacancy mobility but not restricting interstitial flux.

The present results do not support this theory. Swelling is not found to saturate in the fluence range 8 x 10^{22} n/cm^2 (E >0.1 MeV) and no evidence for negative swelling rates due to void shrinkage is found for irradiation temperatures below 600°C. Additionally, this theory is not supported by the work of Spragae et al[2] wherein void swelling of 4.0% was measured in a localized region of TZM after irradiation to 5.4 x 10^{22} n/cm^2 (E >0.1 MeV) at 650°C.

Some indication has been found that the solute segregation mechanism invoked by Evans may play a role. There appears to be a maximum void size irrespective of irradiation temperature. Thus, as the voids grow, they may absorb solute until sufficient solute is built up to inhibit further growth beyond a critical void size. However, a possible impact of such an effect is to promote further void nucleation (a point overlooked by Evans) and this is likely the cause of void rafting and very localized void swelling. (It should be noted that L. E. Thomas of HEDL made a special attempt to demonstrate the presence of technetium on void surfaces in specimen 83H7 using a sophisticated energy dispersive x-ray spectrometer (EDAX) capability, but was unsuccessful.)

It is perhaps worth speculating on the effect of irradiation to even higher fluences. Void swelling would be expected to continue further with increasing fluence beyond 14 x 10^{22} n/cm^2 (E >0.1 MeV). However, the possibility exists that in TZM eventually all voids in a void array will grow to the critical size of 10 nm whereupon the vacancy concentration will be still further supersaturated. At that point, the void swelling rate can be expected to decrease and it is certainly possible

that sufficient point defect recombination will occur leading eventually to a stable microstructure. However, it is unlikely that void shrinkage would occur.

5.1.5 Conclusions

TZM and Nb-1Zr irradiated up to 14.7 x 10^{22} n/cm^2 (E >0.1 MeV) over the temperature range *400* to 650°C swell only slightly. Peak swelling of 3% was found in TZM at 590 and 650°C and peak swelling of 0.6% was found in Nb-1Zr at 650°C. Void shrinkage was not observed and swelling saturation had not occurred.

5.1.6 References

1. J. H. Evans, "Void Swelling and Irradiation-Induced Void Shrinkage in Neutron Irradiated Molybdenum and TZM," *J. Nuc. Mat.*, *88*, **(1980) 31.**
2. J. A. Sprague, F. A. Smidt, Jr., and J. R. Reed, "The Microstructure of Some Refractory Metals and Alloys Following Neutron Irradiation at 650°C," *J. Nuc. Mat.*, 85 *and* 86 (1970) 739.

5.2 EFFECT OF HYDROGEN ON FLAW GROWTH OF TITANIUM ALLOY Ti-6242s - G. W. Wille and P. S. Pao (McDonnell Douglas Corporation)

5.2.1 ADIP Task

Task 1.B.3, Fatigue Crack Growth in Reactive/Refractory Alloys (Path C).

5.2.2 Objective

The objective of this study is to develop quantitative data to determine the effects of both internal and external hydrogen on fatigue crack growth of Ti-6242s alloy at temperatures and hydrogen pressures of interest for fusion reactors.

5.2.3 Summary

Hydrogen charging of Ti-6242s material is complete. Machining of modified-WOL specimens is in progress. No spontaneous hydride precipitation was observed in the material hydrogen charged to 24,100 appm (530 wppm). Room temperature tensile properties were slightly higher fur the hydrogen charged specimens than for the as-received specimens.

5.2.4 Progress and Status

Specimen blanks have been hydrogen charged in three batches at Argonne National Laboratory as described below.[1]

The hydriding was accomplished by stacking the specimens in a fused silica tube (76 mm O.D.), keeping them separated with thin glass rods. The tube was filled with hydrogen and heated to ∿570°C. Hydrogen uptake did not commence until the temperature of the sample reached ∿520°C. Past this temperature very rapid absorption rates were observed. Additional hydrogen was added, as needed, to reach the desired concentration. The plates were equilibrated at 570°C for two days and then slowly cooled to room temperature. Hydriding data are presented in the following table.

Batch	1	2	3
No. of plates[a]	10	10	9
Weight of plates (g)	631.4	632.1	572.3
Weight of H added (g)	0.316	0.402	0.286
Predicted Concentration appm (wppm H)	22,700 ± 450 (500)	28,900 ± 450 (636)	22,700 ± 450 (500)
Source of Hydrogen	Cylinder[b]	Cylinderb	Ti-Sponge

[a]plate dimensions: 57 x 76 x 3.1 mm (2 1/4 x 3 x 1/8 in.)

[b]stated purity 99.999%

Two grades of hydrogen were employed for the experiments. For batches 1 and 2 hydrogen was taken directly from a cylinder containing a gas with a stated purity of 99.999% ("ultra high purity" grade). In both cases the gas caused some discoloration of one end of the plates. For Batch 3 the hydrogen was taken from a heated Ti-sponge bed and, in this case, there was no sign of discoloration on the plates.

Analysis of a sample from Batch 1 conducted at MDC indicated a hydrogen content of 24,100 appm (530 wppm), which is in very good agreement with the predicted values.

No spontaneous hydride precipitation after hydrogen charging to 24,100 appm was observed by metallographic examination. The optical photomicrograph shown in Figure 5.2.1 and the electron micrograph shown in Figure 5.2.2 both reveal the standard alpha-beta microstructure of this alloy. The beta phase surrounds alpha grains and forms a continuous beta network.

After charging, tensile specimens were machined from the blanks. Testing was performed at room temperature using a strain rate of 7×10^{-5} sec^{-1}. The results of these tests are presented in Table 5.2.1 and reveal that the tensile strengths of the hydrogen charged specimens are slightly higher than those of the as-received alloy. The ductilities of the two alloys are equivalent.

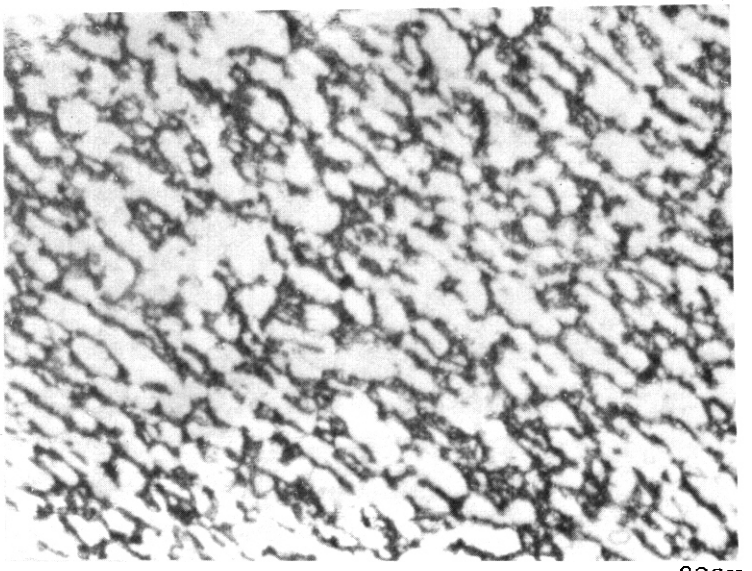

800X

FIGURE 5.2. 1. OPTICAL PHOTOMICROGRAPH OF Ti-6242s WITH 24,100 appm H

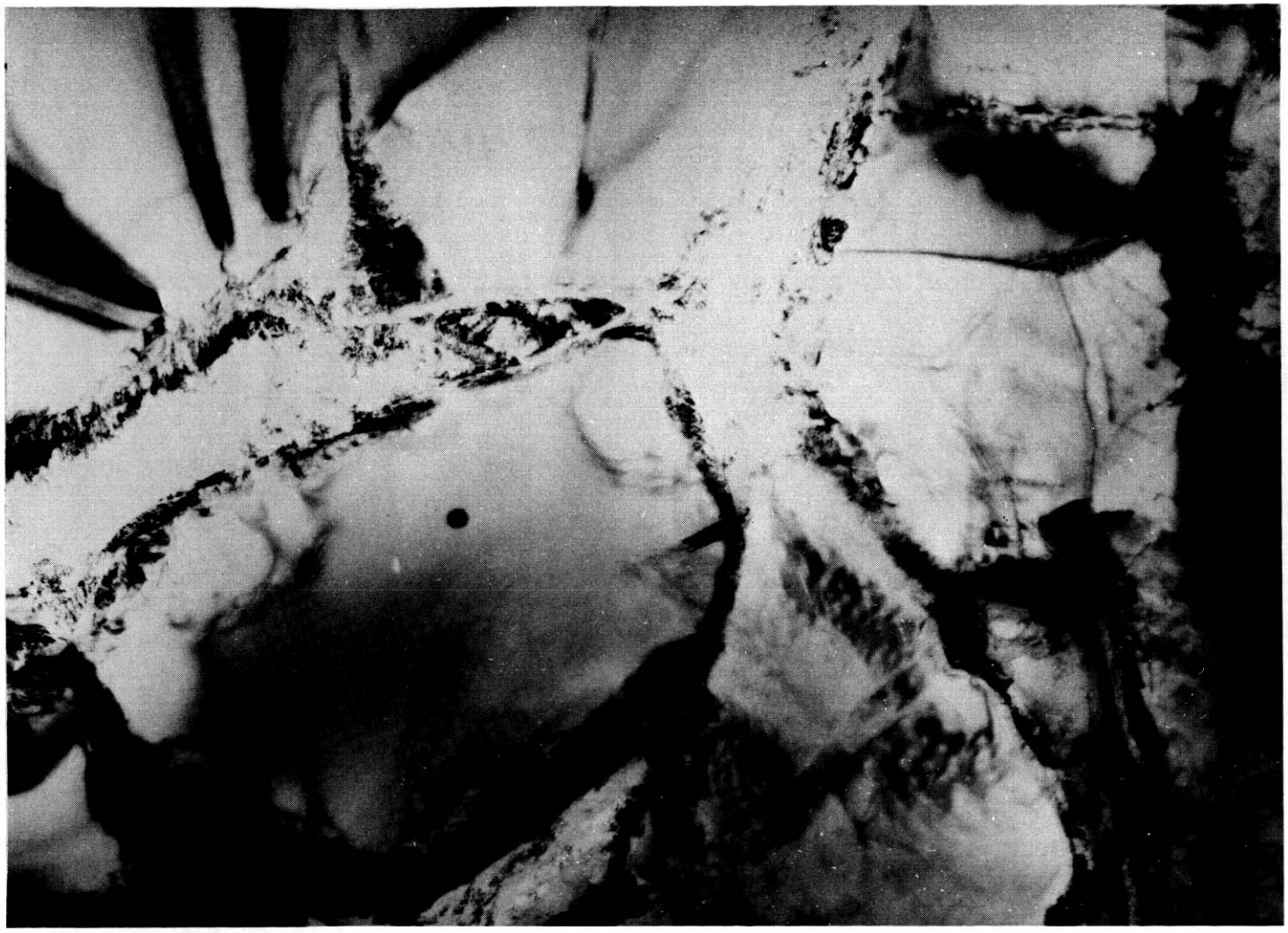

40,000X

FIGURE 5.2.2. ELECTRON MICROGRAPH OF Ti-6242S WITH 24,100 appm H

TABLE 5.2.1 TENSILE PROPERTIES OF Ti-6242-S

Material	Ultimate Tensile Strength, MPa	Ultimate Tensile Strength, ksi	Yield Strength, MPa	Yield Strength, ksi	Elongation, Percent
As-Received Ti-6242s - 2400 appm H (53 wppm H)	1089	158	1027	149	13.4
Charged Ti-6242s 24,100 appm H (530 wppm H)	1130	164	1054	153	13.8

The tensile fracture surfaces of the charged specimens were examined by scanning electron microscopy. Figure 5.2.3 indicates the ductile nature of fracture. Fracture surfaces consists of ductile dimples formed by microvoid coalescence.

After the charged specimen failed in tension, a thin section was cut from the gage portion of the test specimen. Optical photograph, Figure 5.2.4 and transmission electron micrograph, Figure 5.2.5, taken from this section did not reveal any stress assisted hydride formation. The dislocation structure can be seen in Figure 5.2.5.

Machining of MWCL specimens from the as-received Ti-62425 is complete and is in progress for the hydrogen charged material.

Set up of test equipment is in progress.

5.2.5 Conclusions

1. No spontaneous hydride precipitation after charging to 24,100 appm (530 wppm) H was observed.
2. Room temperature tensile properties were slightly higher (approximately 34 MPa) for the hydrogen charged specimens than for the as-received specimens.

5.2.6 Reference

1. E. Velekis to V. A. Maroni memo, dated April 28, 1980, Argonne National Laboratory.

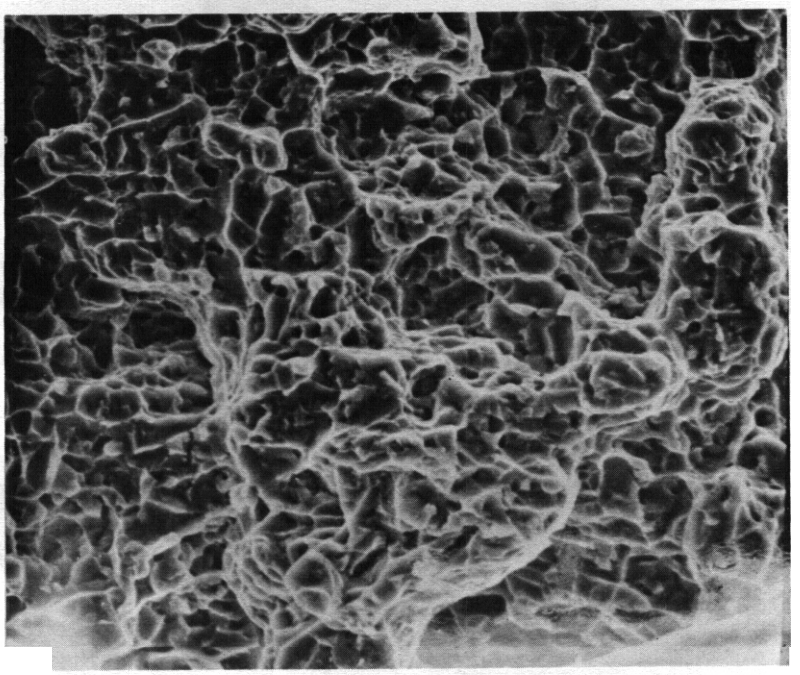

1000X

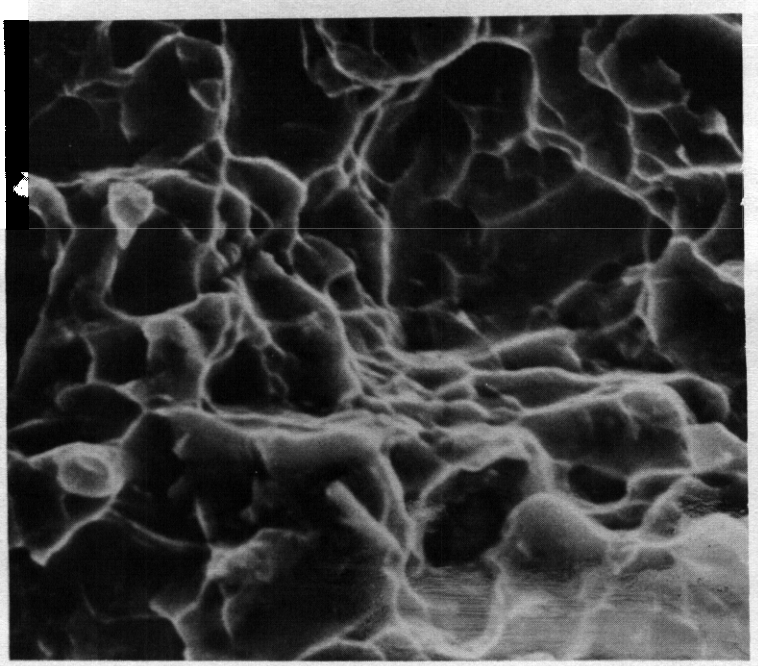

3000X

FIGURE 5.2.3. SEM OF FRACTURE **SURFACE**

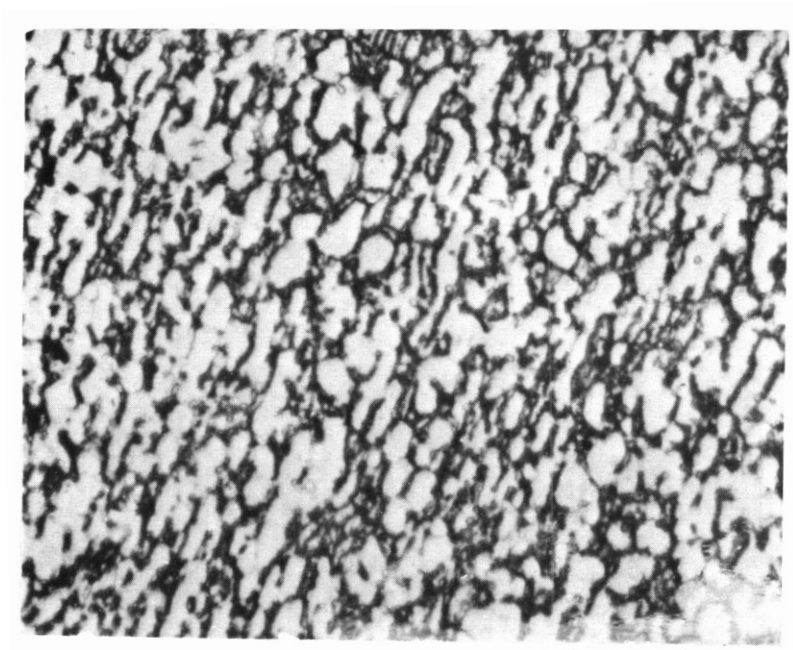

800X

FIGURE 5.2.4. OPTICAL PHOTOMICROGRAPH OF Ti-6242s WITH 24,100 appm H AFTER TENSILE TEST

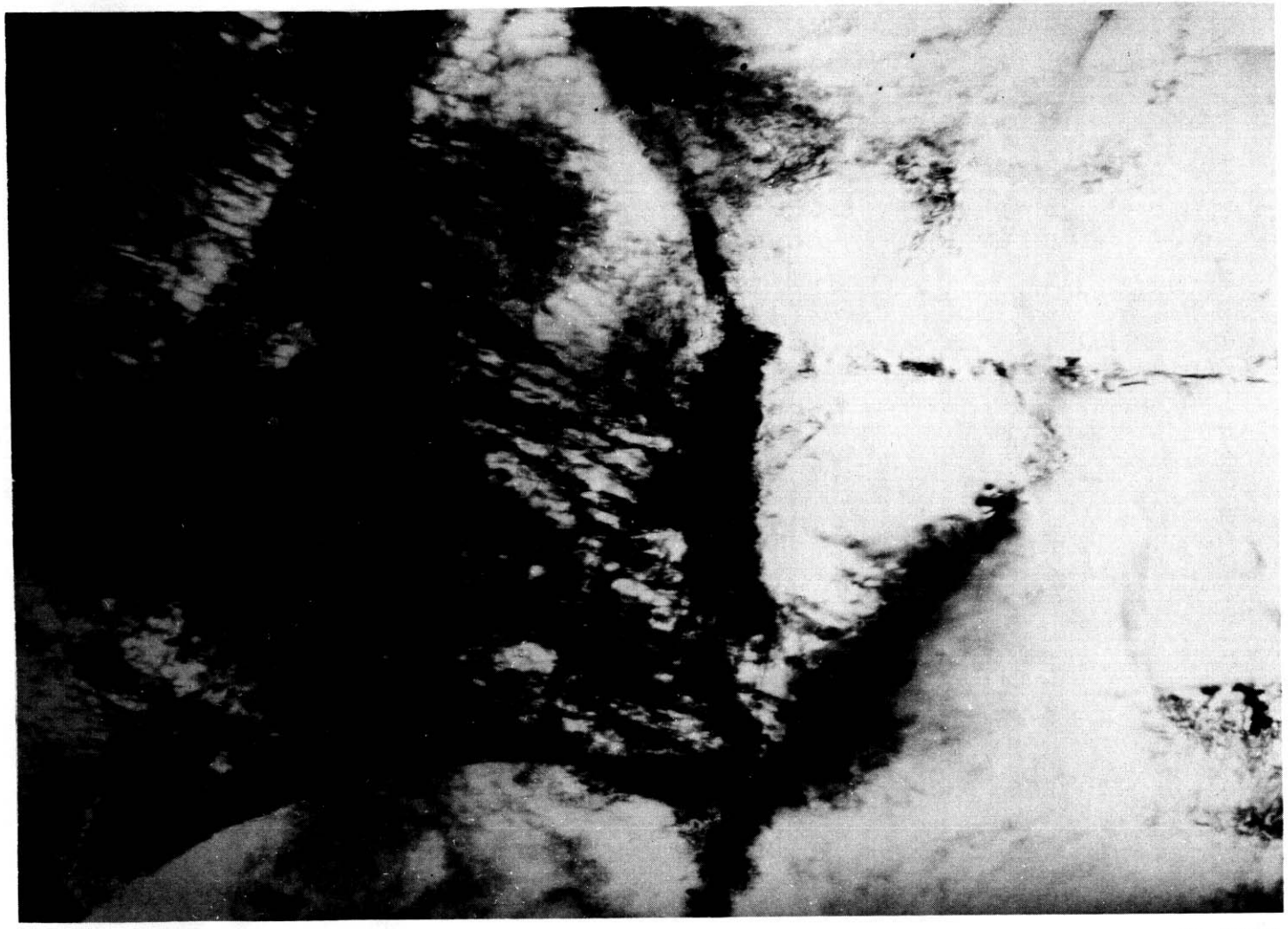

40,000X

FIGURE 5.2.5. TEM OF Ti-6242S WITH 24,100 appm H AFTER TENSILE TEST.

5.3 MECHANICAL PROPERTY TESTING OF UNIRRADIATED PATH C ALLOYS — K. C. Liu (ORNL)

5.3.1 ADIP Task

ADIP Task I.B.3, Fatigue Crack Growth in Reactive and Refractory Alloys.

5.3.2 Objective

The objective of this work is to develop baseline information on fatigue and crack growth behavior for the Path C refractory metal scoping alloys in the unirradiated condition.

5.3.3 Summary

Miniature hourglass-shaped fatigue specimens of V—15% Cr—5% Ti have been machined and heat-treated to the desired microstructure for cyclic fatigue testing. Strain-controlled fatigue tests on Nb—1% Zr indicate that the alloy has about the same fatigue resistance at room temperature and at 650°C. Limited data suggest that this alloy has marginally better fatigue properties than does 20%-cold-worked type 316 stainless steel for low strain ranges at 430°C.

5.3.4 Progress and Status

5.3.4.1 Heat Treatment and Specimen Preparation of Vanadium Alloys

Small cold-worked samples from 6.4-mm-diam bars of three vanadium-based alloys (V—20% Ti, V—15% Cr—5% Ti, and Vanstar 7) from the ADIP reference heats were heat-treated to determine recrystallization behavior. This was done to adjust grain sizes before fatigue testing. The samples were heat-treated at either 1200 or 1300°C for 1 h in a vacuum below 1 μPa. Photomicrographs of as-received (cold worked 80 to 90%) and heat-treated samples are shown in Fig. 5.3.1. Examination of this figure indicates that full recrystallization occurred on annealing at both temperatures. No visible microcracks were seen subsequent to heat treatment. The average grain sizes at the respective annealing temperature were measured and are tabulated in Table 5.3.1.

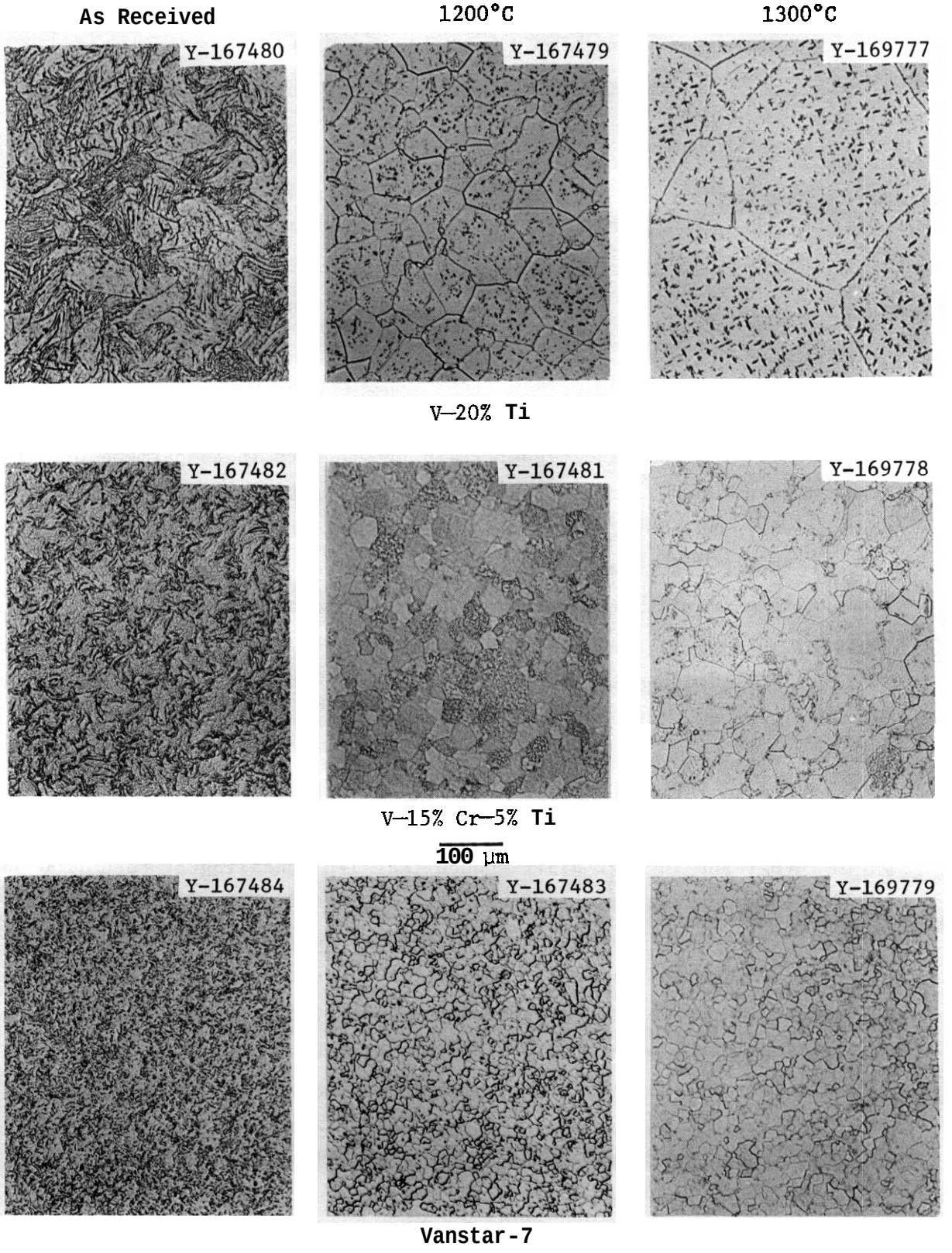

Fig. 5.3.1. Micrographs of Three Vanadium-Based Alloys in As-Received (Cold Worked 80 to 90%) and Annealed (1 h at 1200 and 1300°C, Respectively) Conditions.

Table 5.3.1. Grain Sizes of Three Vanadium-Based Alloys Annealed 1 h at 1200 or 1300°C

Alloys	Average Intercepts, μm		ASTM Number	
	1200°C	1300°C	1200°C	1300°C
V-20% Ti	56	160	5.5	2
V-15% Cr-5% Ti	26	32	7	6.5
Vanstar-7	16	20	9	8

The grain size increased with temperature, as was expected. The V-20% Ti alloy showed the higher grain growth rate in comparison with the other alloys. Some second-phase precipitate particles are apparent in the photomicrographs of V-20% Ti, whereas few were visible in the other alloys.

Grain size is known to be a factor that can influence the cyclic fatigue life of stainless steels[1] and some superalloys, such as alloy 718, tested at high temperature.[2] Results of strain-controlled fatigue tests[2] of alloy 718 at elevated temperatures showed that a small grain size was beneficial to the fatigue resistance, particularly at lower strain ranges.

As a result a medium grain size falling within the range of ASTM No. 6.5 to 7.5 was the desired starting point. Examination of the photomicrographs in Fig. 5.3.1 showed that 1-h annealing at both 1200 and 1300°C resulted in excessive grain growth of V-20% Ti and limited growth in Vanstar-7. Both heat treatments appeared to yield the desired grain size for V-15% Cr-5% Ti. Additional trial heat treatments are now under way to obtain the desired microstructures for Vanstar-7 and V-20% Ti.

Following the studies discussed above, bar stock of V-15% Cr-5% Ti was annealed at 1200°C before machining specimens. A batch of miniature hourglass-shaped fatigue specimens has been machined and stress relieved after machining at 1200°C for 0.5 h in vacuum. Fatigue tests on this alloy will be initiated shortly.

5.3.4.2 Status of Cyclic Fatigue Testing of Nb–1% Zr

As reported earlier[3] the testing system was damaged during a cyclic Eatigue test because of instrument failure. Repair of the system was completed, and cyclic fatigue tests have been resumed.

Since then, three tests on Nb–1% Zr were performed at 650°C in a vacuum below 1 μPa. A test cycled to ±1.0% strain amplitude led to failure after 2,848 cycles. Fatigue lifetime of a similar test at room temperature, however, was 3,308 cycles, as previously reported.[3] Examination of the ruptured specimen tested at 650°C revealed that the fatigue failure could have been accelerated by a plastic instability resulting from compressive buckling. A second test at ±0.5% strain was completed to rupture at 38,420 cycles with no sign of specimen instability. A third test at ±0.3% strain **has** already registered more than 340,000 cycles, and the test is currently in progress. Table 5.3.2 summarizes the test results obtained so far, and the data are also presented in Fig. 5.3.2.

Table 5.3.2. Fatigue Lifetime of Nb–1% Zr

Specimen[a]	Test Temperature (°C)	Total Strain Range (%)	cyclic Lifetime (Cycles)
AN2 111	650	2.0	2,848
AN2 110	650	1.0	38,420
AN2 112[b]	650	0.6	>335,000
ANZ 102	25	2.0	3,308
ANZ 101	25	1.0	31,402
CNZ 1	25	1.0	19,148
CNZ 2	25	0.5	961,447

[a]ANZ = annealed 1 h at 1400°C in vacuum; CNZ = cold worked.

[b]Test in progress.

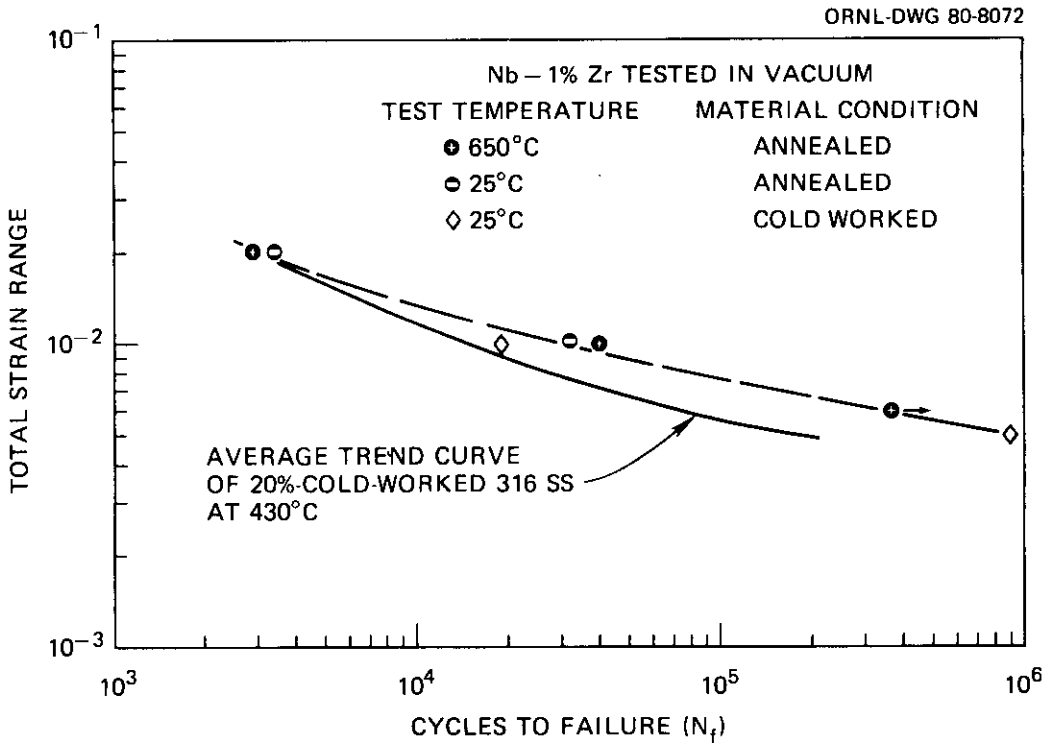

Fig. 5.3.2. Cyclic Fatigue Data for Nb–1% Zr Tested at 25 and 650°C in Vacuum. A trend curve for 20%-cold-worked type 316 stainless steel tested at 430°C is shown for comparison.

5.3.5 Conclusions

Test results of Nb–1% Zr obtained to date indicate that fatigue properties of Nb–1% at 650°C are about the same as at 25°C. Comparison tends to show that fatigue lifetime of Nb–1% Zr is marginally superior to average values obtained for 20%-cold-worked type 316 stainless steel data at low strain ranges.

5.3.6 References

1. P. S. Maiya and S. Majumdar, "Elevated-Temperature Low-Cycle Fatigue Behavior of Different Heats of Type 304 Stainless Steel," *Metall. Trans.* 8A(11): 1651–60 (November 1977).
2. C. R. Brinkman and G. E. Korth, "Strain Fatigue and Tensile Behavior of Inconel 718 from Room Temperature to 650°C," *J. Test. and Eval.* 2(4): 249–59 (1974).
3. K. C. Liu, "Mechanical Property Testing of Unirradiated Path C Alloys," *ADIP Quart. Prog. Rep. Dec. 31, 1979,* DOE/ER-0045/1, pp. 38–41.

6. PATH D ALLOY DEVELOPMENT — INNOVATIVE MATERIAL CONCEPTS

7. PATH E ALLOY DEVELOPMENT — FERRITIC STEELS

7.1 MECHANICAL PROPERTY MEASUREMENTS OF HT-9 IN HYDROGEN: 25 to 400°C – R. E. Stoltz (Sandia National Laboratories, Livermore, CA)

7.1.1 ADIP Task

The Department of Energy (DOE)/Office of Fusion Energy (OFE) has cited the need for these data under the ADIP Program Task, Ferritic Alloy Development (Path E).

7.1.2 Objective

The goal of this study is to evaluate the hydrogen compatibility of 12Cr-1Mo ferritic/martensitic steel for use in first wall and blanket structures. This contribution focuses on tensile properties of HT-9 as a function of hydrogen pressure and test temperature.

7.1.3 Summary

The presence of interstitial hydrogen, in concentrations as low as 1-2 weight ppm, is known to severely affect the fracture behavior of martensitic steels. The embrittling effect increases with lattice concentration of hydrogen and with increases in the yield strength of the alloy in question. The effect of temperature is more complex, however, with a maximum in embrittlement evident near room temperature. This report summarizes the first experiments to evaluate the hydrogen compatibility of HT-9 and to separate the effects of temperature and hydrogen pressure. Tensile tests were performed in air and 15 psi hydrogen at test temperatures of 25, 200, 300 and 400°C and at 25°C in hydrogen pressures of 15, 1000, 2000, 3000 and 5000 psi. The results show that elevated temperatures eliminate any hydrogen effects, consistent with the behavior of other steels having similar strengths. Increasing pressures, however, cause a strong shift in ductility, with an 260% loss in ductility occurring in 5000 psi hydrogen.

7.1.4 Progress and Status

7.1.4.1 Experimental Details

All tests were performed on samples taken from a pipe section

supplied by GA. The composition, as supplied by GA, was:

Table I
Chemistry of HT-9. Wt.%

C	Si	Mn	Cr	Ni	Mo	W	V	P	S
0.22	0.38	0.52	11.3	0.50	0.85	0.50	0.27	0.19	.006

Prior to testing, the specimens were austenitized at 1040°C/30 min. and air cooled, followed by tempering at 750°C/60 min., with a resulting hardness of R_C21. The resulting microstructure was fully martensitic, Figure 1(a), with a distribution of tempered carbides, Figure 1(b). Tensile bars had a nominal 0.125 in. gage diameter and 0.500 in. gage length. All tests were run at 0.02 in./min. extension rates. In the hydrogen experiments, samples were equilibrated at pressure and temperature for 30 min. before testing. Duplicate samples were run at each condition and the fracture surface examined by SEM following completion of the tensile tests.

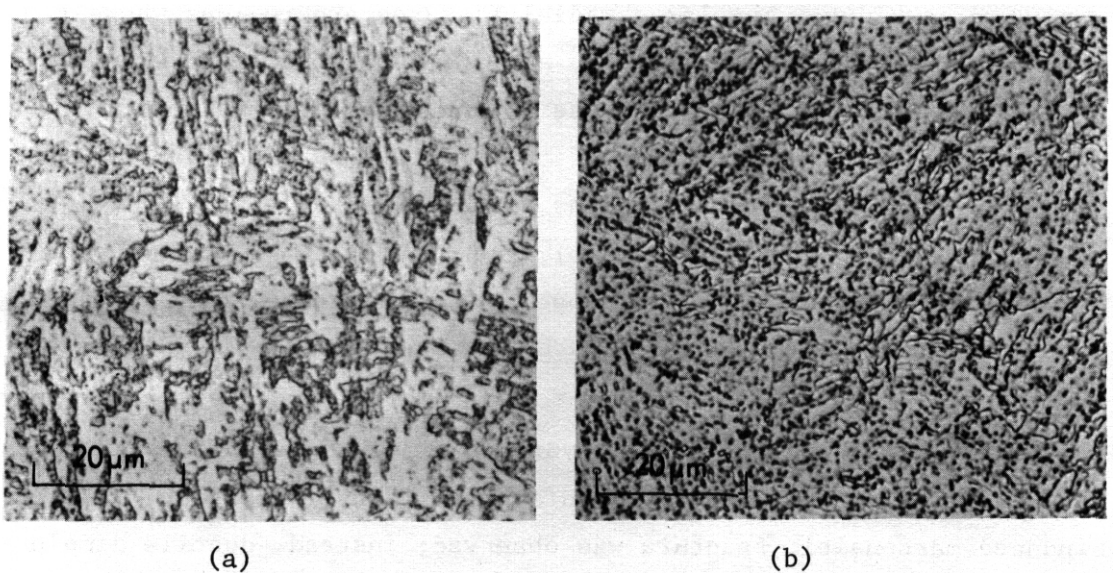

Figure 1. Microstructure of HT-9, Austenitized and Quenched: (a) blocky martensite laths; (b) tempered carbides.

7.1.4.2 Results

The results of all tensile tests are given in Table 2; the values are averages of two tests. In no instance did the presence of hydrogen significantly effect the yield or ultimate strength of the alloy. The effect of hydrogen was manifest in the ductility, as measured by reduction-in-area (RA) at fracture. At 25°C, 15 psi hydrogen reduced the tensile ductility from 68 to 58%. Although this loss in ductility is small, it does suggest that a hydrogen-induced change in fracture behavior has occurred. This effect was verified by comparison of the fracture surfaces of samples tested in air and in 15 psi hydrogen, shown in Figures 2 and 3. The fracture process in air is entirely one of ductile void initiation, growth and coalesence. The overall fracture surface, Figure 2(a), shows a flat central region with radial cracks extending to an outer shear lip. All the air-fracture surfaces exhibit ductile voids, as shown in 2(b). The size of the voids is representative of the spacing between inclusions in the alloy. Comparison of Figures 2(a) and (b) indicates that void intiation occurs at the tempered carbides. The large radial fissures are regions where the ductile cracks join, and the side surfaces of these fissures exhibit elongated dimples similar to those in the shear lip region. In hydrogen, Figure 3, the overall features of the fracture surfaces are similar to those in air. However, in regions A and B, a change in fracture mode is observed. Typified by Figure 3(b), the fracture is dominated by shallow secondary cracks and a "woody" appearance. The size scale of these cracks suggest that fracture occurs at or between the blocky martensite laths.

At elevated temperatures, hydrogen effects are suppressed and the ductilities are comparable in air and 15 psi hydrogen. No hydrogen-induced martensitic fracture was observed; instead, ductile dimple fracture occurred across the 200-400°C temperature range of test.

Table 2
Mechanical Properties of HT-9 in Air and Hydrogen

Temperature	Atmosphere	Yield Strength MPa (ksi)	Ultimate Strength MPa (ksi)	Ductility (Reduction in Area) %
25°C	Air	592 (85.8)	799 (115.8)	67
25°C	15 psi H_2	565 (81.9)	837 (121.3)	58
200°C	Air	533 (77.3)	719 (104.3)	64
200°C	15 psi H_2	545 (79.0)	733 (106.2)	64
300°C	Air	513 (74.4)	695 (100.7)	65
300°C	15 psi H_2	525 (76.0)	689 (99.9)	67
400°C	Air	465 (67.4)	628 (91.0)	62
400°C	15 psi H_2	436 (71.9)	637 (92.3)	63
25°C	1000 psi H_2	715 (103.6)	800 (116.0)	65
25°C	2000 psi H_2	707 (102.5)	788 (114.2)	56
25°C	3000 psi H_2	717 (104.2)	792 (114.8)	53
25°C	5000 psi H_2	724 (105.1)	793 (115.0)	26

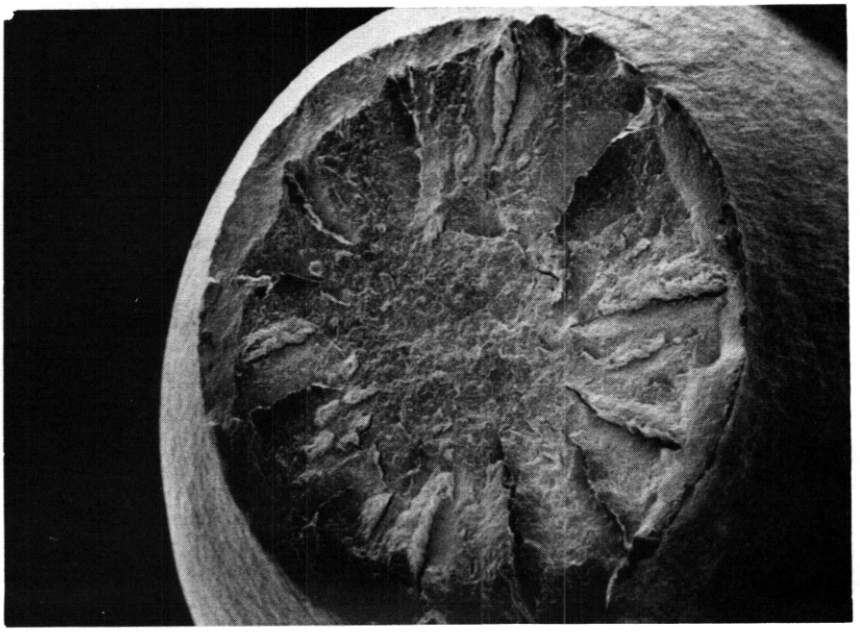

(a)

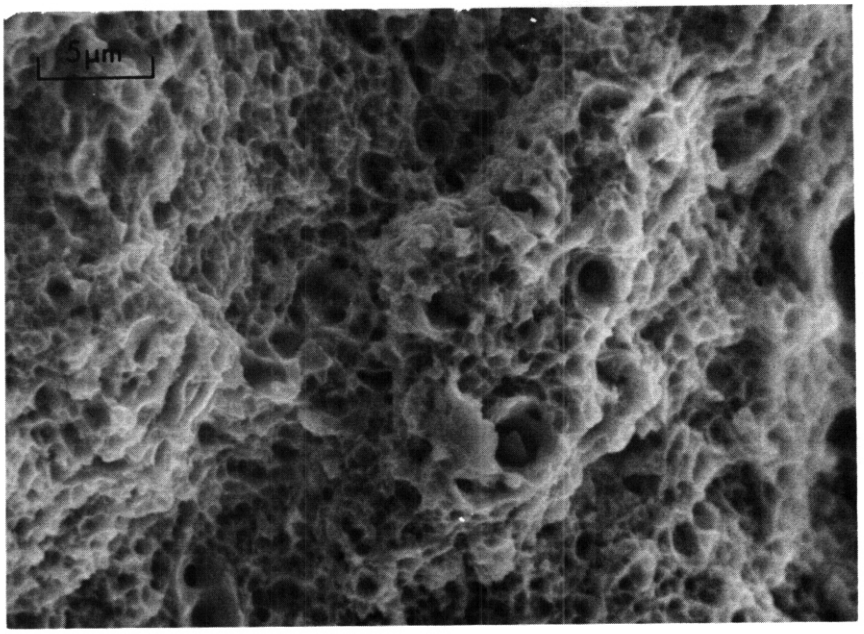

(b)

Figure 2. SEM micrographs of HT-9, tested in air at 25°C: (a) low magnification photograph of tensile bar; (b) high magnification of fracture surface showing dimple rupture initiated at tempered carbides.

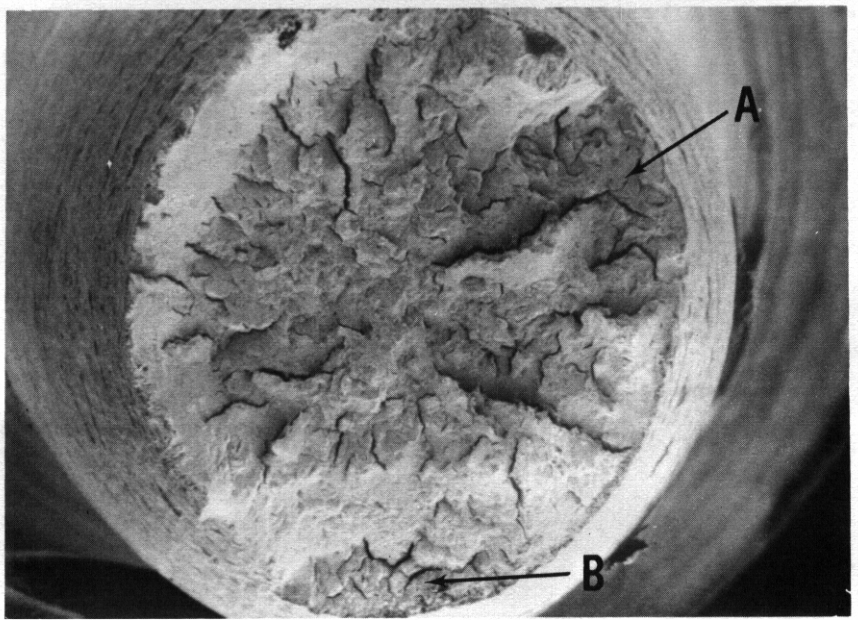

(a)

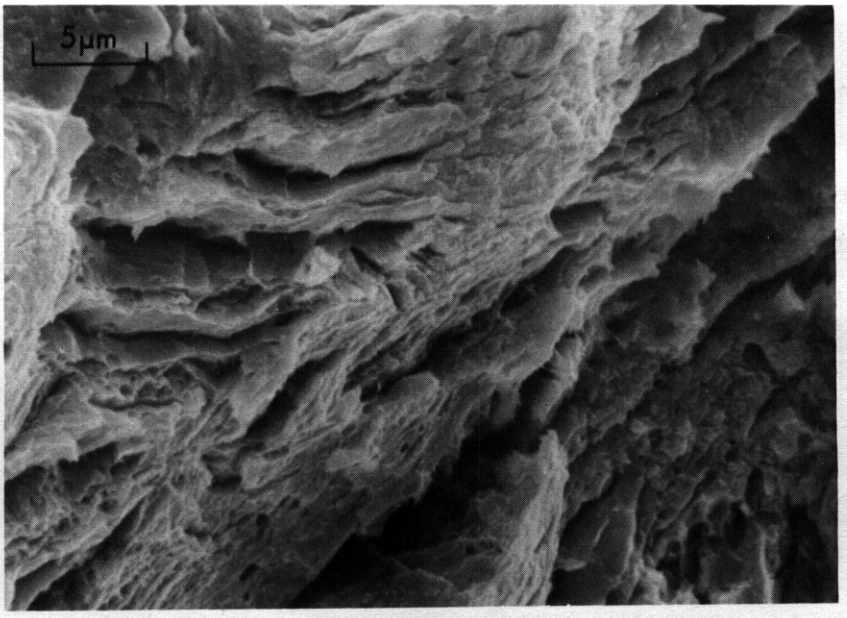

(b)

Figure 3. SEM micrographs of HT-9, tested in 15 psi hydrogen at 25°C: (a) low magnification photograph with A and B indicating regions of hydrogen induced fracture; (b) high magnification of hydrogen induced fracture. Secondary cracks occur on a scale similar to the martensite laths.

In order to study further the effect of hydrogen at ambient temperature, a series of tests was performed at 1000–5000 psi pressure. As indicated in Table 1, a progressive but slight decrease in ductility occurs up to 3000 psi, with a sharp decrease manifest at 5000 psi hydrogen pressure. In the range 1000–3000 psi hydrogen the fracture behavior is similar to that at 15 psi. Small regions of martensitic fracture are observed at the outer part of the fracture surface. As the test pressure is increased the areal percentage of this fracture mode increases. At 5000 psi, Figure 4, the hydrogen affected regions are much larger (A and B), comprising ∿50% of the fracture area. The sample exhibits two fracture regions perpendicular to the tensile axis connected by a ductile shear region. Little overall necking of the sample was observed. When seen at higher magnifications, the flat regions show martensite fracture with secondary cracks similar to that in 15 psi hydrogen. In some regions of the sample, the martensite was oriented nearly perpendicular to the tensile axis, so that the interlath fracture gives a stepped appearance, as indicated by the arrows in Figure 4(b).

7.1.4.3 Discussion

The current results indicate that increasing the external hydrogen pressure has a far more detrimental effect on the compatibility of HT-9 than do increases in the test temperature. It is interesting to compare the theoretical increase in solubility at 15 psi in going from 25 to 400°C and at 25°C in going from 15 psi (1 atm) to 5000 psi (342 atm). The lattice solubility of hydrogen in Fe is given by:

$$C = 3.7\ p^{\frac{1}{2}} \exp\left[-6500/RT\right];\ cm^3\ H_2(STP)/cm^3 Fe$$

An increase in temperature from 25 to 400°C results in a ∿500 fold increase in solubility while an increase from 1 to 342 atm results in an 18 fold increase. On this basis, increasing temperature should increase the effect of hydrogen far more than increasing the pressure. A number of factors suggest the opposite is true and support the data of Table 1. First, the above equation is for lattice solubility. At 25°C and 1 atm a concentration of 0.04 atomic ppm is predicted, while a value

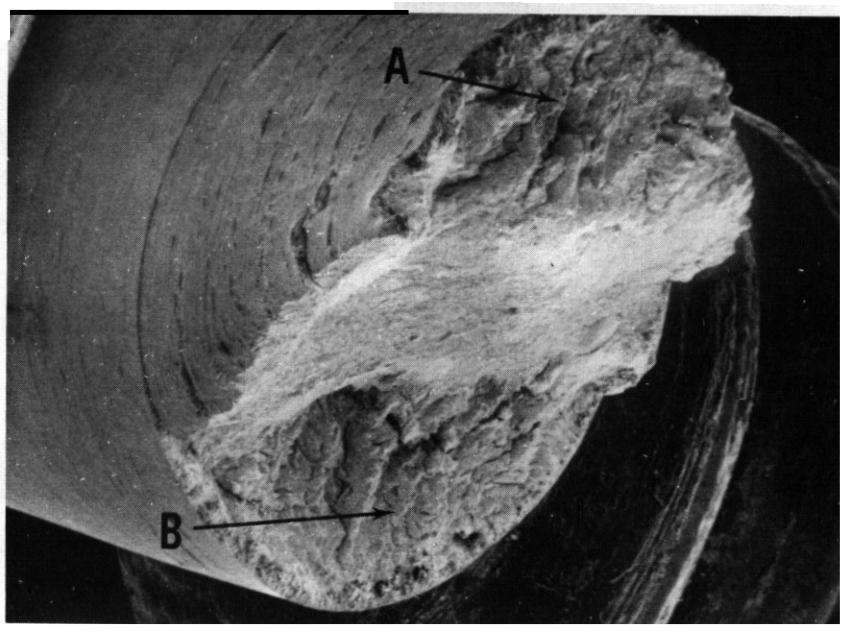

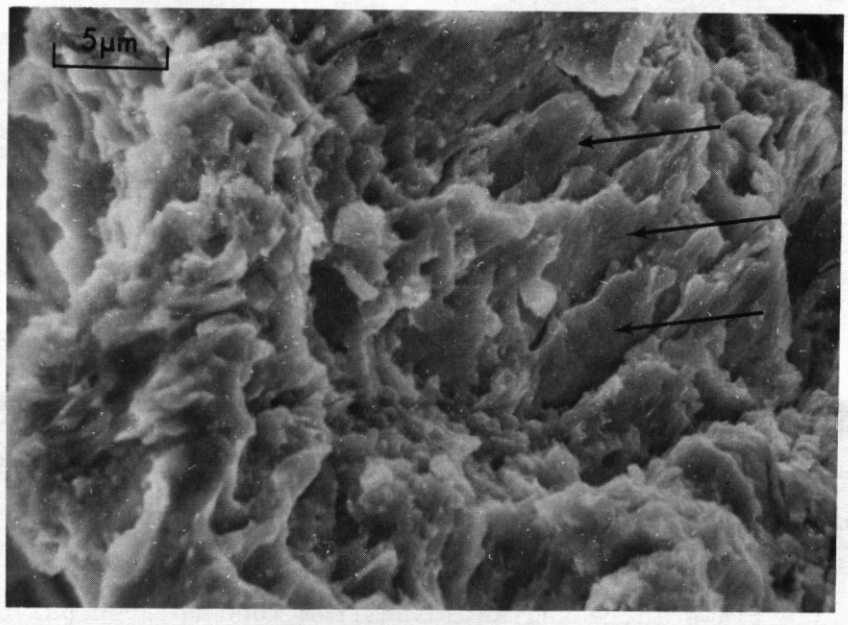

Figure *4.* SEM micrograph of HI-9, tested in 5000 psi hydrogen at 25°C; (a) low magnification photograph with A and B indicating regions of hydrogen induced fracture; (b) high magnification showing the stepped features (at arrows) characteristic of hydrogen induced fracture between martensite laths.

of 1-5 ppm is observed. The solubility is thus dominated by hydrogen trapped at interfaces and defects in the material. The amount of hydrogen trapped is related to the trap depth and trap concentration. As the temperature is raised, less hydrogen is retained in the weaker traps, until finally all the hydrogen is mobile. One may speculate that the martensite lath interfaces are weaker traps (since they are coherent) than the carbide/matrix interfaces, which are incoherent. Thus raising the temperature decreases the amount of hydrogen associated with the lath interfaces compared to that retained at the carbides. In this way ductile fracture at the carbides would be enhanced. Raising the total pressure at 25°C does not affect the partitioning of hydrogen, but rather increases the amount at the carbides and lath interfaces proportionally.

Secondly, the mixed mode of fracture exhibited in the 25°C/15 psi test suggests a competition between the two fracture processes. Ductile void initiation is the result of incompatibility of flow between the hard carbide and softer matrix. At elevated temperature this incompatibility is increased due to the further softening of the matrix. Thus, increasing temperature may not suppress the hydrogen-induced martensite fracture but rather enhance the ductile void process. Future tests at elevated temperatures and higher pressures are planned and will be useful in verifying this hypothesis.

Finally, analysis of the specimens tested in 5000 psi hydrogen demonstrates the strong effect of surface flaws on hydrogen crack nucleation. Occasional surface flaws left from the specimen preparation process served as fracture nucelation sites in 5000 psi hydrogen even though they were only on the order of 0.001 in deep. The incidence of surface flaws increased in going from 1000 to 5000 psi hydrogen pressure. This observation, coupled with the observed increased areal fraction of martensite fracture with increasing hydrogen pressure, suggest that there is a critical pressure and surface strain relationship for initiation of martensite fracture. At 5000 psi this strain is sufficiently low that hydrogen cracks are initiated very early in the tensile test. All subsequent deformation is concentrated

as hydrogen assisted crack growth rather than further reductions in area. This observation suggests that fracture processes dominated by near-surface effects, such as fatigue crack initiation, may be severely affected by hydrogen.

7.1.5 Conclusions

The major conclusions from this contribution are:

1. External hydrogen pressures as low as 15 psi can induce a fracture mode change and lower the ductility of HT-9 at 25°C.

2. Increasing the temperature to 200-400°C eliminates any effect of hydrogen at 15 psi test pressure.

3. Increasing hydrogen test pressure, in the range of 5000 psi, severely reduces the ductility of HT-9 at 25°C. The fracture process shifts from ductile void growth and coalesence to a predominately martensite fracture mode.

4. The incidence of surface cracking increases with increasing hydrogen test pressure at 25°C. This suggests that surface sensitive process such as fatigue crack initiation may be substantially accelerated by hydrogen.

7.2 WELDABILITY OF HT9: THE AUTOGENEOUS GTA PROCESS - J. C. Lippold (Sandia National Laboratories, Livermore, CA)

7.2.1 ADIP Task

The Department of Energy (DOE/Office of Fusion Energy (OFE) has cited the need for these data under the ADIP Program Task, Ferritic Alloy Development (Path E).

7.2.2 Objective

The objective of this portion of our investigation was to characterize the microstructures normally encountered in both the fusion zone and heat-affected zone (HAZ) of autogeneous HT9 weldments, and to rationalize these microstructures in terms of both the continuous-cooling transformation (CCT) behavior and the equilibrium phase diagram.

7.2.3 Summary

The autogenous GTA process was selected in order to produce a variety of microstructures which will normally be observed in HT9 weldments. Evaluation of the as-welded microstructures indicated that the rapid cooling rates associated with the weld thermal cycle imparted full martensitic hardness to the fusion zone and portions of the HAZ. At least four distinct regions have been identified within the HAZ; each region could be related to the equilibrium phase diagram of the Fe-12Cr-0.2C alloy system.

7.2.4 Progress and Status

The candidate ETF first wall/blanket alloy HT9 is a fully transformable, air-hardening martensitic stainless steel capable of being joined by a number of fusion welding processes. As is often the case with martensitic steels, both a preweld and post-weld heat treatment is usually recommended to insure that cracking does not occur in either the fusion zone or the heat-affected zone. The heat treatment requirement is particularly important for

HT9 since without preheat this alloy attains full martensitic hardness in both the fusion zone and HAZ upon cooling after welding. Unfortunately, heat treatment of the relatively massive first wall component of the ETF fusion reactor will likely prove difficult if not impossible, and thus development of a less stringent heat treatment schedule is of prime importance.

7.2.4.1 Experimental Approach

The initial investigation at Sandia National Laboratories of HT9 weldability utilized a section of 1/4 inch wall thickness pipe provided by General Atomic. The chemical composition of the pipe is listed below:

Table I

C	Si	Mn	Cr	Ni	Mo	W	V	P	S
0.22	0.38	0.52	11.3	0.50	0.85	0.50	0.27	.019	.006

In order to produce a range of weld microstructures which would be common to a variety of processes, autogenous bead-on-plate welds were made using the gas tungsten-arc (GTA) procedure and a series of heat inputs ranging from 20 to 60 KJ/in (7.9 to 23.6 KJ/cm). The material was welded in the as-received condition (R_c30) and neither a preheat nor a postweld heat treatment was employed in this phase of the investigation.

Metallographic sections transverse to the welding direction were prepared for both optical and scanning electron mciroscopy. In addition, microhardness traverses were conducted across pertinent areas of the weld region as a means to ascertain microstructure - property relationships.

7.2.4.2 Continuous Cooling Transformation (CCT) Behavior

The transformation on cooling can be predicted from a continuous cooling transformation diagram such as that shown in Figure 1.[1]

Since both the ferrite and bainite transformations are rather sluggish, regions in either the fusion zone or HAZ which have been heated above the A_{c1} can be expected to transform to martensite upon cooling to room temperature. This prediction assumes that the austenite is completely homogenized with a grain size of 7-8 prior to transformation. The behavior of areas within the weld region exhibiting various prior austenite grain sizes and/or incomplete homogenization may depart slightly from the diagram in Figure 1.

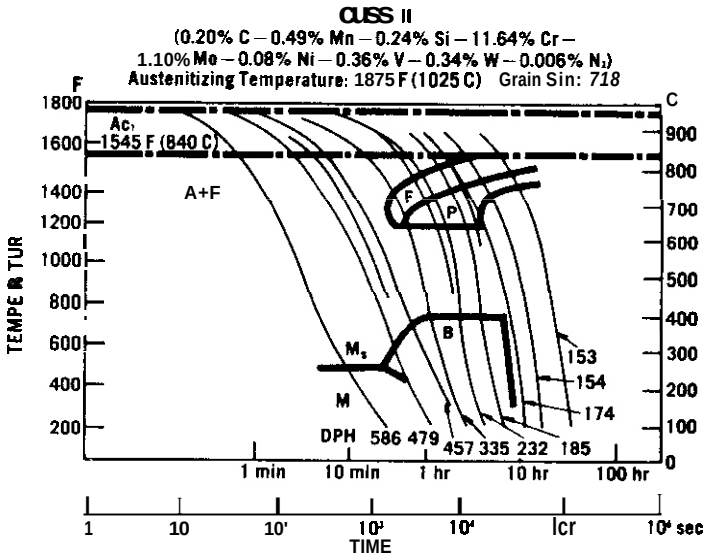

Figure 1. CCT Diagram for an Alloy of Composition Similar to HT9.

7.2.4.3 Microstructural Observations in the Heat-Affected Zone

At least four distinct regions have been identified within the HAZ and associated with the phase diagram in Figure 2. These include:

1. A two-phase region adjacent to the fusion line, containing martensite and a small proportion of ferrite;

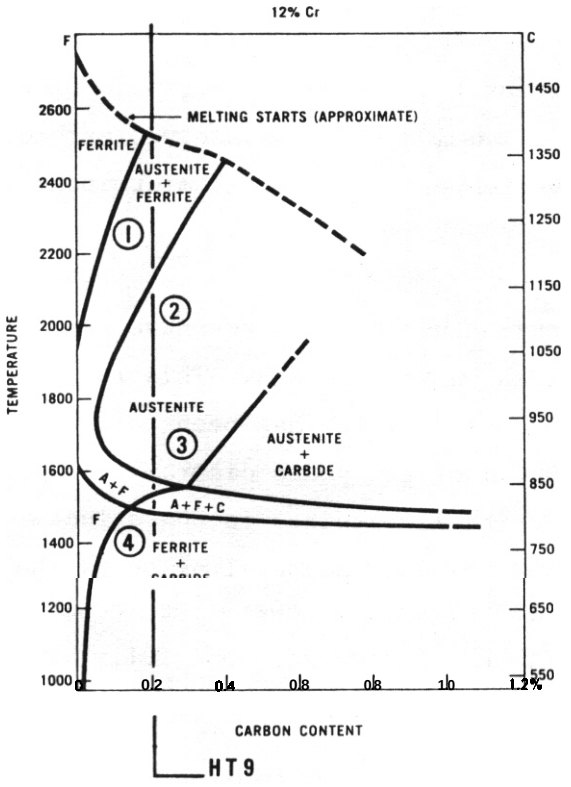

FOUR HAZ REGIONS

① γ + FERRITE+ MARTENSITE + FERRITE

② COARSE-GRAINED $\gamma \rightarrow$ MARTENSITE

③ FINE GRAINED $\gamma \rightarrow$ MARTENSITE

④ OVERTEMPERED B.M.

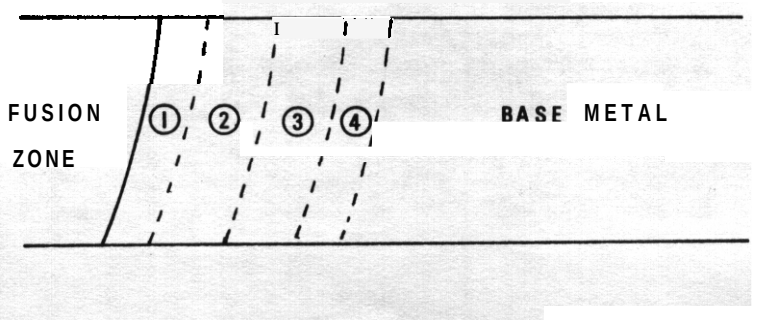

Figure 2. Binary Section of the Fe-Cr-C Phase Diagram at 12%Cr

2. A fully martensitic region exhibiting a relatively coarse prior austenite grain size;

3. A martensitic region exhibiting a finer prior austenite grain size and possibly some undissolved carbides;

4. An overtempered base metal microstructure of martensite and carbide.

The microstructure of the two-phase region adjacent to the fusion line is shown in Figure 3. This region of the HAZ corresponds to an area which has been heated into the austenite + ferrite (δ) region of the phase diagram in Figure 2. Upon cooling the ferrite is retained in the structure and the austenite transforms to martensite upon cooling below the M_s. The presence of ferrite in the structure lowers the local hardness relative to both the adjacent fusion zone and fully martensitic HAZ.

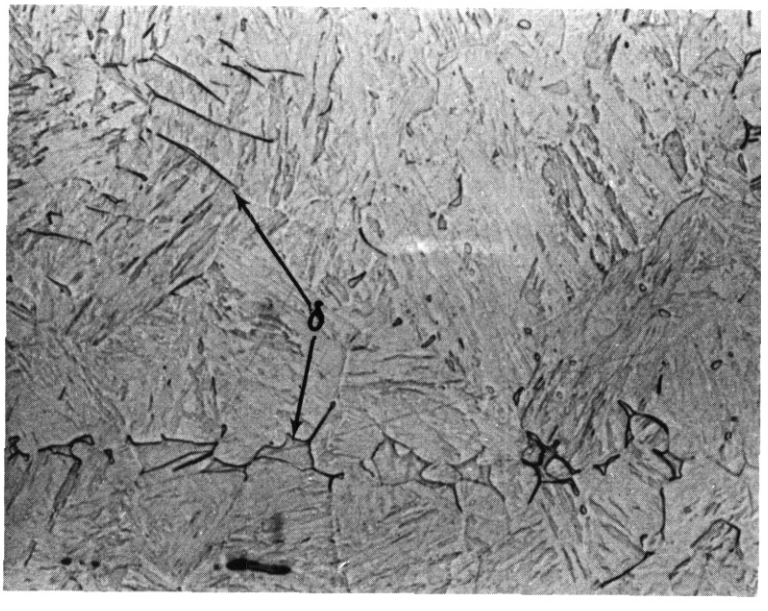

Figure 3. Ferrite and Martensite in HAZ Region Adjacent to the Fusion Line, 800X.

The micrographs in Figure 4 are indicative of the fully martensitic region in the HAZ which exhibited the highest hardness (Region 2 in Figure 2). The coarse prior austenite grain size and complete dissolution of the carbides impart high hardenability to this region.

(a)

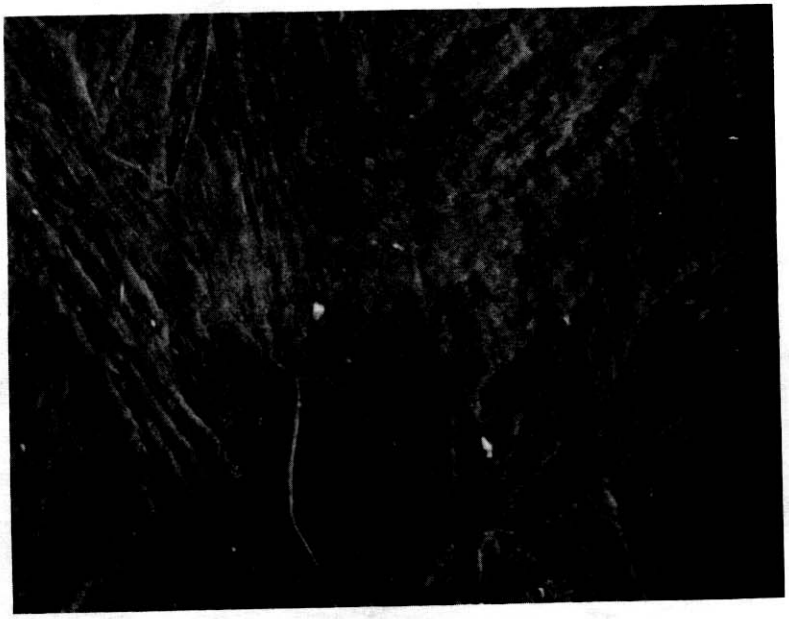

(b)

Figure 4. Coarse-grained HAZ Region: (a) Optical, 400X; (b) SEM, 3000X

Region 3 in Figure 2 corresponds to the portion of the HAZ where carbide dissolution is incomplete and the prior austenite grain size is smaller than in Region 2. As a result the hardenability progressively decreases with distance from the fusion line. The microstructure is a mixture of martensite and carbide as shown in Figure 5.

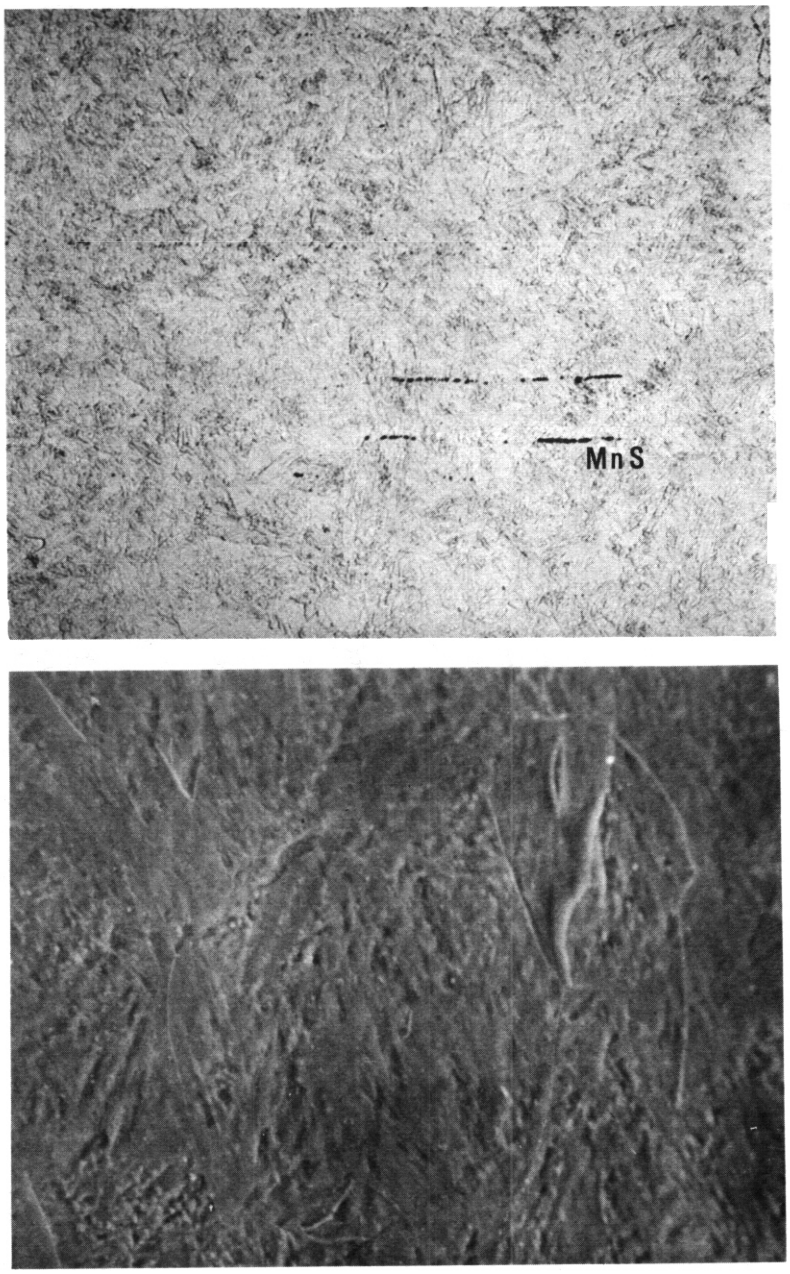

(a)

(b)

Figure 5. Fine-grained HAZ Region: (a) Optical 400X; (b) SEM, 3000X.

Region 4 in Figure 2 represents an area of softening relative to the base metal and probably results from overtempering of the martensite. This portion of the HAZ was heated to a temperature just below the A_c, and thus there was no allotropic transformation upon cooling. The microstructure is typified by coarse martensite plates and carbides as shown in Figure 6. The base metal consists

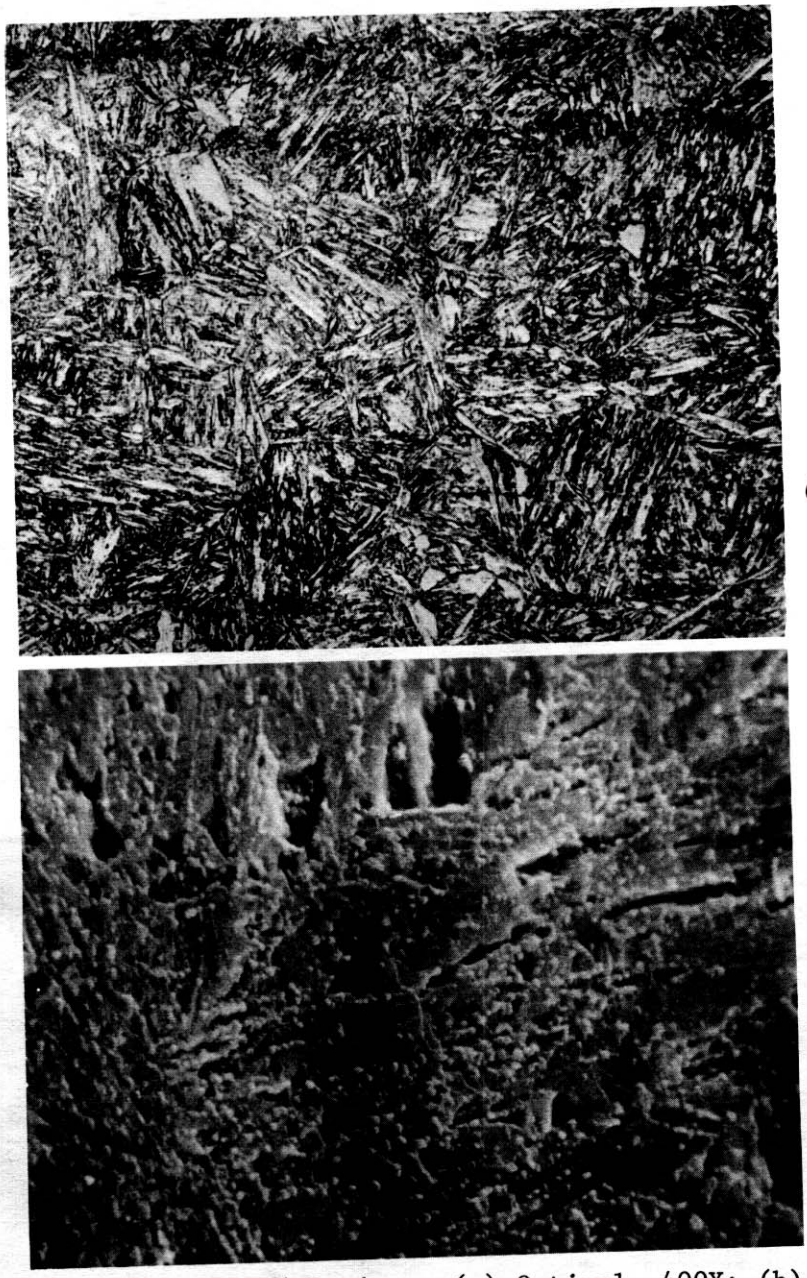

(a)

(b)

Figure 6. Overtempered Region: (a) Optical, 400X; (b) SEM, 6000X.

of amixture *of* tempered martensite and carbides as displayed in Figure 7.

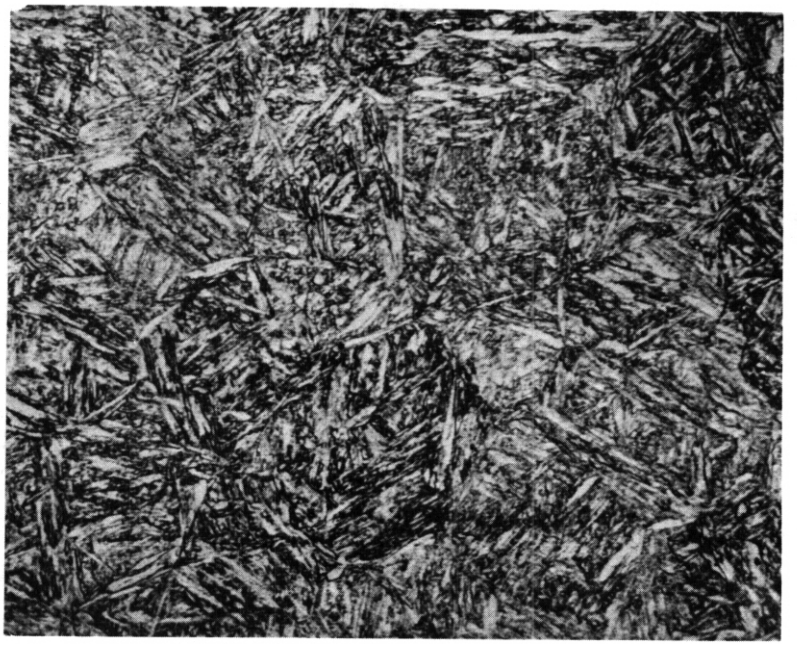

(a)

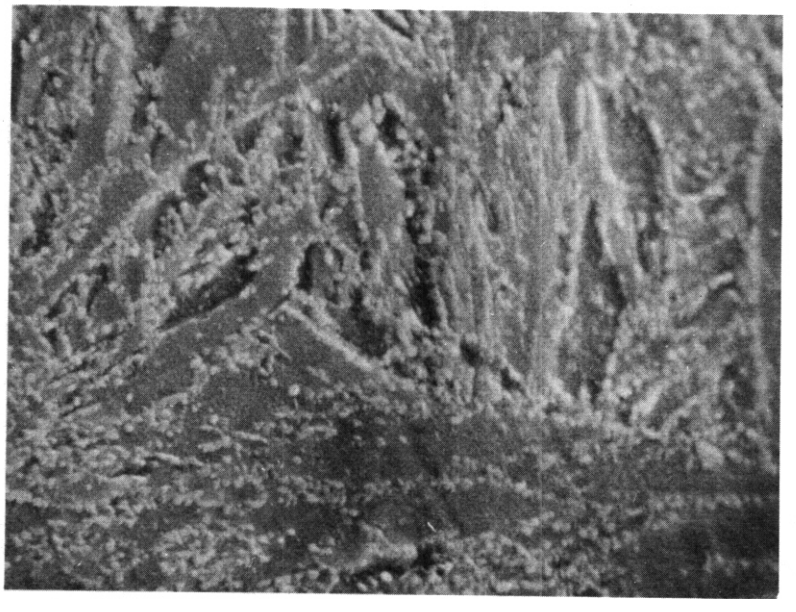

(b)

Figure 7. Base Material: (a) Optical, 400X; (b) SEM, 6000X.

7.2.4.4 Fusion Zone

The fusion zone microstructure consists of a mixture of ferrite (δ) and martensite, as shown in Figure 8. Partitioning of ferrite-forming elements (Cr, Mo) to subgrain boundaries during solidification undoubtedly stabilizes the ferrite in these regions and prevents transformation to austenite upon cooling below the austenite solvus. The bulk of the fusion zone transforms to martensite upon cooling to room temperature. Despite the presence of the softer ferrite phase, the as-welded microstructure exhibits nearly full martensitic hardness, probably because melting and resolidification homogenizes the austenite.

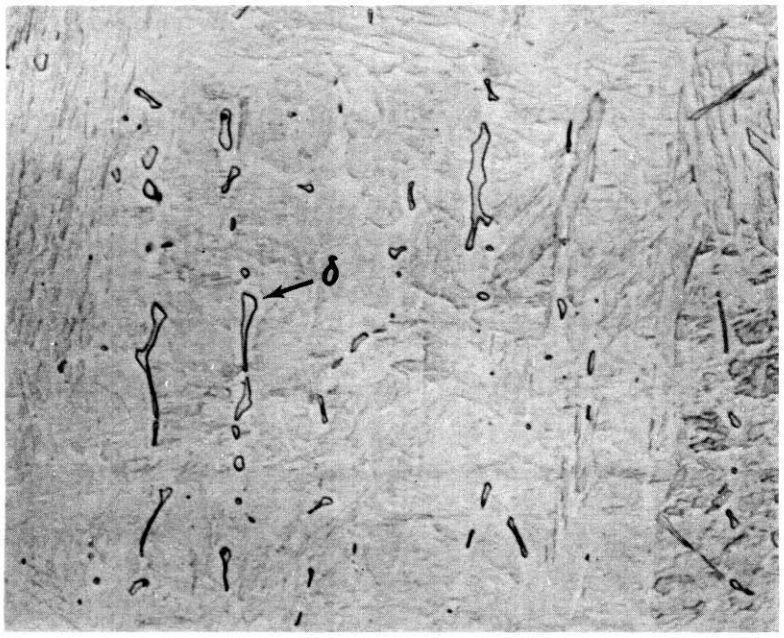

Figure 8. Fusion Zone Microstructure Showing Ferrite Along Subgrain Boundaries, 800X.

7.2.5 Conclusions

Autogeneous GTA welds in HT9 produced a series of microstructures which could be related to the behavior predicted by both the CCT and equilibrium phase diagrams. The as-welded structure

attained full martensitic hardness in both the fusion zone and the coarse prior austenitic grain region of the HAZ. The decreased hardness observed adjacent to the fusion line was associated with a two phase mixture of ferrite and martensite in this region. Further into the HAZ the hardness decreased as a result of both the finer prior austenite grain size and incomplete carbide dissolution. Both of these factors tend to reduce the hardenability relative to the coarse-grained, homogeneous austenite regions.

7.2.6 References

1. E. Kauhausen and P. Kaesmacher, "The Metallurgy of Welded Heat-Resistant 12% Cr Steels + Mo-V-W" Schweissen and Scheiden, 9, 414-419 (1957).
2. R. L. Rickett, W. F. White, C. S. Walton, and J. C. Butler, "Isothermal Transformation, Hardening, and Tempering of 12%Cr Steel", TASM, 44, 138-168 (1952).

7.3 PROCUREMENT OF NATIONAL 12 Cr HEAT AND EVALUATION OF WELDING PROCEDURES FOR IRRADIATION SPECIMENS - T. A. Lechtenberg, R. D. Stevenson, S. N. Rosenwasser, B. E. Thurgood, and L. D. Thompson (General Atomic Company)

7.3.1 ADIP Task

The Department of Energy (DOE)/Office of Fusion Energy (OFE) has stated the need to investigate ferritic alloys under the ADIP program task, Ferritic Steels Development (Path E).

7.3.2 Objective

The primary objective of this study is to establish the feasibility and develop the procedures for the welding and fabrication of 9-12 Cr steels for use in first wall and blanket structures. An additional objective is to develop the methodology for the management of fracture safe design in the use of ferritic steels in fusion, including the generation and analysis of pertinent, unirradiated property data.

7.3.3 Summary

A 14,700 kg (32,500 lb) heat of 12 Cr-1 Mo-0.3 V steel was procured for use by all participants in the National Fusion Ferritic Steel Program. Preliminary analysis indicated that the ingot composition met specifications.

A preliminary evaluation of candidate welding procedures for 12 Cr-1 Mo-0.3 V EBR-II irradiation weld specimens was completed. The procedure selected for producing the specimens was completed. The procedure selected for producing the specimens was gas-tungsten arc (GTA) with a pre-heat temperature of 93°C.

7.3.4 Progress and Status

Section 7.3.4.1 describes the procurement of a 14,700 kg (32,500 lb) heat of 12 Cr-1 Mo-0.3 V steel during this reporting period. Section 7.3.4.2 presents the complete results of a preliminary investigation directed at determining a suitable welding procedure for preparing EBR-II irradiation weld specimens.

7.3.4.1 12 Cr-1 Mo-0.3 V Heat Procurement

Electralloy Corporation in Oil City, PA, poured the 12 Cr-1 Mo-0.3 V heat for the National Fusion Ferritics Program. The 14,700 kg (32,500 lb) heat was processed by the argon-oxygen decarburization (AOD) method and was poured in two product forms, two ESR ingots and two slabs.

Both slabs and both ingots were poured by the bottom pouring method, resulting in less chemical segregation and a greater yield from the pour (no hot top waste). The slabs and ingots were given a ten day cooling period in a soaking pit to minimize cooling residual stress. The surface appearance of all four slabs and ingots was smooth and uniform with no visable surface cracking. Table 7.3.1 gives a breakdown of the weights and sizes of the slabs and ingots produced.

The chemical composition information available at the time this report was being prepared is shown in Table 7.3.2. The ladle analysis plug chemistry is being checked by another company and the chemistries at the ends of the second slab and ingot are also being obtained.

	Weight	Size
Slab No. 1	3,830 kg (8,440 lb)	20.3 cm (8") x 96.5 cm (38") x 251.9 cm (99.2")
Slab No. 2	∿3,830 kg (∿8440 lb)	20.3 cm (8") x 96.5 cm (38") x 251.9 cm (99.2")
ESR Ingot No. 1	3,540 kg (7,800 lb)	40.64 cm (16") dia. x 3.52 m 1138.5") length
ESR Ingot No. 2	3,550 kg (7,820 lb)	40.64 cm (16") dia. x 3.53 m (139.0") length

Slab No. 1 has been shipped to Jessop Steel Co. in Washington, PA, where it will be converted into plate. Table 7.3.3 shows the approximate distribution of plate sizes and weights expected. The other slab and the two ESR ingots will be stored at Electralloy until FY81 when it is decided to convert the second slab into plate, bar and tube, and/or remelt the ingots by the electro-slag remelt (ESR) process.

Table 7.3.3. 12 Cr-1 Mo-0.3 V Plate Sizes and Amounts Expected from Slab No. 1 to be Converted at Jessop Steel Company

Plate Thickness mm (in.)	Weight Total kg (pounds)	No. of 132 cm (52") x 122 cm (48") Plates
3.2 (0.125)	590 (1300)	15
9.5 (0.375)	1430 (3150)	12
15.9 (0.625)	795 (1750)	4
28.6 (1.125)	365 (800)	1
	3,180 kg (7,000 lb)	

7.3.4.2 Development of Welding Procedures for 12 Cr-1 Mo (HT9) Specimens for Irradiation in EBR II

An investigation to determine suitable procedures for producing weldmenta to be exposed in the AD-2 EBR II irradiations was completed during the reporting period, and a procedure was selected and HT9 weldments were produced and shipped to HEDL for fabrication into specimens. The results of this preliminary welding procedure evaluation, including a description of parameters, the qualification tests and metallurgical analyses, are presented and discussed below.

7.3.5 Material and Welding Procedures

The material used in this study was obtained from Sandvik HT9 pipe, which was quartered, flattened and reheat treated. The vendor chemistry by weight percent is: Fe - 0.22 C - 11.3 Cr - 0.85 Mo - 0.50 W - 0.27 V - 0.5 Ni - 0.52 Mn - 0.37 Si - 0.019 P - 0.006 S. Each test plate was welded

from two 30 x 10 x 0.56 cm plates. A description of the investigation to screen five welding procedures was reported in the 8th ADIP quarterly report (Ref. 1). Two welded plates were made using each procedure. Table 7.3.4 shows these procedures and welding parameters. Plates were welded by two processes, gas-tungsten arc (GTA) and shielded metal arc (SMA). Preheat temperatures for the GTA welds ranged from no preheat to 343°C. One SMA weld was done for comparison and was not preheated. Table 7.3.4 details the interpass temperatures and allowed temperatures after welding prior to the post-weld heat treatment (PWHT). Plates were welded in the fully restrained condition. Figure 7.3.1 shows the tack welds used to restrain the plates, and the "run-off" tabs. The GTA procedures evaluated, specifically the preheat and interpass temperatures, covered the ranges recommended by several European producers and fabricators, including Sandvik, Sulzer and Brown Boveri.

The ASME Boiler and Pressure Vessel Code, Sections III and IX, describe the qualification tests used. These included dye penetrant and X-ray radiographs, two face and two root bend tests, and two flat tensile tests with the weld being transverse to the load line. Diamond pyramid microhardness tests are also reported. Charpy impact tests on subsize, non-standard specimens were done for comparison within this study to determine the ductile-brittle transition temperatures, and relative upper and lower sheld energies. The orientation of all specimens with respect to the weld are shown in Figure 7.3.2. Also included are the dimensions of the Charpy V-notch specimens. Optical metallography and scanning electron microscopy were done to complete the metallurgical analysis.

7.3.6 Results and Discussion

Table 7.3.5 lists the results from the ASME Pressure Vessel Code qualification nondestructive examinations, bend tests, and tensile tests. All welds passed each test with the following exceptions: in procedure 3, a bend specimen welded by the GTA process with a 93°C preheat broke Juring testing; and in procedure 5, a tensile specimen welded by the SMA process with no preheat broke prior to yield. The

Table 7.3.2. Summary of Specified, Target, and Vendor Chemical Analysis Performed on 12 Cr-1 Mo-0.3 V Heat #9607 Poured at Electralloy Corporation

Element	Specified Range	Specified Target	Ladle[a] Analysis	ESR Ingot No. 1-3		Slab No. 1[a]	
				Top	Bottom	Top	Bottom
C	0.18/0.22	0.20	0.20	0.23	0.20	0.18	0.21
Si	0.10/0.40	0.25	0.22	0.20	0.21	0.20	0.20
Mn	0.30/0.80	0.55	0.52	0.53	0.52	0.52	0.51
P	0.02 (max)	0.01	0.02	0.02	0.019	0.01	0.01
S	0.01 (max)	0.006	0.006	0.003	0.006	0.01	0.00
Cr	11.0/12.5	11.5	11.63	11.74	11.72	11.73	11.89
Mo	0.80/1.20	1.0	1.00	1.01	1.02	0.98	1.01
Ni	0.40/0.60	0.50	0.50	0.50	0.50	0.50	0.49
V	0.25/0.35	0.30	0.30	0.30	0.29	0.28	0.29
W	0.40/0.60	0.50	0.52	0.50	0.51	0.51	0.52
N	0.02/0.06	0.04	0.047	0.03	0.035	0.04	0.042
Al	0.04 (max)		< .01	< .01	< .01	0.01	0.01
Ti	0.01 (max)		< .01	< .01	< .01	< .01	< .01
Cu		0.10 (max)	0.04	0.04	0.04	0.04	0.04
O_2		0.02 (max)					
Co		0.05 (max)	0.08	0.08	0.07	0.08	0.08
As		0.01 (max)	< .01	< .01	< .01	< .01	< .01
B		0.001 (max)	trace	trace	trace	trace	trace
Bi		0.001 (max)					
Pb		0.001 (max)	0.001	0.009	0.00	0.00	0.001
Sb		0.001 (max)	trace	trace	trace	trace	trace
Sn		0.001 (max)	0.003	0.003	0.00	0.002	0.002
Cb		0.001 (max)					

[a] Analysis performed at Electralloy Co.

Table 7.3.4. Weld Parameter Matrix for 12 Cr-1 Mo-0.3 V (HT9)

Procedure Identification Number	Process[a]	Preheat (°C)	Interpass Range (°C)	Temperature Prior to PWHT (°C) [b]	Postweld Heat[b] Treatment (°C)
1	GTA	343°	288-343°	93° ± 14°	780° ± 14°C/1 hr
2	GTA	205°	149-205°	93° ± 14°	↓
3	GTA	93°	93-149°	93° ± 14°	↓
4	GTA	R.T.	R.T.-52°	R.T.	↓
5	SMA	R.T.	R.T.-52°	R.T.	↓

[a] GTA = Gas-Tungsten Arc Weld
SMA = Shielded Metal Arc Weld

[b] Cooled in air

[c] Heating and cooling rates: 93° to 593° at 200°C/hr

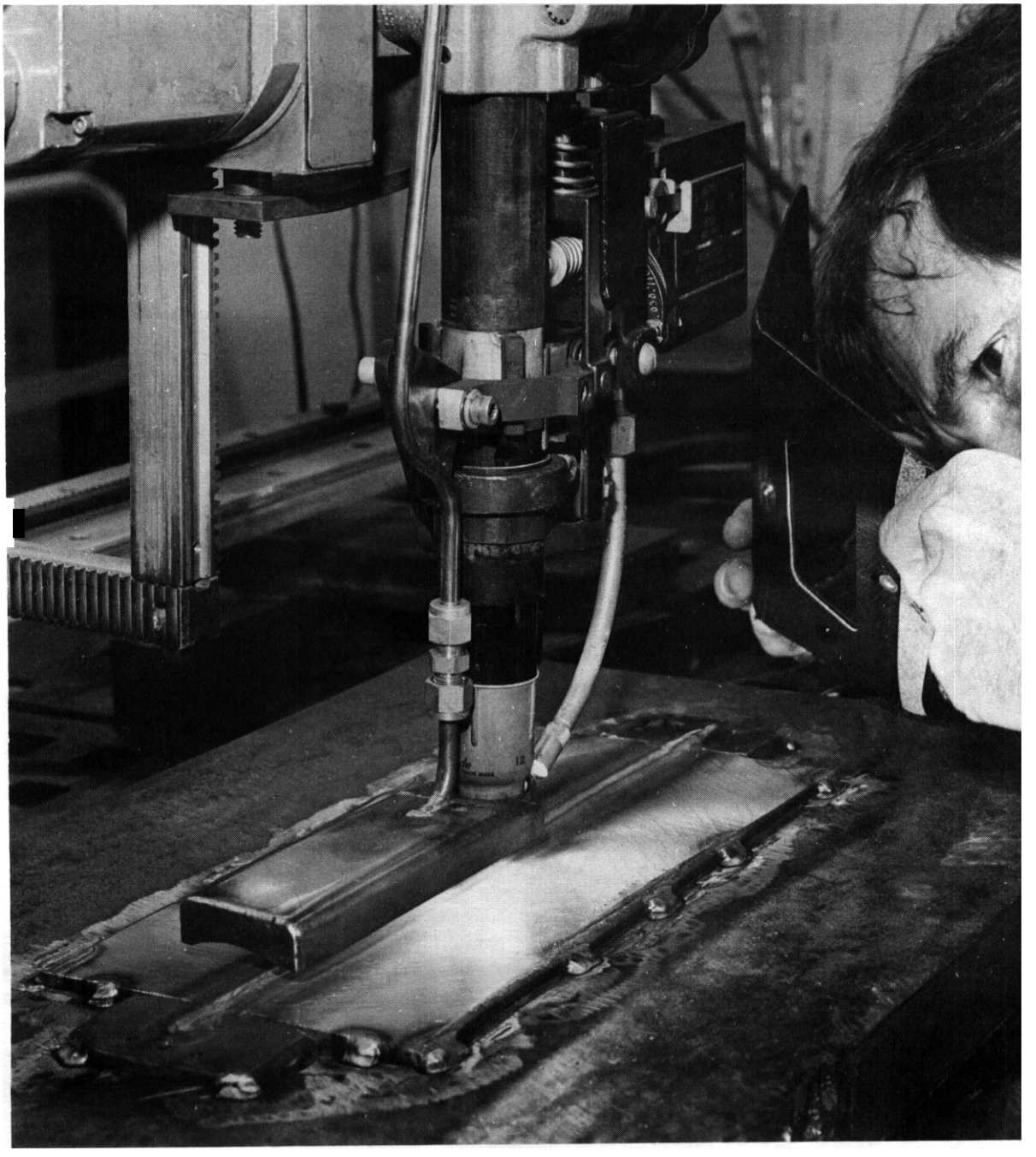

Fig. 7.3.1. Welding machine in operation showing test plate and run-off tabs all in fully restrained condition.

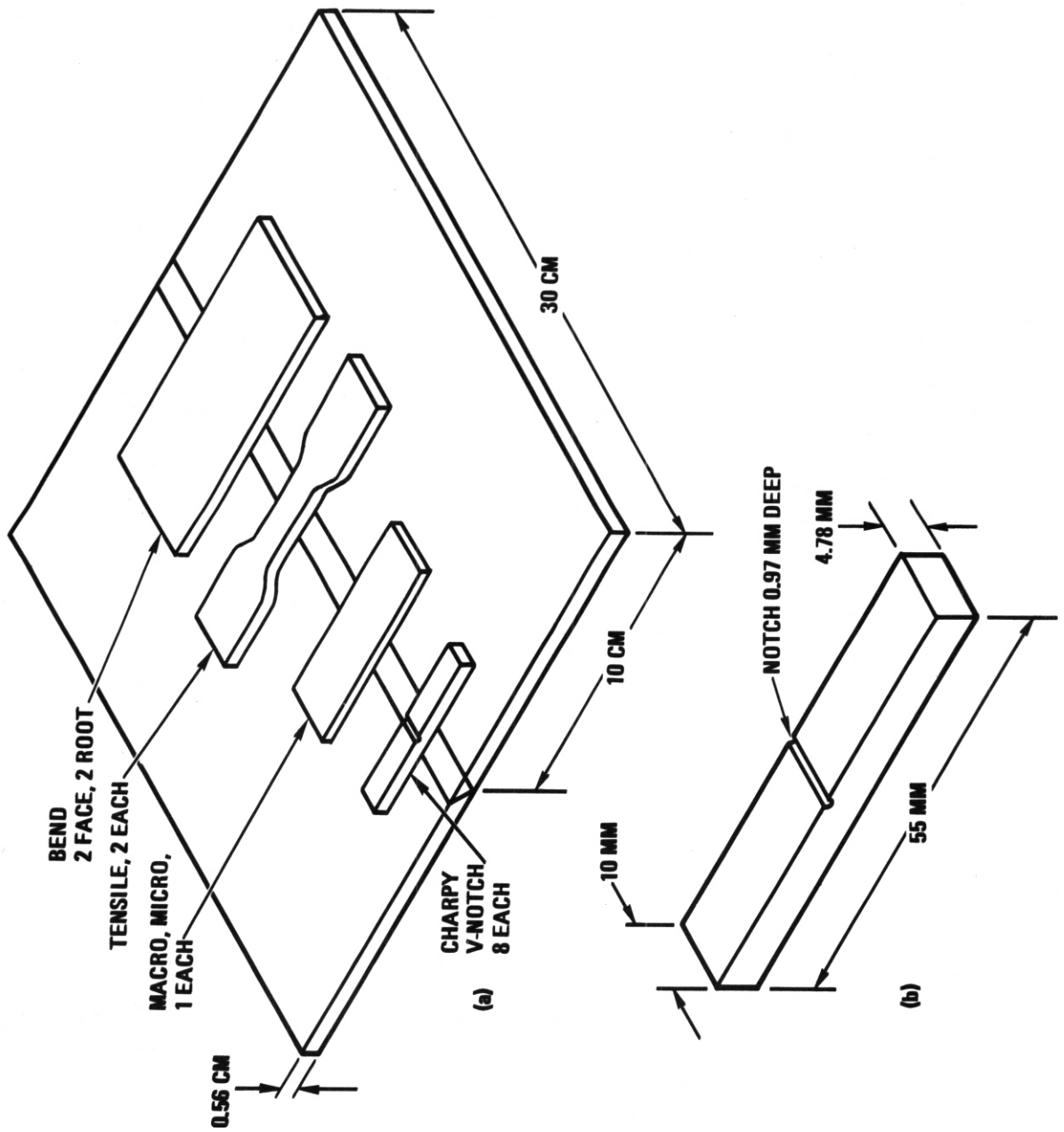

Fig. 7.3.2. Dimensions of (a) weld test plate and the orientation of weld qualification test specimens with respect to the weld, and (b) Charpy impact specimen dimensions.

Table 7.3.5. Results of ASME Pressure Vessel Code Weld Qualification Tests*

Welding Procedure (Identification Number)	Dye Penetrant	X-Ray Radiography	Bend Test		Tensile Test	
			Face	Root	UTS (MPa)	Elongation (%)
GTA 343°C Preheat (1)	Both Welds Passed	Both Welds Passed	Both Passed	Both Passed	758/758	9.1/8.2
GTA 205°C Preheat (2)	Both Welds Passed	Both Welds Passed	Both Passed	Both Passed	792/772	5.9/6.8
GTA 93°C Preheat (3)	Both Welds Passed	Both Welds Passed	One Broke at Weld	Both Passed	779/785	6.8/6.8
GTA No Preheat (4)	Both Welds Passed	Both Welds Passed	Both Passed	Both Passed	779/785	8.2/7.7
SMA No Preheat (5)	One Weld Failed Due to Lack of Penetration	Weld Plate Was Patched, then Passed	Both Passed	Both Passed	462/772	0/7.7

*Identification numbers refer to Table 7.3.4

fracture on the face bend specimen in procedure 3 initiated at the weld, and then propagated into parent metal to complete the failure. Figure 3 shows these two surfaces. Figure 3(a) is a macrograph at 2X. Arrow 1 points to the bright surface which fractured through the weld on the tension side of the bend specimen. It has the appearance of a cleavage fracture. Dendrites appear to have separated along boundaries. This is clearly shown in Figure 3(b) where the fracture is shown from the surface through the weld metal (region 1) and through the parent metal (region 2). The cleavage surface of region 1 is shown at higher magnification in Figure 4(a) and (b). At 200X magnification, the surface shows cleavage facets and separation along dendrite boundaries. A closer inspection at 2000X in Figure 4(b) shows typical cleavage facets for a martensitic steel. Cleavage of martensite laths reveal the acicular structure generally associated with this transformation product. The bend specimen did not fracture solely through the weld metal, however. The crack left the weld and propagated through the heat affected zone or parent metal, as shown by arrow 2 in Figure 3(a). This area lies in region 2 of Figure 3(b). The fracture surface in the parent metal appears differently from the cleavage fracture in the weldment (region 1). At 25X magnification, the fracture in the parent metal appears much more ductile. Figure 5(a) reveals dimple rupture caused by void formation. These voids in the parent metal fracture form by decohesion around particles such as inclusions or carbides. An arrow points to one such particle in Figure 5(b). The voids eventually become linked as they grow, and fracture occurs by tearing of the ligaments separating them.

The tensile specimen in procedure 5 (SMA) fractured at a stress of 462 MPa (67 ksi) and with no measurable elongation. This was probably due to poor fusion. The second specimen, cut from the same welded plate with the same treatment, broke at 772 MPa (112 ksi), and 7.7% elongation. The plate was visually inspected after the welding operation and a few small areas on the back were not fused. These areas were ground and then patched using a hand-held heli-arr

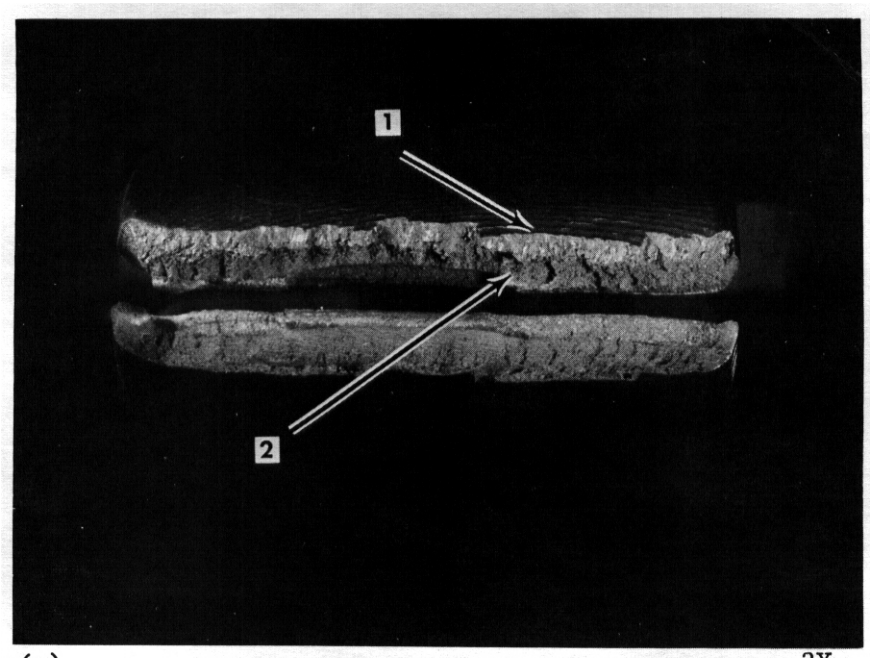

(a) 2X

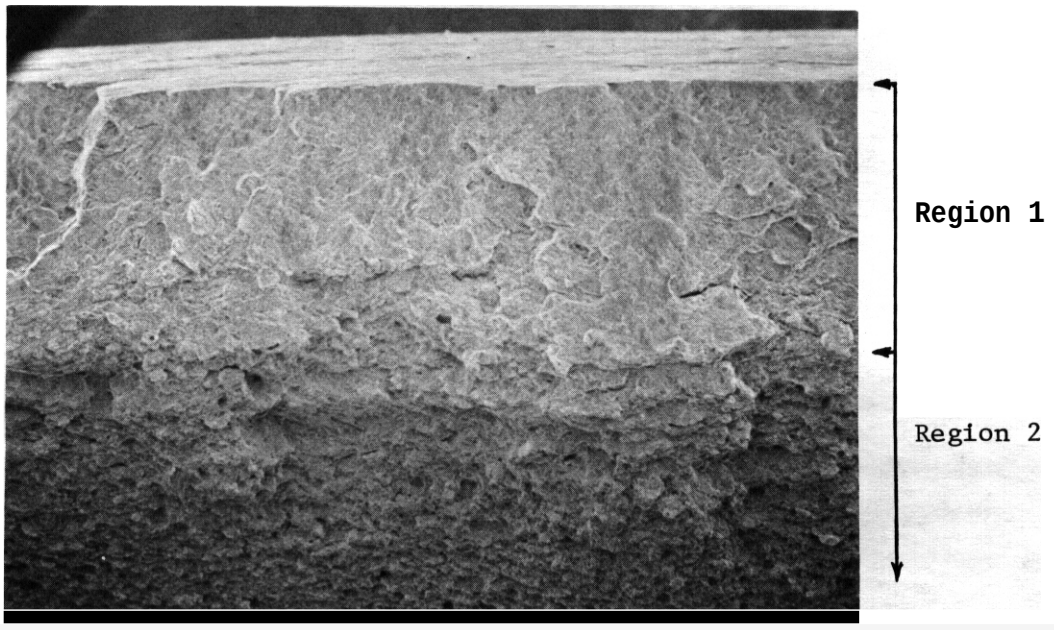

(b) 25X

Fig. 7.3.3 Bend specimen of welded *12* Cr-1 Mo (HT-9) with: (a) optical macrograph at 2X showing fracture through weld metal (arrow 1) and through parent metal (arrow 2), and (b) an SEM photograph at 25X showing the same regions of cleavage fracture through the weld with some dendritic separation (region 1), and ductile fracture through parent metal (region 2).

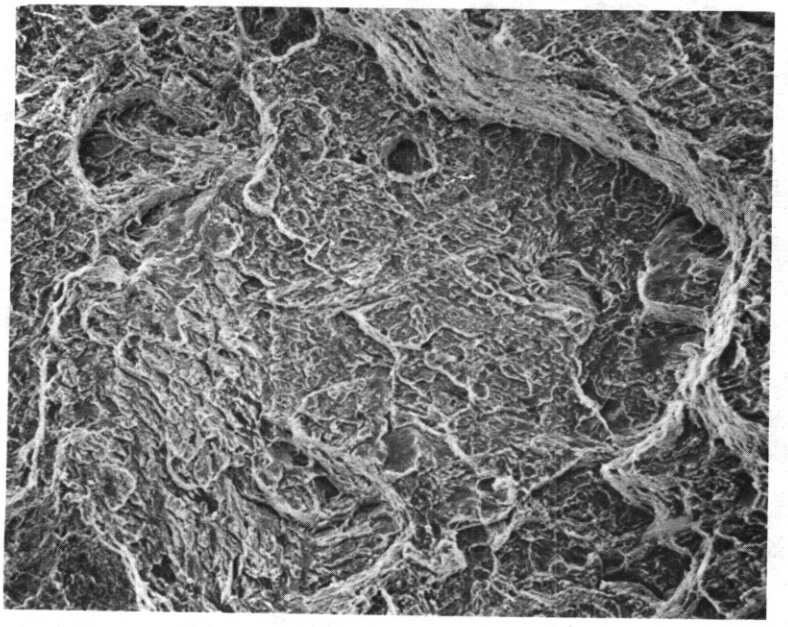

(a) 200X

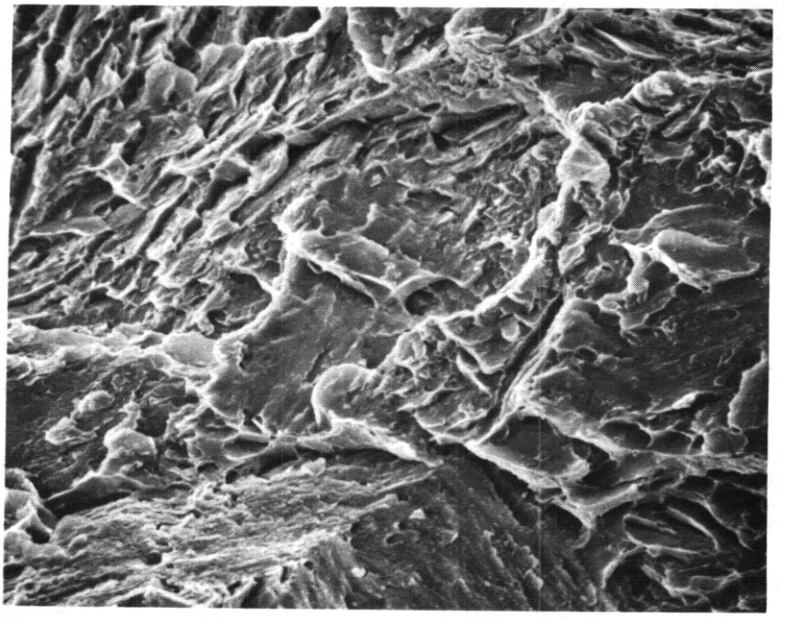

(b) 2000X

Fig. 7.3.4 Scanning electron micrographs of cleavage fracture through region 1 of the bend specimen. Part (a) shows the general surface morphology with well-defined, transgranular cleavage facets and dendrite boundary separation, and (b) shows the fine detail of an area which reveals the acicular-like structure associated with martensite caused by cleavage along laths.

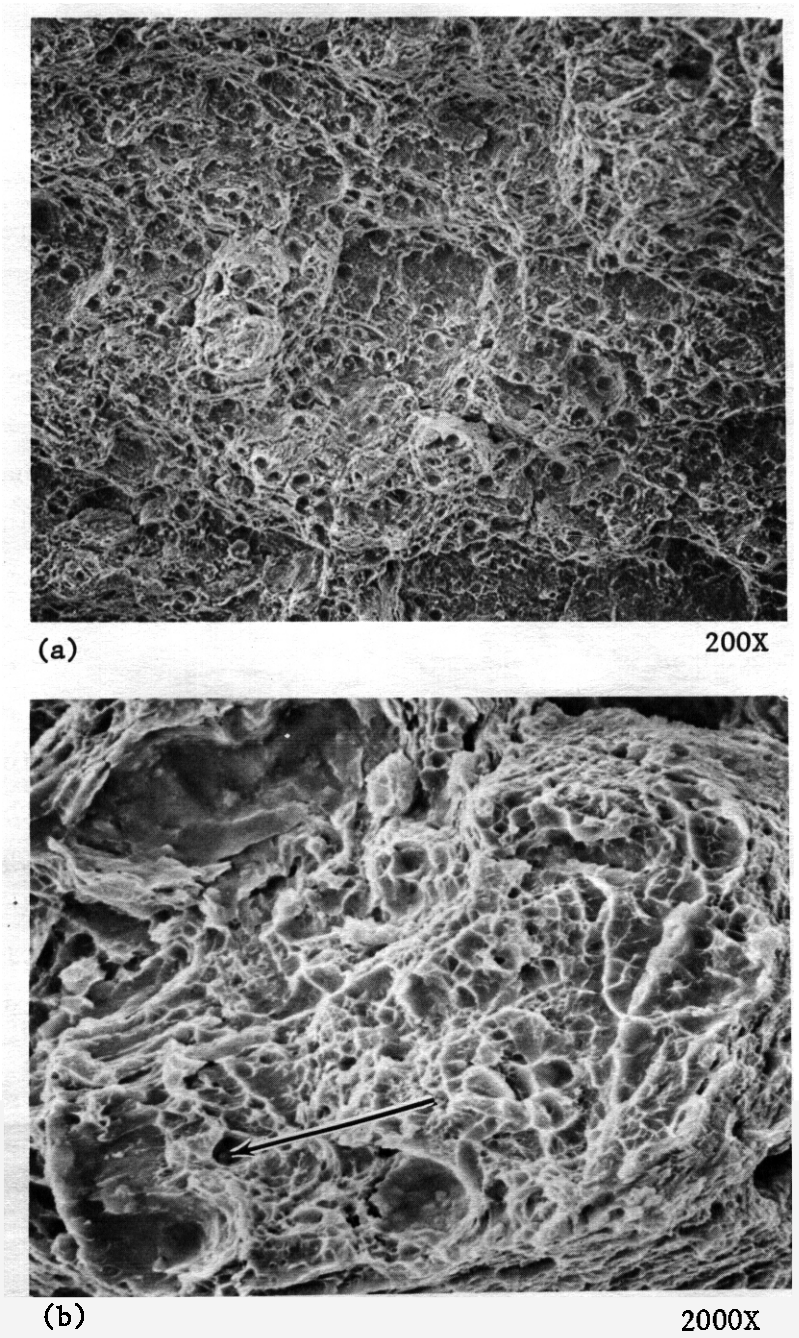

Fig. 7.3.5 Scanning electron micrographs of ductile fracture from region 2 of the bend specimen. Part (a) shows the general dimple rupture morphology at 200X, and (b) shows the fine detail of the void formation and subsequent tearing, and a particle sitting in the void it formed (arrow).

welder. Then the plate was inspected by dye penetrant and X-ray radiography, and passed both examinations. The apparent problem with weld fusion in SMA welds will be studied later in the program.

Table 7.3.6 presents the microhardness data taken from specimens welded by each procedure. Of the four GTA procedures, three had some preheat prior to welding and these three had lower hardnesses in all zones affected by welding. The zones are the weld metal, fusion line, and heat affected zone (HAZ). For example, procedure 4 (no preheat) had a weld metal hardness of 317 dph, whereas the weld in procedures 1, 2 and 3 (preheats 343°, 205°, and 93°C. respectively) had hardnesses of 290, 287, and 283 dph. The difference existed in the fusion line and HAZ, although it was less pronounced than in the weld metal. The SMA process with no preheat had hardnesses comparable to those of the GTA procedures with preheats.

On a specimen from the GTA-343°C preheat weldment, a microhardness traverse across the weld to the parent metal was performed. This was done to determine if any low-strength area existed such as the one reported recently in a modified 9 Cr-1 Mo alloy weldment (Ref. 2). This soft area may be due to severely over-tempered material at the extreme edge of the HAZ. It was thought that if it was evident in the weldment from the procedure producing the lowest hardness differences, then it would probably be evident in the other weldments. The data is presented in Figure 6. It appears that there may be a slight decrease at the edge of the HAZ near the parent metal. The hardnesses hover around 240 dph, whereas the parent metal is closer to 250 dph. The evidence is inconclusive and may be studied further on specimens with no post weld heat treatment.

Ductile-brittle transition temperatures (DBTT), and upper and lower shelf energies were found using Charpy impact specimens with dimensions of 55 x 10 x 4.78 mm and a notch depth of 0.97 mm in the center of the weld, with all other dimensions according to ASTM E23-72. Specimens were broken at temperatures ranging from -20° to 180°C. Table 7.3.7 shows the results of these tests and they are plotted in Figure 7. The transition temperatures of the weld metal

Table 7.3.6. Microhardness Measurements for the Five Candidate Procedures

Welding Procedure (Identification Number)	Hardness (DPH)			
	Weld Metal	Fusion Line	Heat Affected Zone	Parent Metal
GTA 343°C Preheat (1)	290	281	278	243
GTA 205°C Preheat (2)	287	273	276	256
GTA 93°C Preheat (3)	283	266	274	260
GTA No Preheat (4)	317	302	284	257
SMA No Preheat (5)	284	291	268	237

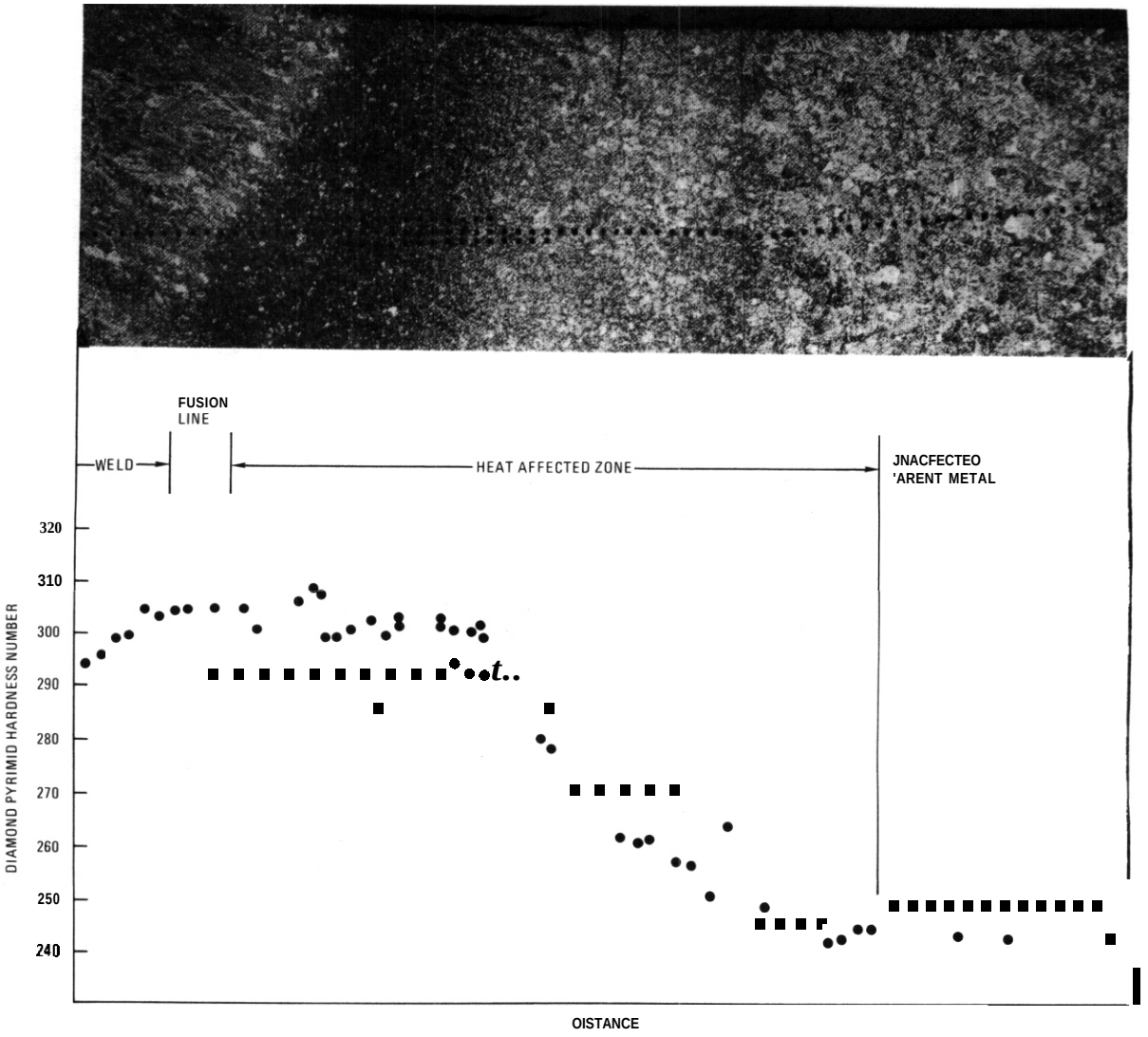

Fig. 7.3.6 Diamond–pyramid hardness values across the weld, heat affected zone, and parent metal, and a micrograph at 30X showing the microstructure and hardness indentions.

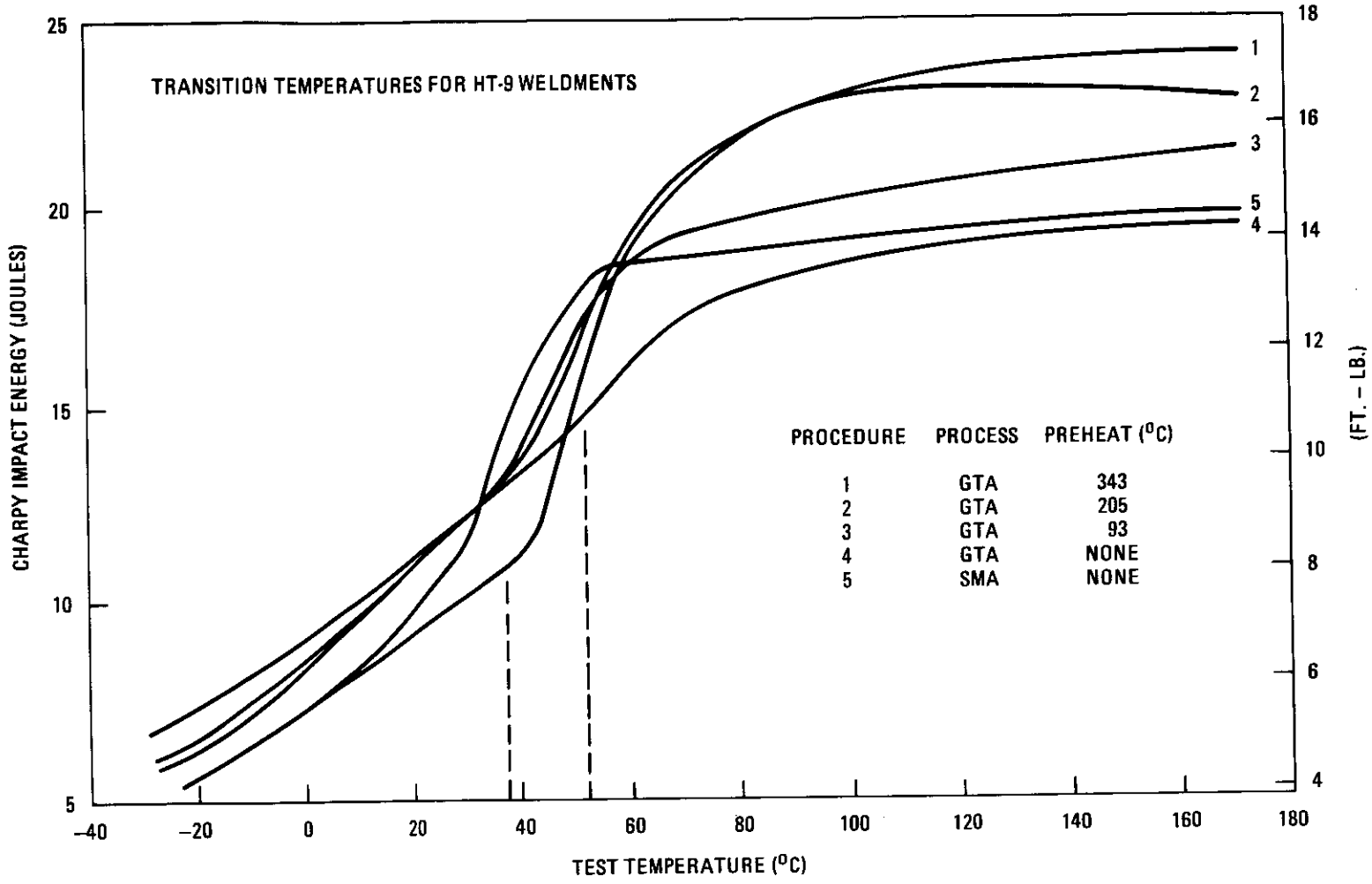

Fig. 7.3.7 Impact energy as a function of test temperature for each procedure to determine the ductile-brittle transition temperature.

for each procedure fell between 40° to 50°C. Within the reproducibility of the test there was no difference between the five welding procedures. The upper shelf energies ranged from 18.6 J (14 ft-lb) to 22.6 J (17 ft-lb). Those welds with some preheating absorbed more energy, while the lowest were for procedures 4 and 5 which had no preheating. There was essentially no difference in the lower shelf energies, which were between 4 and 5 ft-lbs. It should be noted that fracture energies from the sub-size specimens used in this evaluation would be expected to be about a factor of 2 lower than those from full size Charpy specimens.

The impact fracture surfaces generally had two morphologies, cleavage and ductile. The relative amounts of each changed with temperature as expected. A representative example is shown in Figure 8. Part (a) shows the general surface features of the cleavage fracture (labeled A) and the ductile or fibrous fracture (labeled B). Cleavage facets and dendritic separation can be seen. Part (b) shows a closer view of the cleavage fracture, particularly the cracking and subsequent dendrite separation. Part (c) of Figure 8 shows the details of the transition region where the fracture mode changed from ductile/fibrous to cleavage. Figure 9 shows a closer view of the ductile region. Part (a) shows the general fracture appearance, and part (b) the details of dimples and tearing. 'fie cleavage region is shown in Figure 10 where part (a) shows general morphology, and part (b) indicates cleavage facets probably along martensite laths similar to those seen in the bend specimen (Figure 4).

7.3.7 Conclusions and Recommendations

Based on this study, preheat temperature of 343°, 203°, and 93°C do affect the residual properties. Generally, preheating the weld has two effects: decreased residual hardness, and an increase in upper-shelf impact energy. Lower shelf energy was not affected by preheat in this limited investigation. The higher the preheat temperature, the more heat is available for autotempering and other transformations in the weld metal and heat affected parent metal.

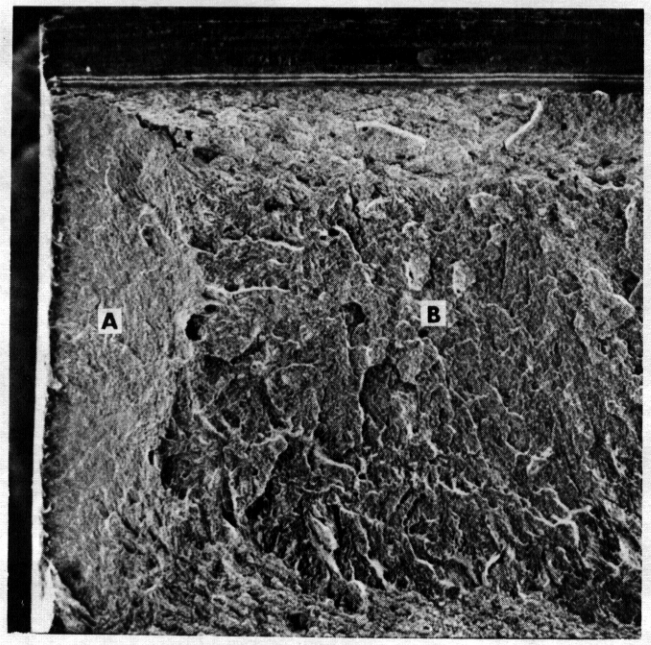

(a) 20X

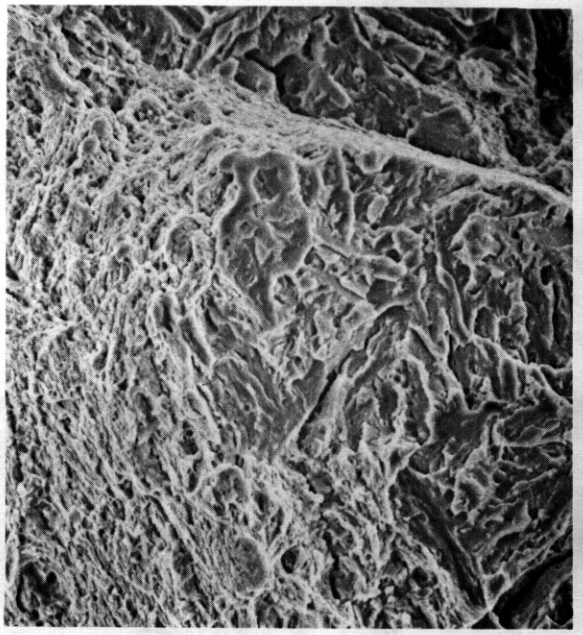

(b) 50X

(c) 500X

Fig. 7.3.8 Scanning electron micrographs from Charpy impact specimen of HT-9 weldment fractured at room temperature showing: (a) general surface features of cleavage (A) and ductile or fibrous (B) fracture, (b) details of cleavage area showing dendritic separation and cracking, and (c) details of transition region from fibrous to cleavage fracture modes.

(a) 500X

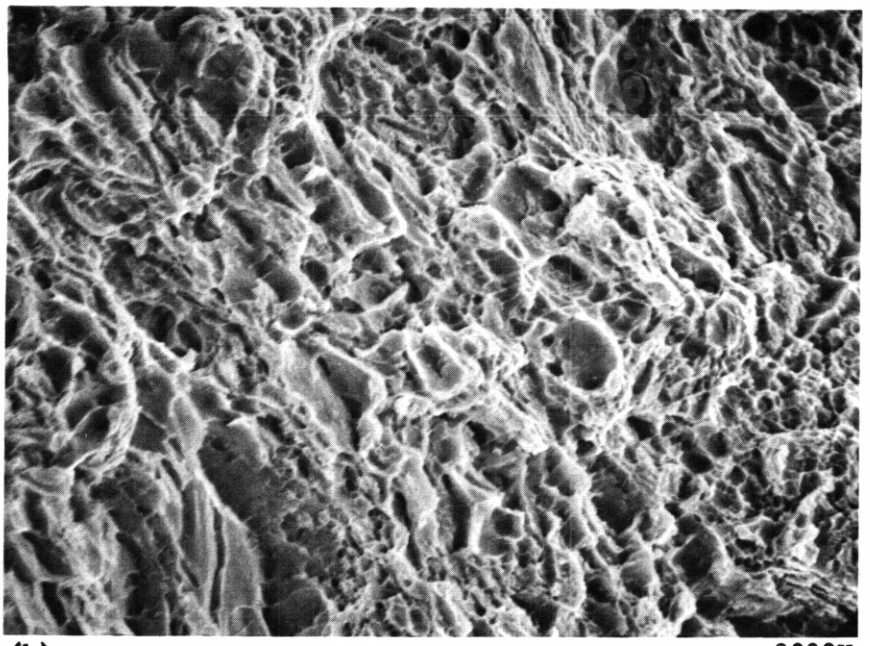

(b) 2000X

Fig. 7.3.9 Scanning electron micrographs of ductile fracture of a Charpy impact HT-9 weld specimen fractured at room temperature. Part (a) shows the fibrous appearance, and (b) the details of tearing and dimples associated with this morphology.

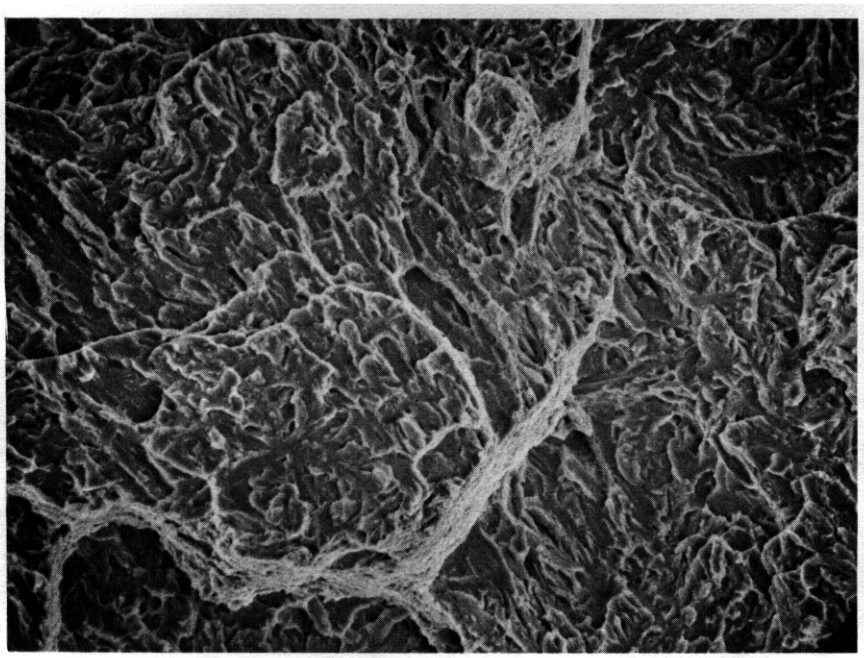

(a) 500X

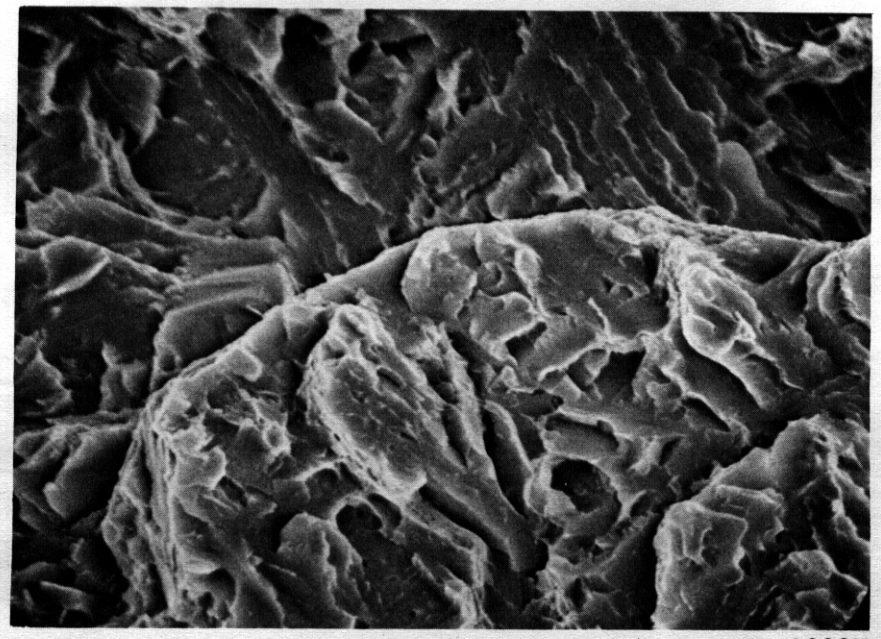

(b) 2000X

Fig. 7.3.10 Scanning electron micrograph of fracture surface through the weld of an HT-9 Charpy impact specimen. Part (a) shows the general fracture appearance with cleavage facets. Part (b) shows details of the cleavage morphology.

There appears to be no significant change in the DBTT or in the transverse weld specimen tensile strength in the preheat range studied. Based on the results of this investigation, it was concluded that the GTA procedure with a 93°C preheat, a 93°–143°C interpass temperature, and a post-weld tempering treatment of 780°C for 1 hr would be used for the EBR II AD-2 weld specimens. The chosen procedure is consistent with commercial welding considerations including the desire to minimize preheat temperature for ease and economy of fabrication while maintaining a finite pre-heat to reduce moisture in the area to be welded. It should be emphasized that the procedure selected for welding the EBR II specimens may not be optimum with respect to unirradiated or irradiated properties for this 0.56 cm section size, and may not be pertinent to thicker sections.

7.4 MICROSTRUCTURAL AND FATIGUE CRACK GROWTH CHARACTERIZATION OF HT-9 –

D. A. Mervyn, D. T. Peterson and F. H. Huang (Hanford Engineering (Development Laboratory)

7.4.1 ADIP Task

Task Number I.B.4 – Fatigue Crack Growth in Special and Innovative Materials (Path E).

7.4.2 Objective

An optimum microstructural condition for nonirradiated HT-9 has been chosen in order that baseline mechanical properties data can be gathered. The fatigue crack growth and fracture toughness behavior of this HT-9 was investigated using the electrical potential technqiues developed to expedite charactedization of first wall materials.

7.4.3 Summary

A microstructural characterization of nonirradiated HT-9 has been completed. Selected thermomechanical heat treatments were chosen €or study. Heat treatment times for 0.30 to 2.54 mm section thickness were identified by characterizing the austenization behavior of the ferritic alloy. A tempering curve was constructed and complementary transmission election microscopy micrographs taken. Fatigue crack growth and fracture toughness studies were completed on four over-temperedconditions of the alloy. Based on the microstructural and mechanical properties studied, an optimum thermomechanical heat treatment for HT-9 was selected.

7.4.4 Progress and Status

7.4.4.1 Introduction

Some of the most promising candidate materials for first wall fusion applications are the Path E ferritic alloys, HT-9, 9Cr-1Mo, and 2-1/4 Cr-1Mo. Twelve Cr steels such as HT-9 are particularly attractive. They have a high resistance to void formation during neutron irradiation at temperatures between 400 and 650°C[1] and acceptable corrosion and decarburization resistance.[2] By using the proper thermomechanical heat

treatments this class of ferritic steels canpossess suitable mechanical properties such as high yield strength, and adequate toughness and rupture ductility.

This study was conducted to characterize the microstructure, fracture toughness and fatigue crack growth properties of HT-9 as a function of thermomechanical heat treatment (TMT). TMTs were chosen in an attempt to optimize those properties important to first wall design; i.e., strength, toughness and crack growth resistance.

The generalaustenitizingand temperingbehavior of 12Cr-Mo-V steels is known.[2] Austenitizing at temperatures between approximately 1000°C and 1150°C and air cooling produces a fully martensitic structure, consisting of thin martensite laths within prior austenite grains. Tempering in the range of 700 to 800°C results in carbide precipitation within the laths as well as along the lath and grain boundaries. In this study, specific details concerning the austenitizing and tempering behavior of Path E, HT-9 were sought.

7.4.4.2 Experimental Procedure

7.4.4.2.1 Austenitizing. Samples of HT-9 in the 40% CW condition were austenitized at 1038°C for periods of 5 to 60 minutes to determine the optimum treatment time for section thicknesses between 0.30 and 6.35 mm. Specimens were encapsulated in 0.25 atm argon with an oxygen getter for treatment. Microstructures were examined optically to determine prior austenite grain size.

7.4.4.2.2 Tempering. Material for metallography and crack growth specimens was received in the austenitized and tempered condition, 1025°C/5 min/AC + 750°C/1 hr/AC. Starting material for the fracture toughness specimens had also been heat treated, as follows: 1050°C/0.5 hr/AC + 780°C/2.5 hr/AC. These specimens were given four heat treatments designed to produce a fine grained, over-tempered microstructure. Additional heat treatments consisting of austenitizing the metallographic specimen material at 1038°C for five minutes, followed by tempering between 450°C and 780°C for times up to seven hours, were carried out to determine the tempering

behavior of HT-9.

For all tempering studies, specimens were encapsulated in 0.25 atm argon with oxygen getter for treatment. Microstructures were examined optically and when necessary by transmission electron microscopy (TEM). Prior austenitic grain size and microhardness were also determined.

Fatigue crack growth tests were performed at 25°C, 425°C and 600°C using the miniature specimen technology and electrical potential technique described previously.[3] Room temperature tests were performed in air at a cyclic frequency of 15 Hz. Tests at 600°C were conducted in helium at 1 Hz, and at 425°C in air at 1 Hz. In all cases the maximum load was 475 lbs, and the load ratio (R) was 0.05.

Fracture toughness was determined using the electrical potential technique described previously.[4] Tests were performed in room temperature air on 2.54 mm thick circular compact tension specimens.

7.4.4.3 Results and Discussion

7.4.4.3.1 Austenization Optimization. Prior austenitic grain size refinement has been reported to decrease the impact transition temperature (ITT) of 12Cr-Mo-V steels, regardless of strength.' A grain size change of $d^{-1/2} = 1\ mm^{-1/2}$ causes a change of about 23°C in the ITT. For example, a grain size decrease from 40 μm to 25 μm decreases the ITT by 25°C to 30°C, but does not affect the upper shelf energy (USE). Thus, it is important to preserve a fine grain size in HT-9.

The austenitizing behavior of HT-9 as a function of temperature and time has been investigated for 0.30 mm thick cold worked sheet[5] (Table 7.4.1). Since the presence of deleterious phases can adversely affect mechanical properties, it is necessary to put all precipitates into solution and minimize the formation of delta ferrite when austenitizing. These considerations narrow the acceptable austenitizing temperatures to between 1025°C and 1150°C. In order to minimize the prior austenite grain size, an austenitizing treatment of 1038°C/5 min/AC was examined. Because of the fine grain size produced by this treatment, it was selected for use during further testing.

Table 7.3.7. Transition Temperatures and Shelf Energies of Weld Procedures on Non-Standard Charpy Impact Specimens

Weld Procedure	DBTT (°C)	Shelf Energy Joules (ft-lb) Upper	Lower
GTA, 343°C Preheat	45	22.6 (17)	4
GTA, 203°C Preheat	45	22.0 (16.5)	5
GTA, 93°C Preheat	40	20.6 (15.5)	5
GTA, No Preheat	40	18.6 (14)	5
SMA, No Preheat	40	18.6 (14)	4

References

1. Rosenwasser, S. N., L. D. Thompson, R. D. Stevenson, T. A. Lechtenberg, B. E. Thurgood and K. H. Holko, "Alloy Development for Irradiation Performance," Quarterly Progress Report for the Period Ending 31 December 1979, DOE/ER-0045/1.

2. Sikka, Vinod, to be published in "Modified 9 Cr-1 Mo Steel Development Program," Progress Report for the Period Ending March 31, 1980.

TABLE 7.4.1

AUSTENITIZING OPTIMIZATION

Treatment	Prior Austenite Grain Size, mm (ASTM #)	Precipitation	δ-Ferrite
950°C/5 min/AC	0.011 (#10)	Excessive	Common
1000°C/5 min/AC	0.011 (#10)	Common	Common
1025°C/5 min/AC	0.011 (1110)	Infrequent	Infrequent
1038°C/5 min/AC	0.016 - 0.011 (#9-10)	Abseat	Infrequent
1050°C/5 min/AC	0.030 (#7)	Absent	Infrequent
1100°C/5 min/AC	0.030 (#7)	Absent	Infrequent
1150°C/5 min/AC	0.022 (#8)	Absent	Very Common

Mechanical testing technqiues use specimens of varying sizes. In order to insure that all mechanical tests were performed on material with comparable grain sizes, the effect of section thickness on prior austenite grain size was studied. Samples varying from 0.30 to 2.54 mm thick were austenitized at 1038°C for various times from 5 to 30 minutes (Figure 7.4.1).

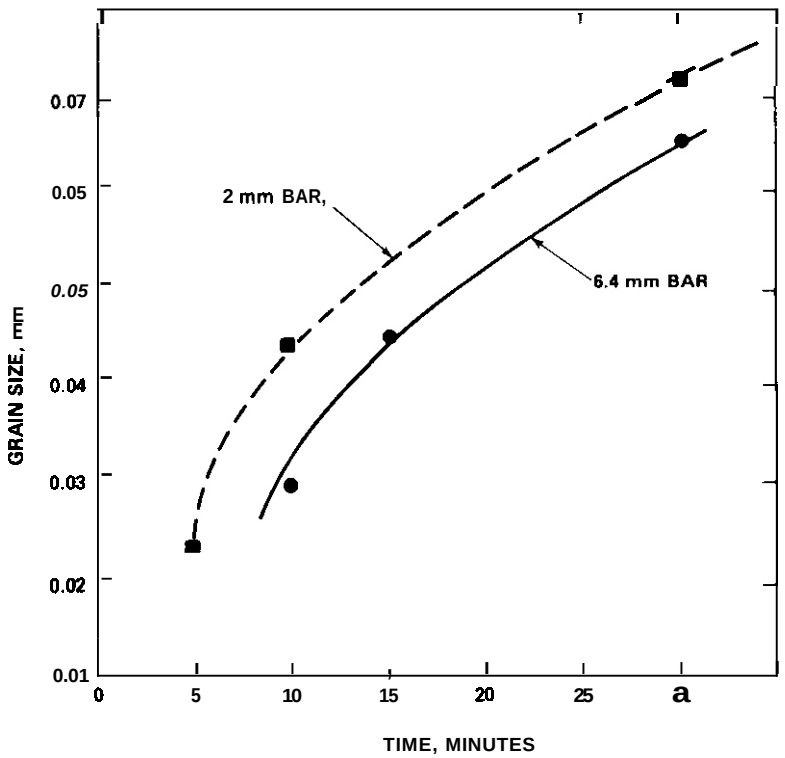

Figure 7.4.1 Austenitizing Effect on Grain Size for Different Bar Thicknesses.

This data was used to construct a curve in which the time at temperature to achieve a ASTM grain size of #7/#8 was described as a function of section thickness (Figure 7.4.2). From these results a five minute austenitizing time was chosen for section thicknesses up to 2.54 mm.

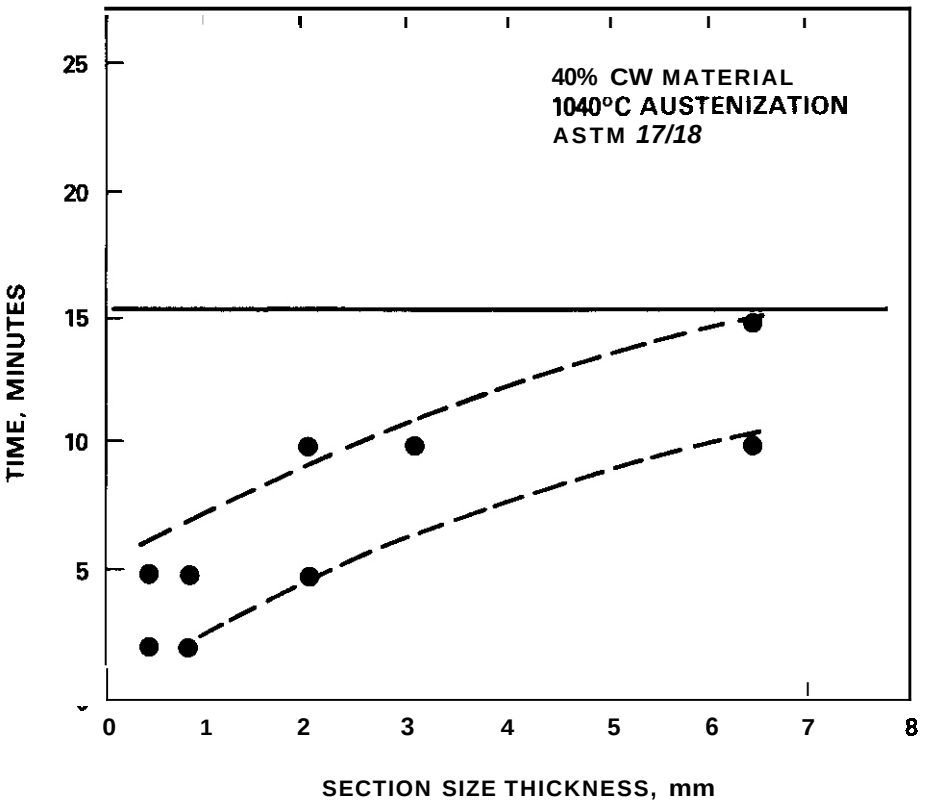

Figure 7.4.2 Austenitizing Optimization.

7.4.4.3.2 Tempering Optimization. Increasing the tempering time or temperature decreases the strength of 12Cr-Mo-V steels and therefore decreases the ITT.[2] This also has the effect of increasing the upper shelf energy (USE). An increase of approximately 0.35 in the USE and decrease of 2" to 5°C in the ITT is produced from a decrease in the proof stress of 10 MN/m^2. Therefore, an over-tempered microstructure is desired to optimize unirradiated fracture toughness properties.

A tempering curve has been developed for 12 Cr-Mo-V steels.[6] This curve utilizes a combined time/temperature parameter $T(20 + \log t) \times 10^{-3}$ to describe tempering. T is the absolute temperature and t time in hours. The result is a simple curve which represents a wide range of different tempering conditions. A similar curve was constructed for HT-9 by varying

the tempering temperatures and times (Table 7.4.2). This data was used to construct the curve shown in Figure 7.4.3. The shape of this curve is slightly different from that for 12Cr-Mo-V steels, but the absolute hardness values are approximately the same.

TABLE 7.4.2

TEMPERING TREATMENTS

Tempering Treatment	$T(20 + \log t) \times 10^{-3}$	Hardness (DPH)
400°C/30 min/AC	13	440
450°C/30 min/AC	14	453
500°C/1 hr/AC	15	444
500°C/2.4 hr/AC	16	456
500°C/7 hr/AC	17	397
600°C/1.8 hr/AC	18	290
650°C/1.8 hr/AC	19	280
740°C/1 hr/AC	20	259
740°C/2.5 hr/AC	21	239

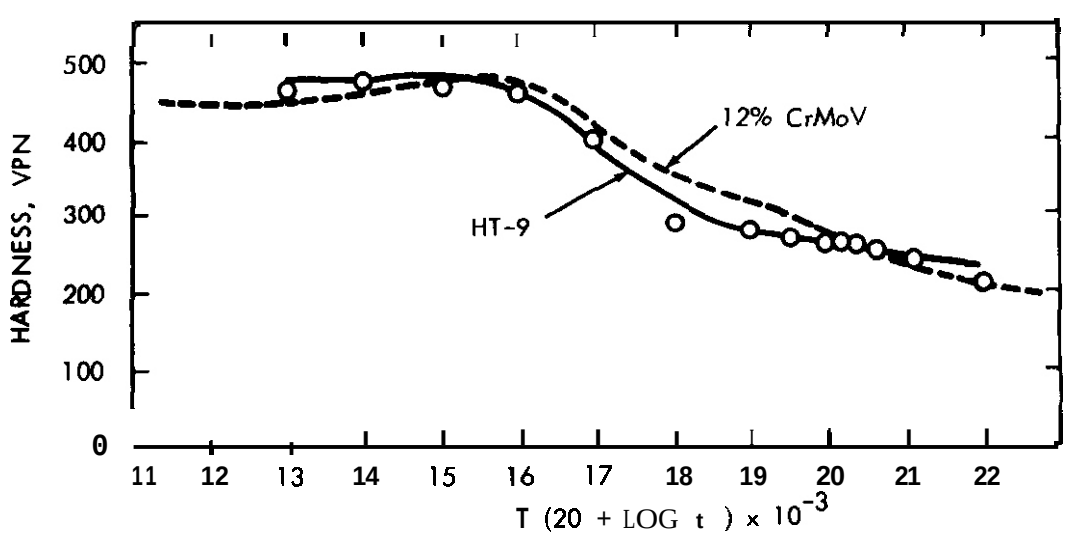

Figure 7.4.3 HT-9 Tempering Curve.

Prior to tempering, the microstructure of HT-9 is characterized by martenite laths with a high dislocation density (Figure 7.4.4). In this condition HT-9 has a hardness of about 510 DPH. Upon tempering. the hardness is reduced by the recovery of the dislocation structure and the removal of carbon from the martensite by the precipitation of carbides. In the temperature range of 750°C the tempering is very rapid. A tempering treatment of 740°C/30 sec/AC resulted in a hardness of 260 DPH. Transmission electron microscopy examination revealed that this treatment produced extensive, but relatively fine, carbide precipitation and considerable recovery of the dislocation structure (Figure 7.4.5). The precipitation was mcst extensive along the prior austenite grain boundaries. Upon further tempering, for example, 780°C/2.5 hr/AC, the dislocations recover into networks and the precipitates coarsen. As the curve in Figure 7.4.3 indicates, little additional decrease in hardness is produced upon tempering beyond 740°C/30 sec/AC.

In order to produce a lightly tempered structure, it was necessary to use tempering temperatures of 450-500°C. A temper treatment of 500°C/7 hr/AC produced a hardness of 400 DPH. The resultant microstructure is illustrated in Figure 7.4.6. The precipitation response at this temperature is significantly different than at 740°C. At 500°C a relatively low number density of fine rod shaped precipitates formed within the martensite laths. Although these precipitates formed extensively within some of the laths, the number of laths in which they were observed was low. Additionally, a very small density of fine globular precipitates was observed at the grain boundaries.

Not only does a decrease in the ITT occur, but also an increase in ductility results from increasing the tempering temperature from 700 to 750°C.[2] Therefore, tempering above 750°C was selected as the optimum condition for testing. Due to vendor recommendations[7] and tempering results, two temperatures were chosen for consideration, 760°C and 780°C.

The HT-9 microstructure, crack growth and fracture toughness specimens were given four temper treatments, two at 760°C and two at 780°C (Table 7.4.3). The austenitizing treatment did not control grain growth in this case, since the material had been given a prior heat treatment which fixed the grain size at that time. All four treatments, therefore,

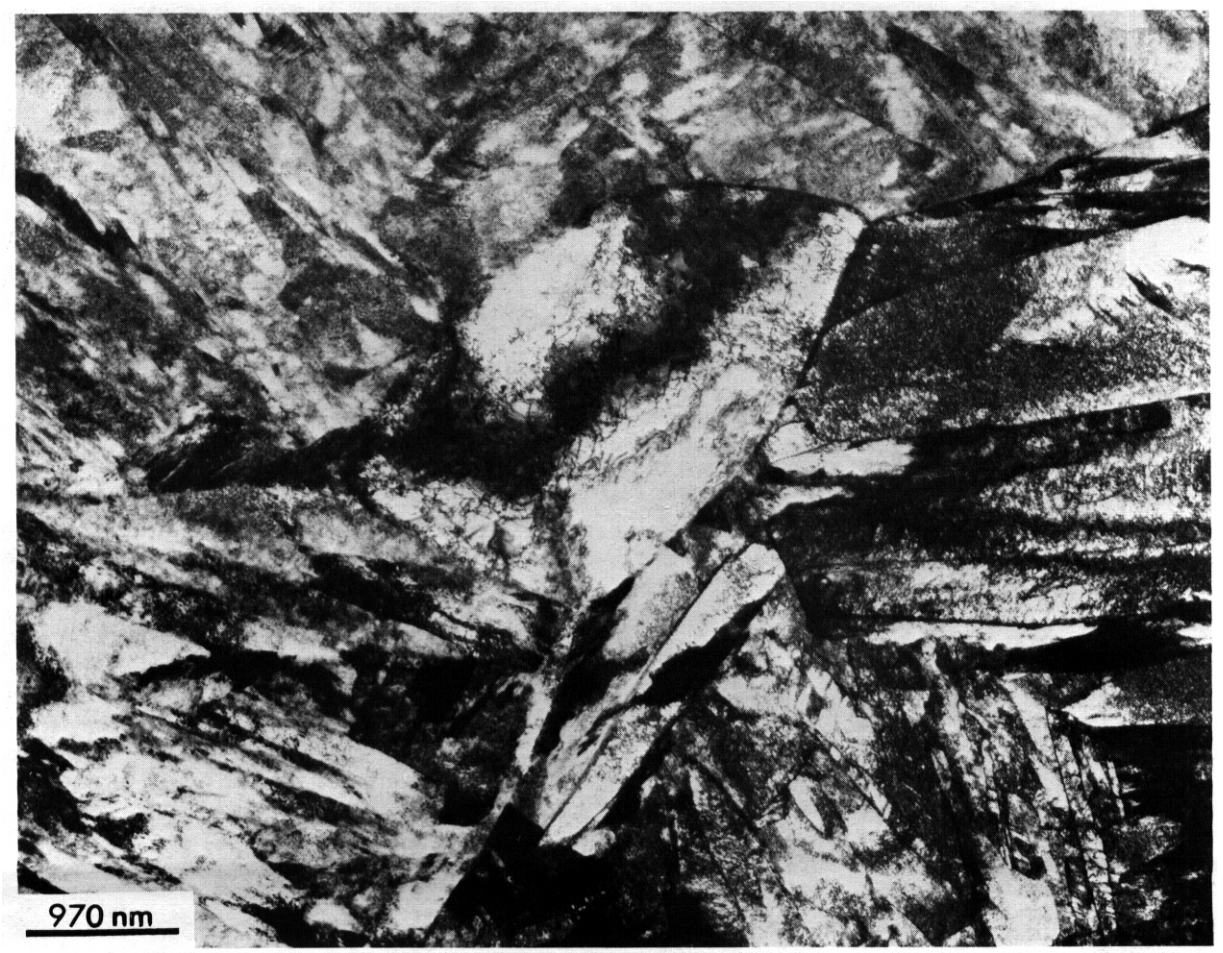

20821B

Figure 7.4.4 The Microstructure of HT-9 After a Treatment of 1038°C/ 5 min/AC:

a) Low magnification shot showing the martensite lath structure and a small δ-ferrite grain within a prior austenite grain boundary.

20819A

Figure 7.4.4 The Microstructure of HT-9 After a Treatment of 1038°C/ 5 min/AC:

b) Higher magnification shot of a group of martenite laths.

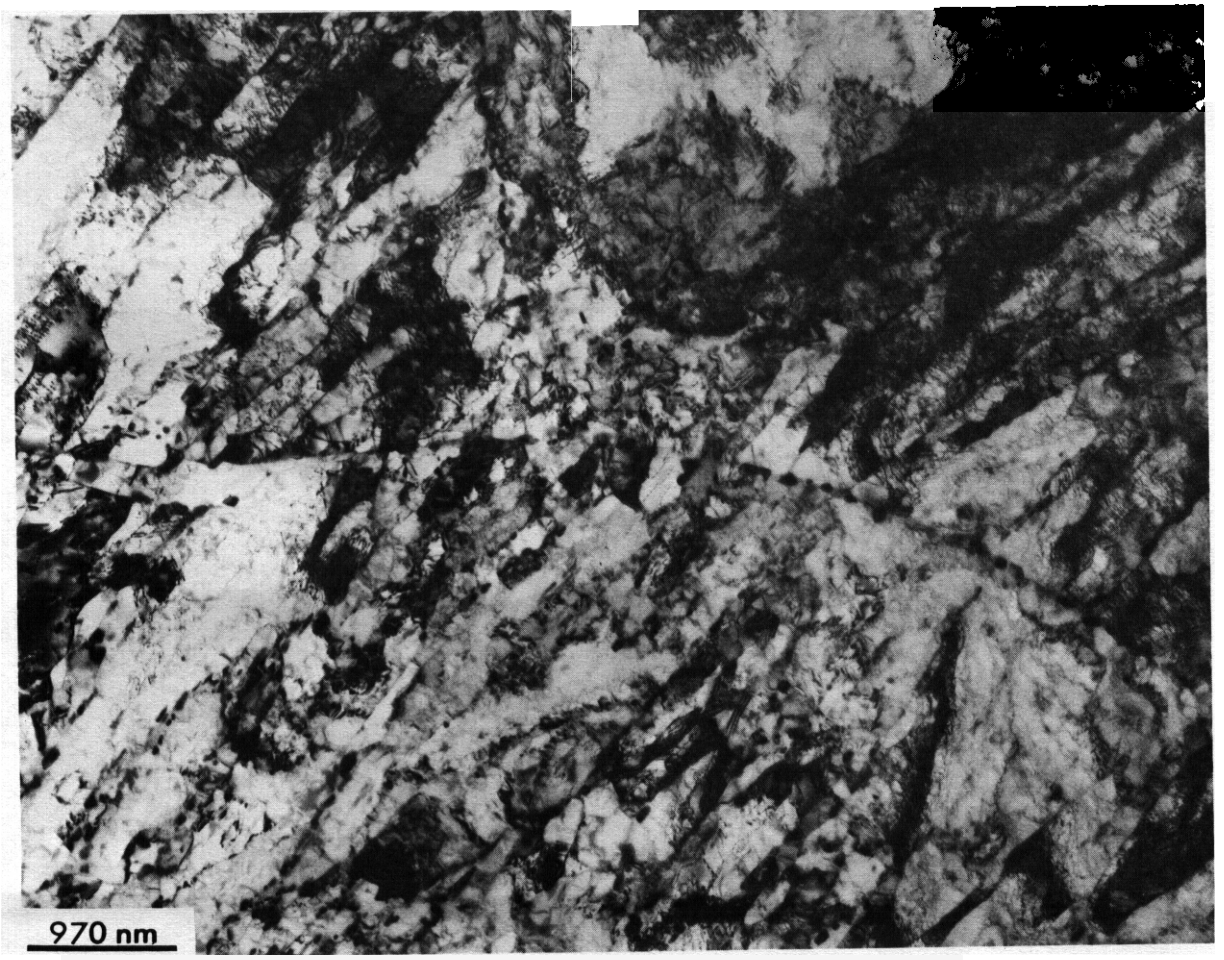

20824C

Figure 7.4.5 **The Microstructure of HT-9 Produced by a Treatment of 1038°C/5 min/AC + 740°C/30 sec/AC:**

a) Precipitation along a prior austenite grain boundary.

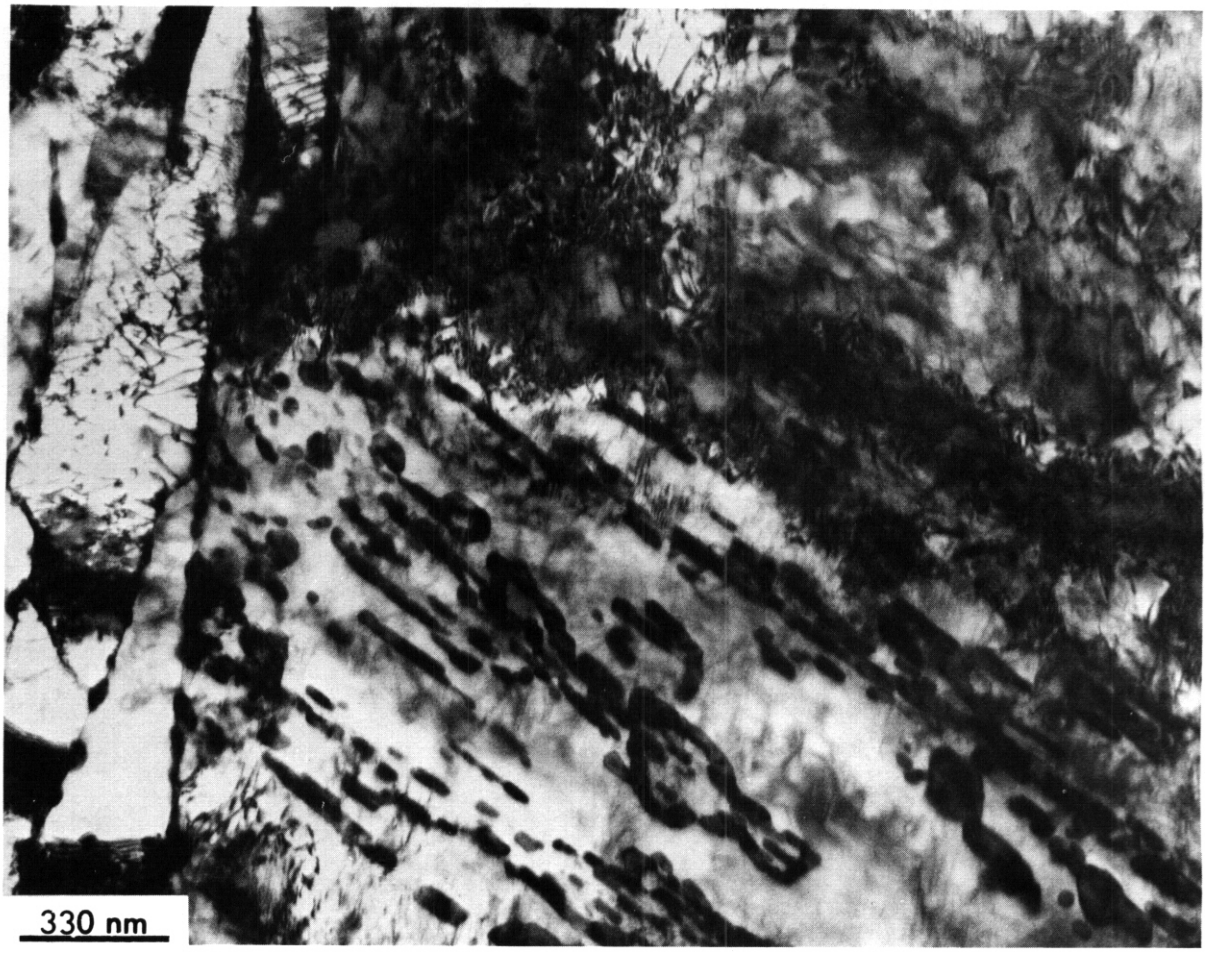

20823B

Figure 7.4.5 The Microstructure of HT-9 Produced by a Treatment of 1038°C/5 min/AC + 740°C/30 sec/AC:

b) Precipitation within a lath.

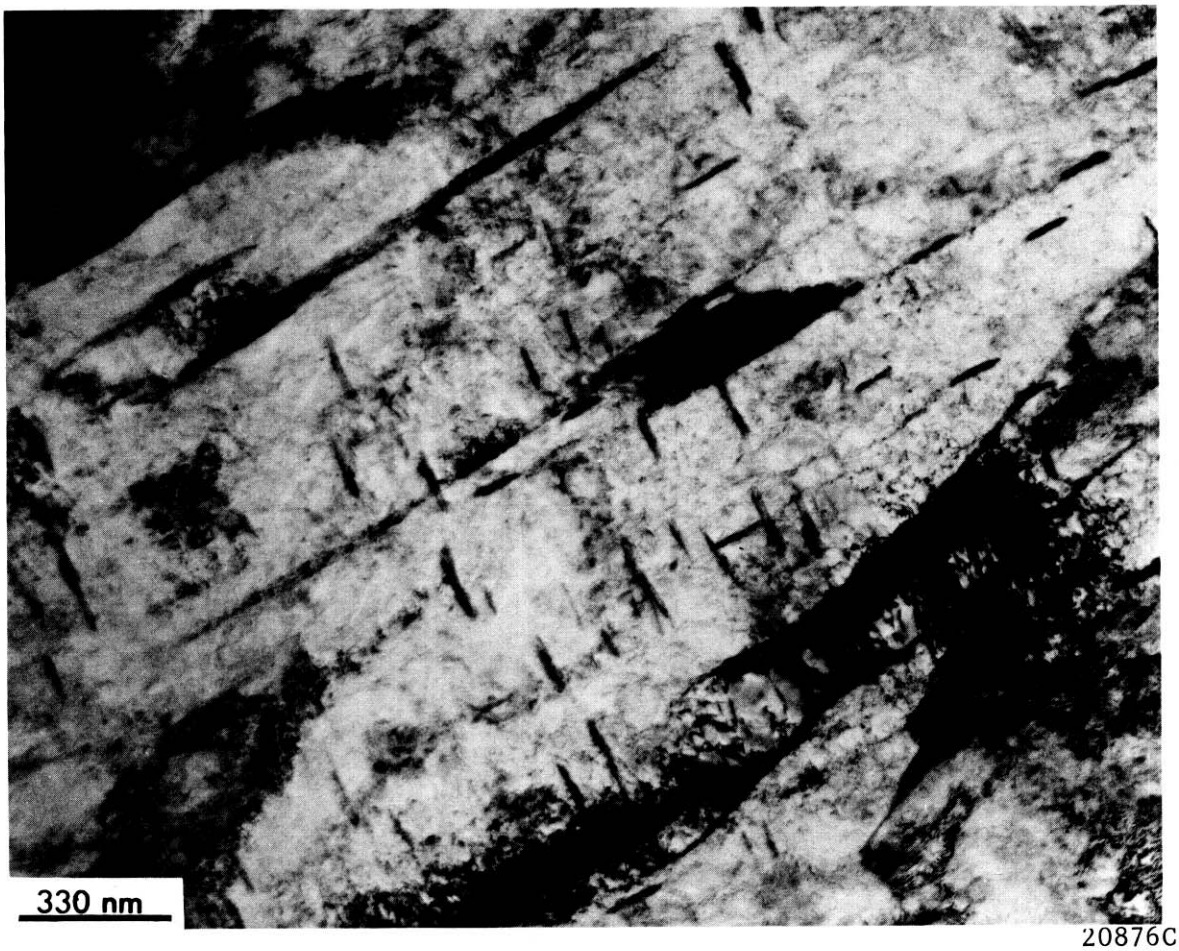

20876C

Figure 7.4.6 The Microstructure of HT-9 After a Treatment of 1038°C/ 5 min/AC + 500°C/7 hr/AC:

a) Rod shaped precipitates within martensite laths.

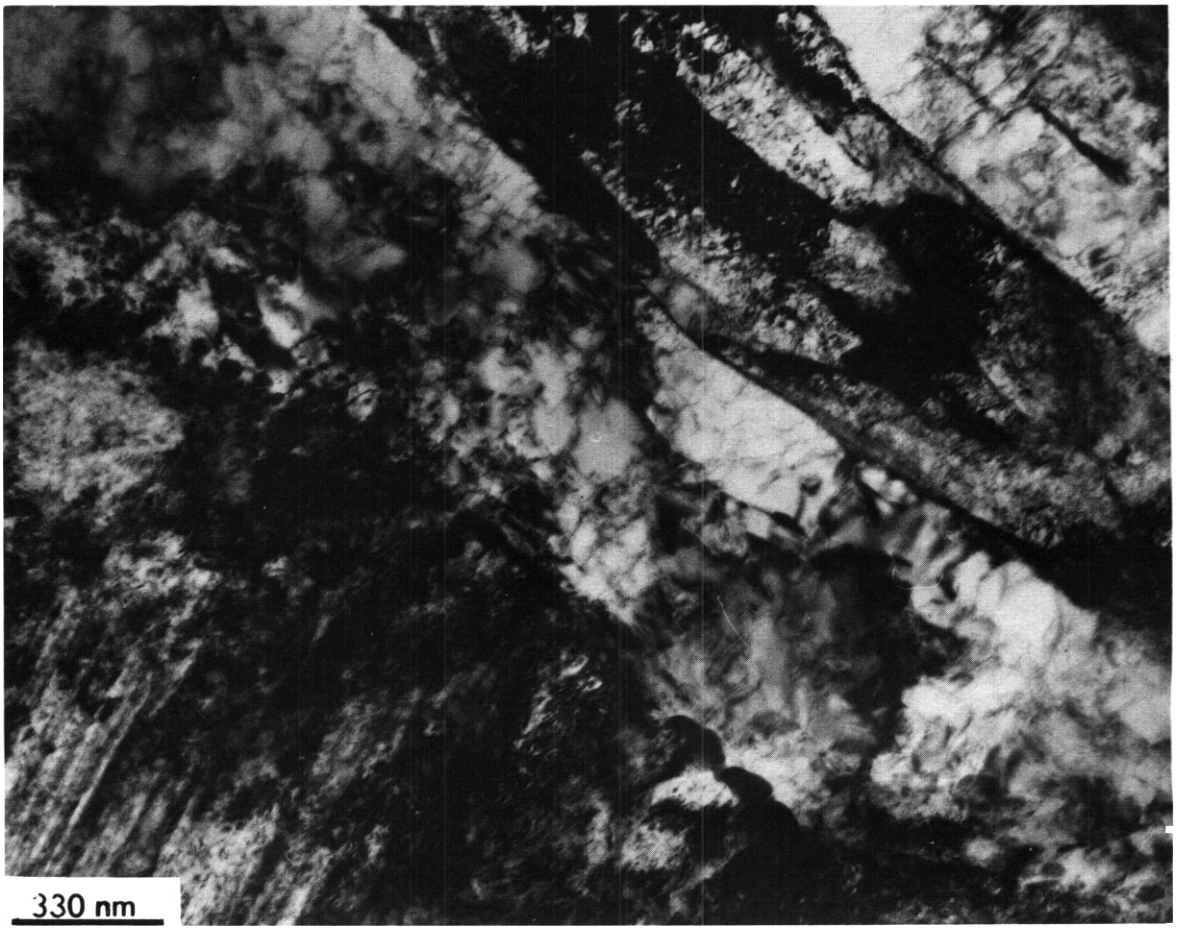

20875A

Figure *7.4.6* The Microstructure of HT-9 After a Treatment of 1038°C/5 min/AC + 500°C/7 hr/AC:

b) Globular precipitates within a prior austenite grain boundary.

TABLE 7.4.3

TEMPERING OPTIMIZATION

Heat Treatment	Prior Austenite Grain Size, mm (ASTM #)	Micro-Hardness (DPH)
1050°C/0.5 hr/AC + 780°C/2.5 hr/AC	0.030 (#7)	222
1038°C/5 min/AC + 760°C/0.5 hr/AC	0.022 - 0.016 (#8-9)	246
1038°C/5 min/AC + 760°C/2.5 hr/AC	0.022 (#8)	242
1038°C/5 min/AC + 780°C/2.5 hr/AC	0.022 - 0.016 (#8-9)	227

maintained an ASTM grain size between 7 and 9. Microhardness results show that there was no difference between tempering at 760°C for 0.5 hours and 2.5 hours. The same can be said for tempering at 780°C. The 780°C treatment over-tempered the structure slightly more than the 760°C treatment.

Grain size variation was the only difference between the four conditions observed by optical microscopy. Aside from this, the microstructures were all similar, consisting of martensite laths enclosed in prior austenite grains (Figure 7.4.7). This is indicative of the HT-9 microstructure, since TEM must be used to observe the effects of tempering.

The microstructure produced by a treatment of 1038°C/5 min/AC + 760°C/0.5 hr/AC is illustrated in Figure 7.4.8. Extensive carbide precipitation occurred along the lath and prior austenite grain boundaries. Precipitation also occurred within the laths. The dislocation structure recovered into networks. This microstructure is typical of all four of the heat treatments tested.

Results from the fatigue crack growth tests conducted at 25 and 600°C are presented in Figures 7.4.9 and 7.4.10. At both temperatures there was no significant difference between the crack growth behavior of the four conditions. All data fell within an experimentally acceptable error band of 3.8 derived from the reproducibility of crack growth tests. Crack growth was an order-of-magnitude higher at 600°C in helium than at 25°C in air (Figure 7.4.11). At 425°C HT-9, in a 1050°C/0.5 hr/AC + 780°C/2.5 hr/AC condition, exhibited a significantly lower crack growth rate

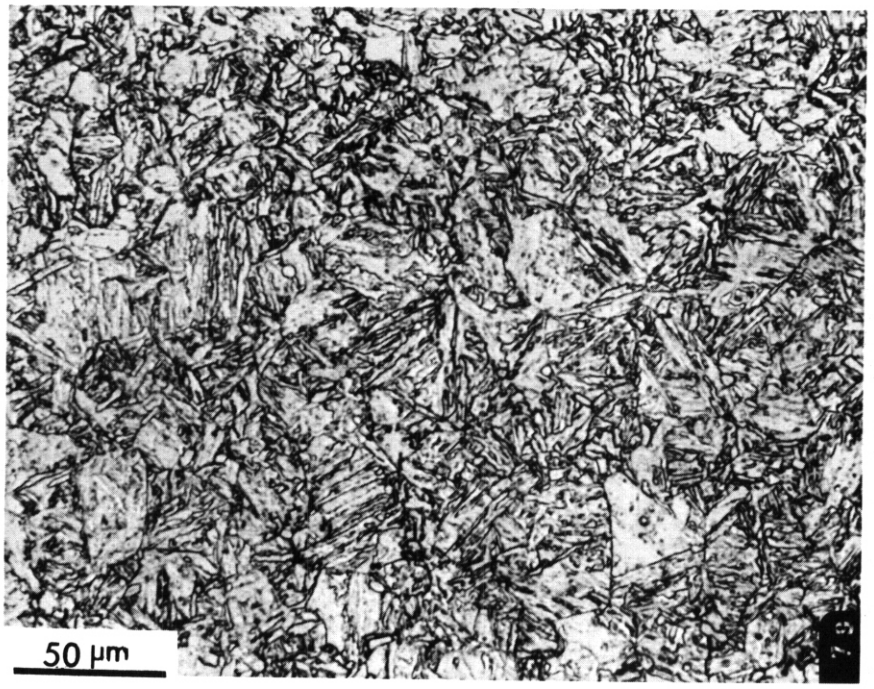

Figure *7.4.7* €IT–9 **Microstructure by Optical Microscopy:**

a) 1038°C/5 min/AC + 780°C/2.5 hr/AC, **Grain Size 8-9.**

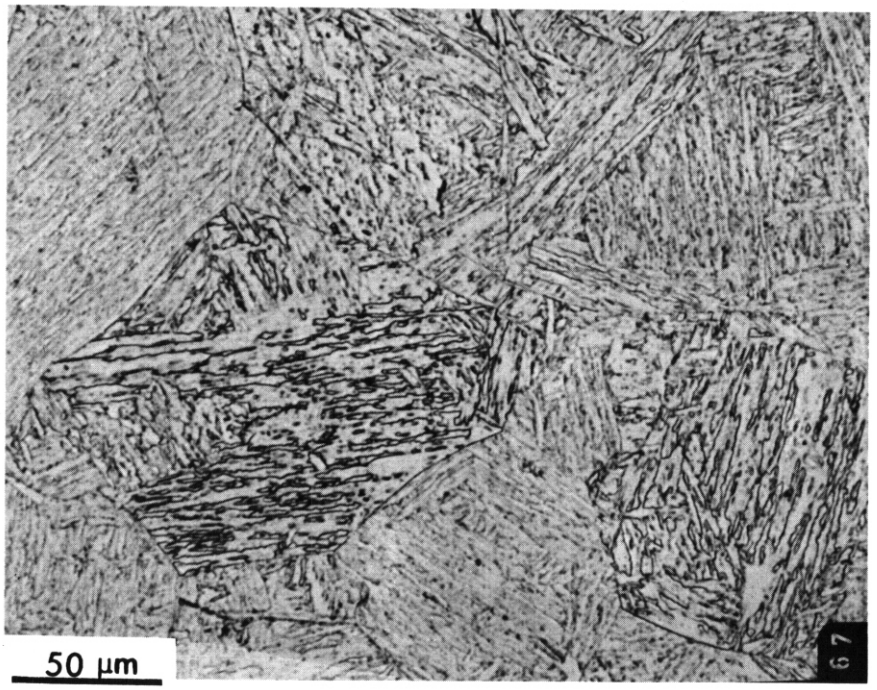

b) 1038°C/2.5 hr/AC + 780°C/2.5 hr/AC, **to show grain structure.**

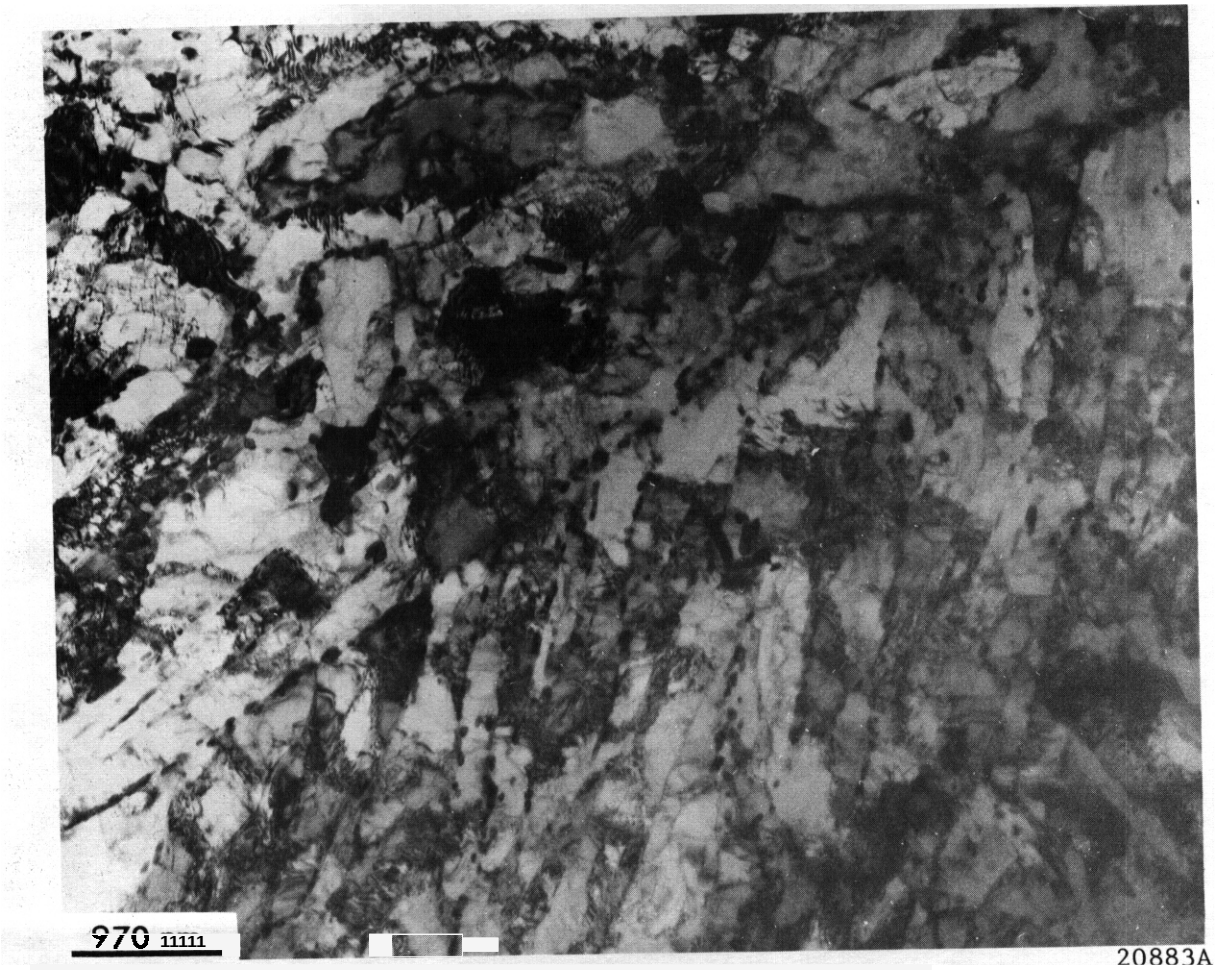

Figure 7.4.8 The Microstructure of HT-9 Produced by a Treatment of 1038°C/5 min/AC + 760°C/0.5 hr/AC:

a) General microstructure.

Figure *7.4.8* **The Microstructure of HT-9 Produced by a Treatment of** 1038°C/5 min/AC + 760°C/0.5 hr/AC:

b) **Dislocation structure.**

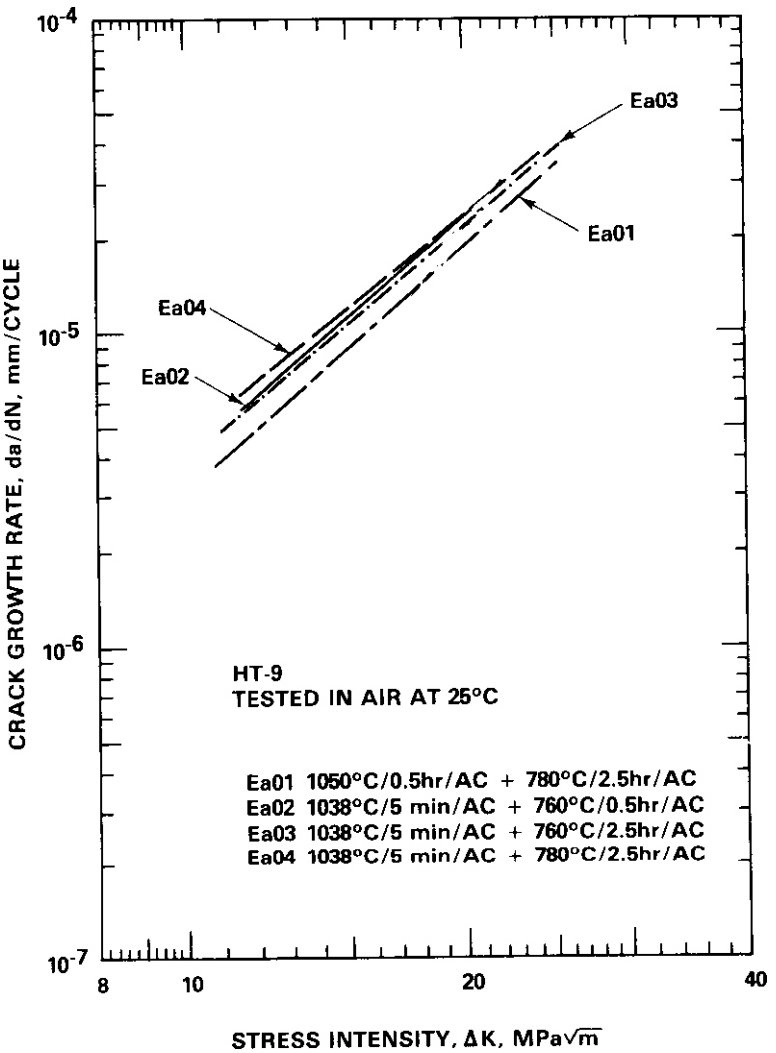

Figure *7.4.9* **Crack Growth Comparison of Treatments,** 25°C **Test.**

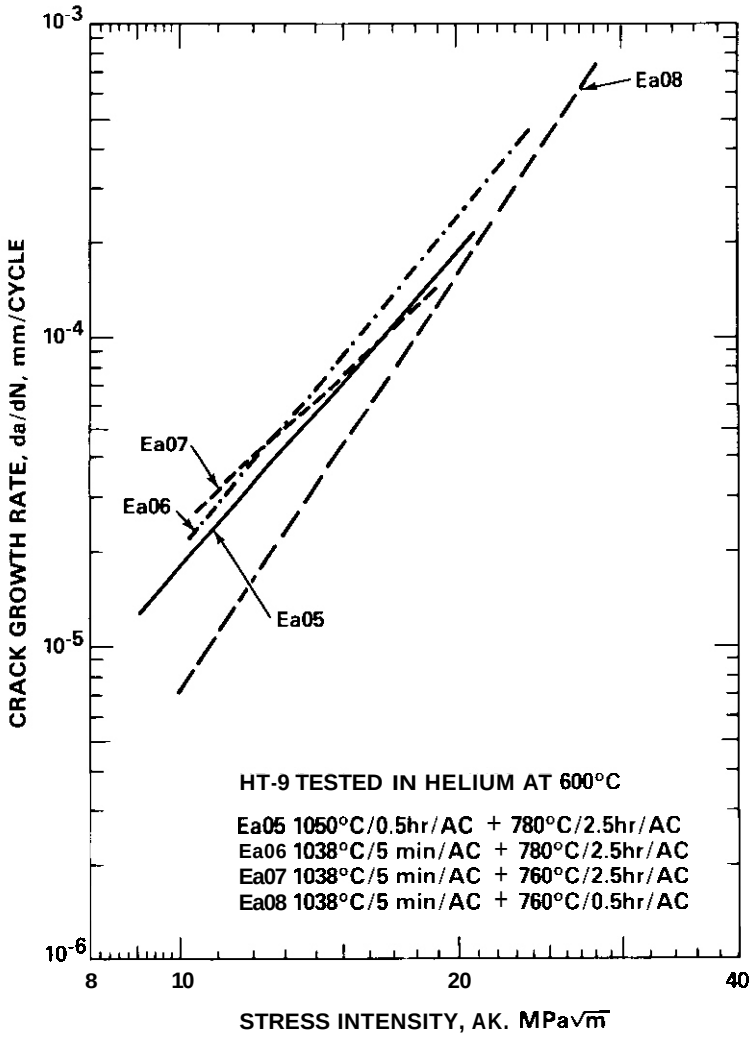

Figure 7.4.10 Crack Growth Comparison of Treatments, 600°C Test.

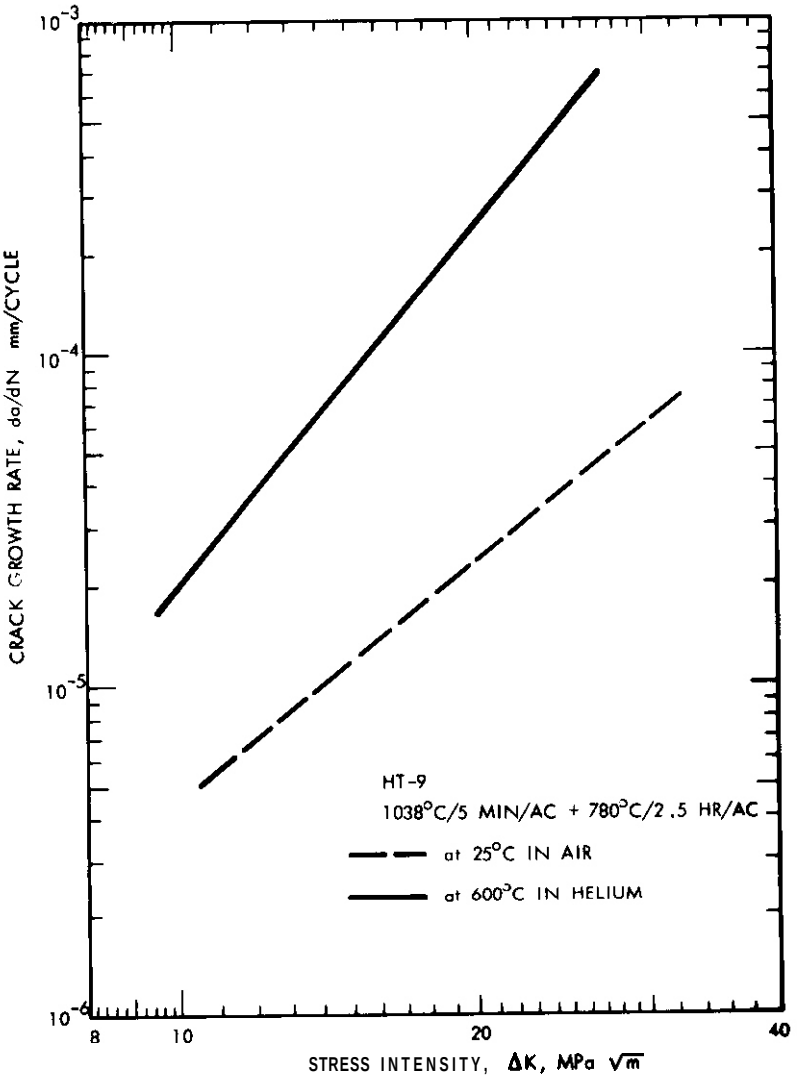

Figure 7.4.11 Comparison of Crack Growth at 25°C vs. 600°C.

than 20% CW 316 SS tested under similar conditions (Figure 7.4.12). Crack growth was also lower than 9Cr 1Mo steel. The fracture toughness behavior of these four conditions at 25°C was also similar (Figure 7.4.13).

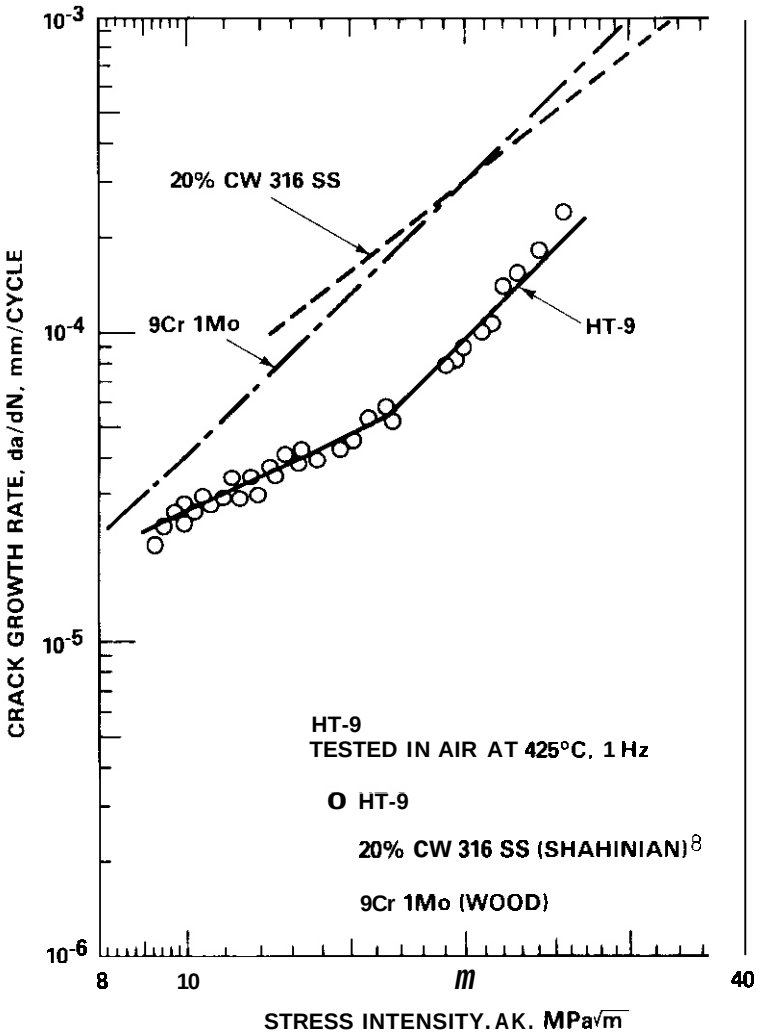

Figure 7.4.12 HT-9 Crack Growth Compared with 9Cr 1Mo and 20% CW 316 SS.

The crack growth, fracture toughness and tempering response of the four conditions was the same. Since the structure was slightly more over-tempered than at 760°C, a 780°C tempering treatment was chosen.

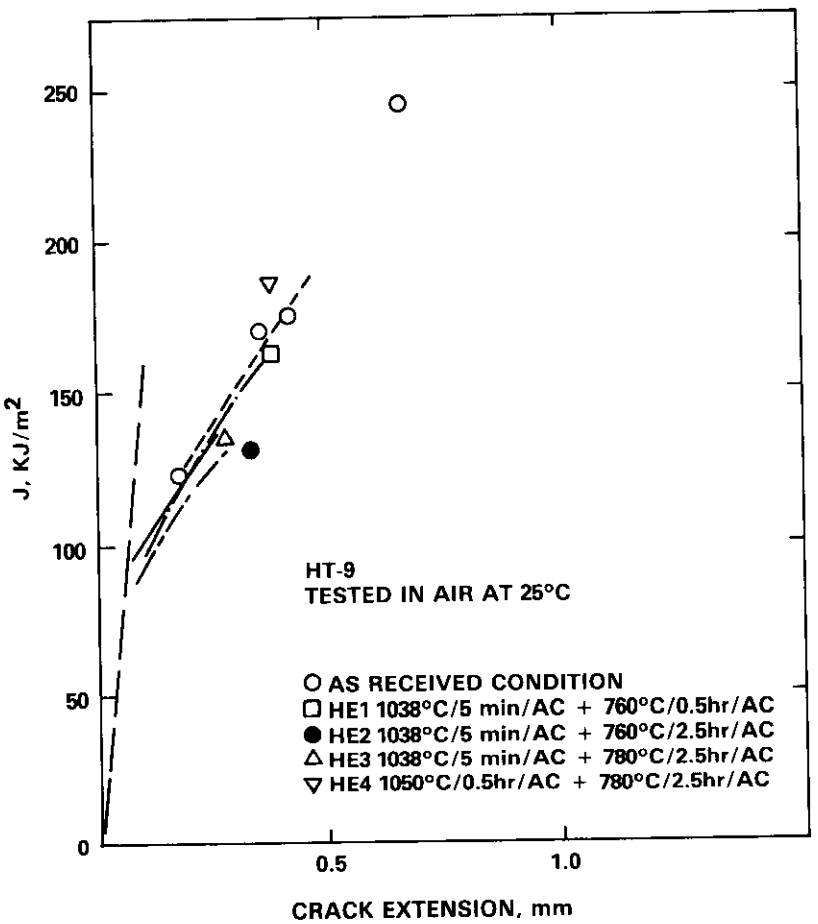

Figure 7.4.13 Fracture Toughness Comparison of Treatments at 25°C

7.4.5 Conclusion

1. An austenitizing and tempering treatment of 1038°C/5 min/AC + 780°C/2.5 hr/AC has been chosen for 0.30 to 2.54 mm thick HT-9.

2. Microstructural characteristics of four solution annealed and tempered conditions of BT-9 have been identified. The structures consist of lath martensite enclosed in fine prior austenite grains with carbide precipitates within the laths and along the lath and grain boundaries.

3. At 25°C and 600°C the fatigue crack growth resistance of the four conditions is the samek there is no difference in the fracture toughness behavior at 25°C.

4. An order-of-magnitude increases in the fatigue crack growth rate occurs going from 25°C to 600°C.

5. HT-9 exhibited higher crack growth resistance than 20% CW 316 SS and 9CR 1MO steel at 425°C in air.

6. A tempering curve for HT-9 has been constructed.

7.4.6 Future Work

A baseline study on nonirradiated HT-9 in a solution annealed and tempered condition, 1038°C/5 min/AC + 780°C/2.5 hr/AC, will be completed. These results will be compared with data generated for other Path E alloys, 9Cr 1Mo and 2-1/4Cr 1Mo Steel.

7.4.7 References

1. J. Erler, A. Maillard, G. Brun, J. Lehmann and J. M. Dupouy, "The Behavior of Ferritic Steels Under Irradiation with Fast Neutrons," *Proceedings of the Conference on Irradiation Behavior of Metallic Materials for Fast Reactor Core Components, June 5, 1979.*

2. E. A. Little, D. R. Harries, F. B. Pickering and S. R. Keown, "Effects of Heat Treatment on Structure and Properties of 12% Cr Steels," *Metals Technology, April 1977.*

3. D. A. Mervyn, M. M. Paxon and A. M. Ermi, "Development of the Miniature Fatigue Crack Growth Machine," *ADIP Quarterly Progress Report, September 30, 1979.*

4. F. H. Huang, B. A. Chin and G. L. Wire, "Application of the Electrical potential Technique to J-Integral Measurements," *ADIP Quarterly Progress Report, September 30, 1979.*

5. D. T. Peterson, private communication.

6. E. A. Little, D. R. Harries, and F. B. Pickering, "Some Aspects of the Structure-Property Relationships in 12%Cr Steels," *Ferritic Steels for Fast Reactor Stem Generators,* BNES, London, 1978.

7. Sandvik, Sandviken, Sweden.

8. P. Shahinian, "Crack Propagation in Cold-Worked Austenitic Stainless Steel at Elevated Temperatures," *Nuclear Technology, Vol. 38, May 1978.*

7.5 FRACTURE TOUGHNESS TESTS ON HT-9 AT ELEVATED TEMPERATURES – F. H. Huang and G. L. Wire (Hanford Engineering Development Laboratory)

7.5.1 ADIP Task

Task Number 1.B.5.1 - Develop Specimens and Test Methods.

7.5.2 Objective

The objective of this work is to evaluate the elevated temperature fracture toughness of HT-9 using the electropotential technique. In addition, the tests provide useful control information for future characterization of irradiation on fracture behavior of fusion first wall materials.

7.5.3 Summary

Single specimen J-integral fracture toughness measurements were made at 149°C and 232°C on HT-9 specimens. The electropotential technique developed in past work was applied for elevated temperature tests to obtain a calibration curve correlating voltage change to crack extension. Based on this calibration curve, the J versus Aa curves were generated from single specimens. The test results show that the electropotential technique for single specimen measurements is successful at elevated temperatures, where temperature gradients are of concern. The upper shelf fracture toughness of HT-9 is evaluated as a function of temperature.

7.5.4 Progress and Status

7.5.4.1 Experimental Technique

Details of the test apparatus and test procedures were described in References 1 and 2. Circular compact tension specimens were fabricated from as received HT-9 bar stock, the schematic diagram of the specimens is shown in Fig. 7.5.1(a). A servo-hydraulic MTS system was used to pre-crack the specimens to 1.3 mm, below a stress intensity factor of 28 Mpa $\sqrt{m}$. The tests were performed at 149°C and 232°C in an argon environment. The positions of the current input and potential measurement leads are shown in Fig 7.5.1(b). A constant DC current of 13.5 amps was applied.

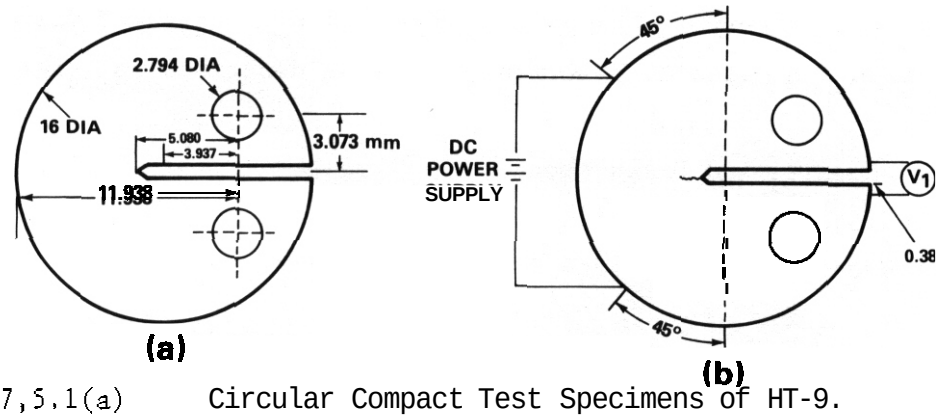

Figure 7.5.1(a) Circular Compact Test Specimens of HT-9.

Figure 7.5.1(b) Schematic Drawing of Electropotential Technique.

The voltage V_1 changes as a result of crack propagation and was measured using a microvoltmeter.

Continuous crack extensions were measured through a calibration curve which was obtained from the measurements of potential changes and their corresponding crack extensions revealed by heat tinting (Figure 7.5.2).

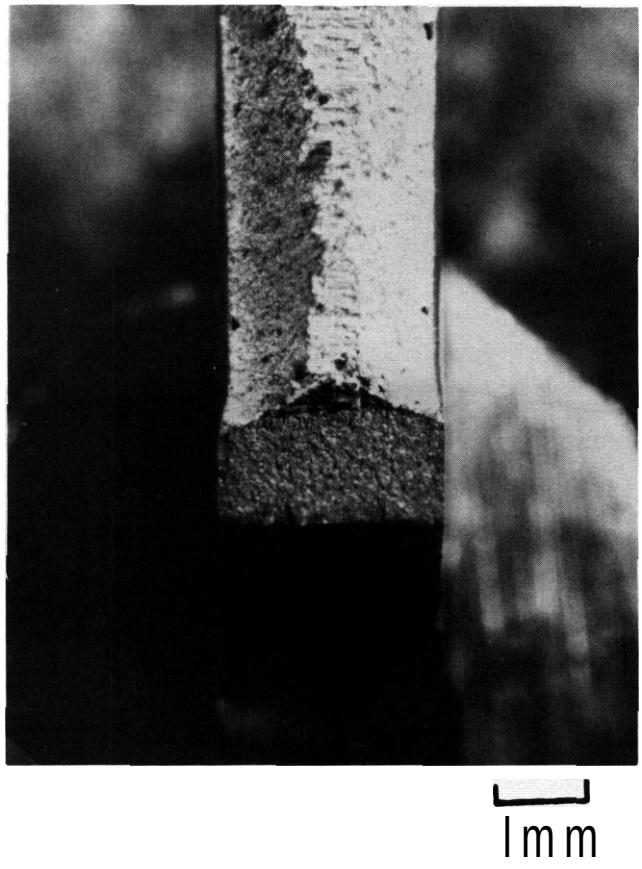

Figure 7.5.2 Crack Extension as Revealed by Heat Tinting for HT-9.

The J versus Δa curves were generated by calculating the J values from load versus load-line displacement curves as described in Reference 2.

7.5.4.2 Results and Discussions

The load and potential change versus load-line displacement for HT-9 specimens tested at 149°C and 232°C were plotted in Figures 7.5.3 and 7.5.4.

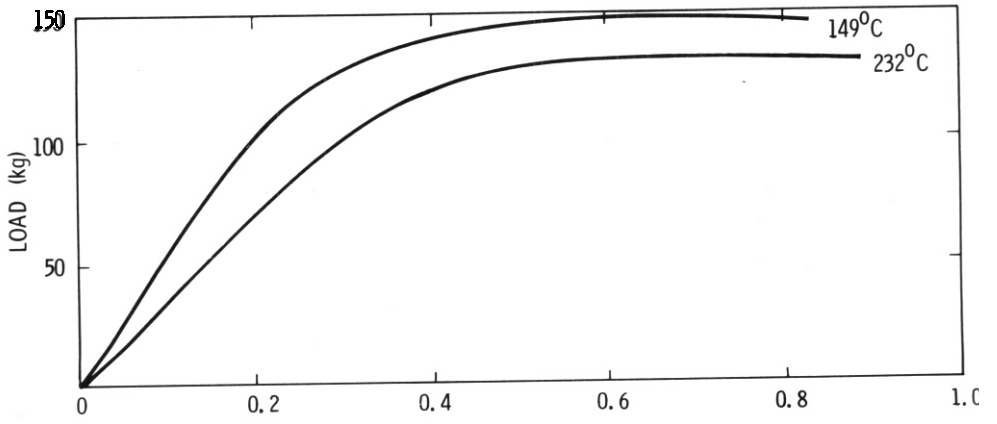

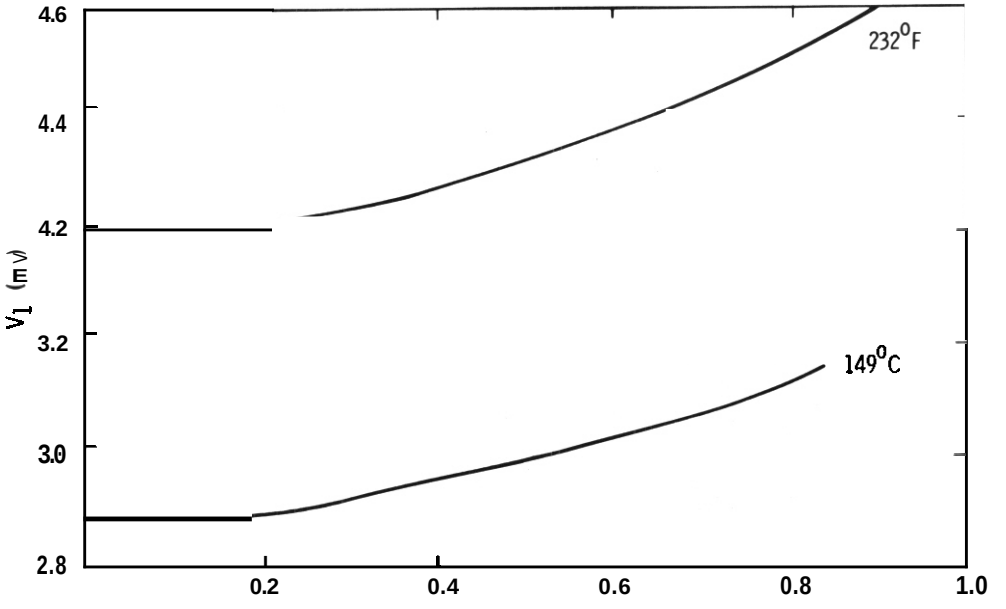

The potential changes and the corresponding crack extensions were plotted in Figure 7.5.5, where V_{10} is the voltage measured before the specimen was loaded. Figures 7.5.6 and 7.5.7 show the J versus Aa curves obtained via the electropotential calibration curve. Also plotted in the figures were J versus Δa data points measured by the multiple specimen method. As can be seen from these figures, they are in good agreement.

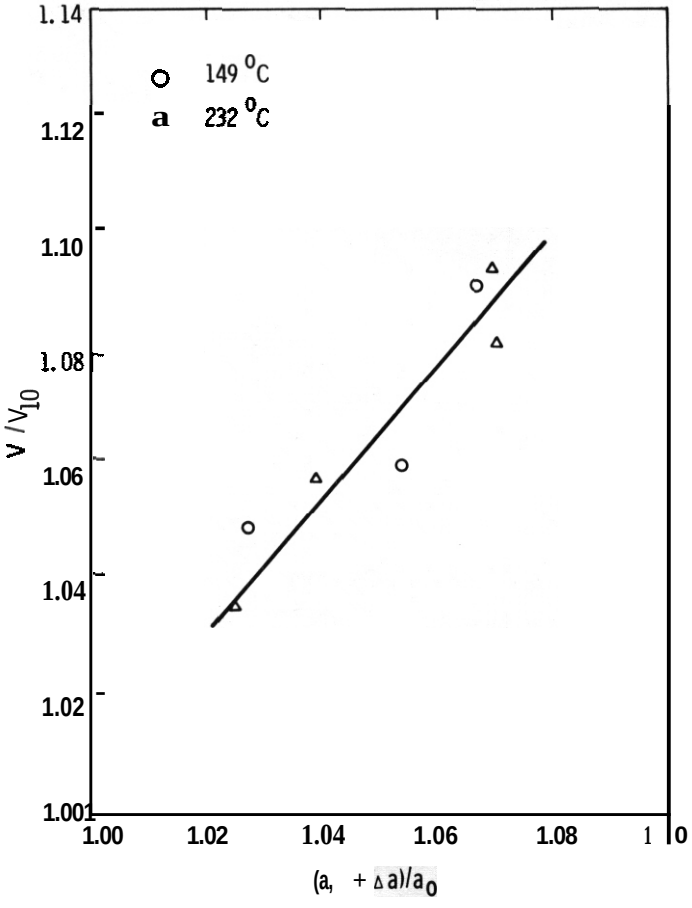

Figure 7.5.5 Electrical Potential Calibration Curve for HT-9.

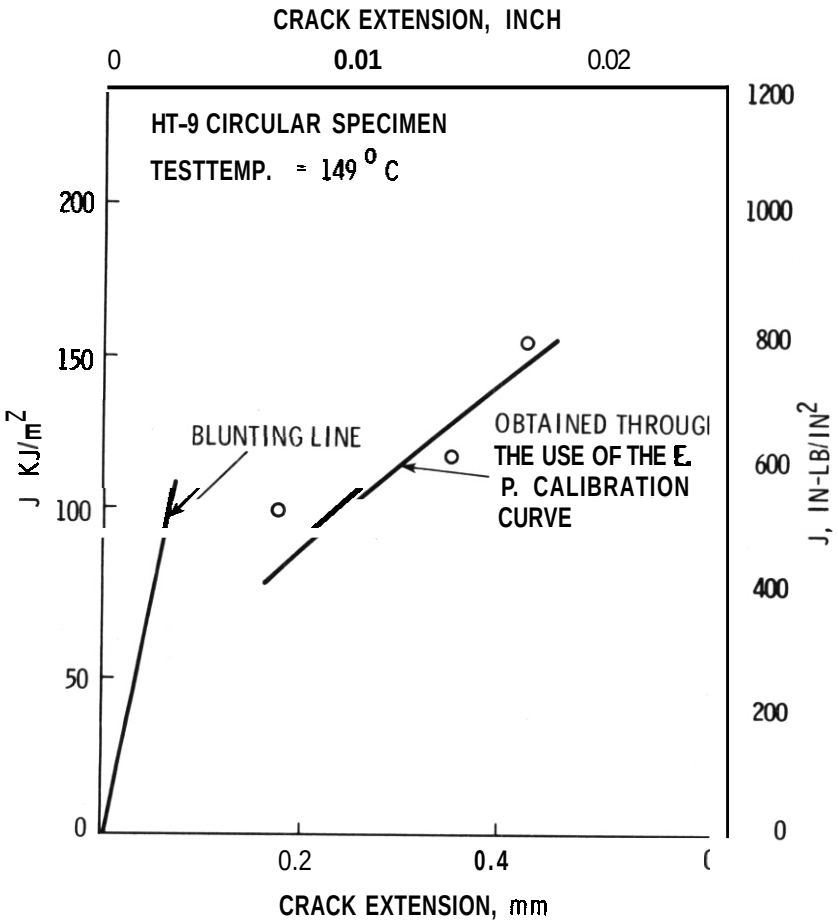

Figure 7.5.6 J Versus Δa Tested at 149°C for HT-9.

The fracture mode of ferritic steels is known to change from cleavage to a ductile tearing mode as the temperature is increased from below 0°C. In general, the value of toughness increases to a maximum and drops off as the test temperature increases. The temperature dependence of ductile fracture toughness3 (J_{1c}) for HT-9 is shown in Figure 7.5.8. It should be noted that there is no general trend for this upper shelf toughness curve; higher temperature toughness values cannot be extrapolated.

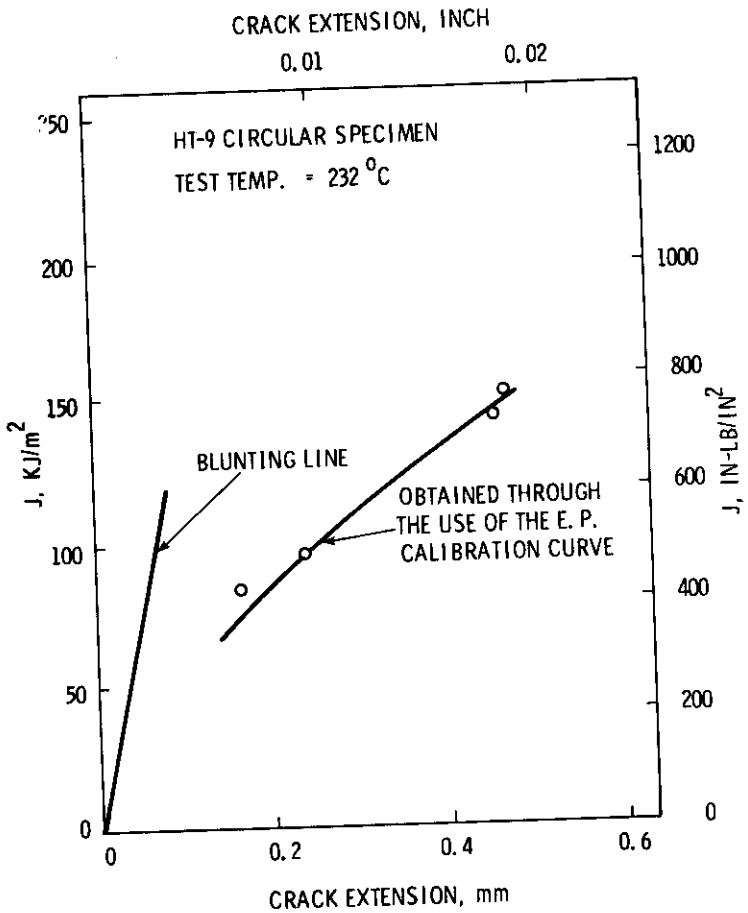

Figure 7.5.7 J Versus Δa Tested at 232°C for HT-9.

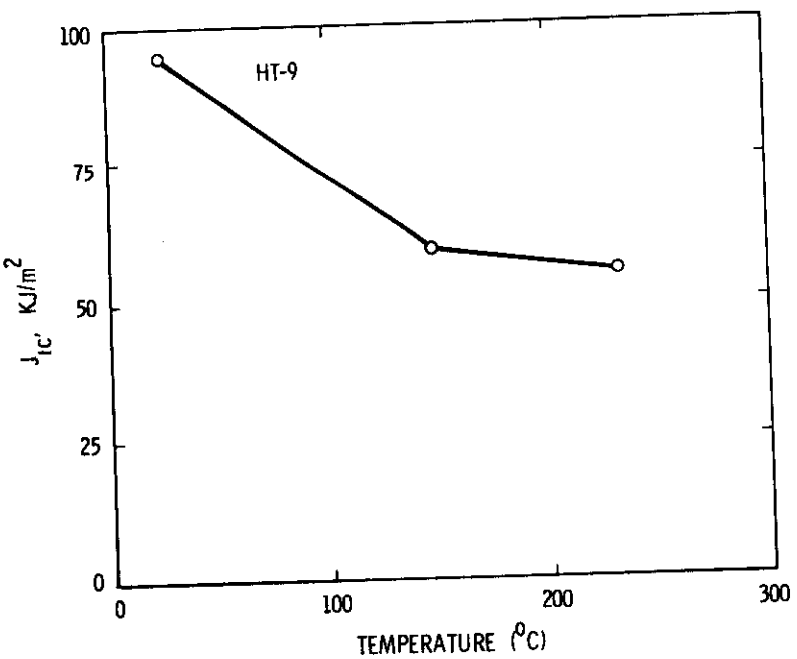

Figure 7.5.8 Temperature Dependence of Fracture Toughness for HT-9.

7.5.5 Conclusions

It is concluded that:

1. The single specimen technique using electropotential crack extension measurements has been successfully demonstrated at high temperature.

2. The upper shelf toughness of HT-9 decreases as temperature is increased from room temperature to 250°C.

7.5.6 Future Work

Fracture toughness tests will be performed at 315°C, 427°C and 539°C. Larger specimens will be tested to assess thickness effects at high temperature. A variety of ferritic composition and thermomechanical treatments will be studied.

7.5.7 References

1. F. H. Huang, B. A. Chin and G. L. Wire, "Application of the Electropotential Technique to J-Integral Measurements," *ADP Quarterly Progress Report, June-September 1979.*

2. F. H. Huang and G. L. Wire, "Initial Test Results on Miniature Compact Tension Fracture Toughness Specimen," *ADIP Quarterly Progress Report, September-December 1979.*

3. J. D. Landers and J. A. Begley, "Test Results from J-Integral Studies: An Attempt to Establish a J_{1c} Testing Procedure", *ASTM, STP* 560, pp. 170, 1974.

7.6 THE FRACTURE RESISTANCE OF HT-9 AFTER IRRADIATION AT ELEVATED TEMPERATURE -- F. A. Smidt, Jr., J. R. Hawthorne, and V. Provenzano[1] (Naval Research Laboratory, Washington D. C.)

7.6.1 ADIP Task

ADIP tasks are not defined for ferritic stainless steels in the 1978 Program Plan.

7.6.2 Objective

The objective of this study is to examine the effect of elevated temperature neutron irradiation on the fracture resistance of the ferritic stainless steel HT-9.

7.6.3 Summary

HT-9, a 12 percent Cr martensitic stainless steel of interest for use in ducts for fast reactors and as a first wall material in magnetic fusion reactors, was irradiated in EBR-II to obtain the first evaluation of fracture toughness changes produced by high temperature-high fluence irradiation in this class of alloy.

Charpy-V notch, precracked Charpy and tensile specimens were used to evaluate the tensile and fracture behavior of this steel in the as-received condition, after 5000 h of aging at 427 and at 538°C and after irradiation to a fluence of 1.1 x 10^{22} n/cm^2 E > 0.1 MeV at 419°C in flowing sodium. The results show some tendency toward temper embrittlement at 538°C and a 108°C shift in the ductile-to-brittle transition after irradiation at 419°C. Charpy-V energies on the upper shelf are also depressed by the irradiation but maintain adequate levels for the applications intended. Possible mechanisms for the observed response are discussed.

7.6.4. Progress and Status

7.6.4.1. Introduction

HT-9 is a martensitic stainless steel which is currently being

---

[1]Current address: Tracor. Inc., Rockville, Maryland

evaluated for duct applications in liquid metal fast breeder reactors in the U. S. Cladding/Duct Alloy Development Program of the Department of Energy (DOE) and for first wall applications in magnetic fusion reactors in the U.S. Magnetic Fusion Materials program of DOE. HT-9 has exhibited excellent swelling resistance in ion bombardment' and neutron irradiation experiments[2], as Well as low irradiation creep rates[3]. The Cr, Mo, and V alloy additions to this alloy provide adequate resistance to over-aging at temperatures up to 600°C. One property which has not been explored in detail is fracture toughness and its change after elevated temperature irradiation to neutron fluences in the 10^{22} to 10^{23} n/cm^2 range. This paper describes the initial evaluation of fracture toughness of HT-9 after irradiation in the EBR-II reactor to a fluence of 1.1 x 10^{22} n/cm^2 E > 0.1 MeV at a temperature of 420°C. The experimental investigation included standard Charpy-V (C_v) tests for notch ductility, fatigue precracked Charpy-V (PCC_v) tests for dynamic fracture toughness (K_J), tensile tests, SEM examinations of the fracture surfaces and a TEM examination of the microstructure.

7.6.4.2. Experimental Methods

7.6.4.2.1 Material. The HT-9 used in these experiments was produced by Carpenter Technology Corporation (Heat No. 91354). The material was supplied to NRL from DOE inventory at Hanford Engineering Development Laboratory in the form of 3.3-cm (1.3-in.) diameter rod stock. Chemical composition in weight percent as supplied by the vendor is as follows: 0.21 C, 0.50 Mn, 0.04 Cu, 0.58 Ni, 12.09 Cr, 1.02 Mo, 0.21 Si, 0.33 V, 0.008 P, 0.003 S, 0.035 Al, 0.54 W, 0.004 N, and balance Fe. The heat treatment consisted of a solution anneal at 1050°C (1922°F) for one-half hour followed by air cooling and tempering at 780°C (1436°F) for two and one-half hours followed by air cooling. The heat treatment is representative of commecial practice for high temperature service although the tempering temperature is somewhat above the range normally used for 12 percent chromium alloys (550 to 700°C, 1022 to 1292°F). The microstructure produced by this heat treatment is shown in the scanning electron microscope (SEM) micrographs of a polished surface etched for one min in Villela's reagent (5 ml HCl, 1 g picric acid, 100 ml ethanol),

Figs. la and lb.

Figure la shows prior austenite grains of approximately 20 μm in size which are outlined more heavily by precipitates than the other features and enclose regions where the elongated martensite laths are aligned along a common direction. HT-9 forms martensite upon cooling from 1050°C but the martensite largely decomposes to polygonized ferrite and carbides during tempering at 780°C. The ferrite grains are 0.5 to 1.5 μm wide by 5 to 10 μm long with a few precipitate-free grains, 2 μm by 5 μm, which appear to have recrystallized. The precipitate structure is more readily visible in Fig. lb where it can be seen that most precipitates lie along ferrite grain boundaries and prior austenite grain boundaries. The material was evaluated in the folowing conditions: as-received material, material aged for 5000 h in air at temperatures of 427 and 538°C, and on the specimens irradiated in EBR-II to a fluence of 1.1 x 10^{22} n/cm^2 at a temperature of 419°C.

7.6.4.2.2 Specimen and Test Procedures. The Charpy-V specimens used for the investigation were ASTM Type A[4] (10 mm x 10 mm x 55 mm with a 45°, 2-mm deep notch). The specimens were tested in a Testing Machine, Inc., remotized impact tester (298J capacity) calibrated against Army Materials and Mechanics Research Center specimen standards[4]. Specimen thermal conditioning was accomplished in controlled temperature liquid baths or a furnace.

Fracture toughness (K_J) determinations were made with PCC_v specimens which were fatigue precracked at a/W ratios of 0.5 prior to irradiation. The maximum K_f level for the last 0.76 mm of fatigue crack growth was 22 MPa $\sqrt{m}$ or less. J-integral assessment procedures were used for K_J determinations and employed energy absorbed to maximum load corrected for specimen and test machine compliance for the calculations. EPRI requirements for K_J determinations were satisfied[5]. Test temperatures were selected to assess the fracture toughness in the C_v transition and at C_v upper shelf which included the projected fuel handling temperature for subassemblies in a fast reactor (232°C).

Tensile specimens employed in this experiment were round specimens with a 6.35-mm gage diameter and a 31.8-mm gage length. The overall

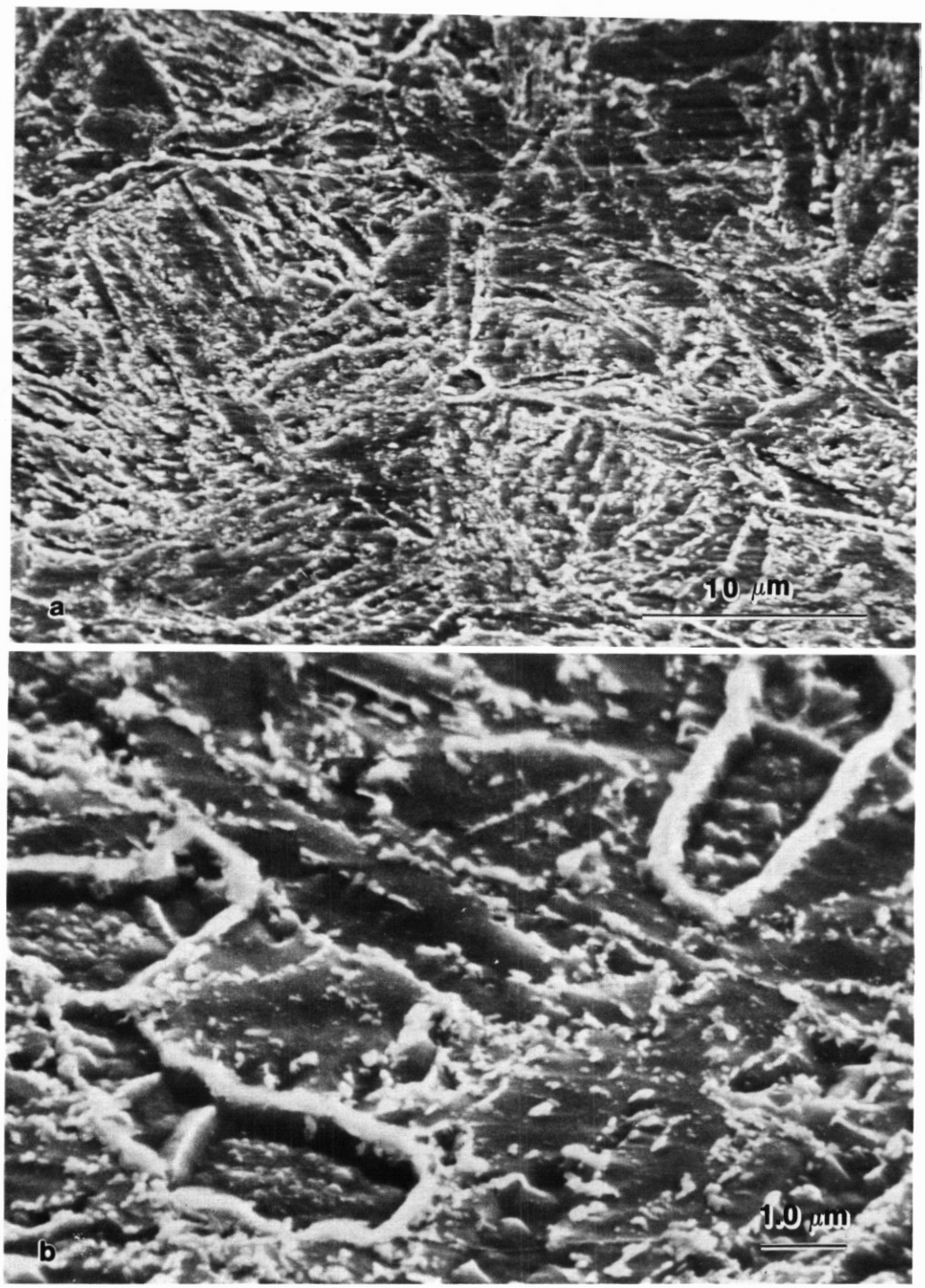

Fig. 7.6.1. SEM micrographs of polished and etched sections of HT-9 in the as-received condition. Figure la shows prior austenite grain boundaries and martensite lath boundaries outlined by carbide precipitates. Figure lb shows the finer precipitation in the matrix. Etched with Villela's reagent for 1 minute.

specimen length was 96.8 mm. Tensile tests were conducted on an Instron tensile tester of 44,480 Newton capacity. The crosshead speed of the tester provided a strain rate in the gage section of 2.7×10^{-4} sec^{-1}. A linear averaging extensometer was employed to monitor specimen strain up to the yield point (0.2 percent offset). The tests were conducted at 25°C and at 232°C to determine the extent of irradiation hardening and degradation of tensile ductilty.

7.6.4.2.3 Irradiation Conditions. The specimens were irradiated in the EBR-II reactor in subassembly X-322, an NRL irradiation assembly of the open type (exposed to flowing sodium). The subassembly resided in position 3E2 during runs 92A through 92C and accumulated 2444 megawatt days (MWD). It was then moved to position 2D1 for runs 93A and B where it accumulated 3028 MWD for a total of 5472 MWD. Total calculated midplane fluence was 1.44×10^{22} n/cm^2. All specimens were located from 7.7 to 13.4 cm below the midplane. Corrections for the axial flux gradient and spectral considerations place the experiment at a fluence of $1.1 \pm 0.1 \times 10^{22}$ n/cm^2 $E > 0.1$ MeV.

Analysis of temperature gradients across the experiment assuming a linear temperature rise across the core from 371 to 501°C would place the specimens at locations of 394 to 414°C. Cross sectional gradients in the specimen produced an additional increase of 9°C in the mean specimen temperature. Irradiation temperature for the experiment is accordingly calculated to be 419°C with ±15°C uncertainty.

7.6.4.3 Experimental Results

The results of C_V tests of the as-received material, material aged 5000 h at 427 and 538°C, and irradiated material are shown in Fig. 2. Charpy energy values for the as-received material ranged from a low of 275 at -40°C to 170J at 566°C with the mid-energy range transition developing at about 5°C and the 40J level at -18°C. Aging for 5000 h at 427°C did not produce any significant change in the ductile-brittle transition or upper shelf energy levels. The 5000 h age at 538°C, however, did produce a substantial elevation of the ductile-brittle transition (39°C for the mid-transition and 33°C for the 40J level) and a

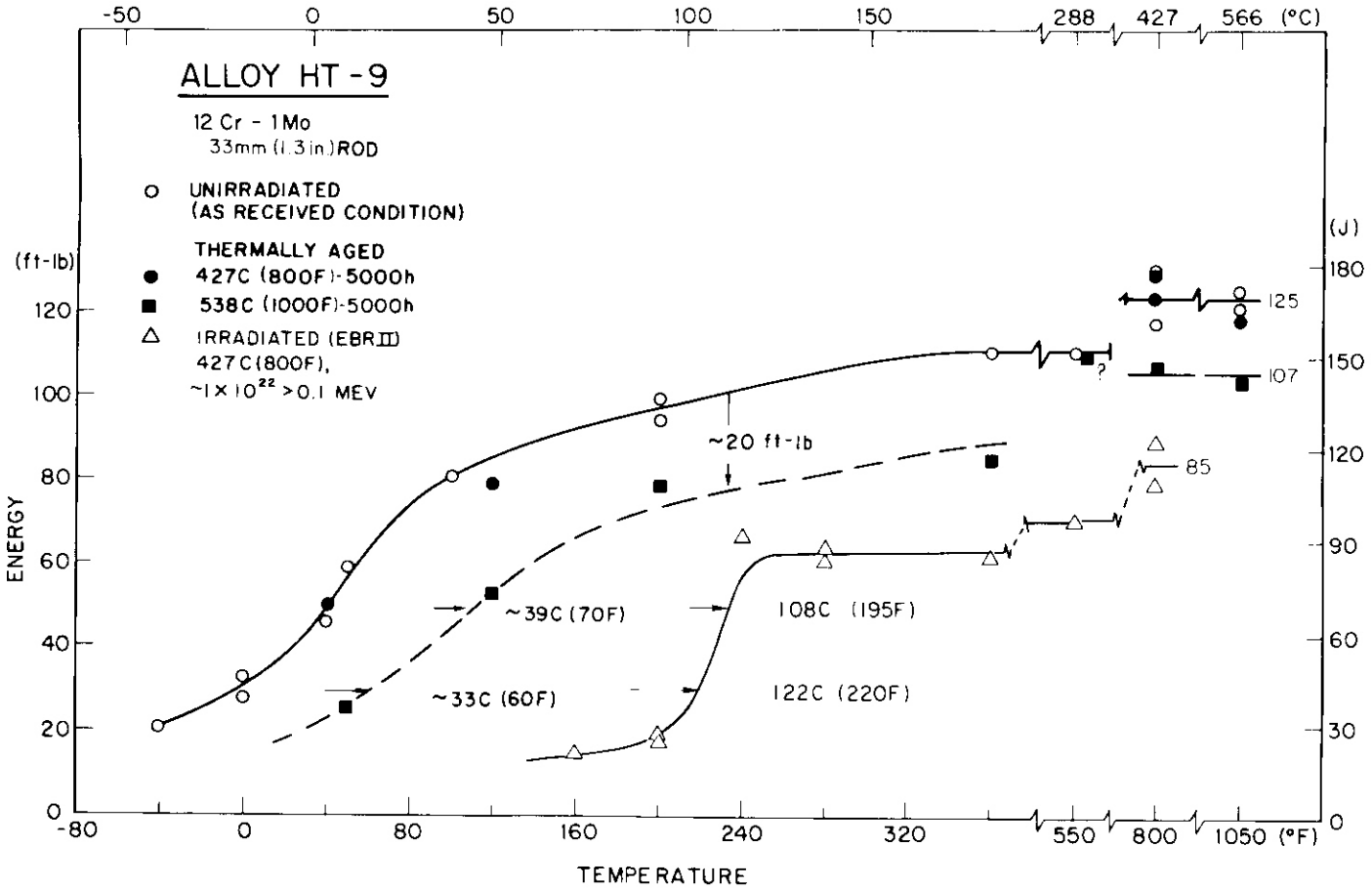

Fig. 7.6.2. Charpy-V energy values as a function of test temperature for HT-9 in the as-received condition, after 5000 h aging at 427°C, after 5000 h aging at 538°C, and after irradiation to a neutron fluence of 1.1×10^{22} n/cm^2 (E 0.1 MeV) at an irradiation temperature of 419°C ±15°C in the EBR-II reactor, Idaho Falls, Idaho.

decrease of 27 J in upper shelf energy.

In view of the 538°C aging results an additional experiment was performed to determine if any recovery of this embrittlement could be produced by a 1 h anneal at 732°C. Three C_v specimens which had been annealed at 538°C for 5000 h were employed in the experiment. Two specimens were annealed at 732°C for 1 h and air cooled: the third was used as a control. The anneal produced no significant change in hardness (Rockwell C 22 vs 23). The three specimens were then tested at 27°C. The control specimen had an energy of 44.55 which fell on the curve for the material aged 5000 h at 538°C but the two annealed specimens exhibited values of 106.6 and 117.5J which fell on the curve for the as-received material. Thus a short-term anneal produced 100 percent recovery of the embrittlement produced by 5000 h aging at 538°C. These results confirm the suspected embrittlement mechanism as temper embrittlement as discussed below.

Irradiation at 419°C to a fluence of 1.1×10^{22} n/cm^2 E > 0.1 MeV caused an elevation in the ductile-brittle transition curve, relative to the as-received material, of 108°C at the midtransition and 122°C at the 40J level to temperatures of 113 and 104°C respectively. The upper shelf energy level dropped by 65J to 88J at 150°C and rose gradually to 115J at 427°C.

TABLE 1 – Summary of tensile test data – HT-9.

Specimen Condition	Test (°C) Temperature	0.2% Y.S. MPa	Ultimate Strength MPa	Uniform Elongation %	Total Elongation %	Reduction in Area %
As received	25	653	823	7.5	16.4	60.5
As received	232	575	714	4.6	12.4	63.8
5000 h/538°C	25	626	821	10.1	18.6	56.1
5000 h/427°C	25	565	767	13.8	22.9	63.6
1.1×10^{22} n/cm^2/419°C	25	971	1037	6.3	13.9	

($\dot{\epsilon} = 2.7 \times 10^{-4}$ sec^{-1}

Tensile test data are summarized in Table 1 for the conditions tested. The largest change in tensile properties produced by the irradiation was an increase in yield strength at 25°C of 318 MPa. Only slight decrease in yield strength and an increase in elongation which gave no hint of the shift in transition temperature observed in the Charpy tests. A 4.4 percent decrease in reduction of area was observed however.

Fracture toughness values obtained from the PCC_V tests are summarized in Table 2. Test temperatures were selected to provide an indication of fracture resistance near the toe of the C_V transition in the irradiated specimens and on the upper shelf of the Charpy energy curve (Fig. 2). The K_{Jd} values cited in Table 2 were calculated using the general relationship

$$K_{Jd} = \left[\frac{E\, J_{Id}}{1 - \nu^2}\right]^{1/2}$$

where E is the elastic modulus, ν is Poisson's ratio, and

$$J_{Id} = \frac{2A}{Bb}$$

where A is the area under the load deflection curve up to the point of maximum load, B is the specimen thickness, and b is the unbroken ligament. The data clearly indicate a fracture toughness transition corresponding approximately to the C_V energy transition with temperature. The transition to higher toughness occurs below the projected fuel handling temperature.

TABLE 2 - Fracture toughness values from dynamic precracked Charpy specimens (K_{Jd} MPa$\sqrt{m}$)

Test Temp. °C	Material Conditions			
		5000 h age at		
	Unirradiated	427°C	538°C	Irradiated
24	207 (shelf)			
93				43, 47 (toe)
149				161, 119 (shelf)
427	257, 289 (shelf)	280, 285 (shelf)	220, 2E6 (shelf)	113, 220 (shelf)
538	271, 211 (shelf)			

SEM examination of the fracture surfaces of the broken Charpy specimens revealed the usual change in fracture mode from cleavage in the toe region of the C_v curve, to mixed cleavage and ductile rupture in the transition region, and to ductile rupture on the C_v upper shelf. The principle fracture surface features in the low energy region were cleavage facets. Cleavage occurred over an area with similarly oriented cleavage planes which appeared to be equivalent in area to several (3 to 5) prior austenite grains. Cracks at different elevations then seemed to link up leaving cliffs normal to the fracture surface. Higher magnification examination of the individual cleavage facets showed them to be equivalent in size and shape to 1 to 3 ferrite grains. Tearing occurred at the facet edges as the crack changed orientation from one cleavage plane to another.

The features of the mid-transition region were cleavage areas (3 to 5 prior austenite grains in size) separated by regions of ductile rupture. The most favorably oriented grains cleaved but less favorably oriented areas failed by ductile rupture.

The features of the shelf region are illustrated in Fig. 3 for a specimen aged at 427°C and tested at 427°C. The surface is covered with a nonuniform size distribution of voids which have nucleated on precipitate particles. The void spacing is on a considerably larger scale than the precipitate distribution in Fig. 1 and it is also apparent that not all precipitates have nucleated voids.

A careful comparison of the microstructural features on all material conditions showed the features were similar at equivalent points on the C_v curve, i.e., toe vs toe, mid-point vs mid-point and shelf vs shelf. The most significant difference noted between the as-received material and that aged at 538°C was the greater tendency toward secondary cracking normal to the surface on the 538°C specimen. The extension of cracks in this lower stress direction would not be likely to occur except along an embrittled interface. The fracture surface also appears to be rougher when viewed at low magnification with "chunks" about the size of prior austenite grains either pulled out or protruding from the surface.

Examination of the irradiated material revealed an even stronger

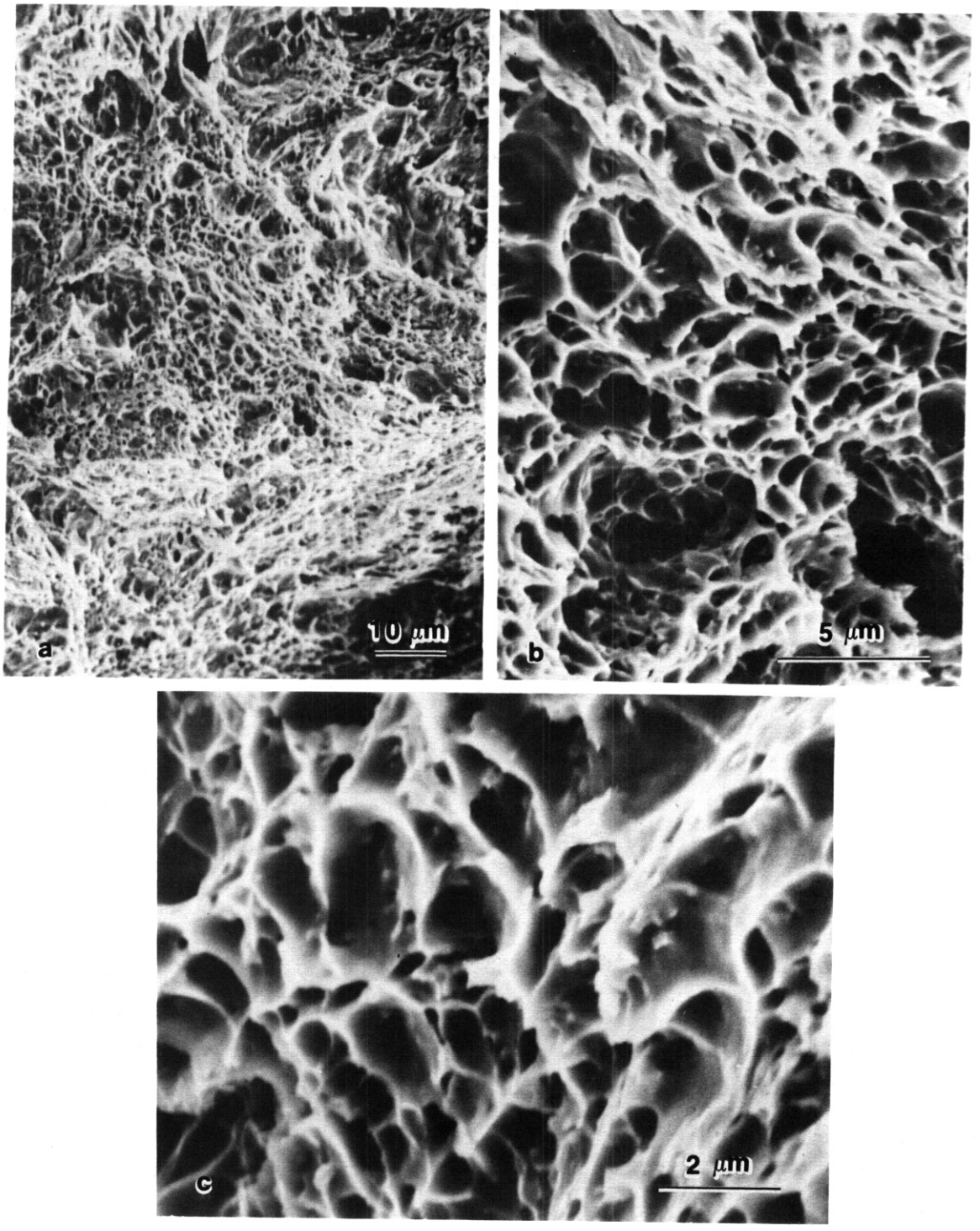

Fig. 7.6.3. SEM micrographs representative of the ductile rupture failure mode observed in all unirradiated specimens tested in the Charpy-V upper shelf energy regime. The micrographs are all from the same region at progressively higher magnification.

tendency toward secondary cracking and surface roughness on a scale of the prior austenite grain size. A significant change in the appearance of the microstructural features in the irradiated specimen tested at 427°C (on the shelf) was noted and is illustrated in Fig. 4. The failure mode is ductile rupture by microvoid coalescence as in the unirradiated specimen of Fig. 3. However, the dimples are not as deep and the ligaments between voids show less ductility than in the unirradiated specimens.

One of the irradiated Charpy specimens was sectioned in the hot cell and a transmission electron microscopy specimen was prepared and examined. The microstructure was similar in appearance to that of the unirradiated material with the exception that fine scale precipitation (20 nm and less in diameter) had occurred within the grains during irradiation.

7.6.4.4 Discussion

7.6.4.4.1 Irradiation Induced Embrittlement. The results described in this paper represent the first known evaluation of fracture toughness for the martensitic stainless steel class of materials subjected to the high temperature, high fluence irradiation conditions which will be encountered in advanced nuclear systems such as the fast breeder reactor and fusion reactors. Previous investigations of this class of materials have included a study of AISI 403 irradiated to a fluence of 6×10^{19} n/cm^2 (E > 1 MeV) at 293°C in a water cooled reactor. The study showed K_{IC} values from 3.8 cm compact tension specimens as low as 32 MPa $\sqrt{m}$ for tests at -75°C and values as high as 88 MPa $\sqrt{m}$ in tests at 23°C[6]. Transition temperature shifts of 44 to 87°C were also reported in Charpy impact tests of seven different heats of AISI 403 irradiated to fluences of 6.0 and 7.5 x 10^{19} n/cm^2 (E > 1 MeV) in a pressurized water reactor at 300°C. The shelf energy also dropped by 205 as a result of the irradiation[7].

Another study of martensitic stainless steels under evaluation in the United Kingdom fast reactor program' involved irradiation of 1/4 thickness (2.5 mm) Charpy-V notch specimens to fluences of 1.2 to 2.7 x 10^{19} n/cm^2 (E > 1 MeV) at irradiation temperatures of 300, 450, and 500°C

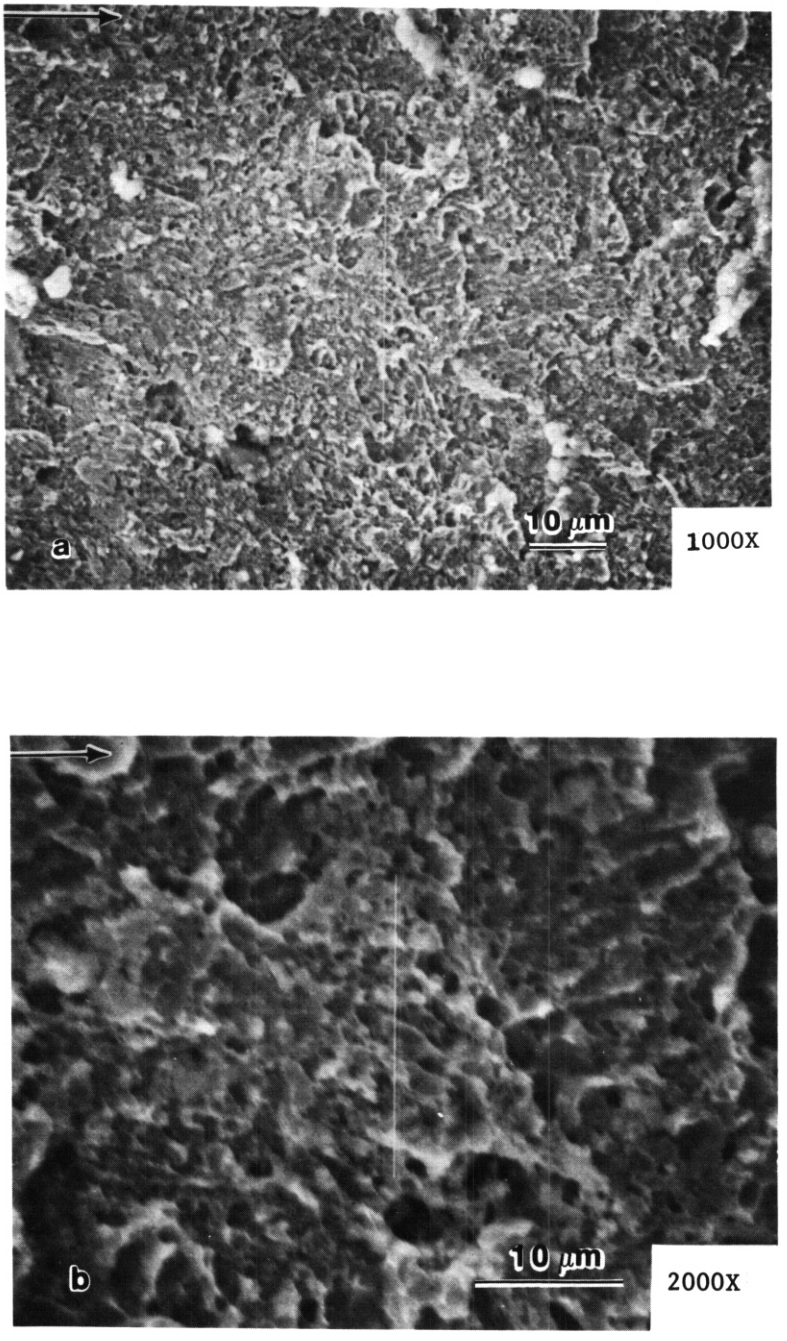

Fig. 7.6.4. SEM micrographs of HT-9 in the irradiated condition tested in the Charpy-V upper shelf energy range. Compare with Fig. 3 and note the more limited ductility apparent in the tearing between voids.

in the PLUTO thermal reactor. Transition temperature shifts of 40 to 60°C were observed after the 300°C irradiation for all three alloys tested. The higher temperature irradiations at 450 and 500°C produced no shift in transition temperature with the exception of a shift which appeared to be related to precipitation in FV607 at the 500°C irradiation temperature. Decreases in upper shelf energy of approximately 0.125 J/mm^2 accompanied the transition temperature shift noted in the 300°C irradiations. By way of comparison, low alloy pressure vessel steels (A302-B and A533-B) irradiated at 288°C in water cooled reactor environments commonly show transition temperature shifts of 80 to 120°C after irradiation to fluences of 1×10^{19} n/cm^2 ($E > 1$ MeV)[9].

The elevation in C_v ductile-brittle transition observed in the present experiment is comparable to shifts observed in pressure vessel steels irradiated in water cooled reactors at 288°C but at fluences 1000 times lower than in the present experiment. The rate of embrittlement under fast reactor conditions is therefore much lower. Irradiation temperature is obviously an important variable for irradiation hardening and elevation of the C_v ductile-brittle transition curves. The lower fluence irradiations of 12 percent chromium steels[6-8], reported in the literature, showed a shift in transition curves at 300°C but no shift at 450°C. The present experiment indicates that high temperature irradiation damage does not saturate at 1×10^{22} n/cm^2 ($E > 0.1$ MeV) unless there is a large change in irradiation hardening between 420 and 450°C. Further irradiation experiments to extend the present data base at 420°C and to explore the temperature dependence of the irradiation hardening and embrittlement are in progress.

The PCC, specimens were used in this experiment for fracture toughness determinations because material limitations and irradiation space constraints would not permit the use of conventional compact toughness specimens. The PCC_v specimen can be used to measure the fracture initiation event but its small size normally does not permit development of full constraint at high temperatures. It is also recognized that, when conducted dynamically, the test provides a higher transition temperature than if the static (slow bend) tests are used and also tends to indicate higher K values for upper shelf temperatures.

An empirical correlation between Charpy-V notch shelf energies and K_{Ic} fracture toughness values has been reported by Barsom and Rolfe[10] and was obtained by testing a variety of ferritic steels with yield strengths down to **825** MPa and fitting the data to a linear relationship:

$$\left(\frac{K_{Ic}}{\sigma_y}\right)^2 = \frac{5}{\sigma_y}\left(CVN \quad \frac{\sigma_y}{20}\right)$$

where K_{IC} is given in units of ksi $\sqrt{in.}$, σ_Y in ksi, and CVN in ft-lb.

Fracture toughness values calculated using the above equation and the measured upper shelf C_V energies were **8** to **12** percent lower than the fracture toughness values from the PCC_V specimens except for the as-received control specimen tested at **427**°C. The value for the latter was **20** percent below the value from PCC_V specimens at the same temperature. In view of the limited data available, the correlation is felt to be reasonably good for this material. More importantly, the fracture toughness values obtained by measurement or by the C_V-K_{Ic} correlation indicate a good retention of fracture resistance after irradiation for projected service temperatures in the upper shelf region. Below the C_V ductile-to-brittle transition, the measured values of **45** MPa $\sqrt{m}$ indicates the need for a careful integration of the component design requirements and material properties.

7.6.4.4.2 Mechanisms for Degradation of Fracture Properties. The experimental evidence points toward two mechanisms contributing to the degradation of the fracture toughness of €IT-9 during irradiation -temper embrittlement and irradiation hardening. The occurrence of temper embrittlement in HT-9 is readily apparent in the shift in transition and decrease in shelf energy after 5000 h aging at 538°C. The 100 percent recovery of Charpy energy after a short term anneal above the temper embrittlement range for this class of steels **(425** to 550°C) with no change in hardness, confirms the presence of temper embrittlement. The tendency toward secondary cracking and separation along prior austenite grain boundaries observed in SEM fractographs is also characteristic of temper embrittlement. Acceleration of diffusion under irradiation could

lower the temperature at which the phenomena appeared so that it may also be present in the specimens irradiated at 419°C. SEM fractographs of the irradiated specimen also showed secondary cracking and failure along prior austenite grain boundaries. Embrittlement of the prior austenite grain boundaries would result in a lower energy fracture mode which would be manifested as a lower shelf energy.

Irradiation hardening was present even at temperatures as high as 420°C as evidenced by the 50 percent increase in yield strength. The transmission electron microscopy results showed some fine scale precipitation and may also show some increase in dislocation density although it is difficult to resolve changes in dislocation density in such a complex structure. Both factors would contribute to an increase in yield strength. Increases in yield strength from small obstacles to dislocation motion produce a shift in transition temperature in bcc metals[11,12], as illustrated in Fig. 5. The stress to initiate cleavage in iron is relatively independent of temperature while the stress to produce plastic deformation increases sharply with decreasing temperature. To a first approximation, the temperature at which cleavage fracture occurs is determined by the intersection of the fracture and plastic flow curves at T_1. The increase in yield strength produced by irradiation shifts the flow curve upward and the point of intersection of the fracture stress and flow curves, T_2, occurs at a higher temperatures. Temper embrittlement can be illustrated on the same diagram as a decrease in fracture energy. The decrease in shelf energy in the irradiated specimen can be explained by the lower ductility and loss in work hardening ability illustrated in Fig. 4. Thus, both irradiation accelerated temper embrittlement and irradiation hardening are believed to contribute to the degradation in fracture properties of HT-9 after irradiation.

7.6.5 Conclusions

This exploration of the response of HT-9 to high temperature (419°C), high fluence (1.1×10^{22} n/cm^2 E > 0.1 MeV) neutron irradiation has lead to the following conclusions:

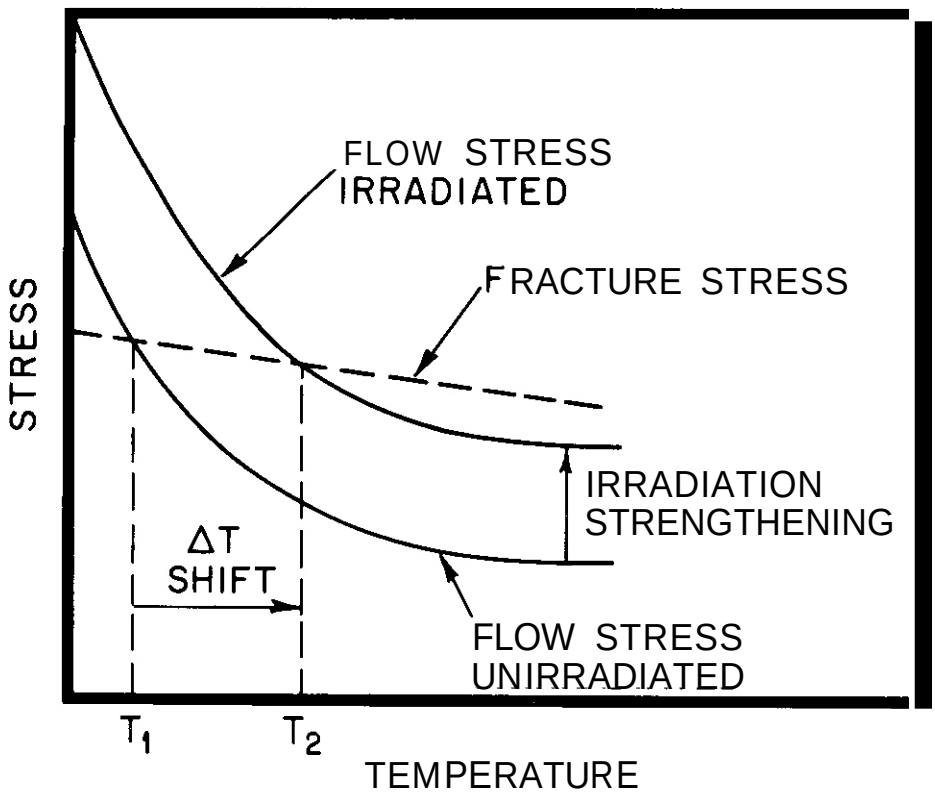

Fig. 7.6.5. A schematic illustration of the mechanism by which irradiation strengthening increases the temperature of the onset of cleavage fracture and thereby elevates the ductile-brittle transition temperature.

1. The C_V ductile-to-brittle transition was elevated by 108°C to 113°C after irradiation.

2. Fracture toughness corresponding to C_V on the upper shelf region was approximately 170 MPa $\sqrt{m}$ when measured by the PCC_V test and should be quite adequate for projected duct applications where service is above the ductile-to-brittle transition region.

3. Fracture toughness below the transition region was measured is ~ 45 MPa $\sqrt{m}$ from PCC_V tests and will require careful integration of the component design requirements and material properties.

4. HT-9 is subject to temper embrittlement at 538°C after 5000 h aging.

5. The probable mechanisms for the observed degradation in fracture toughness with irradiation are irradiation hardening, temper embrittlement accelerated by irradiation, and decreased work hardening ability.

7.6.6 References

1. Smidt, F. A., Jr., Malmberg, P. R., Sprague, J. A., and Westmoreland, J. E., "Swelling Behavior of Commercial Ferritic Alloys, EM-12 and HT-9, as Assessed by Heavy Ion Bombardment" in Irradiation Effects on the Microstructure and Properties of Metals, ASTM STP 611, 1976, pp. 227-241.
2. Unpublished data, F. A. Smidt, Naval Research Laboratory, and J. L. Straalsund and co-workers, Hanford Engineering Development Laboratory (see also Ref. 8 for data on similar alloys).
3. Paxton, M. M., Chin, B. A., Gilbert, E. R., and Nygren, R. E. Journal of Nuclear Materials, Vol. 80, 1979, pp. 144-151.
4. ASTM Standard E-23: Standard Methods for Notch Bar Impact Testing of Metallic Materials, 1978 Book of Standards, Part 10, pp. 235-251.
5. Ireland, D. R., Server, W. L., and Wullaert, R. A., "Procedure for Testing and Data Analysis, Task A - Topical Report," ETI Technical Report 75-43, Effects Technology, Inc., Oct. 1975.
6. Hosbons, R. R., Pacey, A. J., and Wotton, B. L., "Effect of Impurity Concentration on the Change in Fracture Toughness of AISI Type 403

Stainless Steel with Fast Neutron Irradiation," in Properties of Reactor Structural Alloys After Neutron or Particle Irradiation," ASTM STP 570, 1975, pp. 103-116.

7. Hosbons, R. R., and Wotton, B. L., "The Effect of Fast Neutron Irradiation on the Mechanical Properties of Some Quenched and Tempered Steels," in Irradiation Effects on Structural Alloys for Nuclear Reactor Applications, ASTM STP 484, 1970, pp. 142-163.

8. Little, E. A., Arkell, D. R., Harries, D. R., Lewthwaite, G. R., and Williams, T. M., "Development of Ferritic-Martensitic Steels for Fast Reactor Applications," in Proceedings, Ajaccio Conference on Irradiation Behavior of Metallic Materials for Fast Reactor Core Components, 4-8 June 1979, p. 81 (to be published).

9. Steele, L. E., Neutron Irradiation Embrittlement of Reactor Pressure Vessel Steels, IAEA Report 163, International Atomic Energy Agency, Vienna, 1975.

10. Barsom, J. M. and Rolfe, S. T., Engineering Fracture Mechanics, Vol. 2, 1971, p. 341.

11 Smidt, F. A., Jr. and Watson, H. E., Metallurgical Transactions, Vol. 3, 1972, pp. 2065-2073.

12. Hawthorne, J. R. and Fortner, E., "Radiation and Temper Embrittlement Processes in Advanced Reactor Weld Metals,'' Journal of Engineering for Industry, ASME, Aug. 1972, pp. 807-814.

7.7 ENVIRONMENTAL EFFECTS ON PROPERTIES OF FERRITIC STEELS - O. K. Chopra and D. L. Smith (Argonne National Laboratory)

7.7.1 ADIP Task

ADIP tasks are not defined for ferritic steels in the 1978 program plan.

7.7.2 Objective

The objective of this work is to develop a data base on the corrosion, compatibility, and the influence of chemical environment on the mechanical properties of ferritic steels (including welds) under environmental conditions proposed in fusion reactor applications.

This program is part of a more comprehensive program to investigate the potential of ferritic steels for fusion reactor first-wall blanket structures. Test environments to be investigated include lithium, water, and helium with appropriate impurities as well as candidate solid breeding materials and neutron multipliers. Emphasis will be placed on the combined effect of stress and chemical environment on corrosion and mechanical properties of ferritic steels. Initial tests will focus on the Sandvik Alloy HT-9 and a developmental Fe-9Cr-1Mo alloy.

7.7.3 Progress and Status

This program was initiated in the first quarter of FY 1980 with initial phases of the program focused on (1) combined effects of stress and coolant environment on the corrosion behavior and fatigue properties of ferritic steels and (2) the compatibility of ferritic steels with candidate solid tritium-breeding materials and neutron multipliers, viz., Li_2O, $LiAlO_2$, and Li_2SiO_3.

During the current reporting period, modification of an existing facility for fatigue testing in a liquid metal environment was completed. The system consists of a servocontrolled, hydraulic-actuated MTS fatigue machine with an associated liquid lithium loop. A schematic diagram of the fatigue test facility is shown in Fig. 1. The loop, which is constructed of stainless steel, consists of three test vessels and is equipped for control and measurement of nonmetallic element concentrations

in lithium. The quantity of lithium in the loop is 1.20 liters, and the lithium flow rate is ∿1 liter/min.

The fatigue testing equipment consists of a test stand, movable crosshead, hydraulic actuator, and specimen fixture. The actuator of the fatigue machine is mounted on the movable crosshead which is raised or lowered to facilitate removal or insertion of the test specimen into the lithium test vessel. Specimen strain is controlled by standard resistive-type extensometer located on the upper portion of the fixture in an ambient-temperature region. Specimen load is measured by a load cell placed in line with the actuator.

The lithium loop has operated continuously for 2.1200 h; the initial 200 h at a maximum temperature of 2.630 K and the remainder at 1.750 K. The cold-trap temperature was maintained at 480 K. Filtered lithium dip samples were taken after fired intervals for analysis of nitrogen and carbon in lithium. Specimens of zirconium, vanadium, and yttrium are being exposed to lithium to determine the concentrations of oxygen and hydrogen in lithium. The initial concentration of nitrogen in lithium obtained after 1.150 h of operation at 630 K was 1.445 ppm.

Preliminary fatigue tests have been conducted with 2.5-mm-diameter specimens of Type *304* stainless steel and HT-9 at 755 K in flowing sodium and lithium environments to qualify the test procedure. The geometry and dimensions of the test and calibration fatigue specimens have been reported earlier.' Results will be compared with previous tests to ensure the validity of results obtained with the small sample geometry.

The combined effects of stress and liquid lithium environment on the corrosion behavior of ferritic steels will be evaluated by exposing stressed specimens of HT-9 and Fe-9Cr-1Mo steels in the specimen-exposure vessel. For this investigation, tapered specimens will be used and stress applied by deadweights. The design and fabrication of the corrosion specimen holder is in progress.

The second phase of the program that has been initiated involves the compatibility testing of ferritic steels with candidate solid breeding materials. Corrosion specimens of Fe-2¼Cr-1Mo, Fe-9Cr-1Mo, and HT-9 ferritic steels are being exposed with solid Li_2O, $LiAlO_2$, and Li_2SiO_3 at 873 K.

7.7.4 Conclusions

Preliminary fatigue tests have been conducted with Type 304 stainless steel and HT-9 ferritic steel specimens at 755 K in a flowing lithium environment. The lithium loop has operated continuously for ∿1200 h.

Reference

1. D. L. Smith, O. K. Chopra, and R. R. Schlueter, "Environmental Effects on Properties of Ferritic Steels," ADIP Quarterly Progress Report for Period Ending December 31, 1979, DOE/ET-0058/8, pp. 115-118.

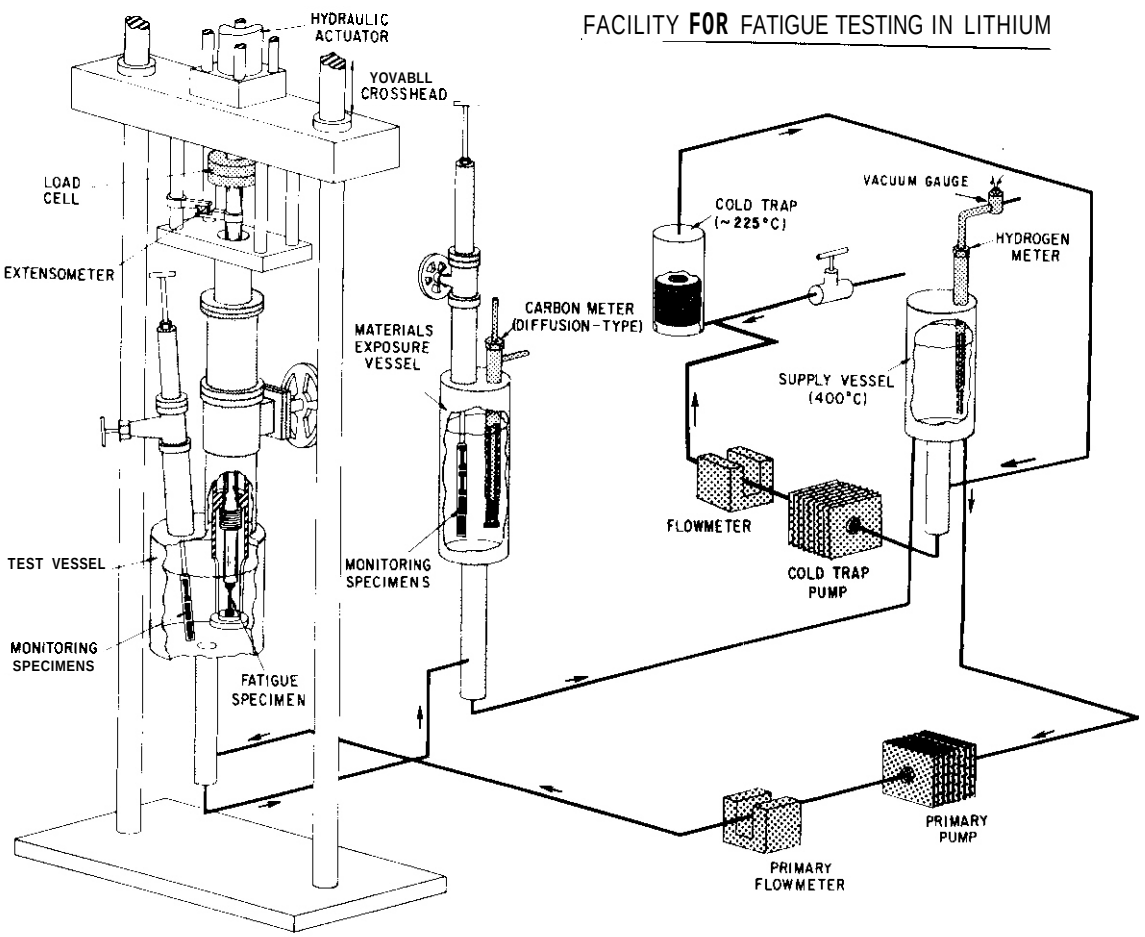

Fig. 1. Schematic of Facility for Fatigue Testing in Lithium.

8. STATUS OF IRRADIATION EXPERIMENTS AND MATERIALS INVENTORY

3.1 IRRADIATION EXPERIMENT STATUS AND SCHEDULE

The following bar charts show the irradiation experiment schedule, including experiments completed, in progress, and planned. Experiments are presently under way in the ORR and the HFIK, which are mixed-spectrum reactors, and in the EBR-II, which is a fast reactor.

The HFIR-CTR-26, -27, -28, and -29 experiments are in the HFIK and are performing satisfactorily.

The ORR-MFE-2 experiment was removed from the ORR after successfully completing 10,950 MW-d of exposure.

Components for ORR-MFE-4 have been manufactured and are now awaiting specimen loading. Irradiation of MFE-4A is scheduled to begin in April 1980 and of MFE-4B in July 1980.

Experiment Designation	Major Objective
A. Oak Ridge Research Reactor	
ORR-MFE-1 / ORR-MFE-2	Experiments to scope the effects of composition and microstructure on the tensile, fatigue, and irradiation creep of representative path A, B, and C alloys.
ORR-MFE-3	Effects of irradiation on postirradiation fatigue crack growth in representative path A, B, and C alloys.
ORR-MFE-4 [2]	Effect of irradiation on tensile, fatigue, and irradiation creep of path A PCA (Prime Candidate Alloy) and path B base research alloys. Spectral tailoring to maintain correct He/dpa ratio. Irradiation on continuing basis.

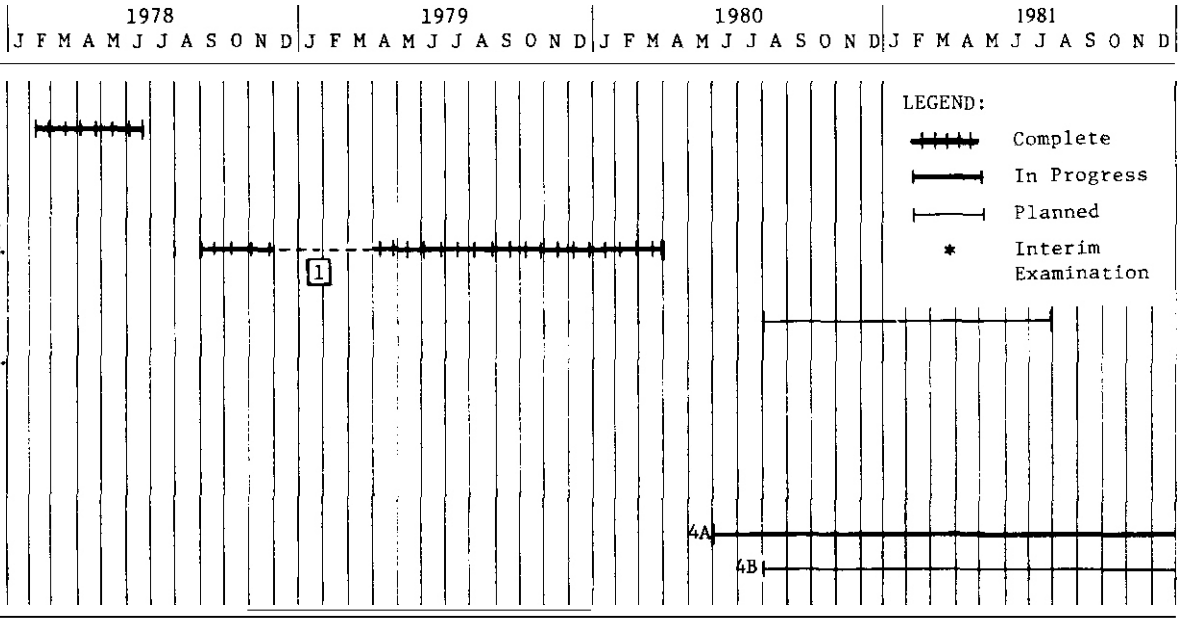

[1] MFE-2 out of reactor for repair of a small leak.

[2] MFE-4A will operate at 300 and 400°C. MFE-4B will operate at 500 and 600°C.

Designation	Major Objective
ORR-MFE-5	In-reactor fatigue crack growth experiment
B. Experimental Breeder Reactor II	
Subassembly X 264	Effect of preinjected helium (2–200 at. ppm) on microstructure and tensile properties of 316 SS, PE-16, V and Nb alloys. Fluence $\leq 2.3 \times 10^{26}$ n/m^2, 500–825°C.
Subassembly X 287	Effect of preinjected helium (2–200 at. ppm He) on microstructure and tensile properties of 316 SS, PE-16, V and Nb alloys. Fluence $\leq 4 \times 10^{26}$ n/m^2, 400–700°C.
Subassembly X 217D	Stress relaxation Ti Alloys
See footnotes [1] [2] and [3]	Effect of irradiation on swelling, tensile, fatigue, and crack growth properties of Ti scoping alloys. 370, 450, and 550°C, fluence $4.5–5.5 \times 10^{26}$ n/m^2.

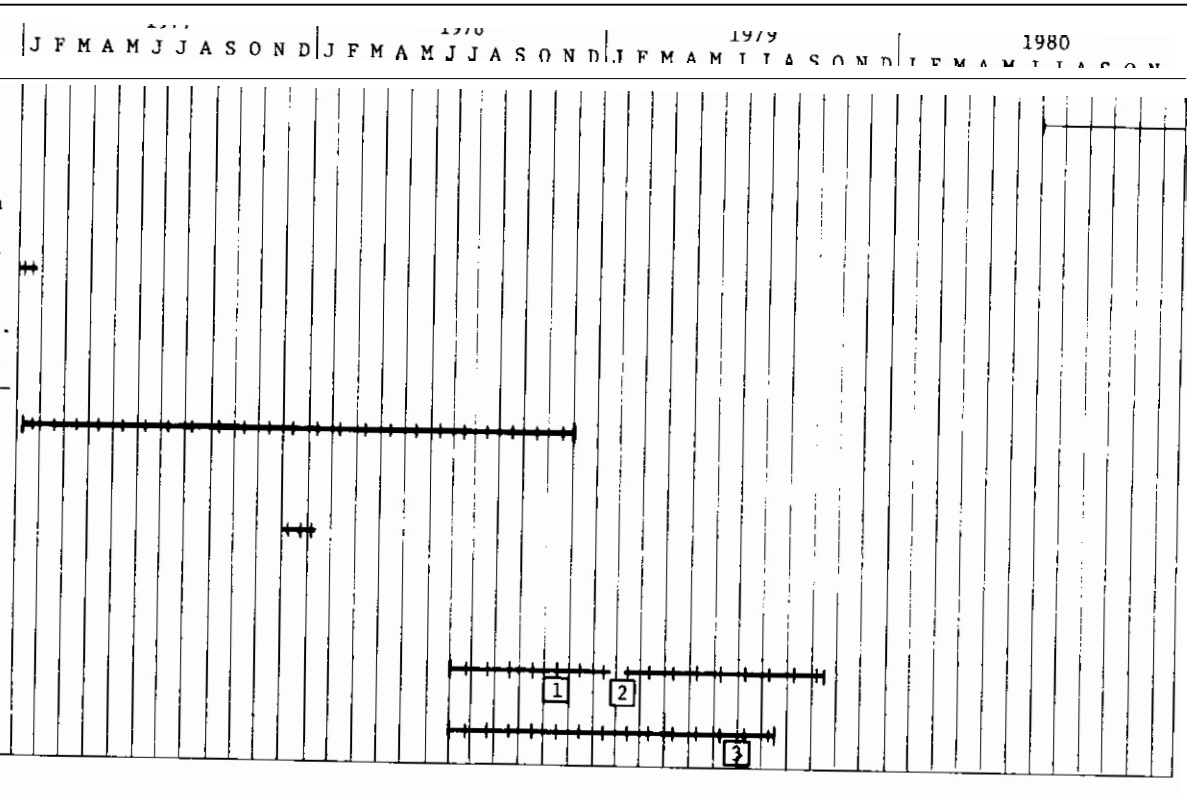

[1] EBR-II, row 2, pins B285 and B286.

[2] Subassembly removed for EBR-II run 99.

[3] Pin B284, row 2 for runs 96–98; row 4 for runs 100–102.

Experiment Designation	Major Objective
Experiment plan depends on alloy availability. EBR-II space not yet identified.	Effect of Irradiation on swelling, tensile, fatigue, and crack growth properties of V and Nb scoping alloys. 370, 450, 550, and 650°C. Position in reactor not finalized, therefore no fluence estimate. [1]
C. High Flux Isotope Reactor (HFIR)	
HFIR-CTR-4	PE-16 for swelling and tensile properties, 300–700°C 2.2–4.5 dpa, 100–350 at. ppm He
HFIR-CTR-7	PE-16 for swelling and tensile properties, 300–700°C 9–18 dpa, 1250–3000 at. ppm He
HFIR-CTR-8	duplicate of -7
HFIR-CTR-9	316 and 316 + Ti for swelling and tensile properties, 280–680°C, 9–18 dpa, 400–1000 at. ppm He

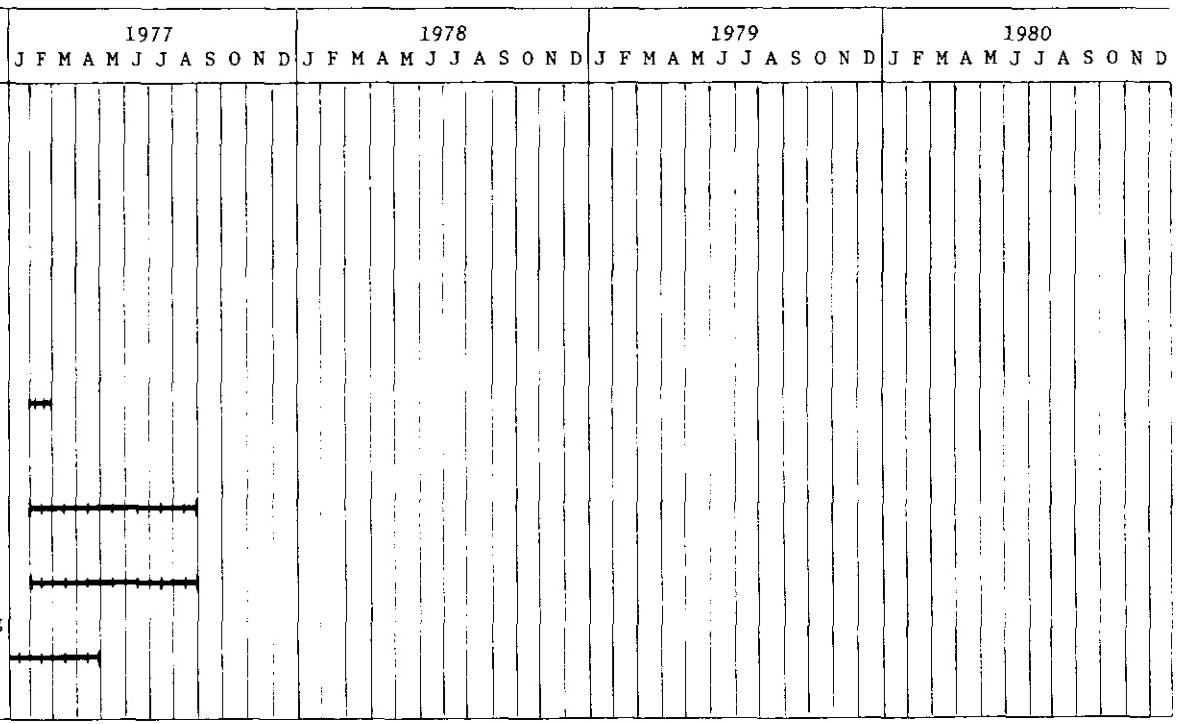

[1] Delayed for undetermined period.

Experiment Designation	Major Objective
HFIR-CTR-10	duplicate of -9
HFIR-CTR-11	duplicate of -9
HFIR-CTR-12	316 and 316 + Ti for swelling and tensile properties, 280–680°C, 5.5–11 dpa, 200–500 at. ppm He
HFIR-CTR-13	duplicate of -12
HFIR-CTR-14	20%-CW 316 for fatigue testing 300°C. 9–18 dpa, 400–1000 at. ppm He
HFIR-CTR-15	20%-CW 316 for fatigue testing 500°C, 5.5–11 dpa, 200–500 at. ppm He
HFIR-CTR-16	316, welds, PE-16, and Inconel 600 for swelling and tensile properties, ~55°C, 5.5–11 dpa, 150–2700 at. ppm He (depending on alloy)
HFIR-CTR-17	Type 316 welded with 16-8-2 filler metal for tensile properties and failure analysis, 280–620°C, 6.7–13 dpa, 180–460 at. ppm He in weld metal

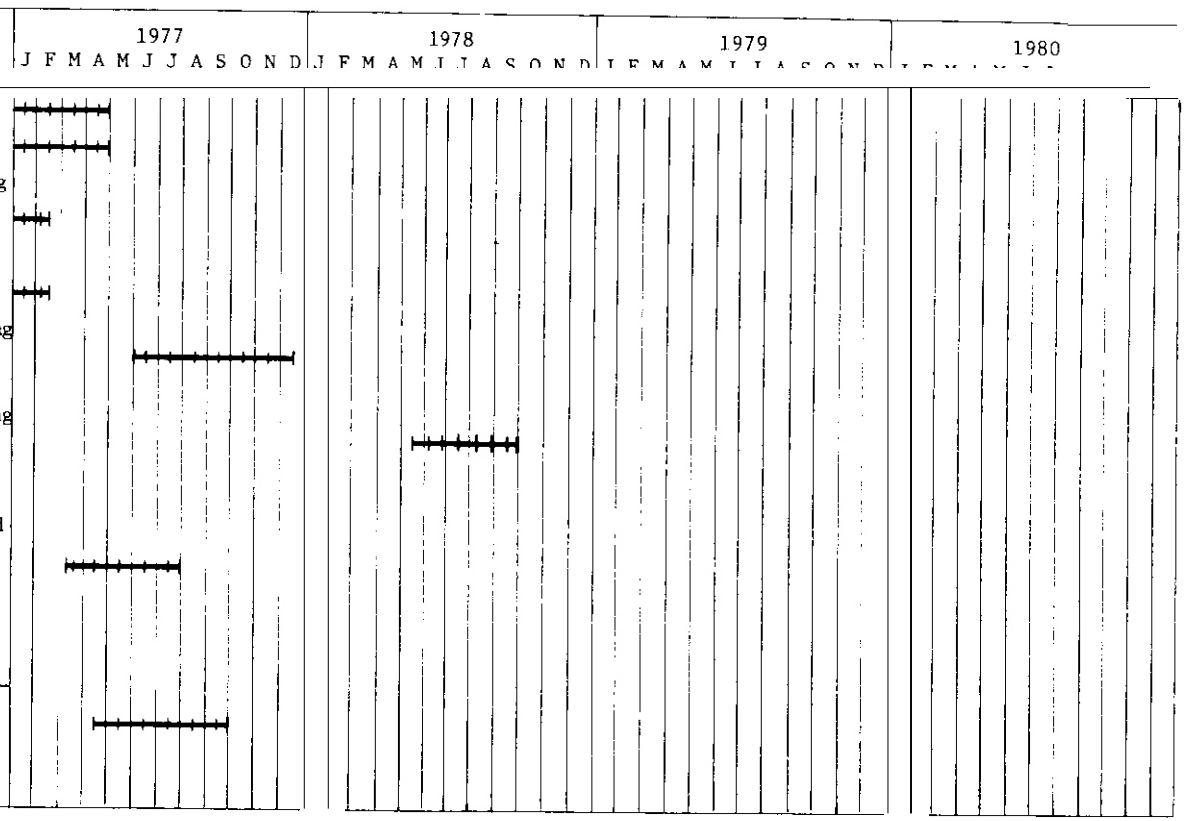

Experiment Designation	Major Objective
HFIR-CTR-18	PE-16 and 20%-CW type 316 for swelling and tensile properties, 280–700°C, PE-16: 17–27 dpa, 3400–5600 at. ppm He 316: 27–34 dpa, 1600–2100 at. ppm He
HFIR-CTR-19	316 welded with 316 filler metal for tensile properties, 280–620°C, 5.5–11 dpa, 200–500 at. ppm He
HFIR-CTR-20	20%-CW 316 for fatigue testing, 300°C, 5.5–11 dpa, 200–500 at. ppm He
HFIR-CTR-21	20%-CW 316 for fatigue testing, 500°C, 9–18 dpa, 400–1000 at. ppm He
HFIR-CTR-22	duplicate of -20
HFIR-CTR-23	PE-16 for fatigue testing, 300°C, 4.4–9 dpa, 370–1000 at. ppm He

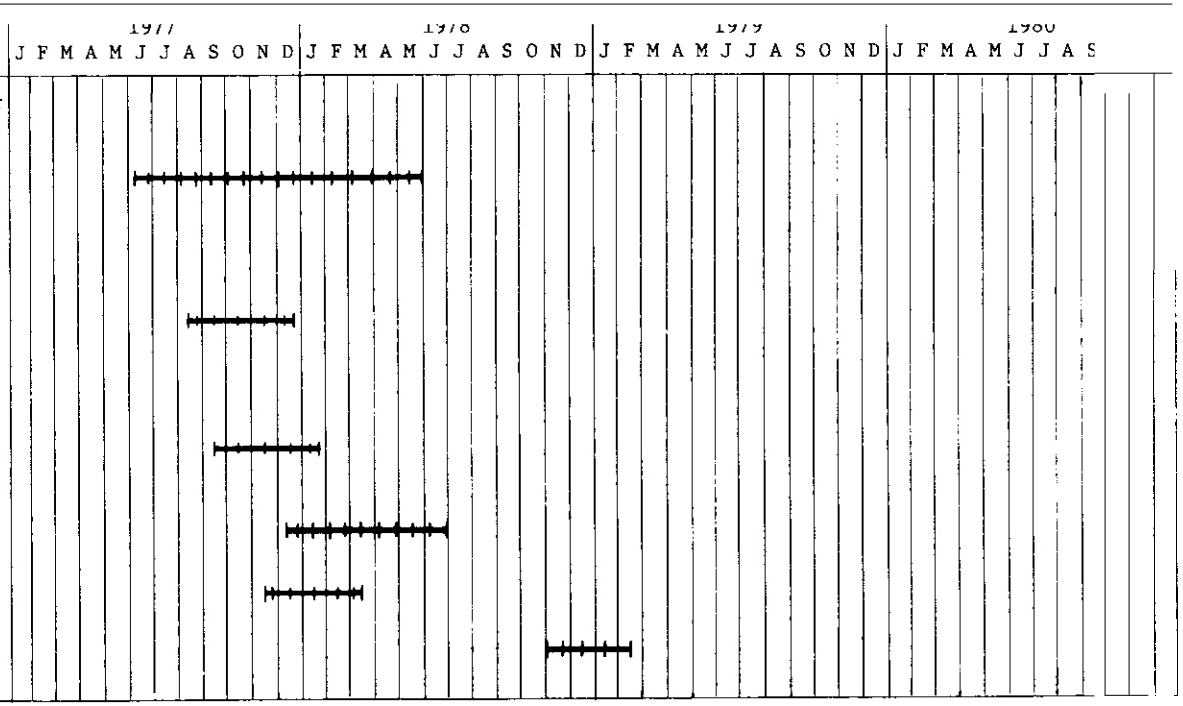

Experiment Designation	Major Objective
HFIR-CTR-24	Temperature calibration, tensile properties of MFE ref. 316, 2.25 dpa, 30 at. ppm He
HFIR-CTR-25	Temperature calibration, tensile properties of MFE ref. 316, 2.25 dpa, 30 at. ppm He [1]
HFIR-CTR-26	Swelling and tensil pro r ies o MFE r f. 316, 32 dpa, 1300 at. ppm He
HFIR-CTR-27	Swelling and tensile properties of MFE ref. 316, 56 dpa, 3450 at. ppm He
HFIR-CTR-28	Swelling and ensile properties of MFE r f. 316, 32 dpa, 1900 at. ppm e
HFIR-CTR-29	Swelling and tensile properties of MFE ref. 316, 56 dpa, 3450 at. ppm He
HFIR-CTR-30	Swelling and tensile properties, Paths A, B, and D micro-structural variations, 40 dpa, 2500 at. ppm He (Path A)
HFIR-CTR-31	Swelling and tensile prop rties Paths A, B and D micro-structural variations, 20 dpa, 1200 ppm He (Path A)
HFIR-CTR-32	Swelling and tensile properties, Paths A, B and D micro-structural variations, 10 dpa, 500 ppm He (Path A)

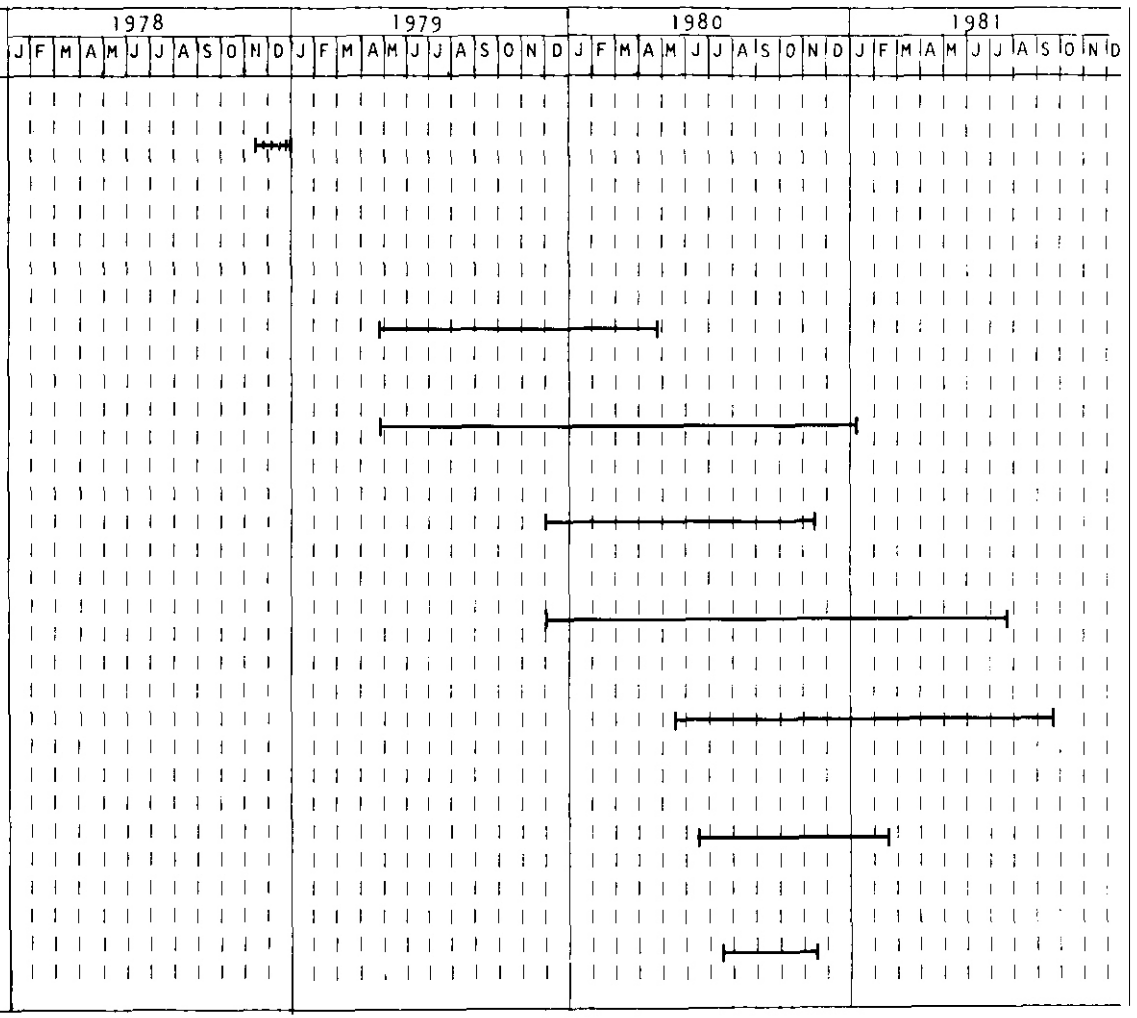

[1] Delayed or undetermined period.

8.2 ETM RESEARCH MATERIALS INVENTORY — F. W. Wiffen, T. K. Roche (ORNL) and J. W. Davis (McDonnell Douglas)

8.2.1 ADIP Task

ADIP Task I.D.1, Materials Stockpile for MFE Programs.

8.2.2 Objective

The Office of Fusion Energy has assigned program responsibility to ORNL for the establishment and operation of a central inventory of research materials to be used in the Fusion Reactor Materials research and development programs. The objective is to provide a common supply of materials for the Fusion Reactor Materials Program. This will minimize unintended materials variables and provide for economy in procurement and for centralized recordkeeping. Initially this inventory is to focus on materials related to first-wall and structural applications and related research, but various special purpose materials may be added in the future.

The use of materials from this inventory for research that is coordinated with or otherwise related technically to the Fusion Reactor Materials Program of DOE, but which is not an integral or directly funded part of it, is encouraged.

8.2.3 Materials Requests and Release

Materials requests shall be directed to ETM Research Materials Inventory at ORNL (Attention: F. W. Wiffen). Materials will be released directly if:

(a) The material is to be used for programs funded by the Office of Fusion Energy, with goals consistent with the approved Materials Program Plans of the Materials and Radiation Effects Branch.

(b) The requested amount of material is available, without compromising other intended uses.

Materials requests that do **not** satisfy both (a) and (b) will be discussed with the staff of the Materials and Radiation Effects Branch, Office of Fusion Energy, for agreement on action.

8.2.4 Records

Chemistry and materials preparation records are maintained for all inventory material. All materials supplied to program uses will be accompanied by summary characterization information.

8.2.5 Summary of Current Inventory and Material Movement in Period Jan. 1 to Mar. 31, 1980

A condensed, qualitative description of the content of materials in the EIM Research Materials Inventory is given in Table 8.2.1. This table indicates the nominal diameter of rod or thickness of sheet for product forms of each alloy and also indicates by weight the amount of each alloy in larger sizes available for fabrication to produce other product forms as needed by the program. Table 8.2.2 lists materials received into the inventory in the quarter covered. Materials distributed from the inventory are listed in Table 8.2.3.

Alloy compositions and more detail on the alloys and on alloy procurement and/or fabrication are given in earlier ADIP quarterly progress reports.

Table 8.2.1. Summary Status of Material Availability in the ETM Research Materials Inventory

Alloy	Product Form: Ingot or Bar,[a] Weight (kg)	Rod,[b] Diameter (mm)	Sheet,[c] Thickness (mm)	Thin-Wall Tubing, Wall Thickness (mm)
		Path A Alloys		
316 SS	900	16 and 7.2	13 and 7.9	0.25
PCA	490	12	13	0.25
		Path B Alloys		
PE-16	140	16 and 7.1	13 and 1.6	0.25
B-1	180	0	0	0
B-2	180	0	0	0
8-3	180	0	0	0
8-4	180	0	0	0
8-6	180	0	0	0
		Path C Alloys		
Ti-64	0	0	0.76	0
Ti-62425	0	0	0.76	0
Ti-5621s	0	0	6.3, 2.5, and 0.76	0
Ti-38644	0	0	0.76	0
Nb-1% Zr	0	6.3	2.5, 1.5, and 0.76	0
Nt-5% Mo-1% Zr	0	6.3	2.5, 1.5, and 0.76	0
V-20% Ti	0	6.3	2.5, 1.5, and 0.76	0
V-15% Cr-5% Ti	0	6.3	2.5, 1.5. and 0.76	0
Vanstar-7	0	6.3	2.5. 1.5, and 0.76	0
Path D Alloys	No Material in Inventory			
		Path E Alloys		
HT-9	0	0	4.5	0
HT-9 + 1%Ni	0	0	4.5	0
HT-9 + 2% Ni	0	0	4.5	0
HT-9 + 2% Ni + Cr adjusted	0	0	4.5	0
T-9 modified	0	0	4.5	0
T-9 modified + 2% Ni	0	0	4.5	0
T-9 modified + 2% Ni + Cr adjusted	0	0	4.5	0
2 1/4 Cr-1 Mo	0	0	9[d]	0
		Miscellaneous		
USSR - Cr-Mn Steel[e]	0	e	e	0

[a]Greater than 25 mm, minimum dimension.

[b]Less than 25 mm in diameter. Some Path A and Path B alloys are available in two different diameters.

[c]Less than 15 mm thick. Some Path A. Path B, and Path C alloys are available in two or three different thicknesses.

[d]Material is thick-wall pipe, rerolled as necessary to produce sheet or rod.

[e]Rod and sheet of a USSR stainless steel supplied under the US-USSR Fusion Reactor Materials Exchange Program. Exact sizes not available.

Table 2 ETM Research Materials Inventory, Fusion Reactor Program, Receipts — 1-1-80 to 3-31-80

Alloy	Heat	Product Form	Dimensions (mm)	Dimensions (in.)	Quantity (kg)	Quantity (lb)	Quantity (m)	Quantity (ft)	Quantity (m^2)	Quantity ($in.^2$)	Quantity (pieces)	Source
				Path A Alloys — Austenitic Stainless Steels								
PCA	K-280	Tubing (20% cold worked)	4.57 OD × 0.25 wall	0.180 OD × 0.010 wall			33.5	110			20	Carpenter Technology
				Path E Alloys — Ferritic Steels								
2 1/4 Cr-1 Mo	72768	Pipe	38 OD × 8.65 wall	1.5 OD × 0.353 wall			7.0	23			1	Babcock and Wilcox through ORNL stores

Table 8.2.3. ΣΠ Research Materials Inventory, Fusion Reactor Program, Disbursements — 1-1-80 to 3-31-80

Alloy	Heat[a]	Product Form	Dimensions (mm)	Dimensions (in.)	Quantity (kg)	Quantity (lb)	Quantity (m)	Quantity (ft)	Quantity (m^2)	Quantity ($in.^2$)	Quantity (pieces)	Sent to[b]
			Path A Alloys Austenitic Stainless Steels									
316 SS[c]	X-15893	Sheet (20% cold worked)	0.25 thick	0.010 thick					0.038	136		Radiation Effects Group, ORNL
PCA	K-280	Bar	102 diam	4 diam	26	58	0.41	16 in.				MIT
		Bar	33.3 diam	1.313 diam			0.84	33 in.				Metals Processing Group, ORNL
		Tubing	4.57 OD × 0.25 wall	0.180 OD × 0.010 wall			0.81	32 in.				Metals Processing Group, ORNL
		Sheet	0.76 thick	0.030 thick					0.074	115		Radiation Effects Group, ORNL
		Sheet	0.25 thick	0.010 thick					0.276	428		Radiation Effects Group, ORNL
		Tubing	4.57 OD × 2.25 wall	0.180 OD × 0.010 wall			3.43	135 in.				Radiation Effects Group, ORNL
		Sheet	1.0 thick	0.040 thick					0.01	16		Westinghouse Res. Dev. Center
		Sheet	0.61 thick	0.024 thick					0.02	33		HEDL
			Path B Alloys High-Strength Fe-Ni-Cr Alloys									
B-1	J-271-1	Plate	4.06 thick	0.160 thick					0.06	91		HEDL
B-2	J-268-2	Plate	4.06 thick	0.160 thick					0.06	91		HEDL
B-3	J-267-1	Plate	4.06 thick	0.160 thick					0.06	91		HEDL
B-4	J-264-1	Plate	4.06 thick	0.160 thick					0.06	91		HEDL
B-6	J-262-1	Plate	4.06 thick	0.160 thick					0.06	91		HEDL
			Path C Alloys Reactive and Refractory Alloys									
V—20 Ti	833	Sheet	0.76 thick	0.030 thick					0.01	19		Westinghouse Res. Dev. Center
V—15 Cr—5 Ti	835 A	Sheet	0.76 thick	0.030 thick					0.01	19		Westinghouse Res. Dev. Center
Vanstar-7	836 Bot	Sheet	0.76 thick	0.030 thick					0.01	15		Westinghouse Res. Dev. Center
V—20 Ti	833	Sheet	1.5 thick	0.060 thick					0.02	36		ANL
	832 Bot	Sheet	2.5 thick	0.100 thick					0.02	27		ANL

Table 8.2.3. ETM Research Materials Inventory, Fusion Reactor Program, Disbursements — 1-1-80 to 3-31-80 (Continued)

Alloy	Heat	Product Form	Dimensions (mm)	Dimensions (in.)	Quantity (kg)	Quantity (lb)	Quantity (m)	Quantity (ft)	Quantity (m^2)	Quantity ($in.^2$)	Quantity (pieces)	Sent to[b]
				Path E Alloys — Ferritic Steels								
2 1/4 Cr-1 Mo	276[c]	Sheet	0.76 thick	0.030 thick					0.04	57		Radiation Effects Group, ORNL
		Sheet	0.25 thick	0.010 thick					0.16	244		Radiation Effects Group, ORNL
T-9 modified	ESR-XA-3590	Sheet	0.76 thick	0.030 thick					0.03	41		Radiation Effects Group, ORNL
		Sheet	0.25 thick	0.010 thick					0.04	62		Radiation Effects Group, ORNL
T-9 modified + 2% Ni	ESR-XA-3591	Sheet	0.76 thick	0.030 thick					0.03	44		Radiation Effects Group, ORNL
		Sheet	0.25 thick	0.010 thick					0.03	50		Radiation Effects Group, ORNL
T-9 modified + 2% Ni[d]	ESR-XA-3593	Sheet	0.76 thick	0.030 thick					0.03	47		Radiation Effects Group, ORNL
		Sheet	0.25 thick	0.010 thick					0.05	71		Radiation Effects Group, ORNL
				Miscellaneous								
USSR — Cr-Mn steel	EP 838	Sheet	0.76 thick	0.030 thick					0.05	72		Radiation Effects Group, ORNL
		Sheet	0.25 thick	0.010 thick					0.04	66		Radiation Effects Group, ORNL

[a]Bot — bottom.

[b]ORNL — Oak Ridge National Laboratory; MIT — Massachusetts Institute of Technology; HEDL — Hanford Engineering Development Laboratory; ANL — Argonne National Laboratory.

[c]Reference heat.

[d]With chromium equivalent adjusted.

9. CORROSION TESTING AND HYDROGEN PERMEATION STUDIES

9.1 HYDROGEN DISSOLUTION AND PERMEATION STUDIES OF ADIP PROGRAM ALLOYS – E. H. Van Deventer and V. A. Maroni (Argonne National Laboratory).

9.1.1 ADIP Task

I.A.4 Hydrogen Dissolution and Permeation Effects. The results presented in this section contribute to Subtask 1.A.4., Milestones I.A.a through I.A.d.

9.1.2 Objectives

The objective of the work reported in this section is to provide base-line hydrogen dissolution and permeation data for alloys currently under study in the ADIP Program. The hydrogen dissolution, outgassing and permeation characteristics of these materials are vital to an understanding of their performance as first-wall and blanket structural materials for fusion devices. A further objective of this work is to examine methods for overcoming any serious hydrogen isotope uptake and migration problems associated with the rather strong hydride-forming nature of some classes of alloys.

9.1.3 Summary

Efforts to characterize the hydrogen dissolution and permeation characteristics of alloys currently under development in the ADIP Program have continued. Two sets of Ti-6Al-2Sn-4Zr-2Mo-0.08Si plates were loaded with controlled quantities of hydrogen using an existing tensimetric apparatus at ANL. Chemical analyses made at MDAC on one of the two sets confirmed the adequacy of the loading method (540-560 wppm H analyzed versus 500 ± 10 wppm H determined from tensimetric additions). During the course of the loadings, it was found that dehydriding of alloy plates (from 500-700 wppm H to lower values) could not be readily achieved without heating the material to well over 600°C. These plates will be used by MDAC to conduct metallurgical and mechanical analyses of hydrogen effects on titanium alloys. In another study, an experiment was conducted to measure the hydrogen permeation characteristics of Fecralloy (Fe-16Cr-5Al-0.3Y) between 190 and 680°C using hydrogen driving pressures

in the range from 2 to 1.5 x 10^4 Pa. Comparison of the data from this study with similar results for Fe-Cr alloys having 0 and 2 wt.% Al showed that the aluminum content required to achieve the maximum hydrogen permeation resistance for these alloys in oxidizing environments may be less than 2 wt.% in some cases and could be related to the chromium content in the alloy.

9.1.4 Progress and Status

This section contains a report of work done during the second quarter of FY 1980 on the hydrogen dissolution and permeation characteristics of ADIP Program alloys. Also in the second quarter, some of the effort normally applied to this task was diverted to the initiation of a study of the corrosivity of solid ceramic breeder materials towards ADIP-specific alloys. The results of work on this new initative will be reported under a separate task heading in subsequent ADIP progress reports.

9.1.4.1 Path A Alloys

No report for this period.

9.1.4.2 Path B Alloys

No report for this period.

9.1.4.3 Path C Alloys

At the request of J. W. Davis and G. W. Wille of MDAC, two sets of Ti-6Al-2Sn-4Zr-2Mo-0.08Si plate specimens (10 plates per set) were loaded with controlled quantities of hydrogen using an existing tensimetric (Sieverts') apparatus. The first loading was found to be 550 ± 10 wppm H by analyses performed at MDAC. This value was in good agreement with the one determined during the actual tensimetric additions, i.e., 500 ± 10 wppm. The second loading was 636 ± 10 wppm (tensimetric), but this set has not been analyzed for hydrogen by MDAC. It was clearly evident from these studies that reversible dehydriding of the plates, starting from concentrations in the 500 to 700 wppm H range, would be

extremely difficult and probably would require dehydriding temperatures well above 600°C.

A third set of specimens will be loaded with hydrogen (to ∿500 wppm) during the third quarter of FY 1980. These samples (all three sets) will be used by MDAC to conduct metallurgical and mechanical analyses of hydrided titanium alloys.

9.1.4.4 Path D Alloys

No report for this period.

9.1.4.5 Path F Alloys

(Work reported in this subsection was initiated during the first quarter of FY 1980, in conjunction with the start of the ADIP Program activity to evaluate ferritic materials for use as fusion reactor construction materials.)

The impetus for the study of ferritic alloys as fusion reactor structural materials was discussed in a previous progress report.[1] Based on results derived from a survey of the hydrogen permeation characteristics of ferritic materials,[2] an experiment has been conducted to measure the hydrogen permeability of an oxidized specimen of Fecralloy (Fe-16Cr-5Al-0.3Y), a developmental alloy for nuclear and thermonuclear applications obtained from Harwell (UKAEA). The purpose of the experiment was to compare the effect on hydrogen permeability of the 5 wt.% aluminum in this alloy with that observed for 0 and 2 wt.% aluminum in other oxidized ferritic alloys having similar chromium contents. In particular, the permeability data obtained for the Fecralloy were correlated with those for 430-SS[2] (12Cr-0Al) and Armco 18-SR[2,3] (18Cr-2Al).

Hydrogen permeation measurements on the oxidized Fecralloy sample were made between 190 and 680°C using hydrogen driving pressures in the range from 2 to 1.5 x 10^4 Pa. The data are shown in Fig. 9.1.1 together with permeability curves for the 430-SS and oxidized Armco 18-SR. The appreciable scatter in the Fecralloy data is typical of that observed for oxidized Fe-Cr-Ni and Fe-Cr alloys, and is generally attributed to cyclic cracking and rehealing of the surface oxide layer.[3,4] The

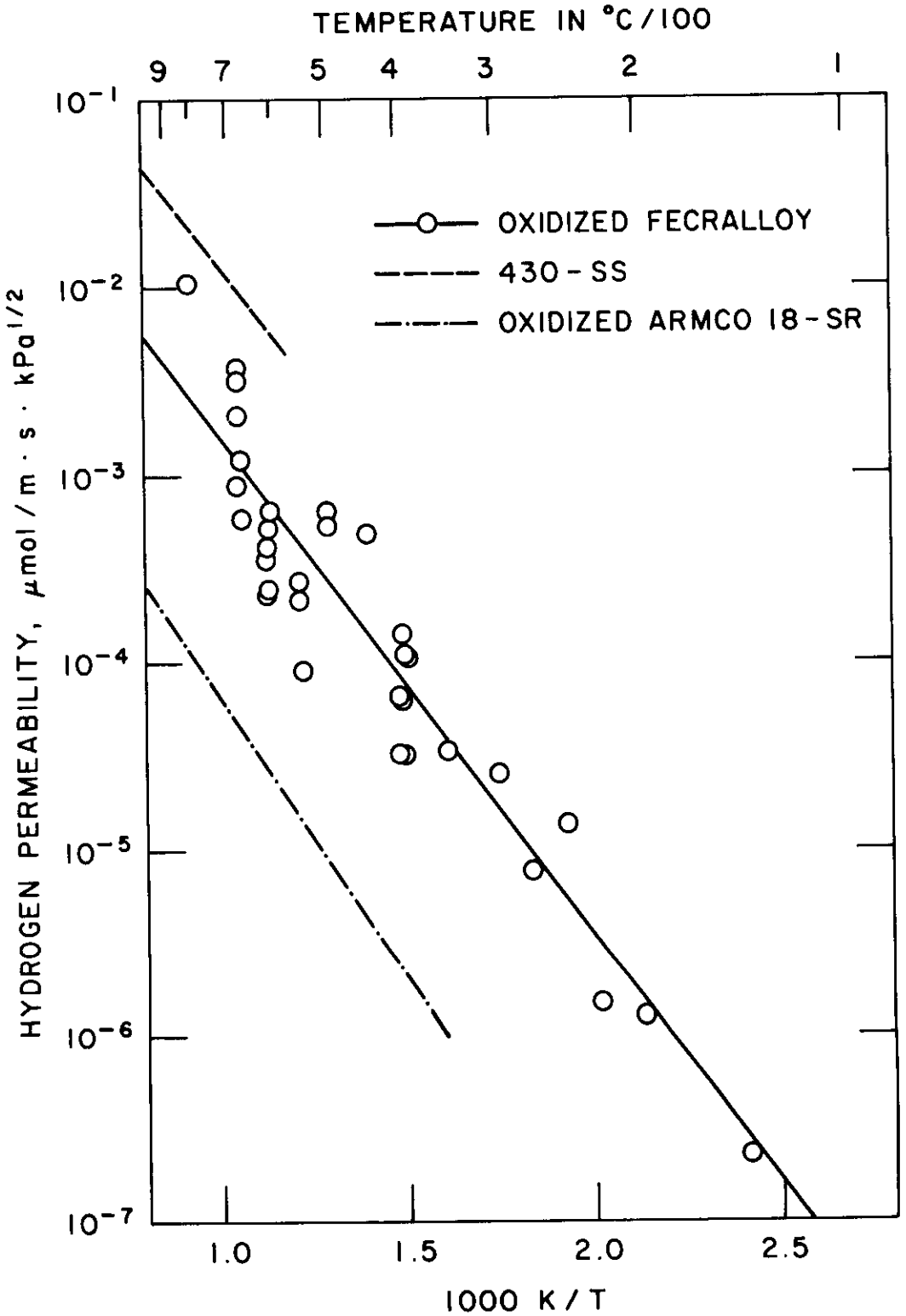

Fig. 9.1.1 Hydrogen Permeation Data for Oxidized Fecralloy (Fe-16Cr-5Al-0.3Y) together with Permeation Curves for 430-SS and Oxidized Armco 18-SR.

observation that the 5 wt.% Al alloy is actually more permeable than the 2 wt.% Al alloy may be indicative of the need for an optimum aluminum content and/or an optimum Al-Cr balance to produce a minimum permeability for oxidized ferritic alloys. The possibility exists that if the oxide-forming potential at the surface of the alloy is too great, a thicker, less-resilient oxide layer tends to form. It may be that the optimum aluminum content for some ferritic alloys actually lies at a value less than 2 wt.%. A search for an 0.5 to 1 wt.% ferritic alloy with 10 to 18 wt.% Cr is in progress.

9.1.5 Conclusions

Results obtained during the tensimetric hydriding of Ti-6Al-2Sn-4Zr-2Mo-0.08Si plates to the 500 to 700 wppm H range show that accurate hydrogen additions to titanium alloys can be made by this method, but that the dehydriding of the plates from the 500 to 700 wppm H range to lower values may require heating of the material to well above 600°C.

The aluminum content of Fe-Cr-Al alloys required for maximum hydrogen permeation resistance in oxidizing environments may be (1) related to the chromium content and (2) less than 2 wt.% for some ferritic alloy systems.

9.1.6 References

1. For a review, see Chapter 7 of the report *Alloy Development for Irradiation Performance Quarterly Progress Report for the Period Ending December 31, 1979*, U.S. Department of Energy Report DOE/ET-0045/1, pp. 81-118 (1980).
2. E. H. Van Deventer, A. G. Rogers, and V. A. Maroni, "Hydrogen Dissolution and Permeation Studies of ADIP Program Alloys," *Alloy Development for Irradiation Performance Quarterly Progress Report Ending for the Period Ending December 31, 1979*, U.S. Department of Energy Report DOE/ET-0045/1, pp. 140-147 (1980).
3. E. H. Van Deventer, V. A. MacLaren, and V. A. Maroni, "Hydrogen Permeation Characteristics of Aluminum-Coated and Aluminum-Modified Steels," *J. Nucl. Mater.* 88: 168-173 (1980).

4. V. A. Maroni and E. H. Van Deventer, "Materials Considerations in Tritium Handling Systems," *J. Nucl. Mater.* 85 & 86: 257-269 (1979).

9.2 VANADIUM ALLOY/LITHIUM PUMPED-LOOP STUDIES - D. L. Smith, R. H. Lee, and R. M. Yonco (Argonne National Laboratory)

9.2.1 ADIP Task

I.A.3. Chemical and Metallurgical Compatibility Analysis. The results presented in this section contribute to Subtask I.A.3.4, Milestones I.A.3.c and I.A.3.d.

9.2.2 Objective

The objective of this work is to develop preliminary data on the compatibility of candidate Path C alloys exposed to a flowing lithium environment. The major effort involves investigations of nonmetallic element interactions in reactive/refractory metal-lithium systems and the effects of lithium exposure on the mechanical properties of refractory metal alloys. Information relating to atmospheric contamination of reactive/refractory metal alloys will also be generated. Specific near-term experiments include measurements of the distribution of nonmetallic elements between selected refractory metals and lithium. The results of this work will contribute to the data base that relates compatibility and corrosion phenomena to other alloy development activities and will provide a basis for selecting candidate Path C alloys for further development.

9.2.3 Summary

The stainless steel-clad vanadium alloy loop with circulating lithium has continued to operate through the second quarter of FY 1980. Test samples of zirconium, vanadium, V-15Cr-5Ti, titanium, and yttrium have been exposed at 600°C to investigate the distribution of nonmetallic elements in lithium/refractory metal systems. The zirconium, titanium, and yttrium exposures are being used to adjust and evaluate the nonmetallic (O, N, H, and C) concentration in lithium. Results of hydrogen analyses of the test samples have been compared with calculated distribution coefficients for hydrogen. Preliminary measurements of the distribution coefficients for nitrogen between vanadium and lithium at 600°C are in good agreement with calculated values.

9.2.4 Progress and Status

The stainless steel-clad vanadium alloy/lithium pumped loop (SS/V-Cr/Li) has now operated for over *8000* h. Results of analytical work on samples from this loop are discussed below.

9.2.4.1 Hydrogen Distribution Studies

The hydrogen distribution in selected metal-lithium systems has been determined using the SS/V-Cr/Li. Table 9.2.1 summarizes results of hydrogen analyses of vanadium, V-15Cr-5Ti alloy, titanium, zirconium, and yttrium after exposure to lithium at 600°C. The titanium, zirconium, and yttrium specimens were used primarily for monitoring and gettering impurities in the lithium. Because of the relatively high diffusion rates of hydrogen in the metals at 600°C, the measured hydrogen concentrations are assumed to be in equilibrium with the hydrogen concentration in lithium. Although the tests were conducted over a period of approximately one year, the hydrogen concentrations in lithium remained nearly constant in all the tests. Results for zirconium and yttrium are the most consistent, partially because of the larger specimen sizes used for the analysis. Based on calculated distribution coefficients, the hydrogen concentration in lithium can be determined and the hydrogen partial pressure in the system can be calculated.[1,2] Based on these distribution coefficients and the average hydrogen concentrations in zirconium and in yttrium, the calculated hydrogen concentrations in lithium are 117 and 103 wppm, respectively. The corresponding hydrogen partial pressures in lithium are 2.0×10^{-2} and 1.5×10^{-2} Pa (1.5×10^{-4} torr), respectively. The hydrogen concentration in lithium calculated from the titanium results is about a factor of three higher.

The measured hydrogen concentrations in vanadium average 9 wppm, which is significantly higher than one would calculate from the distribution coefficient and the average value of ∿110 wppm hydrogen in lithium. For comparison, the measured hydrogen concentrations in the V-15Cr-5Ti alloy (∿17 wppm) are a factor of two greater than those in vanadium; this is due primarily to the presence of titanium.

TABLE 9.2.1 HYDROGEN ANALYSES OF METAL SAMPLES AFTER EXPOSURE TO LITHIUM AT 600°C

Sample Number	Exposure Time, h	Hydrogen Concentration, wppm
Zr-2	168	21,24
Zr-3	550	20,17
Ti-2	550	104,39
Ti-3	240	110
Ti-4	217	35
Ti-5	286	43,47
Ti-6	304	30,40
Ti-7	476	110,40
Y-2	240	1832,1839
Y-3	217	2056,1937
Y-5	476	1730,1810
v-2	110	10,10
v-3	470	19,<1
V-7	286	10,6
V-9	304	10,10
VA-5[a]	505	15,14
VA-8[a]	286	20,20
VA-10[a]	304	20,10

[a]V-15Cr-5Ti

9.2.4.2 Nitrogen Distribution Studies

Investigations on the redistribution of nitrogen in vanadium-alloy/lithium systems have included the measurement of nitrogen concentrations in lithium by the micro-Kjeldahl method and chemical analysis of alloy samples after exposure to lithium at 600°C. The lithium temperature was maintained at 400°C for the first 700 h of operation and at 600°C thereafter. Table 9.2.2 summarizes the results of nitrogen analyses of lithium, showing the decrease from an initial concentration of over 1300 wppm to a value of <20 wppm after nearly 3000 h. The increase in nitrogen concentration indicated for sample VL-7 is attributed to contamination during a 140 h loop shutdown just prior to sampling. Sample VL-8 exhibited a return to concentrations below 20 wppm after extended operation.

TABLE 9.2.2 NITROGEN ANALYSES OF LITHIUM FROM THE VANADIUM-ALLOY TEST LOOP

Sample Number	Operation Time, h	Lithium Temp., °C	Nitrogen Concentration, wppm	Comments
VL-1	305	400	1342 ± 25	Represents initial concentration.
VL-2	308	400	1325 ± 25	Duplicate sample.
VL-4	1389	600	95 ± 25	After exposure of Zr foil for 120 h at 400°C and operation of loop for 720 h at 600°C.
VL-5	1889	600	36	After exposure of Zr foil for 168 h.
VL-6	2875	600	14	After exposure of sample V-3 for 470 h.
VL-7	3860	600	62	Shortly after loop shutdown for 140 h.
VL-8	7410	600	13	After exposure of V sample V-9 for 304 h.

Zirconium specimens were exposed to the lithium to remove the nitrogen. Calculated distribution coefficients for nitrogen indicate that zirconium should be an effective getter for nitrogen in lithium.[3] Because of the relatively low diffusivity of nitrogen in zirconium, nitrogen pickup will be limited to the surface regions. Gold-colored films were observed on the surfaces of zirconium specimens after exposure. Analyses showed the layers to be of complex composition with a significant amount of nitrogen. Electron microprobe analysis revealed a uniform 4-μm layer on zirconium foil samples exposed for 550 h at 600°C. Vacuum fusion analysis of this sample indicated an average nitrogen concentration of 555 wppm. Analysis of the same foil after removal of a 6-μm surface layer showed a net nitrogen concentration of

246 wppm in the foil compared to a preexposure concentration of 101 wppm. A mass balance indicates an average nitrogen concentration of ∿3100 wppm in the surface layers. The calculations indicate that ZrN should form on the surface of zirconium specimens exposed to lithium containing nitrogen concentrations of much less than I wppm.[3]

Vanadium wire and foil samples were exposed to lithium at 600°C for periods of 300 to 500 h. Table 9.2.3 summarizes the results of nitrogen analyses for these samples. Nitrogen concentrations in the samples before exposure are also given in the table. All samples were chemically cleaned before analysis. Based on solid-state diffusion control and the reported diffusivity of nitrogen in vanadium, the measured nitrogen increase for specimen V-3 should be 2.75% of the equilibrium value and the increases in specimens V-7 and V-9 should be ∿94% of the equilibrium values. Since the nitrogen concentration did not change much in any of the specimens, the measured values give a fairly accurate indication of the equilibrium concentration. The nitrogen analysis of lithium designated VL-6 was taken immediately after removal of specimen V-3. From the value of 14 wppm nitrogen in lithium, the calculated distribution coefficient (weight ratio) is 38. This value compares with a calculated distribution coefficient of 138 for V-N-Li.[3] Experimental distribution coefficients obtained from specimens V-7 and V-9 are 60 and 64, respectively, if one assumes a nitrogen concentration in lithium of 13 wppm.

Similar results for nitrogen analyses of V-15Cr-5Ti alloy specimens are also summarized in Table 9.2.3. Both specimens VA-8 and VA-IO show modest increases in nitrogen concentrations compared with the unexposed specimens. Assuming that the diffusivity for nitrogen in the alloy is the same as for vanadium, concentrations of nitrogen in these samples should be near equilibrium values. As indicated in Table 9.2.3, distribution coefficients for these two samples based on 13 wppm nitrogen in the lithium are 69 and 73, respectively. The nitrogen Concentrations in the two alloy specimens are ∿15% greater than the corresponding values for the vanadium specimens (V-7 and V-9); this is attributed primarily to effects of titanium.

TABLE 9.2.3 NITROGEN ANALYSES OF VANADIUM AND V-15Cr-5Ti ALLOY AFTER EXPOSURE TO LITHIUM AT 600°C

Sample Number	Form	Exposure Time, h	Nitrogen in Wire or Foil, wppm	Distribution Coefficient (wt. fraction)
Vanadium				
V-1	0.25-mm wire	0	382,410	-
v-3	0.25-mm wire	470	500	38[a]
V-6	0.12-mm foil	0	769,794	-
V-7	0.12-mm foil	287	775	60[b]
V-9	0.12-mm foil	304	828,844	64[b]
V-15Cr-5Ti				
VA-4	0.11-mm foil	0	760,795	-
VA-8	0.11-mm foil	287	858,927	69[b]
VA-10	0.11-mm foil	304	938,956	73b

[a]Based on 14 wppm nitrogen in lithium.

[b]Based on 13 wppm nitrogen in lithium.

9.2.5 Conclusions

1. Measured hydrogen concentrations of 9 wppm in vanadium and 17 wppm in V-15Cr-5Ti alloy were obtained after exposure to 600°C lithium containing 1.110 wppm hydrogen. The relative hydrogen concentrations in vanadium are somewhat higher than predicted.

2. Measurements of the distribution coefficients for nitrogen between vanadium and lithium at 600°C are in good agreement with calculated values. The nitrogen concentrations in V-15Cr-5Ti alloy specimens are 2.15%greater than in unalloyed vanadium after exposure to lithium at 600°C.

9.2.6 References

1. K. Natesan and D. L. Smith, "Effectiveness of Tritium Removal from a CTR Lithium Blanket by Cold-Trapping Secondary Liquid Metals Na, K, and NaK," *Nucl. Technol. 22: 138* (1974).
2. S. D. Clinton and J. S. Watson, "The Solubility of Tritium in Yttrium at Temperatures from 250-440°C," *J. Less Comm. Met. 66: 51* (1979).
3. D. L. Smith and K. Natesan, "Influence of Nonmetallic Impurity Elements on the Compatibility of Liquid Lithium with Potential CTR Containment Materials," *Nucl. Technol. 22: 392 (1974).*

9.3 COMPATIBILITY OF 2 1/4 Cr-1 Mo STEEL WITH STATIC LITHIUM — P. F. Tortorelli and J. H. DeVan (ORNL)

9.3.1 ADIP Task

ADIP Task I.A.3, Perform Chemical and Metallurgical Compatibility Analyses.

9.3.2 Objective

The purpose of this program is to determine the chemical compatibility of fusion reactor candidate materials with metallic lithium. Specimens are exposed to static lithium-containing selected solute additions to identify the kinetics and mechanisms that govern corrosion by lithium. Specific program objectives are: (1) to determine the effects of N, C, H, and O on apparent solubilities in Li; (2) to determine the C and N partitioning coefficients between alloys and Li; (3) to determine the effects of soluble (Ca, Al) and solid (Y, Zr, Ti) active metal additions on corrosion by Li; and (4) to determine the tendencies for dissimilar-metal mass transfer.

9.3.3 Summary

Tensile specimens of 2 1/4 Cr-1 Mo steel were exposed to static molten lithium at 500°C. After 500 and 1000 h, weight changes were negligible; however, the yield and ultimate tensile strengths of the steel were consistently lower by 4 to 10% than those of specimens thermally aged in argon for the same lengths of time. Analysis of the post-test lithium indicated a transfer of carbon from the steel to the lithium during exposure. Specimens that were normalized and tempered lost less carbon than those that were simply annealed. The carbon concentration of the post-test lithium was greater than predicted by thermodynamic calculations. Therefore, it is believed that the predicted concentrations are in error because the assumption of equilibrium among carbon, molybdenum, and chromium in the steel is not met by the heat treatment conditions used.

9.3.4 Progress and Status

Tests of 2 1/4 Cr-1 Mo steel in static molten lithium were initiated as the first stage in a study of the compatibility of ferritic steels with lithium. These preliminary experiments will be used to establish baseline data on carbon transfer and its effects on mechanical properties as an aid in determining the optimum allay composition and microstructure for lithium compatibility.

Specimens of 2 1/4 Cr-1 Mo steel that were given two different heat treatments were tested. The first heat treatment, HT1, involved austenitizing for 1 h at 930°C in flowing argon fallowed by furnace cooling to room temperature at about 60°C/h. The resulting microstructure is shown in Fig. 9.3.1(a). The second heat treatment, HT2, consisted of a similar austenitizing procedure fallowed by rapid cooling to room temperature in argon and tempering at 700°C for 1 h. This produced the microstructure shown in Fig. 9.3.1(b).

Lithium and tensile specimens of 2 1/4 Cr-1 Mo steels with gage lengths of 12.7 mm and 3.2- by 0.6-mm gage sections were sealed inside 22.1-mm-ID by 1.6-mm-wall capsules. The capsules were identical in composition and heat treatment to the internal test specimens. One control sample from each heat treatment was placed in an argon-filled capsule for each test temperature. The capsules were then placed in tube furnaces at *400,* 500, and 600°C for various times.

At present, static tests of 2 1/4 Cr-1 Mo steel exposed for 500 and 1000 h to 500°C lithium and argon have been completed. Weight change and tensile results are summarized in Table 9.3.1. Note that while the weight changes were negligible, the yield and ultimate tensile strengths of 2 1/4 Cr-1 Mo steel from both heat treatments were consistently lower than those of the specimens that were thermally aged (exposed to argon) under otherwise identical conditions. These differences were greater than the experimental scatter of the data.

The partitioning of carbon between the 2 1/4 Cr-1 Mo steel and lithium is of concern since the properties of the steel are sensitive to its carbon concentration. The redistribution of carbon was determined by analyzing the post-test lithium (see Table 9.3.2); the present data, which

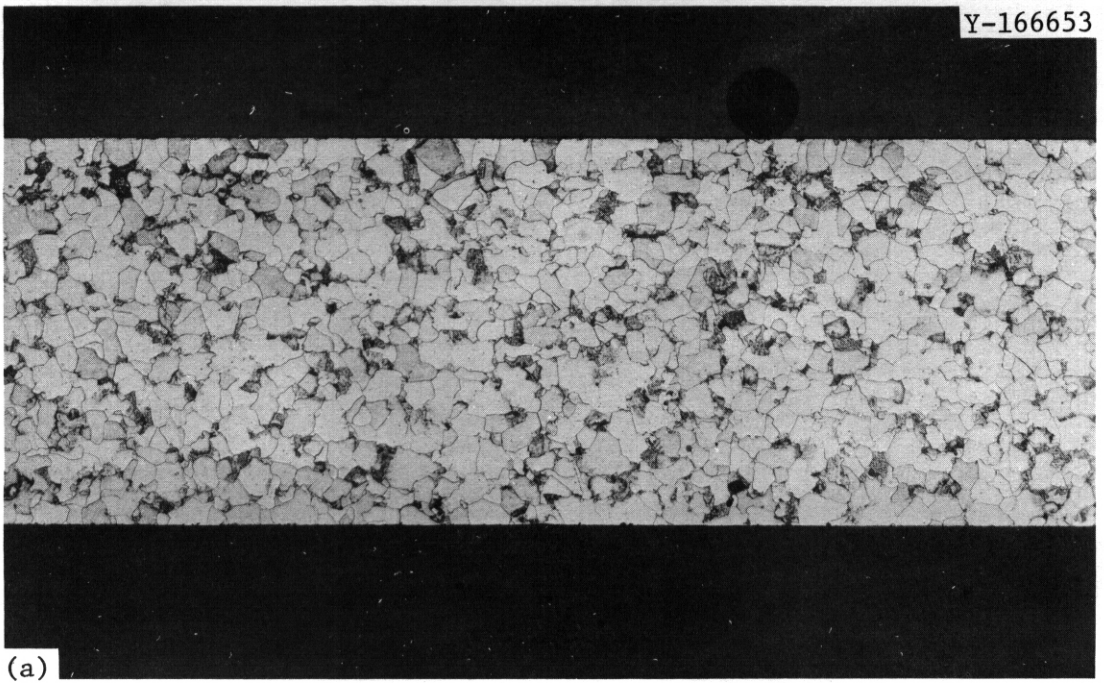

100 μm

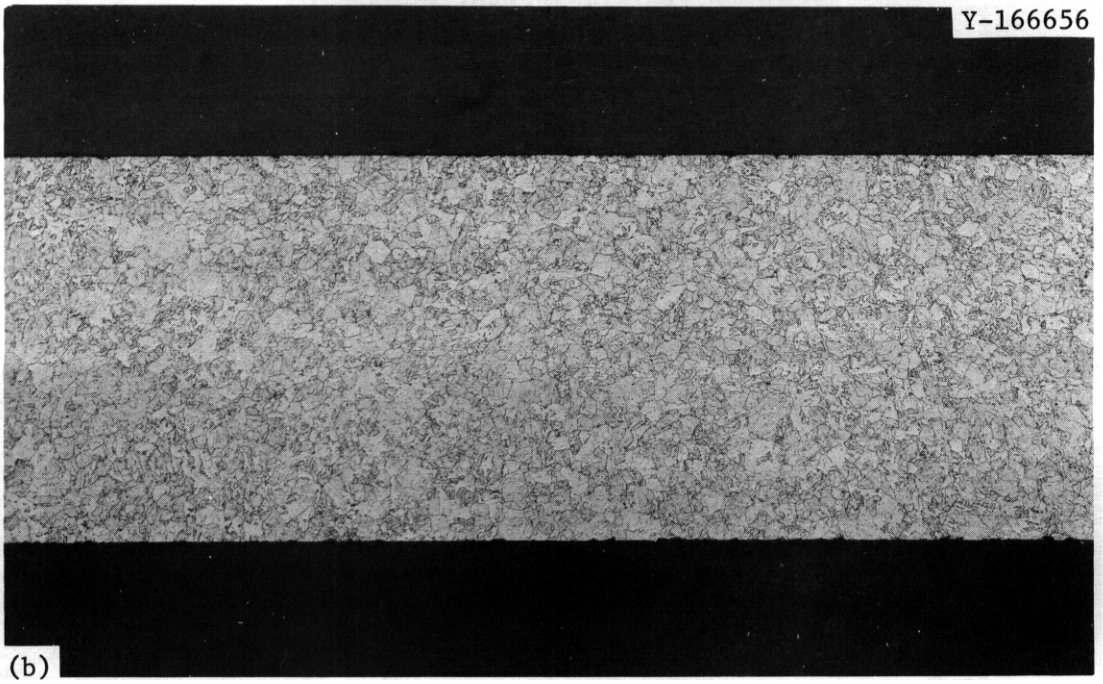

Fig. 9.3.1. The 2 1/4 Cr-1 Mo Before Exposure to Lithium.
(a) Annealed at 930°C for 1 h and cooled at 60°C/h to room temperature.
(b) Normalized at 930°C for 1 h and tempered at 700°C for 1 h.

Table 9.3.1. Weight Change and Tensile Properties[a] of 2 1/4 Cr-1 Mo Steel Exposed to Static Argon and Lithium at 500°C

Heat Treatment	Exposure Time (h)	Environment	Weight Change (g/m^2)	Yield Strength (MPa)	Ultimate Tensile Strength (MPa)	Elongation (%)
HT1	500	Ar	-0.2	265	521	16.4
HT1[b]	500	Li	-0.7	230	495	17.5
HT2	500	Ar	0.0	499	637	10.2
HT2[b]	500	Li	-0.4	480	608	8.2
HT1	1000	Ar	-0.5	265	524	16.5
HT1[b]	1000	Li	-0.8	236	498	15.8
HT2	1000	Ar	-0.7	499	634	8.1
HT2[b]	1000	Li	-0.2	459	568	9.3

[a]Room temperature tensile tests with a strain rate of 1.67×10^{-3}/s.

[b]Average of two specimens.

Table 9.3.2. Concentrations of Carbon in Lithium[a]

Condition of Lithium	Concentration (wt ppm)
Unexposed (control)	3
From 500-h, 500°C HT1 capsule[b]	243
From 500-h, 500°C HT2 capsule[b]	103

[a]Analyses were performed by R. M. Yonco of Argonne National Laboratory using the acetylene-evolution method. This method is described in: E. M. Hobart and R. G. Bjork, "Validity of Determining Carbon in Lithium by Measurement of Acetylene Evolved on Hydrolysis," *Anal. Chem.* 39: 202 (1967).

[b]Filtered lithium samples were taken at 500°C.

is only from the 500-h tests, showed a significant increase in the carbon concentration of the lithium, thereby indicating the transfer of carbon from the steel. The decarburization of the 2 1/4 Cr-1 Mo steel in molten lithium can account for the observed decreases in the yield and ultimate tensile strengths of the exposed specimens (see Table 9.3.1). Metallographic examination of polished cross sections of exposed steel showed no obvious indications of decarburized layers, although this is not unusual for the type of microstructures used for these tests.[1]

It is possible to calculate the equilibrium distribution of carbon between 2 1/4 Cr-1 Mo steel and lithium from a knowledge of the solubilities of carbon in the components and of the free energies of formation of the respective carbides (Li_2C_2 and Cr_7C_3 or $Cr_{23}C_6$).[2,3] These calculations, however, predict less decarburization than the amount actually measured from the carbon uptake by the lithium. The difference between the calculated and measured carbon distribution in these tests may result from the assumption that carbon in solution in the steel is equilibrated with chromium and molybdenum before lithium exposure. Studies of the decarburization of 2 1/4 Cr-1 Mo steel in flowing sodium have shown that decarburization is strongly dependent on the prior heat treatment of the steel[4] and that the effect of the heat treatment is to change the composition and hence the chemical and kinetic stability of the carbides produced. If the equilibrium concentrations of carbon in the steel and in lithium are ultimately set by the Cr_7C_3, the carbon will likely be transferred back to the steel at longer times. Forthcoming data on the carbon concentrations of the lithium after 1000- and 3000-h exposures will greatly aid our understanding of the distribution in this system. As in the present studies, results from sodium work[4] indicate that the carbon loss from normalized and tempered specimens was less rapid than from specimens that were simply annealed.

9.3.5 Conclusions

1. Exposure of 2 1/4 Cr-1 Mo steel to 500°C static lithium resulted in a small (4 to 10%) decrease in its yield and ultimate tensile strength.

2. The carbon concentration of the post-test lithium was greater than the amount predicted by thermodynamic calculations. The amount of carbon loss from specimens that were normalized and tempered was less than that from specimens that were simply annealed.

9.3.6 Reference

1. D. W. Koch and P. J. Kovach, "Materials Examination of a Model Sodiun Heated Steam Generator," BAW-1280-37 (June 1966).
2. T. F. Kassner and D. L. Smith, "Calculation on the Kinetics of Oxygen Solution in Tantalum and Niobium in a Liquid-Sodium Environment," ANL-7335 (September 1967).
3. K. Natesan and T. F. Kassner, "Calculations of the Thermodynamic Driving Force for Carbon Transport in Sodium-Steel Systems," ANL-7646 (December 1969).
4. K. Matsumoto et al., "Carbon Transfer Behavior of Materials for Liquid-Metal Fast Breeder Reactor Steam Generators," *Nucl. Technol.* 28: 452-70 (1976).

9.4 MASS TRANSFER OF TYPE 316 STAINLESS STEEL AND PATH B ALLOYS IN LITHIUM THERMAL-CONVECTION LOOPS — P. F. Tortorelli and J. H. DeVan (ORNL)

9.4.1 ADIP Task

ADIP Task I.A.3, Perform Chemical and Metallurgical Compatibility Analyses.

9.4.2 Objective

The purpose of this task is to evaluate the corrosion resistance of candidate first-wall materials to flowing lithium in the presence of a temperature gradient. Corrosion rates (in both dissolution and deposition) are measured as functions of time, temperature, additions to the lithium, and flow conditions. These measurements are combined with chemical and metallographic examinations of specimen surfaces to establish the mechanisms and rate-controlling processes for dissolution and deposition reactions.

9.4.3 Summary

Metallographic and surface composition data are reported for the corrosion of ADIP alloys B1 and B3 [58 Fe—24.5 Ni—10 Cr—1 Mo—1 Mn—1.5 Al—3 Ti (wt %) and 55 Fe-30 Ni-12 Cr—2 Nb-1 Mn—2 Ti (wt %), respectively] in lithium flowing between 500 and 300°C. At 500°C both alloys were severely depleted of nickel and exhibited porous near-surface regions. Alloy B3 had a larger volume fraction of porosity. Results on deposition rates vs exposure time in lithium-type 316 stainless steel thermal-convection loops are also presented. Deposition rates in lithium flowing between 600 and 450°C are initially much higher than those measured at later operating times. The decrease in the deposition rate can be correlated with observed changes in the deposition process.

9.4.4 Progress and Status

As described previously[1] two types of thermal-convection loops (TCLs) are being used to evaluate the compatibility of Path A and B materials

with lithium. The first type is in the form of a 0.46- by 0.64-m parallellogram that contains interlocking tab specimens of the same material as the loop. The loop is operated without interruption for 3000 to 10,000 h and is then cut open to remove tab specimens for analysis. The second type of TCL is larger (0.48 by 0.76 m) and is designed so that tab specimens can be withdrawn and inserted without altering the loop operating conditions. In this way corrosion rates can he monitored at selected time intervals for a given set of test specimens.

An alloy 800 [46 Fe—32 Ni—21 Cr (wt %)] TCL of the first type has been used to test ADIP alloys B1 and B3 in flowing lithium. The loop circulated lithium between 500 and 300°C for 2832 h before being terminated as a result of flow restrictions. The resulting weight changes of coupons situated around the loop were reported earlier.[2] The corrosion rates of ADIP alloys B1 and B3 were significantly greater than those of type 316 stainless steel exposed to flowing lithium under similar conditions. Metallographic examination of selected loop coupons has now been completed and has shown that the type and extent of attack of alloys B1 and B3 were similar to that of type 316 stainless steel (see Fig. 9.4.1), although the maximum dissolution rates of the Path B alloys were more than four times greater. The average depths of the porosity zones at 500°C were about 18, 15, and 17 μm for type 316 stainless steel, alloy B1, and alloy B3, respectively. Magnified cross-sectional views of alloys B1 and B3 are shown in Fig. 9.4.2. Although the depth of porosity was just slightly greater for B3, the average void size of the higher nickel alloy B3 was larger than for alloy B1. Thus, the enhanced weight loss in flowing lithium of alloy 83 appears to result from dissolution of a larger volume fraction of the near-surface region.

Electron microprobe analysis revealed that the near-surface regions of alloys B1 and B3 at 500°C were depleted in nickel and chromium. This behavior is similar to that observed for type 316 stainless steel:[3] nickel and chromium are preferentially leached, thus leading to a predominately iron-rich surface layer. Since alloys B1 and B3 suffered greater weight losses than type 316 stainless steel in direct correspondence to their respective nickel concentrations, it appears that

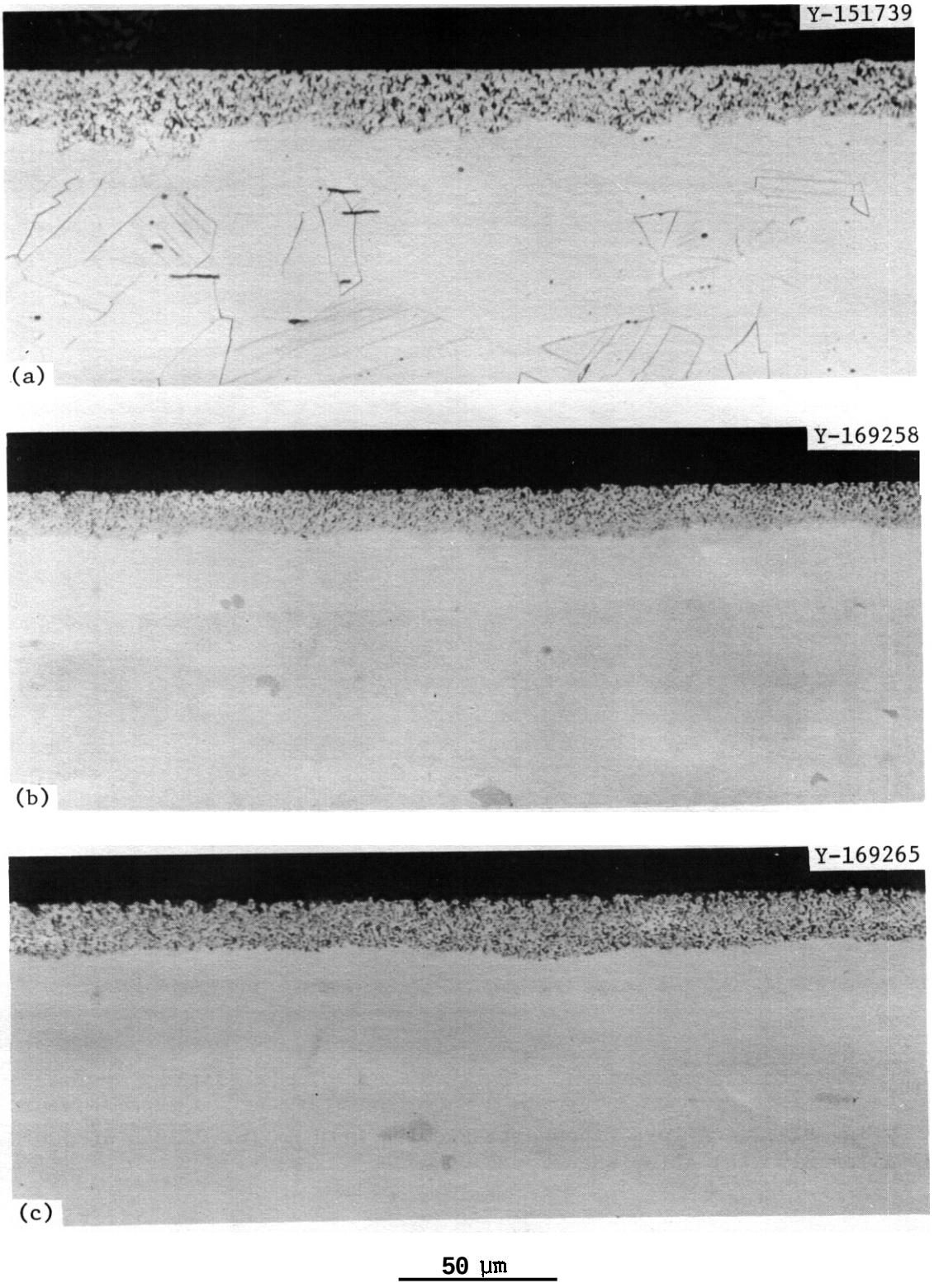

Fig. 9.4.1. Alloys Exposed to Flowing Lithium at 500°C. (a) Type 316 stainless steel, 3000 h. (b) Alloy B1, 2832 h. (c) Alloy B3, 2832 h.

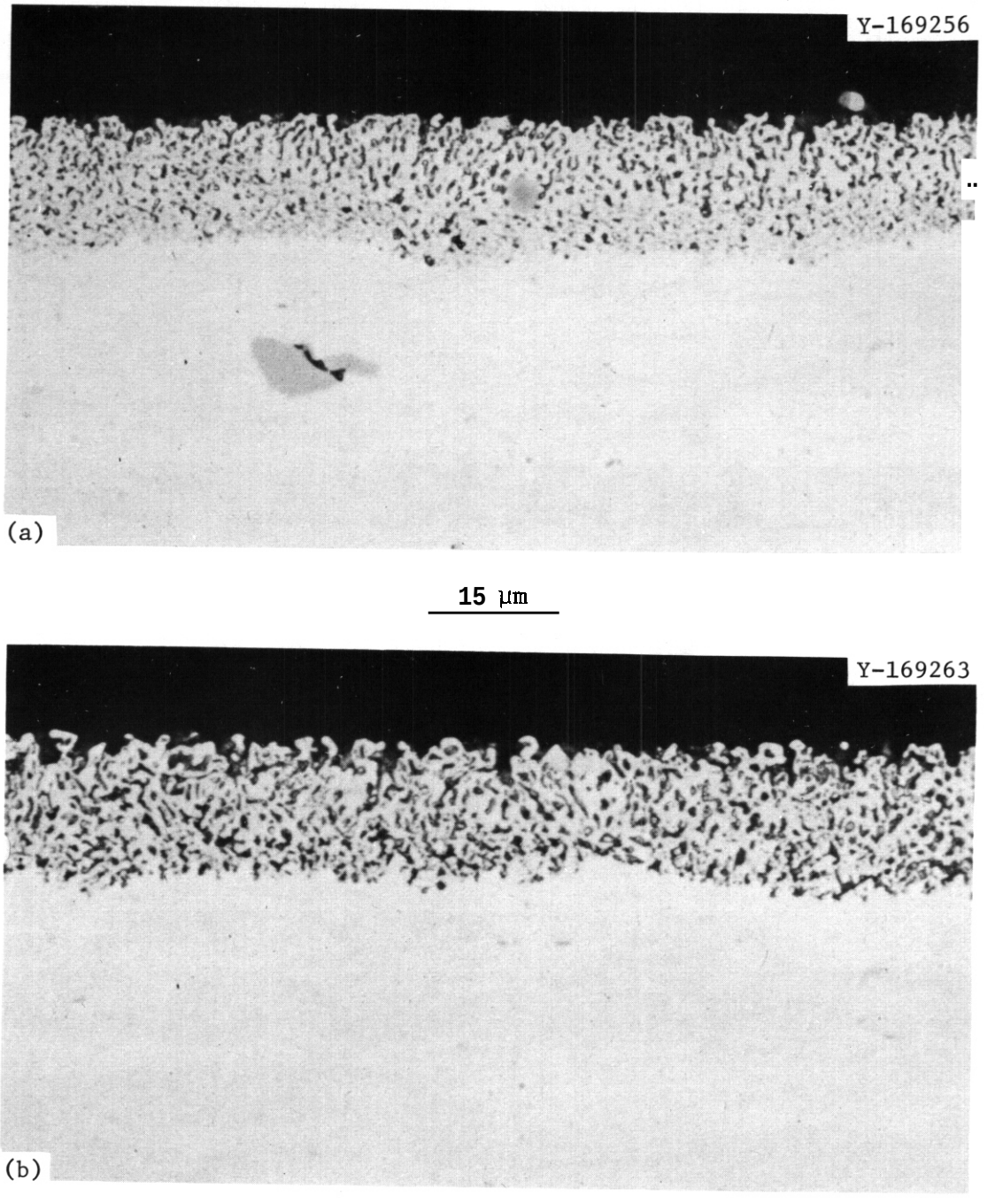

Fig. 9.4.2. Alloys Exposed to Flowing Lithium for 2832 h at 500°C. (a) Alloy B1. (b) Alloy B3.

the higher the starting nickel content of the alloy, the greater the volume of nickel removed from the alloy by the lithium. The average near-surface concentrations of the major elements of the coupons in this loop were determined by x-ray fluorescence, and the results from the dissolution region are given in Table 9.4.1. Note that the degree of nickel and chromium depletion increased with increasing temperature in the loop's hot leg with an average surface layer concentration of about 3 wt % Ni at 500°C for both B1 and B3. Since these concentrations are an average over a depth that is at least equal to the extent of the porosity zone, we can expect the nickel concentration of the surface in contact with the lithium to be considerably less than the 3% average; the electron microprobe results are representative of an area closer to the lithium-alloy interface and revealed nickel concentrations of less than 1 wt % for both alloys B1 and B3 at 500°C.

As discussed earlier[2] the pure nickel wire used to connect the loop coupons was completely dissolved in the hotter region of the loop. At that time we reported that this dissolved nickel was probably deposited

Table 9.4.1. Near-Surface Compositions of Coupons in a Lithium Thermal-Convection Loop Operated for 2852 h[a]

Coupon	B1 Composition.[b] wt %			B3 Composition.[b] wt %		
	Fe	Ni	Cr	Fe	Ni	Cr
Unexposed	58.8	28.3	10.1	53.9	34.1	11.4
21	59.4	27.9	10.4	56.3	31.1	11.6
22	63.6	24.4	9.7	67.9	19.4	11.8
23	68.4	18.9	10.0	69.8	17.4	11.8
24	82.0	7.0	9.3	78.2	9.3	11.6
25	84.9	3.8	8.9	80.2	6.5	12.4
26	86.4	3.2	7.8	86.6	3.0	9.5

[a]As determined by x-ray fluorescence.

[b]Sums of concentrations do not equal 100% as a result of the presence of small quantities of other elements such as Mn, Ti, Nb, Al, and Mo (B1 only).

on the cooler surfaces of the loop and thus accounted for the greater net specimen weight gain over net weight loss. The present x-ray fluorescence results confirmed this behavior: a large amount of nickel was detected on the cooler coupons. We also hypothesized[2] that the dissolution of the nickel wire may have buffered the dissolution of the Path B coupons in the hotter zone of the loop. However, the x-ray fluorescence data showed that this did not occur to any significant degree or over an extended time since the surface concentrations of nickel are not higher in the immediate vicinity of the dissolved wire than at positions further away.

The accumulation of deposits in liquid metal systems can be a more serious operational problem than loss of structural integrity resulting from dissolution. This is because of attendant flow restrictions and, in reactor applications, the aggregation of radioactive species in the coolant circuits. Accordingly, the deposition rate vs exposure time in lithium-type 316 stainless steel TCLs of the second type described above was studied. Cold-leg coupons from three loops operating at a maximum temperature of 600°C were weighed after intervals of at least 500 h. Weight gain-vs-time plots for the coupons in the C8 position (about 460°C, see Fig. 9.4.3) of three loops are given in Fig. 9.4.4. The two sets of data in Fig. 9.4.4(b) represent operation before (A) and after (B) replacing part of its cold leg. The deposition rate for a particular location was determined from the least squares slope of the weight gain-vs-exposure time plot for the specimen at that position. The resultant deposition rates are given in Table 9.4.2. Note that the rates computed for test times greater than 3700 h are significantly less than those from shorter exposure measurements. This decrease in deposition rate with time is also apparent in Fig. 9.4.4(c). The data in Table 9.4.2 also show that the maximum deposition rate occurred near the middle of the cooled region of a loop.

The weight gains of the cold-leg coupons were linear with time to about 3000 to 4000 h, at which point the rate of gain markedly decreased. Along with the varying deposition rates, the deposit morphology and composition also changed with loop operating time; it was reported earlier[4] that chromium-rich dendritic crystals formed initially in the colder

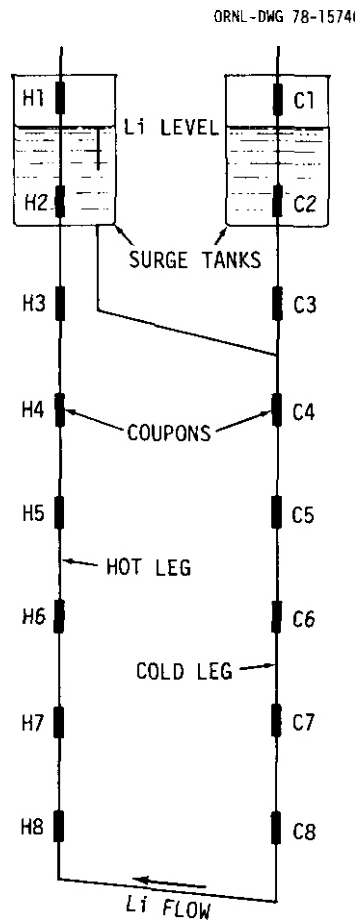

Fig. 9.4.3. Schematic Diagram of Coupons in Positions in a Large LOOP.

region of the loops, but after 9000 h the deposits exhibited a different structure and contained significant amounts of chromium, nickel, and iron. Because of the relatively high surface area per unit volume of these dendritic deposits, they would increase the effective area for deposition over that based on the starting specimen surface area. As the deposit morphology changed to the more layered growth evident at 9000 h, the effective area for deposition would again approximate that of the original specimen surfaces. This factor may be at least partly responsible for the decrease in the apparent deposition rate after 3000 to 4000 h (see Fig. 9.4.4).

The kinetics of the mass transfer process in lithium–stainless steel loops can be treated by the rate equation

$$R = k(i)[C_s(i) - C_x(i)] \quad , \qquad (1)$$

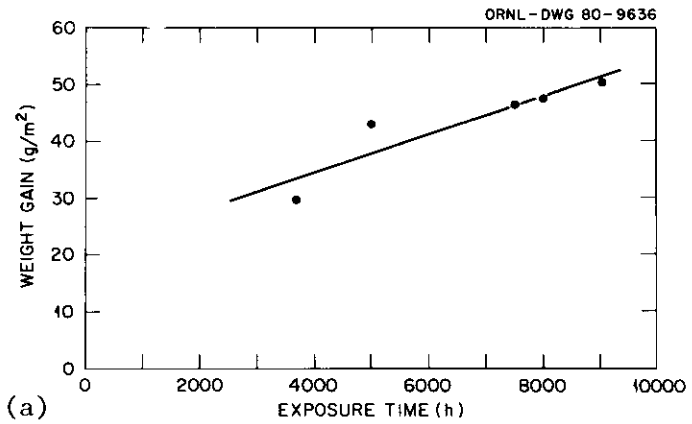

(a)

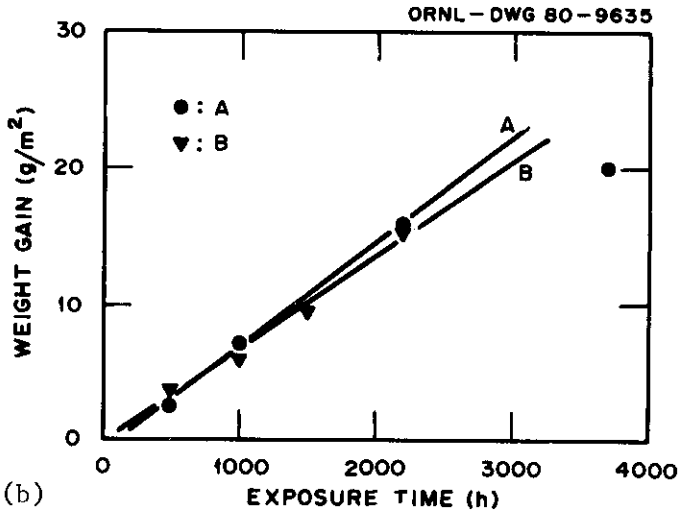

(b)

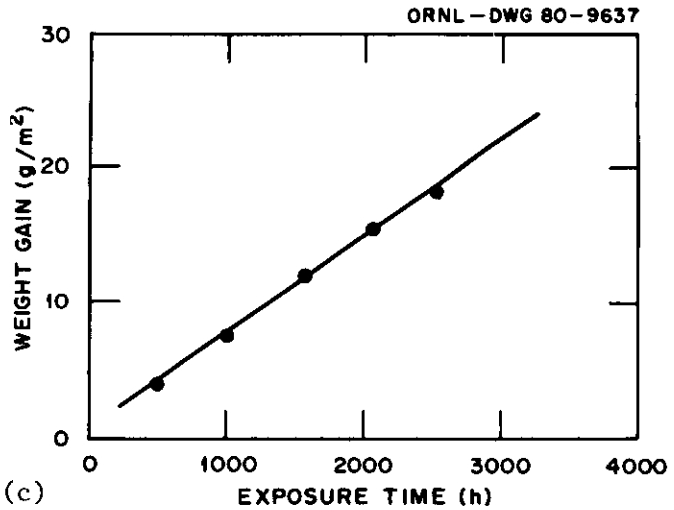

(c)

Fig. 9.4.4. Weight Gains vs Exposure Time for Coupon C8 in Three Lithium-Type 316 Stainless Steel Thermal-Convection Loops. Coupon temperature is about 460°C.

Table 9.4.2. Deposition Rates for Lithium-Type 316 Stainless Steel Thermal-Convection Loops[a]

Coupon	Temperature (°C)	Deposition Rate,[b] mg/m^{2}h			
		LOOP 1	LOOP 2		LOOP 3
		$3750 < t < 9034$ h	$t < 2200$ h		$t < 2520$ h
			A	B	
c4	525	1.3	7.2	5.6	7.5
c5	510	2.8	7.0	8.1	8.6
C6	490	3.2	7.6	8.2	8.0
c7	475	4.2	7.4	7.2	8.1
C8	460	3.3	7.8	7.0	7.2

[a]Maximum loop temperature = 600°C; ΔT = 150°C.

[b]t = time.

where

R = the rate of dissolution (+) or deposition (−),

$k(i)$ = the rate constant for the dissolution (k_s) or deposition (k_p) of element i,

$C_s(i)$ = the solubility of i in lithium at temperature T,

$C_x(i)$ = the actual concentration of i in lithium at point x in the loop, which eventually becomes constant with time.

When C_x is greater than C_s, deposition occurs. We can attribute the occurrence of the maximum deposition rates at the central part of the cold leg (see Table 9.4.2) to a competition between two factors.[5] As seen in Eq. (1) the deposition rate is a product of the rate constant (k) and the supersaturation. Since the former decreases while the latter increases with decreasing temperature, the maximum deposition rate should occur at an intermediate temperature (which happens to be near the middle of the cold leg).

It has been reported in a preceding quarterly[4] that the chromium dendrites that formed initially in lithium-type 316 stainless steel thermal-convection circuits were the cause of cold-leg flow restrictions that eventually forced the termination of two loops after 5000 and 10,000 h of operation. The cold legs of these loops have been replaced, and no change in the flow characteristics of these loops after about an additional *4000* h of operation has been detected. We assume that the deposits now being formed have a morphology and composition similar to those longer term Fe-Ni-Cr deposits described above and that plugging caused by chromium dendrites should be a transient effect associated with initial loop operation. Confirmation of this point would mean that a lithium system could conceivably be designed to accommodate or trap these high aspect ratio crystals during early operation and that deposition rates thereafter would be acceptable in longer term flow restrictions.

9.4.5 Conclusions

1. Alloys B1 and B3 were severely depleted of nickel after exposure to flowing lithium at 500°C for 2832 h and exhibited porous near-surface regions. The higher nickel alloy of the two, B3, had a larger volume fraction of porosity.

2. The deposition rate in lithium-type 316 stainless steel systems with a maximum temperature of 600°C (ΔT = 150°C) attained a steady-state value that was significantly less than the rate during the first 3000 to 4000 h. The decrease in the deposition rate can be correlated with observed changes in the deposition process.

3. Since it appears that plugging of lithium-type 316 stainless steel TCLs is a transient effect associated with initial loop operation, a lithium system possibly could be designed to avoid this problem.

9.4.6 References

1. J. H. DeVan and J. R. DiStefano, "Thermal-Convection Loop Tests of Type 316 Stainless Steel in Lithium," ADIP *Quart. Prog. Rep. Mar. 31, 1978*, DOE/ET-0058/1, pp. 200–08.

2. P. F. Tortorelli and J. H. DeVan, "Corrosion of Type 316 Stainless Steel and Alloys B1 and B3 in Lithium Thermal-Convection Loops," *ADIP Quart. Prog. Rep. Dec. 31, 1979*, DOE/ET-0058/8, pp. 158-65.

3. P. F. Tortorelli and J. H. DeVan, "Thermal-Gradient Mass Transfer in Lithium-Stainless Steel in Lithium," *J. Nucl. Mater.* 85 & 86(II, A): 289-93 (1979).

4. P. F. Tortorelli and J. H. DeVan, "Mass Transfer Deposits in Lithium-Type 316 Stainless Steel Thermal-Convection Loops," *ADIP Quart. Prog. Rep. June 30, 1979*, DOE/ET-0058/6, pp. 89-94.

5. J. H. DeVan, "Corrosion of Iron- and Nickel-Base Alloys in High-Temperature Sodium and NaK," pp. 643—59 in *Alkali Metal Coolants* (Proceedings of a Symposium, Vienna, 28 November-2 December, 1966) International Atomic Energy Agency, 1967.

DOE/ER-0045/2
Distribution
Category
uc-20, 20c

DISTRIBUTION

1–4. Argonne National Laboratory, 9700 South Cass Avenue, Argonne, IL 60439

L. Greenwood
V. Maroni
D. L. Smith
H. Wiedersich

5–6. Battelle-Pacific Northwest Laboratory, P.O. Box 999, Richland, WA 99352

J. L. Brimhall
D. Dingee

7. Carnegie-Mellon University, Schenley Park, Pittsburgh, PA 15213

J. C. Williams

8–203. Department of Energy, Technical Information Center, Office of Information Services, P.O. Box 62, Oak Ridge, TN 37830

For distribution as shown in TID-4500 Distribution Category, UC-20 (Magnetic Fusion Energy), and UC-20c (Reactor Materials)

204–209. Department of Energy, Office of Fusion Energy, Washington, DC 20545

M. M. Cohen
T. C. Reuther, Jr. (5 copies)

210. Department of Energy, Oak Ridge Operations Office, P.O. Box E, Oak Ridge, TN 37830

Office of Assistant Manager for Energy Research and Development

211. General Atomic Company, P.O. Box 81608, San Diego, CA 92138

S. N. Rosenwasser

212–218. Hanford Engineering Development Laboratory, P.O. Box 1970, Richland, WA 99352

D. G. Doran
D. S. Gelles
J. J. Holmes
R. E. Nygren
E. C. Opperman
R. W. Powell
J. L. Straalsund

219–221. Lawrence Livermore Laboratory, P.O. Box 808, Livermore, CA 94550

E.N.C. Dalder
M. Guinan
C. M. Logan

222. Massachusetts Institute of Technology, Cambridge, MA 02139

D. J. Rose

223–224. McDonnell Douglas Astronautics Company, East, P.O. Box 516, St. Louis, MO 63166

J. W. Davis
D. L. Kummer

225–227. Naval Research Laboratory, Washington, DC 20375

Superintendent, Materials Science and Technology Division
J. A. Sprague
H. Watson

228–261. Oak Ridge National Laboratory, P.O. Box X, Oak Ridge, TN 37830

Central Research Library (2 copies)
Document Reference Section
Laboratory Records Department (2 copies)
Laboratory Records Department, RC
ORNL Patent Section
B. G. Ashdown
E. E. Bloom (10 copies)
D. N. Braski
J. H. DeVan
T. A. Gabriel
M. L. Grossbeck
M. R. Hill (3 copies)
K. C. Liu

P. J. Maziasz
C. J. McHargue
T. K. Roche
J. L. Scott
K. R. Thoms
P. F. Tortorelli
F. W. Wiffen

262—263. Sandia National Laboratories, Livermore Division 8316, Livermore, CA 94550

J. Swearengeo
W. Baller

264. University of California, Department of Chemical, Nuclear, and Thermal Engineering, Los Angeles, CA 90024

R. W. Conn

265. University of California, Santa Barbara, CA 93106

G. R. Odette

266. University of Virginia, Department of Materials Science, Charlottesville, VA 22901

W. A. Jesser

267. University of Wisconsin, 1500 Johnson Drive, Madison, WI 53706

W. G. Wolfer

268. Westinghouse Electric Company, Fusion Power Systems Department, P.O. Box 10864, Pittsburgh, PA 15236

R. E. Gold

☆U.S. GOVERNMENT PRINTING OFFICE 1980-640-245/150